Investigation of Wall Pressure Fluctuations Induced by Turbulent Boundary Layer Flow with Pressure Gradients

Bei der Fakultät für Maschinenbau

der Technischen Universität Carolo-Wilhelmina zu Braunschweig

zur Erlangung der Würde

eines Doktor-Ingenieurs (Dr.-Ing.)

genehmigte Dissertation

von:	Nan Hu
geboren in (Geburtsort):	Beijing, China

eingereicht am:	04.01.2018
mündliche Prüfung am:	29.05.2018

Vorsitz:	Jun.-Prof. Dr. R. A. D. Akkermans
Gutachter:	Prof. Dr.-Ing. J. W. Delfs
	Prof. Dr.-Ing. W. Schröder

2018

Abstract

Wall pressure fluctuations induced by turbulent boundary layer flow is one major source of cabin noise. Not only the pressure fluctuation magnitude but also the spatial and temporal properties of the fluctuations are relevant for the resulting surface vibration and the noise radiated into the cabin. The one- and two-point properties of the wall pressure fluctuations are studied experimentally and numerically in thesis thesis.

The wall pressure fluctuations beneath a turbulent boundary layer with zero and non-zero pressure gradients were measured at a flat plate configuration in the Aeroacoustic Wind Tunnel Braunschweig. The fluctuating pressure was measured by an L-shaped array of subminiature pressure transducers. The mean flow velocity profiles and the Reynolds stresses within the turbulent boundary layer were obtained using single and crossed hot-wire anemometers, respectively. Adverse and favorable pressure gradients were realized by installing a turnable NACA 0012 airfoil above the plate. The one-point spectrum, the correlation in the streamwise and spanwise directions and the convection velocity for the wall pressure field are analyzed. The effect of the pressure gradients on the wall pressure fluctuations and the corresponding relevant boundary layer parameters are discussed.

Based on the measured data and a dataset of four other experiments at three other test facilities, an empirical model of wall pressure spectra for adverse pressure gradient boundary layers is proposed. Goody's model, which is the most used wall pressure spectrum model for zero pressure gradient boundary layers, is served as the basis for the development of the new model. Predictions of the new model and comparisons with other published wall pressure spectral models for adverse pressure gradient boundary layers are made for the selected dataset. The new model shows good prediction accuracy for the selected dataset and a significant improvement compared to the other published models.

Furthermore, pressure fluctuations within turbulent boundary layers on a flat plate configuration are simulated using synthetic isotropic and anisotropic turbulence generated by the Fast Random Particle-Mesh Method. The averaged turbulence statistics needed for the stochastic realization is provided by a Reynolds averaged Navier-Stokes simulation. Anisotropy of integral lengths scales and Reynolds stress tensors are implemented for the realization of anisotropic turbulence. To determine the fluctuating pressure, a Poisson's equation is solved with unsteady right-hand side source terms derived from the synthetic turbulence realization. The Poisson's equation is solved via fast Fourier transform using Hockney's method. Due to its efficiency, the applied procedure enables us to study, for high Reynolds number flow, the effect of variations of the modelled turbulence characteristics on the resulting wall pressure spectrum. The contributions to wall pressure fluctuations from the mean-shear turbulence interaction term and the turbulence-turbulence interaction term are studied separately. The results show that both contributions have the same order of magnitude. Simulated one-point spectra and two-point correlations of wall pressure fluctuations are analyzed in detail. Convective features of the fluctuating pressure field are well determined. Good agreement for the characteristics of the wall pressure fluctuations is found between the numerical results and databases from the present measured data and other investigators.

Zusammenfassung

Die durch turbulente Grenzschichtströmung induzierten Wanddruckschwankungen sind eine Hauptquelle von Kabinenlärm. Für die resultierende Oberflächenschwingung und das in die Kabine abgestrahlte Geräusch sind nicht nur die Druckschwankungsstärke, sondern auch die räumlichen und zeitlichen Eigenschaften der Schwankungen relevant. Die Ein- und Zweipunkt-Eigenschaften der Wanddruckschwankungen werden in dieser Arbeit experimentell und numerisch untersucht.

Die Wanddruckschwankungen in einer turbulenten Grenzschicht mit Null- und Nicht-Null-Druckgradienten wurden im Aeroakustischen Windkanal Braunschweig an einer flachen Plattenkonfiguration gemessen. Der schwankende Druck wurde mit einer L-förmigen Anordnung von Subminiatur-Druckwandlern gemessen. Die mittleren Geschwindigkeitsprofile und die Reynoldsspannungen innerhalb der turbulenten Grenzschicht wurden unter Verwendung von einzelnen bzw. gekreuzten Hitzdrahtanemometern ermittelt. Positive und negative Druckgradienten wurden durch die Installation eines drehbaren NACA 0012 Profils über der Platte generiert. Das Einpunkt-Spektrum, die Korrelation in der Strömungsrichtung und der Querrichtung und die Konvektionsgeschwindigkeit für den Wanddruck werden analysiert. Die Auswirkung der Druckgradienten auf die Wanddruckschwankungen und die entsprechenden relevanten Grenzschichtparameter werden diskutiert.

Basierend auf den gemessenen Daten und einem Datensatz von vier weiteren Experimenten an drei weiteren Versuchsanlagen wird ein empirisches Modell von Wanddruckspektren für positive Druckgradientengrenzschichten vorgeschlagen. Das Modell von Goody, welches das am meisten verwendete Wanddruckspektrum für Grenzschichten mit Null-Druckgradienten ist, dient als Grundlage für die Entwicklung des neuen Modells. Vorhersagen des neuen Modells und Vergleiche mit anderen veröffentlichten Wanddruckspektralmodellen für Grenzschichten mit positiven Druckgradienten werden für den ausgewählten Datensatz durchgeführt. Das neue Modell zeigt eine gute Vorhersagegenauigkeit für den ausgewählten Datensatz und eine signifikante Verbesserung im Vergleich zu den anderen veröffentlichten Modellen.

Außerdem werden Druckschwankungen innerhalb turbulenter Grenzschichten auf einer flachen Plattenkonfiguration mit den synthetischen isotropen und anisotropischen Turbulenzen simuliert, wobei diese durch die Fast Random Particle-Mesh-Methode erzeugt werden. Die gemittelte Turbulenzstatistik, die für die stochastische Modellierung benötigt wird, wird durch eine Reynolds-gemittelte Navier-Stokes Simulation bereitgestellt. Anisotropie von Längenskalen und Reynolds-Spannungstensoren werden für die Modellierung von anisotropen Turbulenzen implementiert. Um den schwankenden Druck zu bestimmen, wird eine Poisson-Gleichung mit instationären rechtsseitigen Quellterme gelöst, der aus der synthetischen Turbulenzerzeugung abgeleitet wird. Die Poisson-Gleichung wird mittels schneller Fourier-Transformation unter Verwendung der Hockney-Methode gelöst. Aufgrund seiner Effizienz ermöglicht es das angewandte Verfahren, den Einfluss von Variationen der modellierten Turbulenzeigenschaften auf das resultierende Wanddruckspektrum für eine hohe Reynoldszahl-Strömung zu untersuchen. Die Beiträge zu Wanddruckschwankungen aus dem Mittelscherung-Turbulenz-Wechselwirkungsterm und dem Turbulenz-Turbulenz-Wechselwirkungsterm werden getrennt untersucht. Die Ergebnisse zeigen, dass beide Beiträge die gleiche Größenordnung haben. Simulierte Einpunkt-Spektren

und Zweipunkt-Korrelationen von Wanddruckschwankungen werden im Detail analysiert. Konvektive Eigenschaften des fluktuierenden Druckfeldes werden gut bestimmt. Eine gute Übereinstimmung hinsichtlich der Eigenschaften der Wanddruckschwankungen findet sich zwischen den numerischen Ergebnissen, den vorliegenden Messdaten und externen Forschungsergebnissen.

Acknowledgement

The results of this work have been achieved within the DLR project Comfort and Efficiency Enhancing Technologies (CENT). The completion of the Ph.D study is a learning process, not only in the scientific field, but also on a personal level. All happiness and frustration during the study are important life experience for me. Without the help of my supervisor, my colleagues and my family, I would have never accomplished the study. Therefore, I would like to thank all of you for your support and encouragement.

First of all, I would like to thank my supervisor Prof. Dr.-Ing. Jan Delfs for the valuable discussions and advices throughout the study that helped to improve the quality of the current work. My special thanks go to the reviewer Prof. Dr.-Ing. Wolfgang Schröder and the chairman Jun.-Prof. Dr. Rinie Akkermans. I would like also to thank my indispensable mentors Dr.-Ing. Roland Ewert and Dr.-Ing. Michaela Herr for sharing their knowledge and experience in numerical and experimental aeroacoustics and also in scientific writings. Furthermore, many thanks are due to my office mate M. Sc. Karl-Stephane Rossignol for the pleasant professional and personal conversations. I would like also to thank my colleagues Dipl.-Ing. Nils Reiche and Dr.-Ing. Christina Appel for their help of the numerical studies and Dipl.-Ing. Michael Pott-Pollenske, Dipl.-Ing. Heino Buchholz, Danica Knoblich and Jan Täger for their support and assurance for the performance of the experiments.

Last, but not the least, I am especially grateful to my parents and my wife for their encouragement during my Ph.D study and also my life's tough times.

Contents

Nomenclature

Symbols

α, β	empirical constants for Corcos's model
$\beta_\delta, \beta_\Delta$	Clauser's equilibrium parameter related to other boundary layer parameters, $(\delta, \Delta)/Q \cdot dp/dx$
$\beta_{\delta^*}, \beta_\theta$	boundary layer thickness and displacement thickness based Clauser's equilibrium parameter, $(\delta^*, \theta)/\tau_w \cdot dp/dx$
Δ	boundary layer defect thickness, $\delta^*\sqrt{2/C_f}$, or Laplace operator $\nabla \cdot \nabla$
δ	boundary layer thickness or Dirac delta function
δ^*	boundary layer displacement thickness
Δ_{δ/δ^*}	boundary layer related parameter, δ/δ^*
Γ	coherence
κ	Von Kármán constant
$\mathcal{U}_i$	spatial white noise
∇	gradient of
$\nabla \cdot$	divergence of
$\nabla \times$	curl of
ν	kinematic viscosity
ω	angular frequency
Φ	spectrum
ϕ_m	moving axis spectrum
Π_θ	Cole's wake parameter related to the boundary layer momentum thickness, $0.8 \cdot (\beta_\theta + 0.5)^{3/4}$
Π_{δ^*}	Cole's wake parameter, $0.8 \cdot (\beta_{\delta^*} + 0.5)^{3/4}$
ρ	density
ρ'	density fluctuations
ρ_0	mean ambient density

τ_w	wall shear stress
θ	boundary layer momentum thickness or phase difference
a_0	speed of sound
C_f	skin friction coefficient, τ_w/Q
C_p	pressure coefficient
f	frequency
G	Gaussian filter kernel
H	boundary layer shape parameter, δ/δ^*
k	wavenumber
l	length scale
p	pressure
p'	pressure fluctuations
Q	dynamic pressure, $0.5\rho U_0^2$, or the source term of the Poisson's equation
R	correlation
r	distance
R_T	time scale ratio, $(\delta/U_e)/(\nu/u_\tau^2)$
Re_τ	wall shear stress based Reynolds number, $u_\tau\delta/\nu$
Re_θ	boundary layer momentum thickness based Reynolds number, $U_0\theta/\nu$
Re_δ, Re_Δ	Reynolds number related to other boundary layer parameters, $(\delta, \Delta)U_e/\nu$
t, τ	time
u	velocity
u'	velocity fluctuations
u^+	dimensionless velocity, u/u_τ
u_τ	friction velocity, $\sqrt{\tau_w/\rho}$
u_c, U_c	convection velocity
U_e, U_0	boundary layer edge velocity and local free-stream velocity
x, y, z	spatial coordinates
y^+	dimensionless wall-normal coordinate, yu_τ/ν

Abbreviations

1,2,3-D	one, two, three-dimensional
AOA	angle of attack
APG	adverse pressure gradient
AWB	Aeroacoustic Wind Tunnel Braunschweig
CFAS	Catlett *et al.*
CFD	computational fluid dynamics
CFL	Courant-Friedrichs-Lewy
DNS	direct numerical simulation
FPG	favorable pressure gradient
FRPM	Fast Random Particle-Mesh Method
KBLWK	Kamruzzaman *et al.*
LES	large eddy simulation
MS	mean-shear term
NACA	National Advisory Committee for Aeronautics
PSD	power spectral density
RANS	Reynolds-averaged Navier-Stokes
RRM	Rozenberg *et al.*
TT	turbulence-turbulence term
XFOIL	Subsonic Airfoil Development System
ZPG	zero pressure gradient

1 Introduction

1.1 Motivation and background

Aeroacoustics is a relatively new branch of aerodynamics and it has gained more importance due to the increasing demand for noise reduction and comfort in the field of aircraft, vehicles and wind turbines. Wall pressure fluctuations beneath a turbulent boundary layer are a fundamental topic in flow-induced noise. One major concern is the noise transmission through the elastic structure below the surface due to the fluctuating pressure excitation on the surface. The pressure fluctuations caused by the fluctuating velocities, exert an unsteady loading on the surface and consequently the induced surface vibration radiates noise, which makes the wall pressure fluctuations an important noise source for the cabin, especially for the aircraft cabin. This phenomenon has become more important with the reduction of jet and fan noise during the development of the jet engine over the past decades. Nowadays, the noise caused by wall pressure fluctuations beneath a turbulent boundary layer becomes a major source for aircraft cabin noise in cruise flight [1, 2]. Since cabin noise belongs to one of the decisive conditions for the airline passenger comfort, prediction and reduction of turbulent boundary layer induced wall pressure fluctuations become more involved in the aircraft design process. To achieve a low-noise design, a deep understanding of this phenomenon and applicable design tools are required. The knowledge on wall pressure fluctuations gained over the past decades is mostly restricted to non-ac-/decelerated time averaged flows, i.e. mean flows characterized by zero pressure gradient (ZPG). However, in reality, a non-ZPG boundary layer occurs in most cases. Therefore, there is a high demand for investigations of the effect of pressure gradients on wall pressure fluctuations. Furthermore, numerical tools based on resolving (fully or partially) wall turbulence are hardly applicable for practical design applications (characterized by Reynolds numbers on the order of 100M) due to the extremely high computational costs. Therefore, an efficient numerical method, which can represent the most important features of the wall pressure field relevant to cabin noise excitation, is of particular interest.

The phenomenon of the turbulent boundary layer induced wall pressure fluctuations was pioneered by Kraichnan [3] and Willmarth [4] in the 1950s. The theoretical work from Kraichnan identified that the pressure fluctuations within an incompressible boundary layer is governed by a Poisson's equation and the fluctuating pressure is caused by a linear mean-shear turbulence interaction term and a non-linear turbulence-turbulence interaction term. Willmarth measured some properties for the one-point statistics of the wall pressure fluctuations at different Reynolds numbers and Mach numbers. Since then, extensive theoretical and experimental work has been done to investigate the characteristics of the wall pressure field. Focus of the investigations has not only been on the one-point statistics, but also on the two-point statistics because of the importance of the space-time features to the surface structural response.

A comprehensive understanding of the wall pressure field was firstly gained by the experimental results from Willmarth & Wooldridge [5]. They measured both one- and two-point statistics of the wall pressure fluctuations beneath a thick ZPG boundary layer

in a subsonic wind tunnel and analyzed the properties of the pressure field extensively. Such measurements concentrated on investigations of the wall pressure power spectra, space-time correlations, cross-spectra while investigations on the convective features were conducted by Bull [6], Blake [7], Farabee & Casarella [8] and Leclercq & Bohineust [9].

In the meantime, there has been growing interest in direct measurements of the wall pressure wavenumber-frequency spectra. The wavenumber-frequency spectra are just another interpretation of the space-time properties, and can provide a more intuitive means of analysis of the structure-vibrational response to the wall pressure excitation. In the early stage, Blake & Chase [10] and Farabee & Geib [11] used spatial-filtering to measure the wavenumber-frequency spectra by a couple of microphones arranged in the streamwise direction. With the development of measuring devices and processing techniques, Abraham & Keith [12], Arguillat *et al.* [13], Ehrenfried & Koop [14] and Gabriel *et al.* [15] measured the wavenumber-frequency spectra by using array technology. In their measurements the convective ridge and the acoustic part can be well identified. However, due to the applied array size and the background noise of the test facilities, the obtained spectra in the low-wavenumber or low-frequency range were still not conclusive.

Another general difficulty of experimentally acquiring the wall pressure fluctuations is to precisely measure the spectra in the high-frequency or high-wavenumber range. Due to the averaging effect on waves by a sensor surface, an attenuation of the wall pressure magnitude will be measured at a high wavenumber range with respect to the sensor size. This effect was first studied by Corcos [16], who established the relationship between the sensor size and the caused spectral attenuation beneath a turbulent boundary layer. Later, experimental and theoretical studies on this effect were given by Gilchrist [17], White [18], Chase [19] and Bull [20]. To circumvent this problem, the 'effective' sensor surface needs to be reduced. Therefore, sensors with a pinhole setup were often applied. Even with the pinhole configuration, the measurable frequency range is limited by the Helmholtz resonance frequency. To be able to measure at higher frequencies, a higher resonance frequency is essential, i.e. a smaller sensor is required. In recent experimental studies, sub-miniature pressure sensors were more and more applied. By now, the smallest available sensor for the pressure measurement has a diameter of 1.6 mm. Note, even with the smallest size, a flush-mounted sensor is still too 'large' for measuring the wall pressure in the high frequency range.

Besides wind tunnel measurements, measurements of the wall pressure fluctuations have been also carried out directly on airplanes. The measurement station was placed at the wing in the early flight tests [21, 22]. In the later tests [23, 24, 25, 26], the focus laid on the turbulent boundary layer induced cabin noise and therefore pressure fluctuations on the fuselage were measured. A highlight of the most recent flight test was the measurement of wavenumber-frequency spectra using array technology [27].

There has always been an interest in the prediction of the magnitude and the space-time features of the wall pressure field. Theoretical works of prediction of the mean square pressure were given by Kraichnan [3], Lilley [28], Meecham & Tavis [29] and Chase [30]. Later, Farabee & Casarella [8] and Viazzo *et al.* [31] estimated the magnitude by integrating the one-point spectra in the frequency domain with consideration of the Reynolds number effect. One-point spectral models were proposed by Robertson [32], Chase [30], Efimtsov [33], Howe [34], Smol'yakov [35], Goody [36] and Herr [37]. Most of the models were derived for prediction of low-speed ZPG boundary layers. Robertson's and Efimtsov's models were derived based on in-flight measurements.

Schloemer [38] was the first to measure wall pressure fluctuations under non-ZPGs. Later, Burton [39], Blake [40] and Simpson [41] further studied this problem under different flow conditions. Recent measurements were given by Herrig [42], Catlett *et al.* [43], Salze *et al.* [44] and Suryadi & Herr [45]. Rozenberg *et al.* [46], Kamruzzaman *et al.* [47] and Catlett *et al.* [48] proposed one-point spectral models for wall pressure fluctuations under adverse pressure gradient (APG) boundary layers.

Furthermore, the one-point spectra can be also calculated using integration methods developed by Panton & Linebarger [49] and Blake [50]. The method requires some parameters of the boundary layers, such as mean velocity profiles, Reynolds stresses and turbulent length scales.

A model for the description of the space-time correlations was first proposed by Corcos [51]. Based on experimental results, Corcos found the existence of similarities of the wall pressure cross-spectra for both streamwise and spanwise directions and proposed a cross-spectral model with consideration of the correlation decay and the convective features of the wall pressure field. Chase [30] did a comprehensive theoretical study of characteristics of wall pressure fluctuations and proposed a model in the wavenumber-frequency domain. The compressibility was not taken into account in the proposed models, which was discussed in the works of Ffowcs Williams [52] and Chase [53].

With the booming development of computer technology, the numerical simulation has become a powerful resource for investigating the fluctuating pressure field. Direct numerical simulation (DNS) and large eddy simulation (LES) for the wall pressure fluctuations have been published by Spalart [54], Kim [55], Choi & Moin [56], Chang *et al.* [57], Viazzo *et al.* [31] and Gloerfelt & Berland [58]. The properties of wall pressure fluctuations, which are not possible or hard to measure experimentally, can be studied through numerical work and new insight can be gained. Although the turbulent boundary layer can be solved by DNS and LES, due to the extremely expensive computation resources the application is generally restricted to generic studies for low and medium Reynolds numbers.

For a practical application, the requirements on computational resources need to be further reduced. Stochastic models for calculating the wall pressure fluctuations were applied in the works of Siefert *et al.* [59] and Alaoui *et al.* [60]. Siefert *et al.* synthesized directly the wall pressure fluctuation field concentrating on realization of the relevant features for excitation on a surface structure. The method used by Alaoui *et al.* was based on the coherent vortex structure of a hairpin model.

A summary of the so far acquired knowledge on wall pressure fluctuations beneath a turbulent boundary layer was given by Willmarth [61] and Bull [62]. A comprehensive overview on the subject of wall pressure fluctuations, including also the structural response and the induced sound radiation was given in the monograph of Blake [50].

1.2 State of the art

A brief summary of the background knowledge on wall pressure fluctuations beneath a turbulent boundary layer is given in the previous section. The investigations were mainly concentrated on studies of the sources, the one- and two-point statistics of the pressure field. Some relevant knowledge acquired so far will be addressed in this section.

Kraichnan [3] reformulated the Navier-Stokes equations, and derived a Poisson's equa-

tion, which governs the pressure fluctuations within an incompressible turbulent boundary layer. The source terms consisting of a mean-shear turbulence interaction term $\partial^2\overline{u}_i u'_j/\partial x_i \partial x_j$ and a turbulence-turbulence interaction term $\partial^2(u'_i u'_j - \overline{u'_i u'_j})/\partial x_i \partial x_j$, where $\overline{u}_i$ is the i^{th} cartesian mean flow velocity component and u'_i represents the respective velocity fluctuation component, are placed on the right-hand side of the Poisson's equation. The former and the latter denote the interaction between the mean flow and the turbulent fluctuations and the interaction between the turbulent fluctuations themselves, respectively. The mean-shear term is a linear term and also called the 'rapid' term, because of the rapid response to a change of the mean flow condition. The turbulence-turbulence term is a non-linear term and also called the 'slow' term due to the slow reaction of the change through the turbulence-turbulence interactions [55].

Determination of the relative influence of each source term on the wall pressure fluctuations has always been of particular interest, because in general only the dominant source term needs to be considered. However, a distinction of the contributions and the importance of both source terms is difficult to be achieved experimentally; most works on this topic were conducted theoretically. Kraichnan [3], Hodgson [22] and Meecham & Tavis [29] calculated the contribution from the turbulence-turbulence term based on an assumption of isotropic turbulence with a Gaussian correlation and concluded that the mean-shear term is the dominant source term for the wall pressure fluctuations. Corcos [51] estimated the importance between both sources by comparing the calculated auto-correlation of the mean-shear term and the measured auto-correlation and found the magnitude of wall pressure fluctuations from the mean-shear term to be somewhat more than 3 dB larger than from the turbulence-turbulence term. Chase [30] did a comprehensive theoretical work on modeling the wall pressure spectra contributed from both sources and obtained a similar result as concluded by Corcos. Peltier & Hambric [63] calculated the one-point spectra based on the turbulence statistics provided by Reynolds-averaged Navier-Stokes equations (RANS) calculations. The result showed that the dominance of the mean-shear term is more pronounced for a favorable pressure gradient (FPG) boundary layer. An experimental work was conducted by Johansson [64], who used a conditional averaging technique to measure the relationship between the fluctuating flow field and the wall pressure fluctuations. The results indicated the mean-shear term plays a dominating role.

Other than experiments, numerical methods can provide the opportunity to distinguish the pressure fluctuation contribution of the source terms. In contrast to the previous conclusion that the wall pressure fluctuations are mostly contributed by the mean-shear term, the numerical results from Kim [55] and Chang *et al.* [57] show a comparable magnitude of the wall pressure fluctuations contributed by both source terms.

The wall pressure wavenumber-frequency spectrum for the mean-shear term can be analytically calculated by integrating the source with the appropriate Green's function for the Poisson's equation. For this purpose, information of mean flow velocities, Reynolds stresses and turbulence spectra within the boundary layer is needed. Panton & Linebarger [49] applied a double integral in the wall-normal direction involving a wavenumber-frequency velocity fluctuation spectrum $\Phi_{22}(x_2, x'_2, \mathbf{k}, \omega)$, where x_2 denotes the coordinate in the wall-normal direction, $\mathbf{k}$ the planar wavenumber vector and ω the angular frequency. Blake [50] further simplified the method into a single integral with introduction of an integral length scale of turbulence.

A key parameter for this method is the turbulence length scale, which can directly influence the wall pressure spectral magnitude and also the modelled velocity spectra and

consequently the wall pressure spectra. However, an exact knowledge of the length scale within the boundary layer is still lacking. For application of this method, the value of the length scale is normally modelled through theoretical assumptions [50, 65], experimental results [66, 67, 68] or RANS calculations [69]. A comparison of the value of the length scale obtained by some selected applications is given by Herr *et al.* [70]. The results showed that differences in the value of the length scale are observed between the experimental result and the RANS result, and also among the RANS calculations themselves.

Anisotropy of wall turbulence is also a relevant feature for calculation of the wall pressure. The velocity spectrum of anisotropic turbulence is different from isotropic turbulence. Therefore, the wall pressure spectrum can be affected by anisotropy. Panton & Linebarger [49] and Kamruzzaman *et al.* [68] studied the effect of anisotropic turbulence on the velocity spectrum and the wall pressure spectrum. A LES work which was concentrated on studies of anisotropic turbulence length scales was conducted by Sillero *et al.* [71]. The results determined that the turbulent length scale of the streamwise fluctuating component is much larger than the spanwise and wall-normal fluctuating components.

Another important issue for prediction of the wall pressure spectrum is the decay property of turbulence convection (de-correlation with time) which, however, has only been little studied. In most works, Taylor's frozen turbulence hypothesis [72] was assumed, i.e. the wavenumber spectrum is interchangeable with the frequency spectrum according to $k_1 = \omega/U_c$, where k_1 denotes the wavenumber in the streamwise direction and U_c is the convection velocity. Assumptions departing from a Dirac-like function $\delta(\omega - k_1 U_c)$ and including the de-correlation with time were proposed by Blake [50] and Parchen [65]. Chase [30] discussed that the de-correlation causes a frequency spreading, which is important for the wavenumber spectrum, especially for the low wavenumber range.

Blake [50] calculated the wall pressure frequency spectrum for the mean-shear term by taking advantage of the assumption of frozen turbulence. The results demonstrated a spectral behavior of ω^2, ω^{-1} and ω^{-5} in the low-, medium- and high-frequency regions, respectively. He argued that the ω^2 behavior at low frequencies is a result of contributions by the sources across the boundary layer, the ω^{-1} behavior at medium frequencies is contributed from the logarithmic region of the boundary layer and the sublayer region is responsible for the ω^{-5} behavior at high frequencies. The spectral form with three different-behavior regions has also been identified in the experimental results, however, with some differences in the spectral slope. The high-frequency rapid decrease with a slope of approximately ω^{-5} was verified by many researchers [7, 8, 73, 74, 44]. The slope in the mid-frequency decreasing region was mostly measured in a range from $\omega^{-0.6}$ to $\omega^{-0.8}$ [7, 8, 74, 9, 44], which is smaller than the theoretical prediction ω^{-1}. At low frequencies, the increase with a slope between $\omega^{0.2}$ and $\omega^{0.8}$ was reported [6, 7, 8, 9, 44]. An increase of the ω^2 increasing behavior has been only measured at the very lowest frequency range ($f < 10$ Hz, $\omega\delta/U_e < 0.08$) by Farabee & Casarella [8] using noise cancellation technique. The theoretical work from Chase [30] argued that the frequency spreading due to the turbulence de-correlation (which is not included in the prediction from Blake) can increase the spectral level at very low frequencies and the contribution of the turbulence-turbulence term, which has a much flatter slope at low frequencies, has also an impact for the low-frequency region. These effects can flatten the spectral slope at low frequencies.

Panton & Linebarger [49] estimated the importance of different boundary layer regions (only the mean-shear term considered) to the wall pressure spectra. The results indicated that the wake region and the logarithmic region dominate the contribution to the low

wavenumber range of the wall pressure. The contribution from the wake region to the low wavenumber range further increases in the boundary layer under an APG. This feature was also found by Peltier & Hambric [63]. However, the contribution of the sources decreases very quickly with the increasing wavenumber and wall-normal distance to the wall. This lets the contribution from the wake region die out at higher wavenumbers and the higher the wavenumber is, the more important the region closer to the wall becomes. At very high wavenumbers, the wall pressure is almost only contributed by the sublayer region.

Besides the calculation, wall pressure fluctuations have been modeled by many researchers. Of particular interest is the modeling of the one- and two-point statistics relevant to the structural excitation. Goody [36] proposed an empirical one-point wall pressure spectral model for ZPG boundary layers. The model was derived based on the measured spectra by seven different experiments. Taking advantage of self-similarity of the measured spectra, a spectral formulation is built by an increase with ω^2 at low frequencies, a decrease with approximate $\omega^{-0.775}$ at medium frequencies and a rapid drop with ω^{-5} at high frequencies. A highlight of this model is that the change of the mid-frequency spectral extension due to the Reynolds number effect was considered by introducing a timescale factor.

In practice, non-ZPG flows are of more interest. Recently, more studies concentrating on effects of the pressure gradient on the wall pressure fluctuations have been conducted. Rozenberg [46] analyzed the different spectral features between the boundary layer under a ZPG and an APG based on some selected experimental and numerical results, and showed that a large inaccuracy in the spectral prediction occurs if the Goody model is applied for an APG case. Therefore, modeling of the wall spectrum for the APG boundary layer is of particular interest. It is, however, a difficult task. One major reason is because self-similarity of wall pressure spectra under APGs does not exist even approximitely. Based on the observation that an APG increases the spectral peak level and the spectral drop in the mid-frequency range compared to the ZPG case, Rozenberg modified the Goody model involving some boundary layer parameters, e.g. boundary layer thickness based parameters and Clauser's equilibrium parameter, to capture the spectral changing trend due to the presence of the pressure gradient. Later, other one-point spectral models for APG boundary layers were proposed by Kamruzzaman *et al.* [47] and Catlett *et al.* [48] based on the similar concept.

To predict the feature of wall-pressure two-point statistics, Corcos [51] found that self-similarity also exists for the spectral coherence in both streamwise and spanwise directions and the coherence at different distances in each direction can be well described by a single exponential function, e.g. $\exp(-\alpha|\omega r_1/U_c|)$, where α is an empirical constant and r_1 is the streamwise distance. Based on this observation, a cross-spectral model was proposed. The model involves a constant in each exponential function to define the rate of the decorrelation, which needs to be determined empirically. So far, the experimental results from the literature indicated that the value of the constant for the streamwise direction depends on the Reynolds number, whereas for the spanwise direction it does not. Note that, due to the formulation of the exponential function, the coherence approaches unity when the distance between two points or the spectral frequency is close to zero. However, it is the case only when the distance approaches zero. Experimental results [6, 8, 9] showed that the coherence drops at low frequencies and this also means the Corcos model cannot predict accurately the coherence in the low-frequency range. This feature of decreasing coherence at low frequencies was reproduced by the theoretical work from Chase [30],

who calculated the wall pressure features for both mean-shear and turbulence-turbulence terms in the wavenumber domain with consideration of the effect of decaying convective turbulence.

1.3 Scope and objectives

In the present work, features of the wall pressure field are investigated experimentally and numerically. A generic test setup is established in the Aeroacoustic Wind Tunnel Braunschweig (AWB), which is able to generate both zero and non-ZPG turbulent boundary layers. Since, in reality, decelerated/accelerated flows occur most often and since wall pressure fluctuations under non-zero pressure gradient flows have not been studied as extensively as under zero pressure gradients, major efforts of the present experimental investigation are made to study the effect of mean flow pressure gradients on wall pressure fluctuations.

Wall pressure one- and two-point statistics (in the streamwise and spanwise directions) under zero and non-ZPG also including the respective flow properties within the boundary layer are measured and studied. The effect of the pressure gradient on the boundary layer mean velocity profile, on the wall pressure one-point spectra, on the wall pressure coherence in the streamwise and spanwise directions and on the wall pressure convection velocities are analyzed and discussed. The pressure gradient influences the boundary layer properties and consequently the features of the wall pressure fluctuations. The relationship between the boundary layer properties and the wall pressure one-point spectra is investigated based on the present experimental results. Furthermore, a spectral model to predict wall pressure one-point spectra under APGs (incorporating ZPGs) is proposed. The Goody model, which is suitable for ZPG cases, is used as the basis for developing the model. The basic concept of the model is to use the boundary layer parameters to predict the spectral form departing from ZPG cases caused by presence of the pressure gradient. Predictions from the proposed model and other published models (for the APG cases) are made for five test cases at four different test facilities. Comparisons and assessments of the models are given.

Another goal of the experiment is to establish a database as the validation basis for numerical simulations. The numerical simulation is another means to investigate the features of the wall pressure fluctuations. As mentioned before, due to the extremely high computational resources required, the simulations are restricted to low and medium Reynolds numbers. A more efficient numerical procedure is developed in this work. A stochastic method is used to generate synthetic turbulence with prescribed features from which pressure fluctuations are deduced. The approach enables the study of what effects the variation of turbulence characteristics and key parameters have on the resulting turbulent wall pressure fluctuations. The relative efficiency of the approach enables the study of high Reynolds numbers and the conduct of parametric studies.

For an incompressible flow, the fluctuating pressure field can be expressed with the Poisson's equation. The equation is solved in the present work by using a free-space Green's function and solving the convolution with a spatial fast Fourier transform utilizing Hockney's method [75]. Both the mean-shear and the turbulence-turbulence terms occurring on the right-hand side of the Poisson's equation are considered in the present study. Furthermore, synthetic isotropic and also anisotropic turbulence are applied to calculate the

pressure fluctuations.

The present procedure aims not to resolve the smallest eddies present in the turbulent boundary layer, since they are normally responsible for the high frequencies of the wall pressure spectra. For example, for most practical applications of flow-induced structural vibration the high frequencies are irrelevant due to the poor transmission efficiency.

The features for the wall pressure fluctuations are thoroughly analyzed and compared with published results from the literature. Importance of both the mean-shear and the turbulence-turbulence terms for the wall pressure fluctuations and the effect of the turbulence anisotropy are discussed. Furthermore, simulations for the present experimental cases are conducted. The numerical results for the wall pressure one- and two-point features are compared to the experimental results.

1.4 Outline

Chapter 2 provides the necessary fundamentals on wall pressure fluctuations beneath turbulent boundary layers, consisting of the derivation and the solution of the Poisson's equation for pressure fluctuations within the boundary layer and empirical models for one-point spectra and coherences. The experimental test setups, measurement techniques and the applied numerical approach are described in Chapter 3. Experimental results are discussed in Chapter 4, mainly concentrating on the mean flow properties, the wall pressure one-point spectra, the cross-spectra and the convection velocities. Based on the experimental results, a one-point spectral model for zero and APG cases is proposed in Chapter 5. Also comparison with other exiting models is provided. In Chapter 6, simulated one-point spectra and two-point cross-correlations of wall pressure fluctuations are analyzed in detail. The numerical approach is verified and validated by comparing with the theoretical results and the experimental results from the literature and the present experiment. Conclusions and outlook are addressed in Chapter 7.

2 Fundamentals of wall pressure fluctuations beneath turbulent boundary layers

In this chapter, the fundamentals of the wall pressure fluctuations beneath turbulent boundary layers are provided. For an incompressible flow, the pressure fluctuations within the turbulent boundary layer can be determined by Poisson's equation. A mathematical derivation of Poisson's equation and the analytical solution of it for the wall pressure spectrum contributed from the mean-shear term are given in section 2.1. Furthermore, a brief summary of the empirical models for prediction of the wall pressure spectrum and the cross-spectrum are provided in section 2.2.

2.1 Theoretical approaches

2.1.1 Poisson's equation for pressure fluctuations within boundary layers

The differential forms of the conservation equations for mass and momentum are

$$\frac{\partial \rho}{\partial t} + \nabla \cdot \rho \boldsymbol{u} = 0\,, \tag{2.1}$$

$$\frac{\partial \rho \boldsymbol{u}}{\partial t} + \nabla \cdot \rho \boldsymbol{u}\boldsymbol{u} + \nabla p = \nabla \cdot \boldsymbol{\tau}\,, \tag{2.2}$$

where $\nabla \cdot$ is the divergence operator, ρ is fluid density, t is time, $\boldsymbol{u}$ is the flow velocity vector, p is pressure and $\boldsymbol{\tau}$ is the deviatoric stress tensor. In terms of the pressure fluctuations, the deviatoric stress tensor $\boldsymbol{\tau}$ is generally not relevant. Therefore, for deviation of Poisson's equation to govern the pressure fluctuations within the boundary layer, $\boldsymbol{\tau}$ is neglected.

Taking the partial time derivative of Eq. (2.1) and the divergence of Eq. (2.2) and neglecting of $\boldsymbol{\tau}$, the Eq. (2.1) and Eq. (2.2) become

$$\frac{\partial^2 \rho}{\partial t^2} + \nabla \cdot \frac{\partial \rho \boldsymbol{u}}{\partial t} = 0\,, \tag{2.3}$$

$$\nabla \cdot \frac{\partial \rho \boldsymbol{u}}{\partial t} + \nabla \cdot \nabla \cdot \rho \boldsymbol{u}\boldsymbol{u} + \Delta p = 0\,. \tag{2.4}$$

Combining Eq. (2.3) and Eq. (2.4), we obtain

$$-\Delta p = \nabla \cdot \nabla \cdot \rho \boldsymbol{u}\boldsymbol{u} - \frac{\partial^2 \rho}{\partial t^2}\,. \tag{2.5}$$

The density ρ may be split into a averaged mean part $\overline{\rho}$ and a fluctuating part ρ', expressed as $\rho = \overline{\rho} + \rho'$. We limit our discussion to a steady flow, i.e. $\partial\overline{\rho}/\partial t = 0$. Thus, Eq. (2.5) becomes

$$-\Delta p = \nabla \cdot \nabla \cdot \rho \boldsymbol{u}\boldsymbol{u} - \frac{\partial^2 \rho'}{\partial t^2}\,. \tag{2.6}$$

Isentropy $a_0^2\rho' = p'$ applies approximately whenever the flow is cold and the Mach numbers are subsonic as is true for all cases studied here. Here a_0 denotes the speed of sound in the medium, Eq. (2.6) can be written as

$$\frac{1}{a_0^2}\frac{\partial^2 p'}{\partial t^2} - \Delta p = \nabla \cdot \nabla \cdot \rho \boldsymbol{u}\boldsymbol{u}\,. \tag{2.7}$$

Taking the time average of Eq. (2.7), we obtain

$$-\Delta \overline{p} = \nabla \cdot \nabla \cdot \overline{\rho \boldsymbol{u}\boldsymbol{u}}\,. \tag{2.8}$$

The same as dealing with ρ, we split the pressure into $p = \overline{p} + p'$ and put it into Eq. (2.7), reads

$$\frac{1}{a_0^2}\frac{\partial^2 p'}{\partial t^2} - \Delta \overline{p} - \Delta p' = \nabla \cdot \nabla \cdot \rho \boldsymbol{u}\boldsymbol{u}\,. \tag{2.9}$$

Substituting Eq. (2.8) into Eq. (2.9),

$$\frac{1}{a_0^2}\frac{\partial^2 p'}{\partial t^2} - \Delta p' = \nabla \cdot \nabla \cdot (\rho \boldsymbol{u}\boldsymbol{u} - \overline{\rho \boldsymbol{u}\boldsymbol{u}})\,. \tag{2.10}$$

We can also split the flow velocity into the density weighted time averaged (Favre-averaged) mean part and the fluctuating part, i.e. $\boldsymbol{u} = \tilde{\boldsymbol{u}} + \boldsymbol{u}''$ with $\tilde{\boldsymbol{u}} = \overline{\rho \boldsymbol{u}}/\overline{\rho}$. Thus, $\rho \boldsymbol{u}\boldsymbol{u}$ and $\overline{\rho \boldsymbol{u}\boldsymbol{u}}$ can be expressed as

$$\rho \boldsymbol{u}\boldsymbol{u} = \rho(\tilde{\boldsymbol{u}} + \boldsymbol{u}'')(\tilde{\boldsymbol{u}} + \boldsymbol{u}'') = \rho(\tilde{\boldsymbol{u}}\tilde{\boldsymbol{u}} + \tilde{\boldsymbol{u}}\boldsymbol{u}'' + \boldsymbol{u}''\tilde{\boldsymbol{u}} + \boldsymbol{u}''\boldsymbol{u}'')\,, \tag{2.11}$$

$$\overline{\rho \boldsymbol{u}\boldsymbol{u}} = \overline{\rho}\tilde{\boldsymbol{u}}\tilde{\boldsymbol{u}} + \overline{\rho}\tilde{\boldsymbol{u}}\boldsymbol{u}'' + \overline{\rho \boldsymbol{u}''}\tilde{\boldsymbol{u}} + \overline{\rho \boldsymbol{u}''\boldsymbol{u}''} = \overline{\rho}(\tilde{\boldsymbol{u}}\tilde{\boldsymbol{u}} + \widetilde{\boldsymbol{u}''\boldsymbol{u}''})\,. \tag{2.12}$$

Putting the obtained expression for $\rho \boldsymbol{u}\boldsymbol{u}$ and $\overline{\rho \boldsymbol{u}\boldsymbol{u}}$ into Eq. (2.10), we obtain

$$\frac{1}{a_0^2}\frac{\partial^2 p'}{\partial t^2} - \Delta p' = \nabla \cdot \nabla \cdot \left(\overline{\rho}(\tilde{\boldsymbol{u}}\boldsymbol{u}'' + \boldsymbol{u}''\tilde{\boldsymbol{u}} + \boldsymbol{u}''\boldsymbol{u}'' - \widetilde{\boldsymbol{u}''\boldsymbol{u}''}) + \rho'(\tilde{\boldsymbol{u}}\tilde{\boldsymbol{u}} + \tilde{\boldsymbol{u}}\boldsymbol{u}'' + \boldsymbol{u}''\tilde{\boldsymbol{u}} + \boldsymbol{u}''\boldsymbol{u}'')\right)\,. \tag{2.13}$$

For an incompressible flow, $\overline{\rho} = \rho_0$, $\rho' = 0$, $\tilde{(.)} = \overline{(.)}$, $(.)'' = (.)'$ and $a_0 \to \infty$, Eq. (2.13) becomes Poisson's equation. It reads

$$\Delta p' = -\nabla \cdot \nabla \cdot \left(\rho_0(\overline{\boldsymbol{u}}\boldsymbol{u}' + \boldsymbol{u}'\overline{\boldsymbol{u}} + \boldsymbol{u}'\boldsymbol{u}' - \overline{\boldsymbol{u}'\boldsymbol{u}'})\right)\,. \tag{2.14}$$

If we write Eq. (2.14) in a Cartesian coordinate system, it becomes

$$\Delta p' = -\rho_0 \left(2\frac{\partial^2 \overline{u}_i u_j'}{\partial x_i \partial x_j} + \frac{\partial^2 (u_i'u_j' - \overline{u_i'u_j'})}{\partial x_i \partial x_j}\right)\,. \tag{2.15}$$

For a mean flow in the x_1 direction and a well-developed quasi-parallel two-dimensional (2-D) incompressible turbulent boundary layer, i.e. $\partial u_i/\partial x_i = 0$, $\overline{u}_{2,3} \to 0$ and $\partial \overline{u}_1/\partial x_{1,3} \to 0$, Poisson's equation becomes

$$\Delta p' = -\rho_0 \left(2\frac{\partial \overline{u}_1}{\partial x_2}\frac{\partial u_2'}{\partial x_1} + \frac{\partial^2 (u_i'u_j' - \overline{u_i'u_j'})}{\partial x_i \partial x_j}\right)\,. \tag{2.16}$$

2.1.2 Solutions to Poisson's equation

The source term on the right-hand side of Eq. (2.16) comprises two parts. The first part is the mean-shear turbulence interaction term and the second part is the turbulence-turbulence interaction term. If the boundary is a rigid flat surface, the fluctuating pressure can be calculated from the convolution of the free-space Green's function of the Poisson's equation with the right-hand side source term, i.e.,

$$p'(\mathbf{x},t) = \int_{\mathbf{V_s}+\mathbf{V_s'}} Q(\mathbf{y},t) \cdot G(\mathbf{x}-\mathbf{y})\,\mathrm{d}V(\mathbf{y}), \tag{2.17}$$

where

$$Q(\mathbf{y},t) = -\rho_0\left(2\frac{\partial \overline{u}_1}{\partial x_2}\frac{\partial u_2'}{\partial x_1} + \frac{\partial^2(u_i'u_j' - \overline{u_i'u_j'})}{\partial x_i \partial x_j}\right), \tag{2.18}$$

$$G(\mathbf{x}-\mathbf{y}) = -\frac{1}{4\pi|\mathbf{x}-\mathbf{y}|}. \tag{2.19}$$

In Eq. (2.17) the integration is carried out over the original source area $\mathbf{V_s}$ plus a source area $\mathbf{V_s'}$ that represents an image of $\mathbf{V_s}$ mirrored at the solid wall in order to realize the appropriate wall boundary condition $(\partial p/\partial n)_{x_2=0} = 0$ of the pressure fluctuations [50].

At the plane surface, the pressure fluctuations contributed from the virtual mirrored source is identical to the one from the real source. Restricting the source term within the boundary layer and putting Eq. (2.19) into the Eq. (2.17), the expression for calculating the wall pressure fluctuations can be written as

$$p'(x_1,0,x_3,t) = -\frac{1}{2\pi}\int_\delta \frac{Q(\mathbf{y},t)}{r}\,\mathrm{d}V(\mathbf{y}), \tag{2.20}$$

where $r = |\mathbf{x}-\mathbf{y}|$ and δ denotes the boundary layer thickness. It is more convenient to analyze the stochastic wall pressure fluctuations in wavenumber-frequency domain by taking three-dimensional (3-D) Fourier transform,

$$\hat{p'}(\mathbf{k},\omega) = \frac{1}{(2\pi)^3}\int_{-\infty}^{\infty}\int_{-\infty}^{\infty}\int_{-\infty}^{\infty} p'(x_1,0,x_3,t)\exp\left[-i\left(\mathbf{k}\cdot\mathbf{x_s}-\omega t\right)\right]\mathrm{d}S(\mathbf{x_s})\mathrm{d}t, \tag{2.21}$$

where $\mathbf{k}$ and $\mathbf{x_s}$ are the wave vector and spatial vector in the surface plane, i.e. $\mathbf{k} = (k_1, k_3)$ and $\mathbf{x_s} = (x_1, x_3)$. Substituting Eq. (2.20) into Eq. (2.21) and taking the Fourier transform with respect to t, we obtain

$$\hat{p'}(\mathbf{k},\omega) = -\frac{1}{(2\pi)^3}\int_\delta \hat{Q}(\mathbf{y},\omega)\int_{-\infty}^{\infty}\int_{-\infty}^{\infty}\frac{\exp\left(-i\mathbf{k}\cdot\mathbf{x_s}\right)}{r}\,\mathrm{d}S(\mathbf{x_s})\,\mathrm{d}V(\mathbf{y}). \tag{2.22}$$

From the identity (refer to [50]),

$$\frac{1}{2\pi}\int_{-\infty}^{\infty}\int_{-\infty}^{\infty}\frac{\exp\left(-i\mathbf{k}\cdot\mathbf{x_s}+ik_0r\right)}{r}\,\mathrm{d}S(\mathbf{x_s}) = \frac{i\exp\left(iy_2\sqrt{k_0^2-k^2}\right)\exp(-i\mathbf{k}\cdot\mathbf{y_s})}{\sqrt{k_0^2-k^2}}, \tag{2.23}$$

where $|\mathbf{k}| = k = \sqrt{k_1^2+k_3^2}$, $k_0 = \omega/a_0$ and $\mathbf{y_s} = (y_1, y_3)$, Eq. (2.22) for $a_0 \to \infty$ and $k_0 = 0$ becomes,

$$\hat{p'}(\mathbf{k},\omega) = -\frac{1}{(2\pi)^2}\int_\delta \hat{Q}(\mathbf{y},\omega)\frac{\exp(-ky_2)\exp(-i\mathbf{k}\cdot\mathbf{y_s})}{k}\,\mathrm{d}V(\mathbf{y}). \tag{2.24}$$

Using

$$\hat{Q}(\mathbf{k},\omega) = \frac{1}{(2\pi)^2}\int_{\delta}\hat{Q}(\mathbf{y},\omega)\exp(-i\mathbf{k}\cdot\mathbf{y_s})\,\mathrm{d}V(\mathbf{y}), \tag{2.25}$$

Eq. (2.24) finally yields,

$$\hat{p'}(\mathbf{k},\omega) = -\int_0^{\delta}\hat{Q}(\mathbf{k},\omega)\frac{\exp(-ky_2)}{k}\,\mathrm{d}y_2. \tag{2.26}$$

The source term Q consists of two parts, i.e. the mean-shear term and the turbulence-turbulence term,

$$Q = Q_{ms} + Q_{tt}, \tag{2.27}$$

where

$$Q_{ms} = -2\rho_0\frac{\partial\overline{u}_1}{\partial x_2}\frac{\partial u_2'}{\partial x_1}, \tag{2.28}$$

$$Q_{tt} = -\rho_0\frac{\partial^2(u_i'u_j' - \overline{u_i'u_j'})}{\partial x_i\partial x_j}. \tag{2.29}$$

Since the Poisson's equation is linear, the mean-shear term and the turbulence-turbulence term can be separately solved, thus,

$$\hat{p'}_{ms}(\mathbf{k},\omega) = -\int_0^{\delta}\hat{Q}_{ms}(\mathbf{k},\omega)\frac{\exp(-ky_2)}{k}\,\mathrm{d}y_2, \tag{2.30}$$

$$\hat{p'}_{tt}(\mathbf{k},\omega) = -\int_0^{\delta}\hat{Q}_{tt}(\mathbf{k},\omega)\frac{\exp(-ky_2)}{k}\,\mathrm{d}y_2. \tag{2.31}$$

The source term for the mean-shear term follows,

$$\hat{Q}_{ms}(\mathbf{k},\omega) = \frac{1}{(2\pi)^2}\int_{-\infty}^{\infty}\int_{-\infty}^{\infty}\hat{Q}_{ms}(\mathbf{y_s},\omega)\exp(-i\mathbf{k}\cdot\mathbf{y_s})\,\mathrm{d}S(\mathbf{y_s}). \tag{2.32}$$

Combining with Eq. (2.28), Eq. (2.32) becomes

$$\hat{Q}_{ms}(\mathbf{k},\omega) = -2\rho_0\frac{\partial\overline{u}_1}{\partial x_2}\frac{1}{(2\pi)^2}\int_{-\infty}^{\infty}\int_{-\infty}^{\infty}\frac{\partial\hat{u}_2'}{\partial x_1}(\mathbf{y_s},\omega)\exp(-i\mathbf{k}\cdot\mathbf{y_s})\,\mathrm{d}S(\mathbf{y_s}) \tag{2.33}$$

$$= -2\rho_0\frac{\partial\overline{u}_1}{\partial x_2}ik_1\hat{u}_2'(\mathbf{k},\omega). \tag{2.34}$$

The same process for the turbulence-turbulence terms, the terms become

$$\hat{Q}_{tt11}(\mathbf{k},\omega) = \rho_0k_1^2\widehat{u_1'u_1'}(\mathbf{k},\omega), \tag{2.35}$$

$$\hat{Q}_{tt12}(\mathbf{k},\omega) = -\rho_0ik_1\frac{\partial\widehat{u_1'u_2'}}{\partial x_2}(\mathbf{k},\omega), \tag{2.36}$$

$$\hat{Q}_{tt13}(\mathbf{k},\omega) = \rho_0k_1k_3\widehat{u_1'u_3'}(\mathbf{k},\omega), \tag{2.37}$$

$$\hat{Q}_{tt22}(\mathbf{k},\omega) = -\rho_0\frac{\partial^2\widehat{u_2'u_2'}}{\partial x_2\partial x_2}(\mathbf{k},\omega), \tag{2.38}$$

$$\hat{Q}_{tt23}(\mathbf{k},\omega) = -\rho_0ik_3\frac{\partial\widehat{u_2'u_3'}}{\partial x_2}(\mathbf{k},\omega), \tag{2.39}$$

$$\hat{Q}_{tt33}(\mathbf{k},\omega) = \rho_0k_3^2\widehat{u_3'u_3'}(\mathbf{k},\omega). \tag{2.40}$$

For the mean-shear term, an analytical solution can be derived. Combining Eq. (2.30) and Eq. (2.34), the pressure fluctuations contributed from the mean-shear term can be calculated with

$$\hat{p'}_{ms}(\mathbf{k},\omega) = \int_0^\delta 2\rho_0 \frac{\partial \overline{u}_1}{\partial x_2} i k_1 \hat{u}'_2(\mathbf{k},\omega) \frac{\exp(-ky_2)}{k}\,\mathrm{d}y_2. \tag{2.41}$$

Using Eq. (2.41), the wall pressure spectrum for the mean-shear term can be derived as

$$\Phi_{ppms}(\mathbf{k},\omega) \simeq 4\rho_0^2 \frac{k_1^2}{k^2} \int_0^\delta \int_0^\delta \frac{\partial \overline{u}_1(y_2)}{\partial x_2} \frac{\partial \overline{u}_1(y'_2)}{\partial x_2} \Phi_{22}(y_2, y'_2, \mathbf{k}, \omega) \exp\left[-k(y_2+y'_2)\right]\,\mathrm{d}y_2\,\mathrm{d}y'_2, \tag{2.42}$$

where

$$\Phi_{22}(y_2, y'_2, \mathbf{k}, \omega) = < \hat{u}'_2(y_2, \mathbf{k}, \omega) \hat{u}'_2(y'_2, \mathbf{k}, \omega) > . \tag{2.43}$$

The brackets <> denote an ensemble average. $\Phi_{22}(y_2, y'_2, \mathbf{k}, \omega)$ represents the cross spectral density of the velocity fluctuations in the wall-normal direction and can be expressed in a separable form,

$$\Phi_{22}(y_2, y'_2, \mathbf{k}, \omega) = \Phi_{22}(y_2, \mathbf{k}, \omega) R_{22}(y_2 - y'_2), \tag{2.44}$$

where $R_{22}(y_2 - y'_2)$ represents the correlation for the velocity fluctuations u'_2 between the wall-normal positions y_2 and y'_2. By integrating $R_{22}(y_2 - y'_2)$ in the wall-normal direction, we obtain the integral length scale Λ_{22},

$$\Lambda_{22}(y_2) = \int_0^\delta R_{22}(y_2 - y'_2)\,\mathrm{d}y'_2. \tag{2.45}$$

Integrating over y'_2 and with the help of Eqs. (2.44–2.45) and an approximation of $R_{22}(y_2 - y'_2) = \Lambda_{22}(y_2, y'_2)\delta(y_2 - y'_2)$, the solution of the wall pressure spectrum for the mean-shear term becomes

$$\Phi_{ppms}(\mathbf{k},\omega) = 4\rho_0^2 \frac{k_1^2}{k^2} \int_0^\delta \left[\frac{\partial \overline{u}_1(y_2)}{\partial x_2}\right]^2 \Phi_{22}(y_2, \mathbf{k}, \omega) \Lambda_{22}(y_2) \exp(-2ky_2)\,\mathrm{d}y_2. \tag{2.46}$$

Letting

$$\Phi_{22}(y_2, \mathbf{k}, \omega) = \Phi_{22}(y_2, k_1, k_3) \phi_m(\omega - U_c k_1), \tag{2.47}$$

where $\Phi_{22}(y_2, k_1, k_3)$ is the velocity wavenumber spectrum, U_c denotes the eddy convective velocity and $\phi_m(\omega - U_c k_1)$ is the so-called moving axis spectrum, e.g. for frozen turbulence $\phi_m(\omega - U_c k_1) = \delta(\omega - U_c k_1)$. Taking integration of Eq. (2.46) in the wavenumber domain and combining Eq. (2.47), we obtain the solution for the spectrum $\Phi_{ppms}(\omega)$

$$\begin{aligned} \Phi_{ppms}(\omega) \;=\; & 4\rho_0^2 \int_0^\delta \int_{-\infty}^{\infty} \int_{-\infty}^{\infty} \frac{k_1^2}{k^2} \exp(-2ky_2) \left[\frac{\partial \overline{u}_1(y_2)}{\partial x_2}\right]^2 \Phi_{22}(y_2, k_1, k_3) \\ & \phi_m(\omega - U_c k_1) \Lambda_{22}(y_2)\,\mathrm{d}k_1 \mathrm{d}k_3 \mathrm{d}y_2. \end{aligned} \tag{2.48}$$

With this expression, the wall pressure spectrum $\Phi_{ppms}(\omega)$ contributed from the mean-shear term can be evaluated if the parameters δ, $\partial\overline{u}_1(y_2)/\partial x_2$, $\Phi_{22}(y_2, k_1, k_3)$, $\phi_m(\omega - U_c k_1)$ and $\Lambda_{22}(y_2)$ are provided. However, only the boundary layer thickness δ and the wall-normal gradient of the mean velocity $\overline{u}_1$ can be easily measured or estimated by RANS

calculations. The other parameters are hard or not possible to measure, which are usually estimated by assumptions. Note that, the result of the wall pressure spectrum is influenced by the following factors: 1, the integral area, which is generally defined by the boundary layer thickness δ; 2, the gradient of the mean velocity profile $\partial\overline{u}_1(y_2)/\partial x_2$, i.e. the shape of the mean velocity profile; 3, the wavenumber velocity spectrum $\Phi_{22}(y_2, k_1, k_3)$; 4, the moving axis spectrum $\phi_m(\omega - U_c k_1)$, i.e. decay of the convective eddies; 5, the integral length scale $\Lambda_{22}(y_2)$. And following influences of these factors can be summarized: 1, a thicker δ can lead to a larger pressure spectral level; 2, a different boundary layer profile shape may change the shape of the wall pressure spectrum and also the locations of the source weighting for the wall pressure fluctuations. This indicates that the wall pressure spectral shape of zero or non-zero pressure gradient boundary layers could be different; 3, an increase of the intensity of the velocity fluctuations Φ_{22} will increase the spectral level and a different shape of the spectrum $\Phi_{22}(y_2, k_1, k_3)$ may influence of the wall pressure spectral shape; 4, the moving axis spectrum $\phi_m(\omega - U_c k_1)$ represents the turbulence decay during convection and combines the spectrum in the wavenumber domain and in the frequency domain, e.g. for a frozen turbulence $k_1 = \omega/U_c$. The spectrum of ϕ_m will affect the distribution of the energy and consequently the shape of the wall pressure spectrum; 5, an increase of the length scale $\Lambda_{22}(y_2)$ will increase the spectral level and also impacts the spectrum of $\Phi_{22}(y_2, k_1, k_3)$, which can shift the energy from a higher wavenumber region to a lower wavenumber region.

2.2 Empirical model approaches

2.2.1 One-point spectral model

Spectral model for zero pressure gradient boundary layers

Prediction of the wall pressure spectra is of great practical interest. Many spectral models [32, 30, 76, 34, 35, 36, 37] for zero pressure gradient (ZPG) boundary layers were proposed. The most used one is Goody's model [36], which is briefly summarized below in this section. Goody utilized self-similarity of wall pressure fluctuation spectra induced by ZPG boundary layers and incorporates Reynolds number effects in the high frequency range with a time scale ratio R_T, expressed as

$$\frac{\Phi(\omega)U_e}{\tau_w^2\delta} = \frac{a \cdot (\omega\delta/U_e)^b}{[(\omega\delta/U_e)^c + d]^e + [fR_T^g \cdot (\omega\delta/U_e)]^h} , \tag{2.49}$$

where U_e is the boundary layer edge velocity, defined as $0.99U_0$ (U_0 is the local free-stream velocity). The value of parameters $a - h$ was obtained by fitting measurement data from the literature, $a = 3$, $b = 2$, $c = 0.75$, $d = 0.5$, $e = 3.7$, $f = 1.1$, $g = -0.57$ and $h = 7$. They control the shape of the non-dimensional spectrum. The formulated spectrum has three different regions with different spectral slopes. The spectrum increases at low frequencies, decreases at medium frequencies and rolls off rapidly at high frequencies. The spectral slopes in the different frequency ranges are driven by a combination of b, c, e and h. The parameter b fixes the slope at low frequencies, the function $c \cdot e - b$ is in charge of the slope at medium frequencies and $h - b$ at high frequencies. The formulated spectrum of Goody's model has a shape with a slope of ω^2 at low frequencies, $\omega^{-0.775}$ at medium frequencies and ω^{-5} at high frequencies. The spectral amplitude is adjusted by the value of a. The

parameters f, g combined with R_T determine the extension of the mid-frequency range, e.g. a larger R_T corresponds to a longer extension of the slope at medium frequencies into higher frequencies. The spectral peak location is affected by the value of d.

Spectral model for adverse pressure gradient boundary layers

The wall pressure spectra induced by non-ZPG boundary layers become more complicated and can not be well predicted by Goody's model. Experimental studies [38, 39, 40, 41, 42, 43, 44, 45] for pressure gradient effects on wall pressure fluctuations showed that the wall pressure spectra lose their self-similarity. A group of sensors was installed at different streamwise positions to measure the spectral development due to the impact of pressure gradients [43, 45]. For adverse pressure gradient (APG) boundary layers, the spectral slope at medium frequencies becomes successively steeper moving downstream. This is because the boundary layer development is influenced by the APG for a longer distance at downstream positions. Furthermore, the stronger the pressure gradient, the steeper the mid-frequency slope is.

Several empirical models for APG boundary layers were proposed to predict the changing trends from ZPG to APG boundary layers. A brief summary of the published spectral models for APG boundary layers is provided below.

Rozenberg *et al.* [46] (RRM) analyzed the spectral variation between ZPG and APG boundary layers from some experimental and numerical results and summarized the changing trends through a combination of boundary layer characteristic parameters. Based on the basic form of Goody's model, an empirical spectral model including APG effects was proposed by Rozenberg *et al.* [46], expressed as

$$\frac{\Phi(\omega)U_e}{\tau_w^2\delta^*} = \frac{\left[2.82{\Delta_{\delta/\delta_*}}^2 \cdot (6.13{\Delta_{\delta/\delta_*}}^{-0.75} + F_1)^{A_1}\right]\left[4.2 \cdot (\Pi_\theta/\Delta_{\delta/\delta_*}) + 1\right](\omega\delta^*/U_e)^2}{[4.76 \cdot (\omega\delta^*/U_e)^{0.75} + F_1]^{A_1} + \left[8.8R_T^{-0.57} \cdot (\omega\delta^*/U_e)\right]^{A_2}}, \tag{2.50}$$

where

$$\begin{aligned} F_1 &= 4.76 \cdot (1.4/\Delta_{\delta/\delta_*})^{0.75} \cdot [0.375 \cdot A_1 - 1], \\ A_1 &= 3.7 + 1.5\beta_\theta, \\ A_2 &= \min(3, 19/\sqrt{R_T}) + 7, \\ \beta_\theta &= \theta/\tau_w \cdot dp/dx, \\ \Pi_\theta &= 0.8 \cdot (\beta_\theta + 0.5)^{3/4}, \\ \Delta_{\delta/\delta^*} &= \delta/\delta^*. \end{aligned}$$

Clauser's equilibrium parameter β_θ [77] is used to manage the slope variation at medium frequencies, the larger the value of β_θ, the steeper the slope. The formulated spectrum shifts to a higher frequency and a larger amplitude as Δ_{δ/δ_*} increases. Both β_θ and Δ_{δ/δ_*} are in charge of the spectral amplitude.

Kamruzzaman *et al.* [47] (KBLWK) proposed a spectral model for the prediction of the airfoil trailing edge noise. The wall pressure fluctuation spectra as measured by different investigators [42, 78, 79, 80, 81, 82] were used to develop the model. The formulation of the model reads

$$\frac{\Phi(\omega)U_e}{\tau_w^2\delta^*} = \frac{0.45\left[1.75 \cdot ({\Pi_{\delta^*}}^2 \cdot {\beta_{\delta^*}}^2)^m + 15\right](\omega\delta^*/U_e)^2}{[(\omega\delta^*/U_e)^{1.637} + 0.27]^{2.47} + [(1.15R_T)^{-2/7} \cdot (\omega\delta^*/U_e)]^7}, \tag{2.51}$$

where $\beta_{\delta^*} = \delta_*/\tau_w \cdot dp/dx$, in which dp/dx represents the pressure gradient in the streamwise direction, $\Pi_{\delta^*} = 0.8 \cdot (\beta_{\delta^*} + 0.5)^{3/4}$ and $m = 0.5 \cdot (H/1.31)^{0.3}$. Except for the mid-frequency extension determined by R_T, the formulated spectrum has a constant shape for different pressure gradient configurations, i.e. a constant decreasing slope of approximately ω^{-2} at medium frequencies and a constant spectral peak location at the non-dimensional frequency. The spectral amplitude is adjusted by a combination of Clauser's equilibrium parameter β_{δ^*} [83], Cole's wake parameter Π_{δ^*} [84, 85] and boundary layer shape factor H.

Catlett *et al.* [43, 48] (CFAS) measured the wall pressure fluctuations on tapered trailing edge sections of a flat plate with three different opening angles and proposed an empirical spectral model based on the measured data, which reads

$$\frac{\Phi(\omega)U_e}{\tau_w^2\delta} = \frac{a \cdot (\omega\delta/U_e)^b}{[(\omega\delta/U_e)^c + d]^e + [fR_T^g \cdot (\omega\delta/U_e)]^h}\ , \tag{2.52}$$

$$\begin{aligned}
\ln(a - a_G) &= 4.98 \cdot (\beta_\Delta {Re_\Delta}^{0.35})^{0.131} - 10.7,\\
b &= 2,\\
c - c_G &= 20.9 \cdot (\beta_\delta {Re_\delta}^{0.05})^{2.76} + 0.162,\\
d - d_G &= 0.328 \cdot (\beta_\Delta {Re_\Delta}^{0.35})^{0.310} - 0.103,\\
e - e_G &= -1.93 \cdot (\beta_\delta {Re_\delta}^{0.05})^{0.628} + 0.172,\\
f - f_G &= -2.57 \cdot (\beta_\delta {Re_\delta}^{0.05})^{0.224} + 1.09,\\
g - g_G &= 38.1 \cdot (\beta_\delta H^{-0.5})^{2.11} + 0.0276,\\
h - h_G &= 0.797 \cdot (\beta_\Delta {Re_\Delta}^{0.35})^{0.0724} - 0.310,
\end{aligned}$$

where $\beta_{\delta,\Delta} = (\delta, \Delta)/Q \cdot dp/dx$, $Re_{\delta,\Delta} = (\delta, \Delta)U_e/\nu$ and $\Delta = \delta^*\sqrt{2/C_f}$. The parameters $a - h$ are derived by fitting to the measured spectra. The constants $a_G - h_G$ from Goody's model with correspondent positions in Eq. (2.52) are replaced with the functions based on boundary layer parameters, except for $b = 2$, which stands for an ω^2 increase at low frequencies. The spectral amplitude, peak location and slope at medium frequencies are affected by Clauser's equilibrium parameter and Reynolds numbers defined with different length scales.

2.2.2 Cross-spectral model

The combined spatio-temporal properties of the wall pressure fluctuations are also important features in terms of the flow-induced surface vibration. The space-time correlation for the wall pressure fluctuations over (x_1, x_3) plane is defined by,

$$R_{pp}(\mathbf{x}, \mathbf{r}, \tau) = < p'(\mathbf{x}, t)p'(\mathbf{x} + \mathbf{r}, t + \tau) > \tag{2.53}$$

where $\mathbf{x} = (x_1, x_3)$ and $\mathbf{r} = (r_1, r_3)$. $R_{pp}(\mathbf{x}, \mathbf{r}, \tau)$ denotes the correlation at the surface point (x_1, x_3). If the wall pressure fluctuation field can be treated as a homogeneous field, so the correlation is not location-dependent, $R_{pp}(\mathbf{x}, \mathbf{r}, \tau) \sim R_{pp}(\mathbf{r}, \tau)$. This assumption is well fulfilled for fully developed 2-D turbulent boundary layers at high Reynolds numbers. Thus, the cross-spectrum can be defined by

$$\Phi_{pp}(r_1, r_3, \omega) = \frac{1}{2\pi}\int_{-\infty}^{\infty} R_{pp}(r_1, r_3, \tau)\exp(-i\omega\tau)\,\mathrm{d}\tau, \tag{2.54}$$

The most used model for describing the spatial and temporal properties of the wall fluctuating pressure field is the one proposed by Corcos [51]. He chose a separation form to model the cross-spectrum also regarding the convecting effects of the fluctuating field, expressed as

$$\Phi_{pp}(r_1, r_3, \omega) = \Phi_{pp}(\omega) A(\omega r_1/U_c) B(\omega r_3/U_c) \exp(i\omega r_1/U_c), \tag{2.55}$$

where $\Phi_{pp}(\omega)$ is the wall pressure one-point spectrum, $A(\omega r_1/U_c)$ and $B(\omega r_3/U_c)$ represent the coherence function for the streamwise and spanwise directions and $\exp(i\omega r_1/U_c)$ denotes the phase difference due to the (passive) convection of the fluctuating field. Corcos found similarity of the coherences in both streamwise and spanwise directions, and the coherences can be well expressed by using exponential functions. Thus, the formulation of Corcos's model reads

$$\Phi_{pp}(r_1, r_3, \omega) = \Phi_{pp}(\omega) \exp(-\alpha|\omega r_1/U_c|) \exp(-\beta|\omega r_3/U_c|) \exp(i\omega r_1/U_c), \tag{2.56}$$

where α and β are empirical constants which can be determined from the measurement. The values of α and β represent the loss in coherence of the wall pressure fluctuations in the streamwise and spanwise directions, respectively. A larger value implies a stronger decay. From the literature, we found $0.1 < \alpha < 0.15$ for ZPG boundary layers on a smooth surface. The value is Reynolds number dependent. Generally, for a larger Reynolds number the value of α is rather smaller, which may indicate the decay of the pressure fluctuation field is smaller. The turbulent flow on a rough surface causes a stronger turbulence decay in the streamwise direction, which leads to a larger value of $\alpha = 0.32$ measured by Blake [50]. The decay is also larger for APG boundary layers. The stronger the pressure gradient, the larger the value of α [48]. In contrast, for a favorable pressure gradient (FPG) boundary layer, the value tends to be smaller. The value of β implies the size of the correlated structure in the spanwise direction. The value of β is found around $\beta = 0.7 - 0.72$. There is no evidence found that the value is dependent on the Reynolds number. For APG boundary layers, the value tends to be smaller which indicates a larger correlated structure in the spanwise direction.

The coherence for the wall pressure fluctuations is defined by,

$$\Gamma_{pp}(r_1, r_3, \omega) = \frac{\Phi_{pp}(r_1, r_3, \omega)}{\sqrt{|\Phi_{pp}(x_1, x_3, \omega)\Phi_{pp}(x_1 + r_1, x_3 + r_3, \omega)|}}. \tag{2.57}$$

Because of the homogeneous assumption,

$$\sqrt{|\Phi_{pp}(x_1, x_3, \omega)\Phi_{pp}(x_1 + r_1, x_3 + r_3, \omega)|} = |\Phi_{pp}(r_1, r_3, \omega)|, \tag{2.58}$$

using Corcos's formulation the coherence can be expressed as

$$\Gamma_{pp}(r_1, r_3, \omega) = \exp(-\alpha|\omega r_1/U_c|) \exp(-\beta|\omega r_3/U_c|) \exp(i\omega r_1/U_c). \tag{2.59}$$

Note that, in this expression the coherence approaches 1 when $r_{1,3} \to 0$ or $\omega \to 0$. The first condition $r_{1,3} \to 0$ indicates that a closer distance has a larger coherence and the coherence between the same position is equal to 1. This is verified by the definition of the coherence, according to Eq. (2.57). The second condition $\omega \to 0$ indicates that the coherence increases as the frequency decreases. This is true for the higher frequencies, where the similarity of

the coherence holds. Measurements [6, 8, 9] showed that a loss in similarity occurs at low frequencies and the coherence decreases consequently. Farabee & Casarella [8] argued that the decrease in the coherence is a physical requirement, otherwise, the eddies could produce low-frequency fluctuations which would convect without decay over an infinite distance. A cutoff frequency for the coherence is found located between $1.3 < \omega\delta/U_c < 2.7$. The cutoff frequency decreases as the distance r_1 increases. A noteworthy finding is that the cutoff frequency occurs at the region where the spectral maximum of the wall pressure fluctuations is located. This may indicate that the lowest-decay eddies contribute the most to the wall pressure fluctuations.

3 Methods

The characteristics of wall pressure fluctuations beneath turbulent boundary layers were experimentally and numerically investigated. Experiments were conducted at a flat plate model in the Aeroacoustic Wind Tunnel Braunschweig (AWB) [86]. Effects of the pressure gradients on the characteristics of the wall pressure fluctuations were studied by installing an adjustable National Advisory Committee for Aeronautics (NACA) 0012 airfoil with a chord length of 40 cm above the flat plate. The static wall pressure was measured in the streamwise and spanwise directions on the plate model by static pressure ports. The dynamic wall pressure was measured by an 'L-shaped' array of subminiature Kulite pressure transducers. In addition, the mean velocity profiles and the Reynolds stress tensors within the turbulent boundary layer were obtained using hot wire anemometers. Details of the test setups and the measurement techniques are described in section 3.1.

The wall pressure fluctuations are obtained by solving Poisson's equation. The source terms on the right-hand side of the Poisson's equation including the mean-shear and the turbulence-turbulence terms are realized using synthetic isotropic and anisotropic turbulence generated by the Fast Random Particle-Mesh Method (FRPM) [87]. The averaged turbulence statistics needed for the stochastic realization is provided by the Reynolds averaged Navier-Stokes (RANS) calculation. Anisotropy of the turbulence length scales can be applied using different integral length scales in different directions. Reynolds stress anisotropy can be gained by using a scaling tensor for the relation between the anisotropic stress provided by the RANS calculation and the respective isotropic expression for the Reynolds stress. The Poisson's equation is solved by using the convolution theorem in the wavenumber domain with a free-space Green's function. For an exact realization of the Green's function in conjunction with a Fourier transform method on a finite domain, Hockney's method [75] is applied to the Poisson problem. A brief description of the applied numerical method is provided in section 3.2.

3.1 Experimental test cases

3.1.1 Test setups

The wall pressure fluctuations beneath a turbulent boundary layer with zero and non-zero pressure gradients were measured at a plate model in the open-jet anechoic test section of the AWB. Details of the experimental setup are documented in Fig. 3.1. A flat wooden plate was placed 10 mm downstream of the nozzle exit in the nozzle mid-height position. The plate surface was aligned with the flow direction.

To design the plate model, following considerations were made. The background noise of the AWB increases significantly at low frequencies < 300 Hz [86], which may disturb the low frequency range of the wall pressure spectra, especially for higher flow velocities. In order to measure at least the maximum of the wall pressure spectra without disturbances, the spectral maximum should be located at > 300 Hz. Considering a thicker boundary layer thickness for adverse pressure gradient (APG) boundary layers and the respective

frequency shift for the spectral maximum to lower frequencies, the maximum for the zero pressure gradient (ZPG) boundary layers should be located at much larger than 300 Hz, especially for higher flow velocities. The maximum position for the ZPG boundary layers can be estimated based on $\omega_{max}\delta/U_e \approx 2$ [36], where ω_{max} denotes the angular frequency of the spectral maximum, δ is the boundary layer thickness and U_e is the boundary layer edge velocity. For example, for a given velocity the thicker the boundary layer thickness is, the lower the maximum frequency is. For this reason, a very thick boundary layer thickness at the measurement position is not desired. On the other hand, the boundary layer thickness at the measurement position should also be thick enough, so that the log-law region of the boundary layer can be resolved experimentally based on the available measurement equipment, so that consequently, the wall shear stress can be well estimated. Summing up, a boundary layer thickness on the order of 2 cm satisfies the above criteria. A 2 cm boundary layer thickness denotes an approximate 4 mm log-law region, which can be well measured and determined. Meanwhile, the maximum is estimated located at about 950 Hz for $U_e = 60$ m/s, which is much larger than the criterion 300 Hz. To develop a boundary layer of 2 cm thickness on a flat plate, the needed length downstream from the plate nose can be estimated according to $\delta \approx 0.37x/Re_x^{1/5}$ [88], where x denotes the streamwise distance away from the leading edge and Re_x is the streamwise distance based Reynolds number. This results in a length of about 1.2 m. Furthermore, the measurement position (about 1.2 m downstream of the leading edge of the plate) should be far enough away from the trailing edge of the plate, so that there is no disturbances from the trailing edge at the measurement position. On the other hand, to determine the Reynolds stress of the boundary layer, a crossed hot-wire placed parallel or with a possible small angle to the plate surface is required. This is because, to measure the spanwise velocity fluctuations, a yaw-angle in the wall-normal direction may induce measurement error and the error cannot be corrected based on the yaw-angle calibration. Therefore, the distance between the measurement position and the trailing edge of the plate is limited by the accessible distance of the hot-wire probe away from the support arm of the traverse system (see Figs. 3.1(b,d)), which is about 180 mm. This allows the support arm to be placed behind the plate, which enables the hot-wire probe to be set with a small angle to the plate surface.

The thickness of the plate should be large enough to ensure the setup is stable and allow to insert the sensors and the cables. Thus, a length of 1350 mm and a thickness of 42 mm for the plate model were chosen. The plate span is needed to be larger than the nozzle exit in order to prevent the interaction of the AWB open-jet shear layers between the top and bottom sides of the plate. The spreading angle of the free shear layer can be estimated at about 7° [89]. The spreading angle of the shear layer on a plate may be larger than of a free shear layer. Thus, an angle of 10° was used to estimate the spreading distance of the shear layer at the trailing edge of the plate, which results in a distance of about 240 mm. Finally, a plate span of 1300 mm was determined, which is 250 mm wider than the nozzle exit on each side, see Fig. 3.1(d).

A 125 mm long superellipse ($n = 3$) shaped leading-edge part was selected to avoid flow separation [90] and manufactured by 3-D printing. Both sides of the plate were tripped at 120 mm behind the leading-edge tip with 0.3 mm zigzag trip strips. A 12° beveled trailing edge on the bottom side of the plate was used to realize a ZPG turbulent boundary layer on the topside in the rear area [91]. The 5-mm thick trailing-edge tip was extended by foam serrations to avoid vortex shedding and to reduce trailing-edge noise.

Pressure gradients were realized by placing an adjustable NACA 0012 airfoil with 400 mm chord length and 1800 mm span width above the plate, see Fig. 3.1. The airfoil was installed 120 mm above the plate relative to the wing's chord at the geometric angle of attack (AOA) of 0°. The rotation axis was at 41% of the chord length. The geometric AOA of the airfoil was varied between -14° and 14°. The leading edge of the airfoil was located at $x = 850$ mm ($x = 0$ for the leading-edge tip of the plate). Both sides of the airfoil were tripped at 20% chord length with 0.4 mm zigzag trip strips to avoid a possible laminar vortex shedding noise originated at the large AOA.

3.1.2 Measurement techniques

A 370 mm long, 270 mm wide and 5 mm thick aluminium panel equipped with 25 static pressure ports and twelve Kulite pressure transducers was placed at mid-span in the rear portion of the plate, see Fig. 3.2. The rear edge of the panel was located at 90 mm upstream of the trailing edge of the plate. The static pressure ports (0.5 mm diameter) covered 290 mm in the streamwise direction and 180 mm in the spanwise direction.

The wall pressure fluctuations were measured by twelve pinhole-mounted Kulite pressure transducers without the protection screen, model LQ-062-0.35 bar. The diameter of the pinhole was 0.5 mm and the depth was 0.5 mm. The Kulite sensor with a diameter of 1.6 mm was glued with silicone in a 1.8 mm diameter hole behind the pinhole. A photo and an installation sketch of the Kulite sensor is shown in Fig. 3.3.

The selection of the Kulite sensor and the pinhole construction was determined based on the following considerations. To measure the wall pressure fluctuations, two types of mounting constructions, namely flush mounting and pinhole mounting, can be used.

In general, for the flush mounting construction the sensor size is too large to measure the wall pressure fluctuations at high frequencies. An attenuation of the measured wall spectra at high frequencies will be caused due to the finite sensor size. This is because the sensor measures an averaged pressure fluctuations over the whole sensor area, and the higher the frequency is (smaller wave length), the stronger the attenuation is. A noticeable attenuation of about 1 dB may occur at about $\omega r/U_c = 0.3$, estimated based on the Corcos correction [16], where r is the sensor radius and U_c is the convective velocity of the wall pressure fluctuations, which is usually estimated between $U_c = 0.6 - 0.8U_0$. Thus, the frequency range without attenuation (<1 dB) for the wall pressure spectra can be estimated for a given flow velocity and sensor size. The smallest available Kulite sensor has a diameter of 1.6 mm with a so called 'B-screen' (eight 0.2 mm diameter holes around a 1.2 mm diameter circle), so the radius of the effective sensor area can be roughly estimated to be 0.6 mm. For a flow velocity $U_0 = 60$ m/s and U_c estimated at $0.7U_0$, the frequency range without attenuation is estimated to extend to about 3.3 kHz, which is too low to investigate the features of the wall pressure fluctuations. Therefore, the flush mounting construction was discarded.

For the pinhole mounting construction, the key criterion is the Helmholtz resonance frequency. It should be high enough to avoid its impact on the measured wall pressure spectra. The Helmholtz resonance frequency can be estimated by

$$f_{res} = \frac{a_0}{2\pi}\sqrt{\frac{S_0}{V_0 \cdot L}}, \tag{3.1}$$

where S_0 and L denote the pinhole area and the length of the pinhole, respectively, and

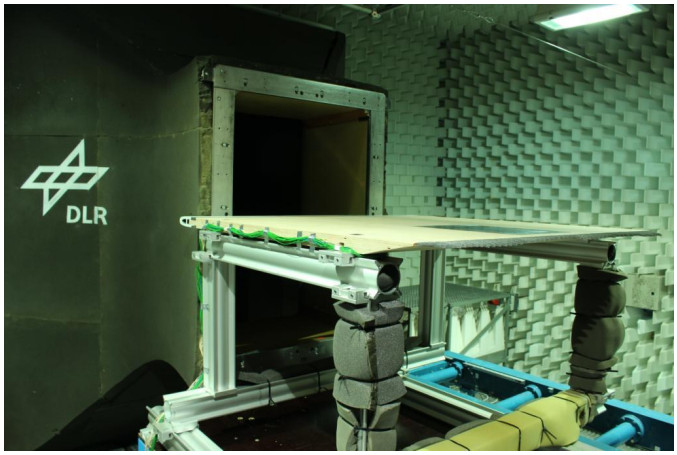

(a)

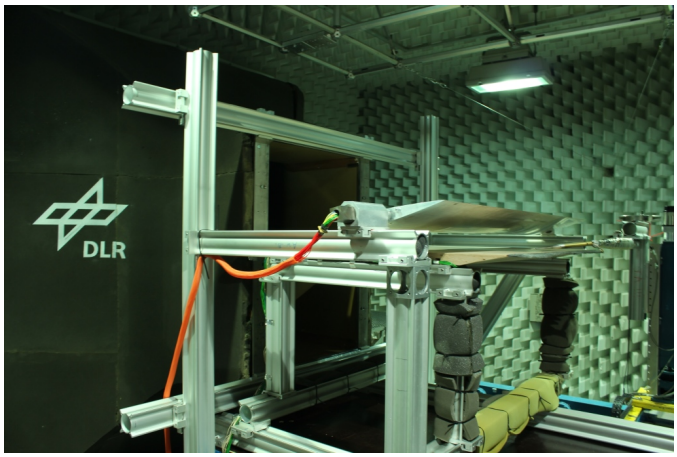

(b)

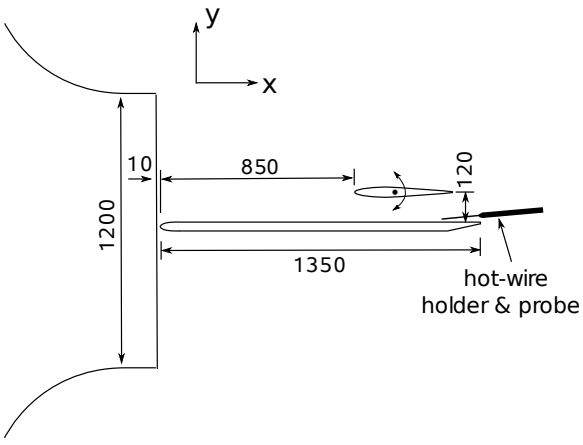

(c)

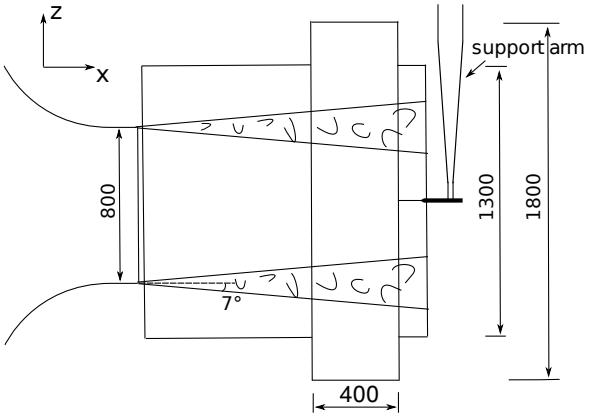

(d)

Figure 3.1: Experimental setup in AWB; (a) zero pressure gradient test case; (b) non-zero pressure gradient test case; (c) side view sketch; (d) top view sketch.

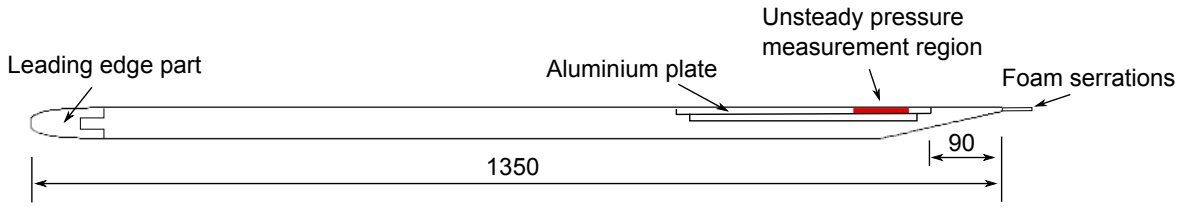

(a)

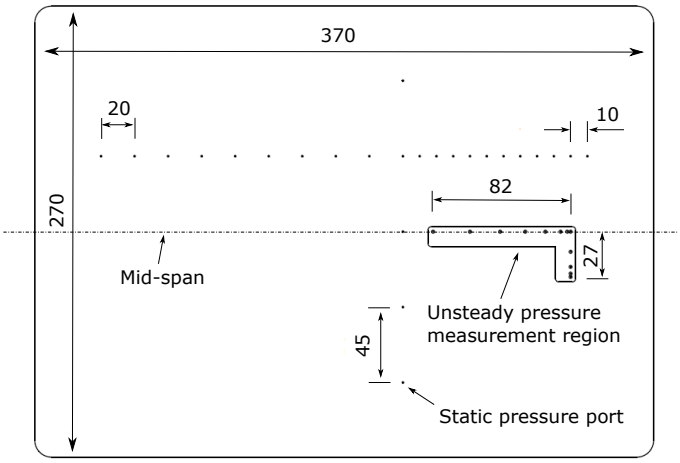

(b)

Figure 3.2: (a) Schematic view of the plate configuration; (b) layout for the Kulites and the static pressure ports on the aluminium panel.

V_0 denotes the sealed volume between the pinhole and the sensor surface. To obtain a higher resonance frequency, we need a larger pinhole area, a smaller length of the pinhole and a possibly smaller sealed volume behind the pinhole. Thus, the available smallest Kulite sensor model LQ-062 (1.6 mm diameter) was used. Furthermore, to keep the sealed volume behind the pinhole as small as possible and prevent a complex geometry of the 'Helmholtz resonator' construction, the protection screen of the Kulite sensor was discarded. A 0.5 mm diameter and a 0.5 mm length of the pinhole was determined from experience [37, 45]. Based on the pinhole construction shown in Fig. 3.3, the Helmholtz resonance can be located at up to 60 kHz for a perfect installation. This resonance frequency is satisfactory for the experimental purposes. Therefore, the pinhole mounting construction of the Kulite sensor was chosen for the experiment.

The Kulite sensors were located in the streamwise direction between 1128 mm $\leq x \leq$ 1210 mm and in the spanwise direction between 0 mm $\leq z \leq$ 27 mm ($z = 0$ for the mid-span position). The layout for the Kulite sensors is shown in Fig. 3.2. During the measurement the sampling rate was set at 100 kHz and the data were recorded for 20 s. A preamplifier with a gain factor of 250 and a high pass filter with cut-off frequency at 200 Hz was applied. The measured power spectra shown in this thesis are corrected using the filter frequency response curve.

The mean velocity profiles for the turbulent boundary layer were measured by a single hot-wire anemometer. The Reynolds stresses were determined using a crossed hot-wire anemometer. The jaw angle of the hot-wire probes to the plate surface was about 6° in the

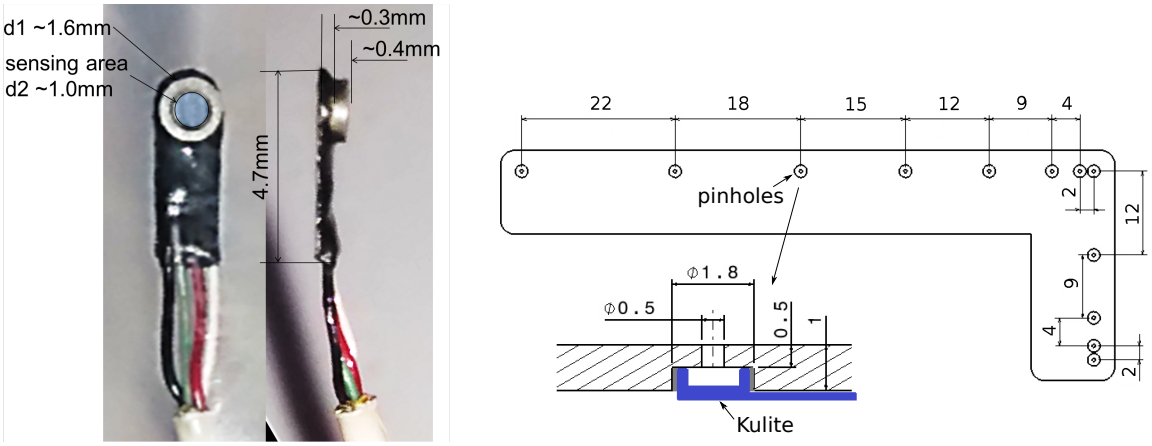

(a) (b)

Figure 3.3: (a) Dimension of the Kulite sensor (picture taken from Suryadi and Herr [45]) (b) layout and construction for the Kulite setup.

measurement. The hot-wire data were recorded for 10.3 s with a sampling rate of 50 kHz and a low pass filter of 20 kHz.

3.2 Numerical approach

3.2.1 Poisson's equation

Pressure fluctuations in an incompressible turbulent boundary layer are governed by a Poisson's equation. The derivation of the Poisson's equation can be found in section 2.1. For a turbulent boundary layer along a wall located at $x_2 = 0$, the Poisson's equation resulting from a mean flow in the positive x_1-direction becomes

$$\Delta p' = -\rho_0 \left(2\frac{\partial \overline{u}_1}{\partial x_2}\frac{\partial u_2'}{\partial x_1} + \frac{\partial^2}{\partial x_i \partial x_j}(u_i'u_j' - \overline{u_i'u_j'}) \right). \tag{3.2}$$

Here, $\overline{u}_1$ denotes the mean-flow velocity component in the x_1-direction and u_i' indicates velocity fluctuations; the x_2-direction is the wall normal direction and the x_3-direction is the spanwise direction, refer to the coordinate system shown in Fig. 3.4; ρ_0 is the mean air density and p' is the fluctuating pressure. The source term on the right-hand side of Eq. (3.2) comprises two parts. The first part is the mean-shear turbulence interaction term and the second part is the turbulence-turbulence interaction term. As addressed in section 2.1, the pressure fluctuations can be calculated from the convolution of the free-space Green's function of the Poisson's equation with the right-hand side source term,

$$p'(\mathbf{x},t) = -\int_{\mathbf{V_s}+\mathbf{V_s'}} \rho_0 \left(2\frac{\partial \overline{u}_1}{\partial x_2}\frac{\partial u_2'(\mathbf{y},t)}{\partial x_1} + \frac{\partial^2}{\partial x_i \partial x_j}(u_i'u_j' - \overline{u_i'u_j'})(\mathbf{y},t) \right) \cdot g(\mathbf{x}-\mathbf{y})\,\mathrm{d}V(\mathbf{y}), \tag{3.3}$$

where $\mathbf{V_s} + \mathbf{V_s'}$ denotes the original source area plus the mirrored source area at the solid wall. The free-space Green's function for a 3-D Poisson problem is given by

$$g(\mathbf{x}-\mathbf{y}) = -\frac{1}{4\pi|\mathbf{x}-\mathbf{y}|}. \tag{3.4}$$

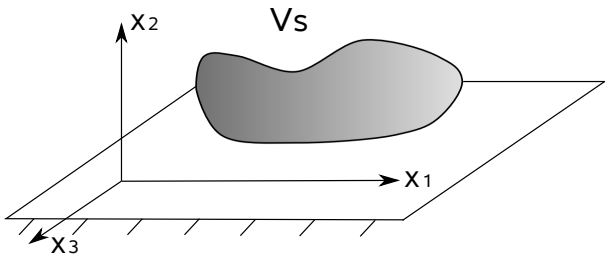

Figure 3.4: Sketch of the coordinate system.

If we let $f(\mathbf{y}, t)$ represent the source terms, the convolution integral Eq. (3.3) can be expressed as

$$\int_{\mathbf{V_s}+\mathbf{V_s'}} f(\mathbf{y}, t) \cdot g(\mathbf{x}-\mathbf{y})\, \mathrm{d}^3 y = (f * g)(\mathbf{x}, t). \tag{3.5}$$

Using the specific orientation of the coordinate system indicated in Fig. 3.4, the wall boundary condition becomes $\partial p'/\partial x_2 = 0$. The equation is solved in wavenumber domain by using the convolution theorem:

$$\mathcal{F}\left\{f * g\right\}(\mathbf{x}, t) = \mathcal{F}\left\{f\left(\mathbf{x}, t\right)\right\} \cdot \mathcal{F}\left\{g\left(\mathbf{x}\right)\right\} = \hat{f}\left(\mathbf{k}, t\right) \cdot \hat{g}\left(\mathbf{k}\right). \tag{3.6}$$

Here $\hat{f}\left(\mathbf{k}, t\right) = \mathcal{F}\left\{f\left(\mathbf{x}, t\right)\right\}$ denotes the 3-D spatial Fourier transform from the consecutive application of the one-dimensional (1-D) spatial Fourier transform for all spatial coordinates x_i as defined by Eq. (A.2) in the Appendix. Consequently, a solution to the Poisson problem for pressure is obtained at a given time level by multiplying the spatial Fourier transform of the time-dependent source term with the Fourier transform of the free-space Green's function and subsequently transforming back the result into physical space:

$$p'\left(\mathbf{x}, t\right) = \mathcal{F}^{-1}\left\{\hat{f}\left(\mathbf{k}, t\right) \cdot \hat{g}\left(\mathbf{k}\right)\right\}. \tag{3.7}$$

As indicated above, the appropriate wall boundary condition is already realized by taking into account an image source region underneath the wall surface. However, the Fourier transform approach in general is applied on a finite computational domain and inherently realizes periodicity across the domain boundaries. For an accurate numerical solution with this approach, one must assess whether the extension of the domain is large enough to ensure that despite the artificial truncation and periodicity of the Green's function represented on the finite domain, it still provides a good approximation to the free-space Green's function.

To circumvent this problem, in this work the modification as introduced by [75] is applied, which provides an exact realization of the free-space Green's function in conjunction with a Fourier transform method on a finite domain. For Hockney's method applied to the Poisson problem, the computational core domain can be limited to the extension of the considered right-hand side source term plus its mirror image. Then, the resulting complete computational domain follows by doubling the core domain in each spatial direction, refer to the sketch shown in Fig. 3.5(a). The Green's function is prescribed on the entire domain. A source distribution for the complete domain is obtained by zero padding of the

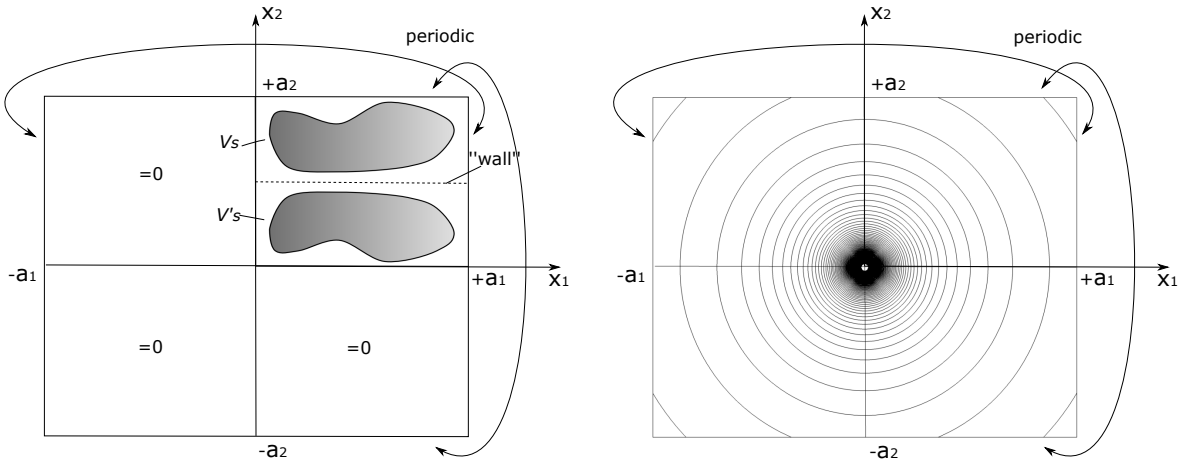

Figure 3.5: 2-D sketch to illustrate application of Hockney's method with free field boundary condition; (a) source distribution with location of solid wall; (b) contour lines of free-space Green's function Eq. (3.4).

source in the appended domains. Hence, the source function and the Green's function for the resolved domain become

$$f(\mathbf{x}) = \begin{cases} f(\mathbf{x}), & 0 \leq x_i \leq a_i; i \in \{1...3\}. \\ 0, & \text{else.} \end{cases} \tag{3.8}$$

$$g(\mathbf{x}) = -\frac{1}{4\pi|\mathbf{x}|}, \quad -a_i \leq x_i \leq a_i; i \in \{1...3\}. \tag{3.9}$$

To sketch the basic idea behind Hockney's approach, it is convenient to consider the underlying spatial convolution Eq. (3.5). If we seek for a solution to the Poisson problem just in a core source domain of spatial extensions a_i, the convolution integral includes products of the source term with the free-space Green's function evaluated at a shifted position, which involve at maximum a shift in each direction given by a_i. Hence, if a Green's function with periodic continuation is applied that is specified over twice the width of the core source distribution, i.e. $2a_i$, Fig. 3.5(b), and no further source contribution is considered in the extended domain (zero padding), Fig 3.5(a), the convolution integral will provide inside the core domain an exact solution to the Poisson problem based on the free-space Green's function.

3.2.2 Fast Random Particle-Mesh Method

Anisotropic synthetic turbulence

To calculate the fluctuating pressure an appropriate fluctuating velocity field within the turbulent boundary layer is needed. We use FRPM [87] to generate synthetic turbulent velocity fluctuations to prescribe the right-hand side source term of Eq. (3.2). FRPM uses averaged turbulence statistics to synthesize the turbulent velocity fluctuations. One- and

two-point statistics are realized. The basic idea is to generate a fluctuating velocity vector from the convolution of spatial white noise $\mathcal{U}_i$ with a spatial Gaussian filter kernel G,

$$u_i'(\mathbf{x},t) = \hat{a}_{ik}(\mathbf{x}) \int_{V_s} \epsilon_{klm} \frac{\partial G\left(\mathbf{x}-\mathbf{x}'\right)}{\partial x_l} \mathcal{U}_m(\mathbf{x}',t) \mathrm{d}^3\mathbf{x}' \tag{3.10}$$

where ϵ_{klm} denotes the Levi-Civita symbol (permutation tensor), $\mathbf{x} = (x_1, x_2, x_3)^T$ defines field coordinates and $\mathbf{x}' = (x_1', x_2', x_3')^T$ defines white noise field coordinates. The Gaussian filter is defined by the consecutive application of 1-D Gaussian filters based on separate length scales l_i for each spatial direction,

$$G(\mathbf{x}-\mathbf{x}') = g(x_1 - x_1', l_1)\, g(x_2 - x_2', l_2)\, g(x_3 - x_3', l_3) \tag{3.11}$$

with

$$g(y,l) := \exp\left(-\frac{\pi}{2}\frac{y^2}{l^2}\right). \tag{3.12}$$

The tensor $\hat{a}_{ik}$ provides the proper scaling so that the anisotropic Reynolds stress tensor can be realized by the synthesized fluctuating velocity fields. Note, the summation rule is applied over all equal indices.

In this work a generic study is conducted on the influence of length scale anisotropy on the resulting wall pressure spectrum. For this purpose, anisotropy in length scales is considered using separate filter length scales l_i in the streamwise, wall-normal and spanwise directions, respectively. Furthermore, the streamwise length scale is increased by a stretching factor γ compared to the wall normal scale, $l_1 = \gamma l_2$, whereas the length scales in the wall-normal and spanwise directions are kept equal, $l_2 = l_3$. For the present study, the stretching factor is treated as a constant parameter throughout the computational domain. Note, in general three spatial length scales are associated with each Reynolds stress component, yielding a third-rank tensor with 18 generally non-equal components. This anisotropic length scale information is not provided by RANS. In [92] an approach to stochastically model anisotropic length scales from RANS parameters for non-equilibrium turbulence has been proposed.

In general, the length scale from RANS l_s is considered as a scalar scale representing all anisotropic scales [93] assuming the relationship $l_s = (l_1 l_2 l_3)^{1/3}$, which yields $l_2 = l_3 = l_s \gamma^{-1/3}$.

The scalar turbulent length scale l_s is determined from the RANS solution via

$$l_s = \frac{c_l}{C_\mu} \frac{\sqrt{k_t}}{\omega}, \tag{3.13}$$

where $k_t = R_{ii}/2$ is the turbulent kinetic energy and ω is the specific rate of dissipation. The constant $C_\mu = 0.09$ and c_l is estimated to be 0.54 [94], so the prefactor $c_l/C_\mu \simeq 6.0$.

The white noise field $\mathcal{U}_i$ is defined in a Lagrangian frame moving at local flow velocity $\mathbf{U}$. Altogether, the properties of white noise are defined in a fixed Eulerian frame by

$$< \mathcal{U}_i(\mathbf{x}',t) > \;=\; 0, \tag{3.14}$$

$$< \mathcal{U}_i(\mathbf{x}',t)\mathcal{U}_j(\mathbf{x}'+\mathbf{r},t+\tau) > \;=\; \delta(\mathbf{r}-\mathbf{U}\tau)\delta_{ij}. \tag{3.15}$$

where the bracket means an ensemble average, δ_{ij} is the Kronecker symbol and $\delta(\mathbf{r}-\mathbf{U}\tau)$ describes frozen turbulence moving with the flow velocity $\mathbf{U}$. Additional temporal turbulence decay can be modeled by a Langevin equation, which introduces the de-correlation in

the two-points statistics [87]. In the Eulerian frame a modification of the cross-correlation is given by

$$< \mathcal{U}_i(\mathbf{x}', t)\mathcal{U}_j(\mathbf{x}' + \mathbf{r}, t + \tau) >= \delta(\mathbf{r} - \mathbf{U}\tau) \exp\left(-\frac{|\tau|}{\tau_s}\right) \delta_{ij}. \tag{3.16}$$

In this expression $\exp(-|\tau|/\tau_s)$ describes the turbulence decay, i.e. the field is spatially white and correlated in time with time scale τ_s. The local time scale can be determined from RANS solutions by

$$\tau_s = c_\tau \frac{l_s}{\sqrt{k_t}}, \tag{3.17}$$

where the prefactor c_τ needs to be determined. [95] modeled the time scale in a $k-\epsilon$ model and determined the prefactor empirically by fitting experimental results of jet flows, which resulted in $c_\tau \simeq 0.91$. In this work, a constant $c_\tau = 1.2$ is applied which is based on a consistent result of the streamwise coherence of the wall pressure fluctuations compared to the experimental results. The additional effect of the temporal turbulence decay for turbulence velocity fluctuation spectra is discussed in Appendix A.

Scaling tensor

For a stationary turbulent problem, straightforward manipulation of expression Eq. (3.10) yields the Reynolds stresses expressed in terms of the scaling tensor,

$$R_{ij}(\mathbf{x}) = \left\langle u_i'(\mathbf{x}, t)u_j'(\mathbf{x}, t)\right\rangle = \hat{a}_{ik}(\mathbf{x})\hat{a}_{jn}(\mathbf{x}) \int_{V_s} \epsilon_{klm}\epsilon_{nop} \frac{\partial G\left(\mathbf{x} - \mathbf{x}'\right)}{\partial x_l} \frac{\partial G\left(\mathbf{x} - \mathbf{x}''\right)}{\partial x_o} \left\langle \mathcal{U}_m(\mathbf{x}', t)\mathcal{U}_p(\mathbf{x}'', t)\right\rangle \mathrm{d}^3\mathbf{x}'\mathrm{d}^3\mathbf{x}'' \tag{3.18}$$

Based on Eq. (3.16) with $\tau = 0$ and $\mathbf{r} = 0$, the integration over the delta function related to $\mathbf{x}''$ can be carried out. Using the definition

$$\mathcal{I}_{ij}(\mathbf{x}) := \int_{V_s} \frac{\partial G\left(\mathbf{x} - \mathbf{x}'\right)}{\partial x_i} \frac{\partial G\left(\mathbf{x} - \mathbf{x}'\right)}{\partial x_j} \mathrm{d}^3\mathbf{x}', \tag{3.19}$$

the Reynolds stresses eventually read (dependence on spatial coordinate not explicitly shown)

$$R_{ij} = \hat{a}_{ik}\hat{a}_{jn}\epsilon_{mlk}\epsilon_{mon}\mathcal{I}_{lo}. \tag{3.20}$$

Furthermore, using the identity $\epsilon_{mlk}\epsilon_{mon} = \delta_{lo}\delta_{kn} - \delta_{ln}\delta_{ko}$, it follows

$$R_{ij} = \hat{a}_{ik}\hat{a}_{jl}S_{kl}, \tag{3.21}$$

where $S_{kl} = \delta_{kl}\mathcal{I}_{mm} - \mathcal{I}_{lk}$ defines a symmetric diagonal matrix, since $\mathcal{I}_{lk} = 0$ for $l \neq k$ as a result of its definition Eq. (3.19) with filter function Eq. (3.11). Let $s_{km} = c_{(k)}\delta_{km}$ (the brackets indicate omission of the summation rule) denote the diagonal matrix that follows by taking the square root of the diagonal elements of $S_{kl} = c_{(k)}c_{(l)}\delta_{kl}$ (i.e. $S_{kl} = s_{km}s_{lm}$) and let r_{ij} denote the Cholesky decomposition of the Reynolds stress tensor, i.e. $R_{ij} = r_{im}r_{jm}$, then the scaling tensor needed to evaluate Eq. (3.10) is defined by $r_{im} = \hat{a}_{ik}s_{km}$, respectively,

$$\hat{a}_{ik} = r_{ik}/c_{(k)}. \tag{3.22}$$

From the previous discussion it follows that the scaling explicitly is defined by $c_{(k)} = \sqrt{\mathcal{I}_{ll} - \mathcal{I}_{k(k)}}$.

Using the definition of the integral Eq. (3.19) together with the length scale definitions from the beginning of this section and applying the definition of the Gaussian filter, Eq. (3.11), the scaling parameters $c_{(k)}$ can be explicitly evaluated, yielding

$$c_{(1)} = \sqrt{\pi l_s}\gamma^{1/3}, \quad c_{(2)} = \sqrt{\frac{\pi l_s}{2}}\frac{\sqrt{1+\gamma^2}}{\gamma^{2/3}}, \quad c_{(3)} = \sqrt{\frac{\pi l_s}{2}}\frac{\sqrt{1+\gamma^2}}{\gamma^{2/3}}. \tag{3.23}$$

Next, the Cholesky decomposition of the in general anisotropic Reynolds stress tensor R_{ij} from RANS with Reynolds stress model is deduced from

$$(r_{ij}) = \begin{pmatrix} \sqrt{R_{11}} & 0 & 0 \\ R_{21}/r_{11} & \sqrt{R_{22}-r_{21}^2} & 0 \\ R_{31}/r_{11} & (R_{32}-r_{21}r_{31})/r_{22} & \sqrt{R_{33}-r_{31}^2-r_{32}^2} \end{pmatrix}, \tag{3.24}$$

which can be solved starting with the first row and using successively for the evaluation of the consecutive rows already computed components of r_{ij}.

According to this procedure, the tensor S_{kl} can be Cholesky decomposed into the matrix s_{km} and the final scaling matrix follows by multiplying r_{im} with the inverse of s_{km}, $\hat{a}_{ik} = r_{im}s_{km}^{-1}$. The properties as defined by Eq. (3.19) guarantee that S_{kl} is diagonal and can be used to derive the scaling $c_{(k)}$ by taking the square root and the inverse of the diagonal elements, which essentially represents the Cholesky decomposition of S_{kl} and leads to scaling equation (3.22).

Eventually, the final anisotropic simulation is conducted by using the such determined scaling matrix $\hat{a}_{ik}$.

Isotropic turbulence

For isotropic turbulence the following relationships hold: $\hat{a}_{ik}(\mathbf{x}) \rightarrow \hat{a}(\mathbf{x})\delta_{ik}$, $\gamma = 1$ (i.e. $l_1 = l_2 = l_3 = l_s$), $R_{11} = R_{22} = R_{33} = 2/3k_t$, and $R_{ij} = 0$ for $i \neq j$. Consequently, from Eq. (3.22) the scalar scaling function for isotropic turbulence infers as

$$\hat{a}\,(\mathbf{x}) = \sqrt{\frac{2}{3\pi}\frac{k_t\,(\mathbf{x})}{l_s\,(\mathbf{x})}}\,. \tag{3.25}$$

Furthermore, for homogeneous isotropic turbulence $\hat{a} = const.$ and integral Eq. (3.10) can be rewritten as

$$\mathbf{u}' = \nabla \times \boldsymbol{\phi}, \tag{3.26}$$

with $\boldsymbol{\phi} = (\phi_1, \phi_2, \phi_3)^T$ and

$$\phi_i := \int_{V_s} \hat{a}\, G\, \mathcal{U}_i \mathrm{d}^3\mathbf{x}'. \tag{3.27}$$

The two-point correlations of the velocity fluctuations realise the normalized correlation tensor of homogeneous isotropic turbulence $\hat{R}_{ij}(r)$ for two points $\mathbf{x}_i$ and $\mathbf{x}_j$ with distance $r = |\mathbf{x}_i - \mathbf{x}_j|$ and the expected relationship between streamwise and spanwise correlation functions $f(r)$ and $g(r)$, respectively [96],

$$\hat{R}_{ij} = (f(r) - g(r))\frac{r_i r_j}{r^2} + g(r)\delta_{ij}, \tag{3.28}$$

$$g(r) = f(r) + \frac{r}{2}\frac{df(r)}{dr}. \tag{3.29}$$

For a Gaussian filter kernel defined by Eq. (3.11), the resulting streamwise correlation function for homogeneous isotropic turbulence is also a Gaussian [97] defined by

$$f(r) = \exp\left(-\frac{\pi r^2}{4l_s^2}\right). \tag{3.30}$$

Based on the specific scaling of the Gaussian filter function Eq. (3.11), which leads to the streamwise correlation Eq. (3.30), the length scale used therein complies with the integral length scale L derived from the streamwise function,

$$L := \int_0^\infty f(r)\mathrm{d}r = l_s. \tag{3.31}$$

The length scale related to the spanwise correlation function obeys

$$\int_0^\infty g(r)\mathrm{d}r = \frac{l_s}{2}. \tag{3.32}$$

Numerical realization

For the quadrature of the integral in Eq. (3.10) the computational domain is formally split into equal sized non-overlapping control volumes δV_p of constant size, continuously covering the resolved source domain without holes. A random particle is assigned to the center of each control volume $\mathbf{x}_p$. All resulting particles are moving with their local convection velocity at the particle location. The control volumes are bounded by liquid-line surfaces, i.e. the boundary surface is drifting with the flow and in incompressible flow the control volume δV_p is invariant over time. The extension of the procedure to compressible flow was discussed in [87]. Random variables are attached to each particle. Their random variates at time level t^{n+1} formally are defined by the integral over the control volume of the stochastic fields at the current time level, i.e.,

$$r_{ip}^{n+1} := \int_{\delta V_p} \mathcal{U}_i(\mathbf{x}', t^{n+1})\mathrm{d}^3\mathbf{x}'. \tag{3.33}$$

The notion 'random variate' is used here to indicate the specific value of a random variable at a specific time level, e.g. random variates r_{ip}^{n+1} indicate the value of random variables r_{ip} at time level $n+1$. Eventually, the convolution Eq. (3.10) is approximated at discrete time level $n+1$ by summation over all control volumes,

$$u_i'^{n+1}(\mathbf{x}) \simeq \sum_p \hat{a}_{ik}\epsilon_{klm}\frac{\partial}{\partial x_l}G(\mathbf{x}-\mathbf{x}_p)\; r_{mp}^{n+1}. \tag{3.34}$$

Numerically, only random variables r_{mp} are realized and the stochastic field $\mathcal{U}_i$ serves only to facilitate the derivation of a discretized random process to generate the actual variates of each random variable.

The numerical procedure to realize the simulation steps as discussed before relies on an additional block structured mesh that defines the domain where synthetic turbulence is generated, hereafter denoted as 'FRPM domain'. In this work a Cartesian equidistant mesh is used. However, also general curvilinear meshes could be used. The mean flow as well as the local amplitude scaling function of the fluctuations, Eq. (3.25), and the local length and time scales, Eq. (3.13) and (3.17), respectively, are evaluated from the RANS solution and interpolated onto the FRPM mesh.

For frozen turbulence, the random value carried by each particle is constant over time. Hence, its value is generated when a random particle is entering the computational domain and kept constant while the particle is convected through the computational domain. When a random particle is leaving the computational domain it is reseeded with an updated random value at the upstream boundary so that the number of particles remains invariant and the mean particle density is conserved.

For decaying turbulence a discretized Langevin equation is solved for each random variate, refer to Ref. [87], whose discretized form reads [98]

$$r_{ip}^{n+1} = \left(1 - \frac{\Delta t}{\tau_s}\right) r_{ip}^{n} + \left(\frac{2\delta V_p\, \Delta t}{\tau_s}\right)^{1/2} \sigma_{ip}^{n}, \tag{3.35}$$

where σ_{ip}^{n} are mutually uncorrelated standardized Gaussian random variates, which are independent of themselves at different times ($\left\langle \sigma_{ip}^{n} \right\rangle = 0$, $\left\langle \sigma_{ip}^{n} \sigma_{jq}^{m} \right\rangle = \delta_{ij}\delta_{pq}\delta_{nm}$), and which are independent of r_{ip}^{m} at past times (e.g., $\left\langle \sigma_{ip}^{n} r_{jq}^{m} \right\rangle = 0$ for $t^m \leq t^n$. The time increment between time levels t^{n+1} and t^n is given by $\Delta t < \tau_s$. Furthermore, δV_p indicates the control volume associated with each particle according to Eq. (3.33).

For frozen turbulence ($\tau_s \to \infty$), from the previous procedure it follows that $r_{ip}^{n+1} = r_{ip}^{n}$, i.e. the random variate is invariant over time. For frozen turbulence, the initial variance of the random variate associated with each particle scales with δV_p, i.e. the inverse local particle density.

Mean flow and other quantities needed at a specific particle position are obtained similar to particle-in-cell (PIC) methods by trilinear mapping of the mean-flow information stored on the FRPM patch mesh from the corners of a specific hosting cell to the actual particle position inside the cell.

The complete algorithm to generate a fluctuating velocity field at time level $n + 1$ can be summarized as follows:

- based on the mean-flow velocity at the particle position, move the particles from old position at time level n to the new one at time level $n + 1$,
- realize with Eq. (3.35) new variates of all random variables attached to each particle,
- distribute random variates via discretized convolution Eq. (3.34) onto the source domain,
- evaluate the right-hand side source term of the Poisson's equation (3.2) and solve it via Hockney's method to predict the wall pressure at time level $n + 1$.

The discretized convolution consists of a projection step, where the random variates are mapped from the actual particle position to the surrounding hosting cell nodes and the spatial filter steps are pursued sequentially on the FRPM mesh along each coordinate direction using direction-dependent filter length scales l_i.

In order to avoid a particle convecting on further away than into a cell attached to the actual hosting cell, the maximum time step is limited by a Courant–Friedrichs–Lewy (CFL)–like condition based on the mesh spacing and the local mean-flow convection velocity.

A discussion of the methods applied for the seeding of particles at inflow boundaries (and removal at outflow boundaries) and the efficient realization of the discrete convolution via recursive Gaussian filters can be found in Refs. [87] and [99].

4 Experimental results

In this chapter, the experimental results for the zero and non-zero pressure gradient boundary layer configurations are shown and discussed. Firstly, the mean flow characteristics are obtained and summarized in section 4.1. The analysis of the measured one-point wall pressure spectra and their two-point features, namely the cross-spectra and the convective velocities, are discussed in section 4.2 and section 4.3.

4.1 Mean flow characteristics

The mean velocity profiles for the zero pressure gradient (ZPG) cases were measured at $x = 1210$ mm. The measurement position is about 60δ (boundary layer thickness at the measurement location) distance downstream from the leading edge of the plate and is the location of the most downstream Kulite sensors. Five test velocities between 20 m/s $< U_0 <$ 59 m/s were selected for ZPG flow measurements. Spanwise measurements confirmed an approximate 500-mm extent of uniform 2-D flow conditions at $x = 1210$ mm, refer to Figs. C.1-C.2 in Appendix C. ZPG conditions in the current study effectively correspond to weak adverse pressure gradient (APG) conditions, i. e. to $dC_p/dx \leq 0.1$ m^{-1} between 930 mm $\leq x \leq$ 1220 mm (refer also to Fig. 4.2).

Fig. 4.1 shows the measured ZPG mean velocity profiles for all test velocities. The mean velocities for locations $y < 1.5$ mm are estimated using Spalding's equation [100],

$$y^+ = u^+ + e^{-\kappa B}\left[e^{\kappa u^+} - 1 - \kappa u^+ - \frac{(\kappa u^+)^2}{2} - \frac{(\kappa u^+)^3}{6}\right], \tag{4.1}$$

where $u^+ = u/u_\tau$ and $y^+ = yu_\tau/\nu$. The friction velocity u_τ is obtained by fitting the measurement data to the log-law region. The present estimate applies constant $\kappa = 0.41$ and $B = 5.0$ [101]. Spalding's formula comprises all boundary layer regions in one single expression and provides an excellent fit from the sublayer to the log-law region [85].

When normalized with the local free-stream velocity U_0 and the boundary layer thickness δ, Fig. 4.1(a), the profiles for $U_0 \geq 39.2$ m/s exhibit identical shapes, whereas the lower Reynolds number cases (20.3 m/s and 30.2 m/s) slightly deviate. The relevant characteristic parameters for the ZPG boundary layers are listed in Table 4.1. Accordingly, the observed scatter of the normalized velocity profiles for varying test speeds is well represented by the shape factor H, where $H = 1.42$ for 20.3 m/s and $H = 1.41$ for 30.2 m/s are a little larger than $H = 1.37$–1.38 for the higher velocities. Following Clauser [77], H is a function of Re_x for equilibrium boundary layers, e.g. for $10^6 < Re_x < 10^7$ ZPG values of H are expected to vary between 1.26–1.35. Nikuradse [102] measured the boundary layer for pipe flow in a range of $1.7 \cdot 10^6 \leq Re_x \leq 1.8 \cdot 10^7$. He found a universal mean velocity distribution which is independent of Re_x within the measurement range and derived constant $H = 1.3$. In a more recent study from Chauhan *et al.* [103], they collected an extensive experimental dataset and established a relationship between the shape factor H and the boundary layer based Reynolds number. In the range of $3500 < Re_\theta < 8700$,

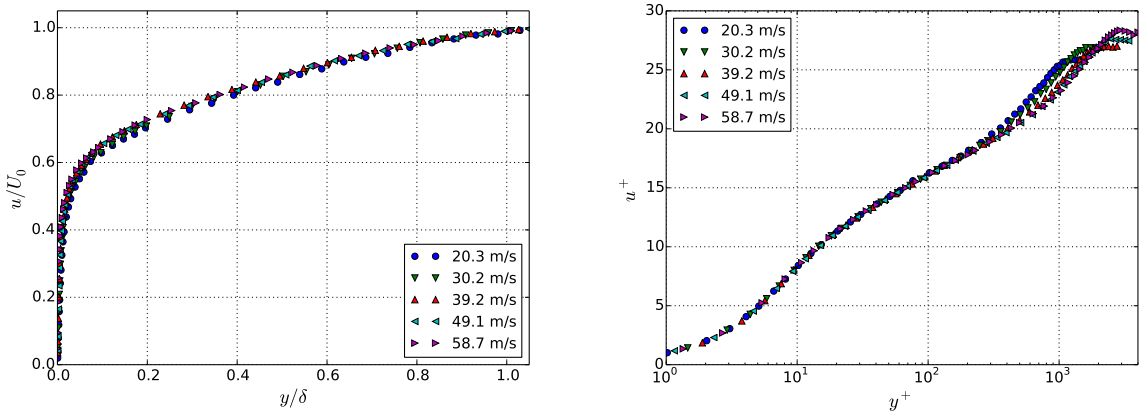

(a) (b)

Figure 4.1: Boundary layer mean velocity profiles for ZPG at velocities between 20 m/s $< U_0 <$ 59 m/s, $x = 1210$ mm.

Table 4.1: Boundary layer parameters for ZPG.

U_0 (m/s)	δ (mm)	δ^* (mm)	θ (mm)	H	u_τ (m/s)	$Re_x = U_0\, x/\nu$	$Re_\tau = u_\tau \delta/\nu$	$Re_\theta = U_0\theta/\nu$	dp/dx (Pa/m)	β_{δ^*}
20.3	20.4	3.8	2.67	1.42	0.785	$1.6 \cdot 10^6$	1040	3522	18	0.09
30.2	19.7	3.51	2.49	1.41	1.125	$2.4 \cdot 10^6$	1439	4889	42	0.10
39.2	18.8	3.15	2.28	1.38	1.455	$3.1 \cdot 10^6$	1776	5806	79	0.10
49.1	18.5	3.15	2.29	1.38	1.78	$3.9 \cdot 10^6$	2138	7286	128	0.11
58.7	18.5	3.13	2.28	1.37	2.08	$4.6 \cdot 10^6$	2499	8685	184	0.11

the shape factor is between 1.35–1.4. Overall, the obtained values of H from the current measurement are slightly larger than the results from the literature, which is probably due to the present little APG in the plate rear region.

APG boundary layers were realized by means of the NACA 0012 airfoil at geometric angles of attack (AOAs) of -6°, -10° and -14°, and favorable pressure gradient (FPG) boundary layers at 12° and 14°. The following analysis of the data under pressure gradients is limited to the free-stream velocity of 30.2 m/s. Fig. 4.2 shows the measured distributions of the pressure coefficient C_p between 930 mm $\leq x \leq$ 1220 mm. Due to the presence of the airfoil, the shear layer from the nozzle and the flow field underneath the airfoil can be impacted, e.g. an acceleration of the flow underneath the airfoil will cause a locally lower pressure, which can suck the shear layer towards the midline. The measured C_p distributions in the spanwise direction confirmed a nearly 2-D flow condition in the measurement region, refer to C.3 in Appendix C.

Velocity profiles were measured at two positions $x = 1128$ mm and $x = 1210$ mm, where the most upstream and downstream Kulite sensors were located. Fig. 4.3 shows the mean velocity profiles for ZPG, APG and FPG boundary layers at $x = 1210$ mm. The measured trends show good agreement with the experimental results from the literature [85]. The FPG boundary layer shows a larger velocity increase in the inner layer, when compared to the ZPG case. Contrarily, the APG boundary layer exhibits a steeper velocity increase

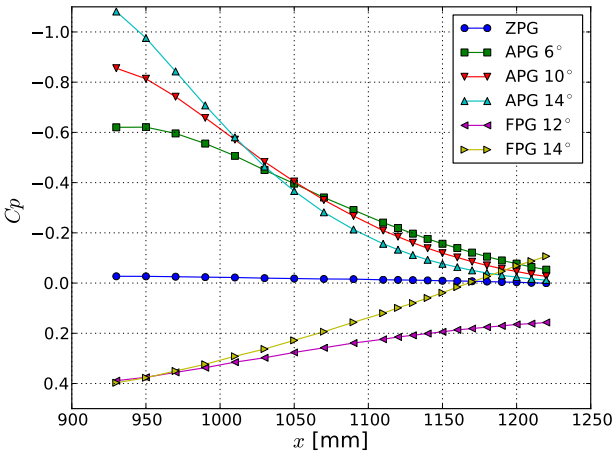

Figure 4.2: Cp distributions in the streamwise direction between 930 mm $\leq x \leq$ 1220 mm.

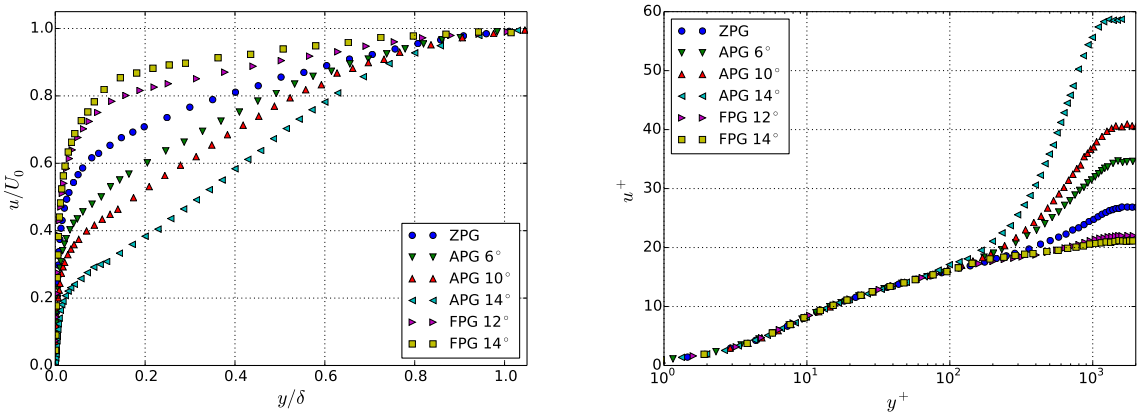

(a) (b)

Figure 4.3: Mean velocity profiles for ZPG and non-ZPG at $x = 1210$ mm for the free-stream velocity of 30.2 m/s.

in the outer layer. For a very strong APG boundary layer, e. g. the APG -14° case, an inflection point occurs at the transition region between the inner and outer layers, i. e. at about 0.1–0.2 δ. If we plot the profiles in log-law representation, all profiles collapse to a single curve in the inner layer, as shown in Fig. 4.3(b).

Table 4.2 summarizes the relevant APG and FPG boundary layer parameters for the two selected velocity measurement positions at the rear part of the plate. Note that for the APG cases the local pressure gradients dp/dx and the NACA 0012 geometrical AOAs show inconsistent trends, whereas consistent trends are limited to the more upstream locations (refer to Fig. 4.2).

From Fig. 4.3 ($x = 1210$ mm) one could conclude, that both the shape factor H and Clauser's equilibrium parameter $\beta_{\delta*}$ can be used to correctly represent the described ZPG and APG effects on the mean velocity profile shape. However, compared to H, $\beta_{\delta*}$ is directly impacted by the local pressure gradient, and a stronger local dp/dx does not

Table 4.2: Boundary layer parameters for APG and FPG at the free-stream velocity of 30.2 m/s.

	U_0 (m/s)	δ (mm)	δ^* (mm)	θ (mm)	H	u_τ (m/s)	Re_τ	Re_θ	dp/dx (Pa/m)	β_{δ^*}
$x = 1128$ mm										
APG -14°	31.2	26.3	7.38	3.87	1.91	0.645	1102	7831	1084	16.2
APG -10°	32.0	23.0	5.09	3.12	1.63	0.88	1314	6492	1225	6.8
APG -6°	32.3	20.0	3.88	2.56	1.52	1.03	1338	5362	1156	3.5
FPG 12°	26.1	18.1	2.55	1.92	1.32	1.12	1316	3258	-373	-0.6
FPG 14°	28.2	16.2	1.73	1.35	1.28	1.295	1362	2469	-1060	-0.9
$x = 1210$ mm										
APG -14°	29.9	35.0	12.07	5.69	2.12	0.51	1159	11046	320	12.5
APG -10°	30.4	28.7	7.68	4.39	1.75	0.745	1388	8670	518	6.0
APG -6°	30.8	24.4	5.61	3.49	1.61	0.89	1410	6979	643	3.8
FPG 12°	27.2	15.9	1.96	1.52	1.29	1.235	1275	2683	-209	-0.2
FPG 14°	31.1	13.8	1.28	1.01	1.26	1.47	1317	2040	-1006	-0.5

necessarily indicate the upstream boundary layer developmental history of a much stronger initial APG or FPG.

For example, if we compare β_{δ^*} and H as derived at the two different measurement positions for the APG -10° and APG -14° cases, the values show reverse trends: when moving downstream from $x = 1128$ mm to $x = 1210$ mm, the parameter H increases, whereas β_{δ^*} decreases. In Fig 4.4(a) it is documented, that the measured velocity profiles cannot be sorted in the correct order based on β_{δ^*}. On the contrary, H perfectly captures the developed trends. The measured profile shapes indicate that the velocity profiles at $x = 1210$ mm are still significantly affected by the strong initial APG conditions. A plot of the corresponding defect profiles is shown in Fig 4.4(b). An equilibrium boundary layer presents a larger velocity gradient in the outer layer for a greater value of β_{δ^*} [77, 83, 104]. The measured APG boundary layers in the current study show reversed trends, indicating that Clauser's equilibrium parameter β_{δ^*} is not suited to define the shape of the velocity profiles for arbitrary non-equilibrium boundary layers, especially for cases with fast pressure gradient changes.

4.2 One-point spectra

Fig. 4.5(a) shows the wall pressure one-point power spectral densities (psd) for ZPG boundary layers at $x = 1210$ mm. Spectral levels in this thesis are referenced to a 20 μPa reference pressure. The measured one-point spectra are analyzed with a window length of 4096 samples. The sampling rate is 100 kHz, which results in a resolution of about 24 Hz. The spectra show a good overall agreement with predictions using Goody's [36] model. Especially for the higher velocities the measured spectra are contaminated by setup-related disturbances at both low and high frequencies; the spectral increase at frequencies below about 230 Hz for U_0 =58.7 m/s is due to the impact of the open-jet free shear layer (featuring a much higher velocity scaling exponent than the turbulent boundary layer wall

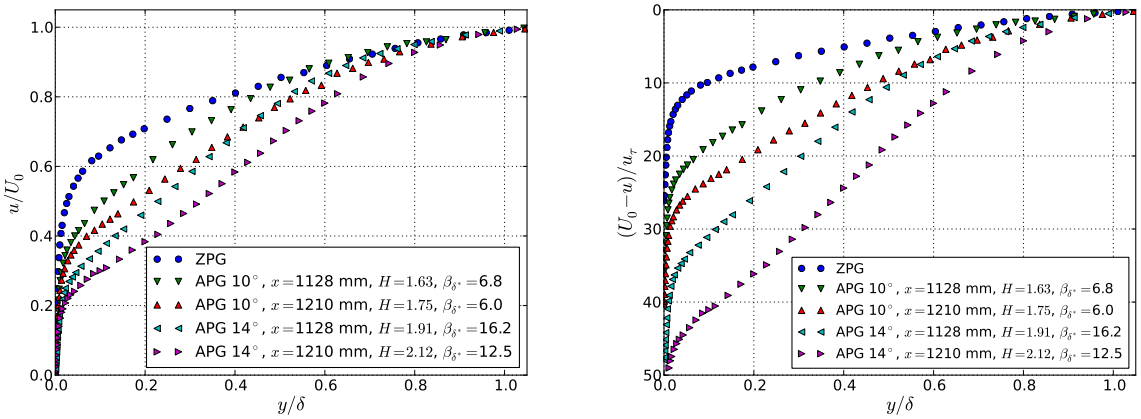

(a) (b)

Figure 4.4: Mean velocity profiles for ZPG and APG -10° & -14°.

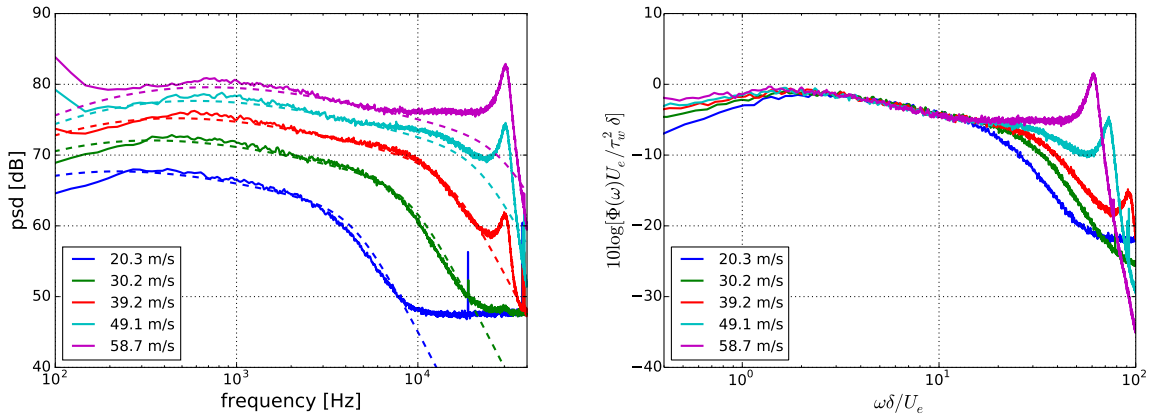

(a) (b)

Figure 4.5: (a) One-point spectra for different velocities compared with predictions according to Goody [36], $x = 1210$ mm; (-), measured spectra; (- -), Goody spectra; (b) spectra scaled by τ_w as pressure scale and δ/U_e as time scale.

pressures) while the resonance frequency for the Kulite-pinhole-arrangement was located at about 30 kHz. However, an impact of the resonance is found down to 7 kHz for 49.1 m/s and 58.7 m/s. Spectral levels below 48 dB are buried by the electrical noise of the applied Kulite sensor.

When scaled based on mixed parameters, as Goody proposes, the normalized spectra collapse to a single curve at mid Strouhal numbers $\omega\delta/U_e$ with a slope of $\omega^{-0.7}$, see Fig. 4.5(b). The boundary layer edge velocity U_es is herein set to $U_e = 0.99\,U_0$. This mid Strouhal number range is primarily attributed to the log-law region of the boundary layer at a ZPG [50]. The similarity of the velocity profile might predominantly contribute to the collapse of the spectra at these medium frequencies. A Reynolds number effect at high frequencies is expressed as an elongated mid-frequency $\omega^{-0.7}$ range, which is well identified by Goody using the model parameter $R_T = Re_\tau\sqrt{C_f/2}$, where C_f is the skin

friction coefficient. Minor deviations are observed at the low Strouhal number range, where the measured spectra appear free of disturbances: the present measurements indicate a dependence of the low-frequency slope and the maximum location on the Reynolds number, whereas Goody proposes identical spectral shapes in the low and medium Strouhal number ranges. Particularly, at $U_0 = 20.3$ m/s the spectral increase is steeper at low Strouhal numbers and the maximum is located at a higher Strouhal number compared to the spectra for the other velocities. Similar observations were made by Farabee & Casarella [8] and Leclercq & Bohineust [9]. Panton & Linebarger [49] and the author (refer to Fig. 6.6) calculated the contributions from different decks of the boundary layer and found that the spectra at low frequencies are composed of contributions from both the inner and outer layers. Based on this argument it is reasonable to conclude that an elongated mid-frequency range might change the shape of the spectra also at low frequencies. Note that, the slightly changed velocity profile shape at smaller U_0, also discussed as a Reynolds number effect, is in line with the observation of a changed shape of the corresponding wall pressure spectrum.

Figs. 4.6(a–e) show the wall pressure one-point spectra for APG and FPG boundary layers at the free-stream velocity of 30.2 m/s. The corresponding ZPG spectrum is plotted as reference. The spectral form in dependence of the initial pressure gradient conditions is well illustrated. Compared to the ZPG spectra the APG spectra feature an increase in maximum level and a steeper slope at medium frequencies with consistent trends as observed for the corresponding velocity profiles. For a given initial APG configuration, when moving downstream, the spectra shift towards lower frequencies and the slope at medium frequencies becomes successively steeper. For the FPG configurations the spectral slope at higher frequencies > 1 kHz is successively flattened, when moving downstream. The higher spectral level at lower frequencies < 1 kHz, especially even larger than the ZPG case, is unexpected. A flattened spectral slope at lower frequencies was measured by Salze *et al.* [44] and Suryadi & Herr [45]. This hump measured at lower frequencies may be caused by some unexpected effects due to the present NACA airfoil. A strong interference occurs at low frequencies for the FPG 14° case, which is probably caused by the fully separated flow on the suction side of the NACA airfoil.

Fig. 4.6(f) shows the scaled spectra for ZPG, APG and FPG boundary layers at $x = 1210$ mm using the same scaling parameters as for the ZPG spectra. Unlike the good collapse of the ZPG spectra, normalized levels diverge by up to 20 dB. Again, the evolution of the mid-frequency slope from a FPG boundary layer to an APG boundary layer is well illustrated. Note that the roll-off slope of ω^{-5} at high frequencies appears to be unaffected for both APG and FPG spectra. A very good collapse for the ZPG and APG spectral maxima is found by scaling with $u_\tau/Q^2\theta$ and $\omega\theta/U_0$, see Fig. 4.7(a). All the measured APG spectra at $x = 1128$ mm and 1210 mm including the free-stream velocities of 20.3 m/s and 39.1 m/s are scaled using these parameters and a good collapse of the spectral maxima is shown in Fig. 4.7(b). It is worth to note that a comparably good collapse is also found for spectral scaling based on $u_\tau/Q^2\delta$ or $U_0/Q^2\delta^*$, refer to Fig. C.4 in Appendix C. All the scalings are based on the dynamic pressure Q. It seems to be more reasonable to scale the APG spectra using the outer pressure scale Q instead of τ_w. However, different from the commonly used outer parameters $U_0/Q^2\delta$, a mixed representation for the involved time scales is used to consider the effect of an APG boundary layer. It is also worth to mention that if the FPG spectral level does not increase at lower frequencies < 1 kHz, the spectral peak for the FPG cases can also collapse with the ZPG and APG spectra by using a scaling

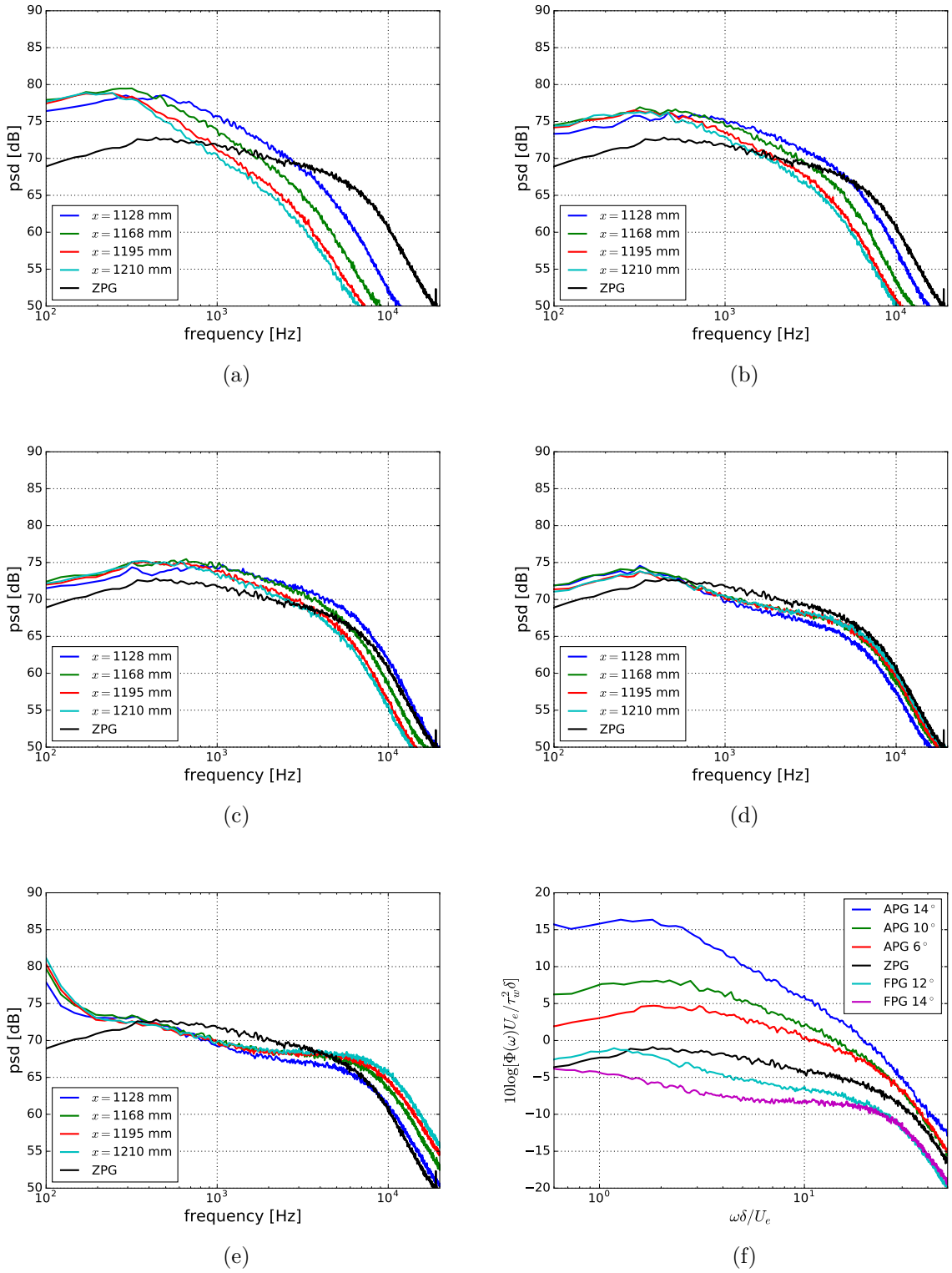

Figure 4.6: One-point spectra for the free-stream velocity of 30.2 m/s; (a) APG -14°; (b) APG -10°; (c) APG -6°; (d) FPG 12°; (e) FPG 14°; (f) spectra at $x = 1210$ mm, scaled by τ_w as pressure scale and δ/U_e as time scale.

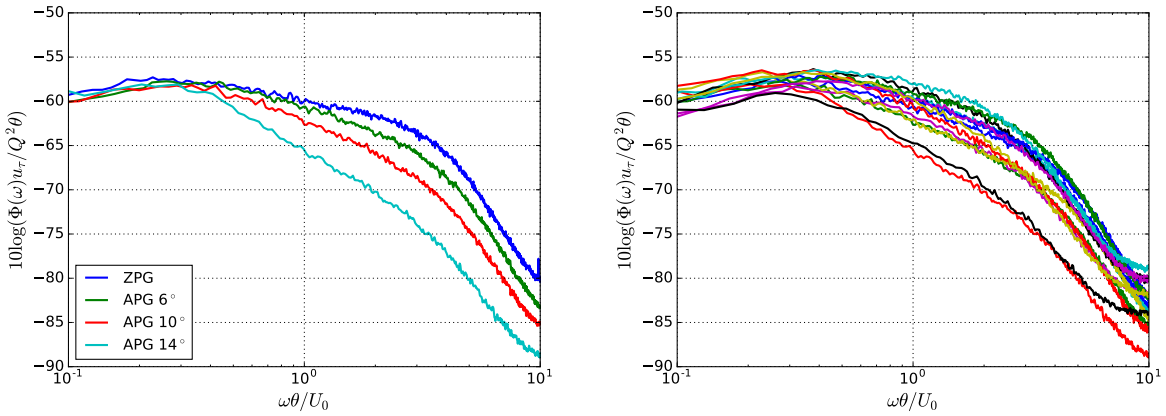

(a) (b)

Figure 4.7: Spectra scaled by $u_\tau/Q^2\theta$ and θ/U_0; (a) spectra for ZPG and APG at $x = 1210$ mm for the free-stream velocity of 30.2 m/s; (b) spectra for APG 6°, 10° and 14° at $x = 1128$ mm and $x = 1210$ mm for the free-stream velocities of 20.3 m/s, 30.2 m/s and 39.2 m/s.

based on Q, refer to Fig. C.5 in Appendix C.

4.3 Cross-spectra and convective velocities

From the two-point statistics obtained from the sensors located in different streamwise and spanwise positions, the spatial and temporal properties of the wall fluctuating pressure field can be studied. Corcos [51] used exponential functions (addressed in section 2.2) to characterize the streamwise and spanwise coherences of the pressure field by taking advantage of the similarity of the coherence decay, expressed as

$$|\Gamma(r_1, r_3, \omega)| = \exp(-\alpha\omega r_1/U_c)\exp(-\beta\omega r_3/U_c), \tag{4.2}$$

where α and β are empirical constants which are in charge of prescribing the turbulence decay in the streamwise and spanwise directions, respectively. The value of α depends on the Reynolds number. Generally, a smaller value relates to a larger Reynolds number. In the present measurement for ZPG boundary layers the obtained value of α decreases from 0.15 to 0.125 as the Reynolds number Re_τ increases from 1040 to 2499. A similar trend was reported by Farabee & Casarella [8], with $\alpha = 0.145$ for $Re_\tau = 1169$ and $\alpha = 0.125$ for $Re_\tau = 2010$. The obtained value of β shows no noticeable dependence on Reynolds number, $\beta = 0.72$ for all measured velocities in ZPG boundary layers. The value of β is reported only in few experiments. Bull [6] obtained $\beta = 0.715$ in a ZPG boundary layer, which is consistent with the present results.

In Eq. (4.2), U_c is the convective phase velocity of the wall fluctuating pressure field and it is defined by $U_c(r_1, \omega) = r_1\omega/\theta(r_1, \omega)$, where $\theta(r_1, \omega)$ is the phase difference of $\Gamma(r_1, 0, \omega)$. The phase velocity depends on the streamwise separations. To present the coherence with a separation of r_1 in the streamwise direction, a phase velocity $U_c(r_1, \omega)$ obtained at the same streamwise separation is used. However, the application for the phase velocity U_c in the spanwise direction is not explicit. Bull [6] used an averaged $U_c(\omega)$ obtained from the

streamwise direction. Brooks & Hodgson [82] applied a streamwise separation dependent $U_c(r_1, \omega)$, which used $r_1 = r_3$ to calculate the spanwise coherence at a separation of r_3. It is the authors' understanding that a phase velocity $U_c(r_1 \to 0, \omega)$ which indicates the local phase velocity is more meaningful to apply. However, $U_c(r_1 \to 0, \omega)$ cannot be measured. In this work the phase velocity $U_c(\omega)$ obtained from the two closest sensors $r_1 = 2$ mm at the most downstream direction is used to represent the spanwise coherence.

Figs. 4.8-4.9 show the streamwise and spanwise coherences at the free-stream velocity of 30.2 m/s for ZPG, APG and FPG boundary layers, respectively. A window length of 2048 samples is used to calculate the coherence. The streamwise coherence for APG and FPG boundary layers are only calculated from the sensors located between 1183 mm$<$ x $<$1210 mm where very similar spectra are measured. This implies a similar boundary layer condition within this range. The spanwise coherence was measured at x =1210 mm. The streamwise and spanwise coherence curves for the ZPG boundary layer collapse at higher frequencies and can be well fitted by the exponential functions with $\alpha = 0.14$ and $\beta = 0.72$, see Figs. 4.8(a)-4.9(a). The obtained exponential function for prescribing the streamwise and spanwise coherences of the ZPG boundary layer is also plotted in the results for APG and FPG boundary layers for comparison. It is worth to note that the convection of the flow field results in an offset for samples in the streamwise direction and therefore reduces the obtained streamwise coherence [25]. To reduce this effect, the time shift between the different streamwise positions is calculated using the mean flow velocity $U_c(r_1)$ and the time shift is applied to calculate the streamwise coherence.

Figs. 4.8(b-d) show the streamwise coherence for APG boundary layers. It clearly illustrates that an APG boundary layer causes an increased coherence decay in the streamwise direction. The larger the APG, the stronger the decay. This implies the APG enhances the turbulence decay rate during the eddies downstream convection in the boundary layer. Similar observations were reported by Schloemer [38], Brooks & Hodgson [82] and Catlett *et al.* [48]. Note that, even for the strongest initial APG (APG -14° case) the streamwise coherence shows the similarity scaling behavior, although the trend can be not necessarily characterized using a single exponential function. The larger frequencies share a stronger decay rate (a larger constant for the exponential function), this feature may be related to the different phase velocity trends from low frequencies to higher frequencies between ZPG and APG boundary layers, see Fig. 4.10. The phase velocity of the APG boundary layers shows that the velocity at higher frequencies is much smaller than at lower frequencies compared to the ZPG boundary layer, and a smaller velocity means a longer travel time over a constant distance which could cause a larger decay. Figs. 4.8(e-f) show a slightly increased streamwise coherence in FPG boundary layers.

Figs. 4.9(b-f) show a smaller decay rate for the spanwise coherence in an APG boundary layer and a larger decay rate in a FPG boundary layer. Note that the coherence curves collapse in FPG boundary layers but not any more in strong APG boundary layers, e.g. the APG -10° and APG -14° cases.

Fig. 4.10 shows the convective phase velocities at the free-stream velocity of 30.2 m/s for ZPG, APG and FPG boundary layers. A larger velocity is measured at a larger streamwise distance for all the configurations. This is because the smaller eddies close to the wall moving with a slower velocity decay faster as convecting downstream, thus at the larger distance the velocity is rather attributed to the larger eddies moving with a higher velocity. It is found that the obtained velocity decreases for an APG boundary layer compared to the ZPG boundary layer while it increases for a FPG boundary layer. This

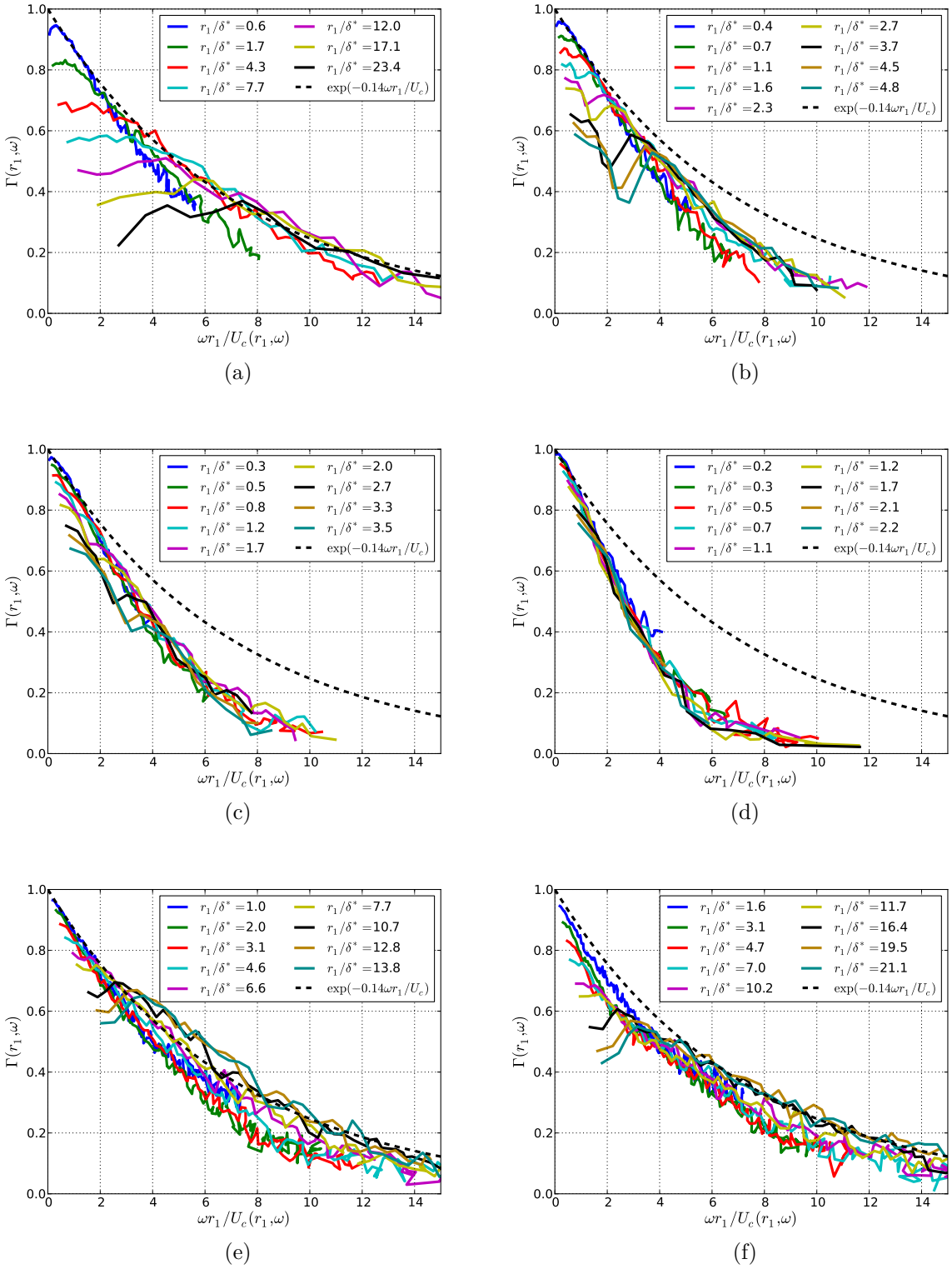

Figure 4.8: Streamwise coherence as a function of $\omega r_1/U_c(r_1,\omega)$ at the free-stream velocity of 30.2 m/s; (a) ZPG; (b) APG -6°; (c) APG -10°; (d) APG -14°; (e) FPG 12°; (f) FPG 14°.

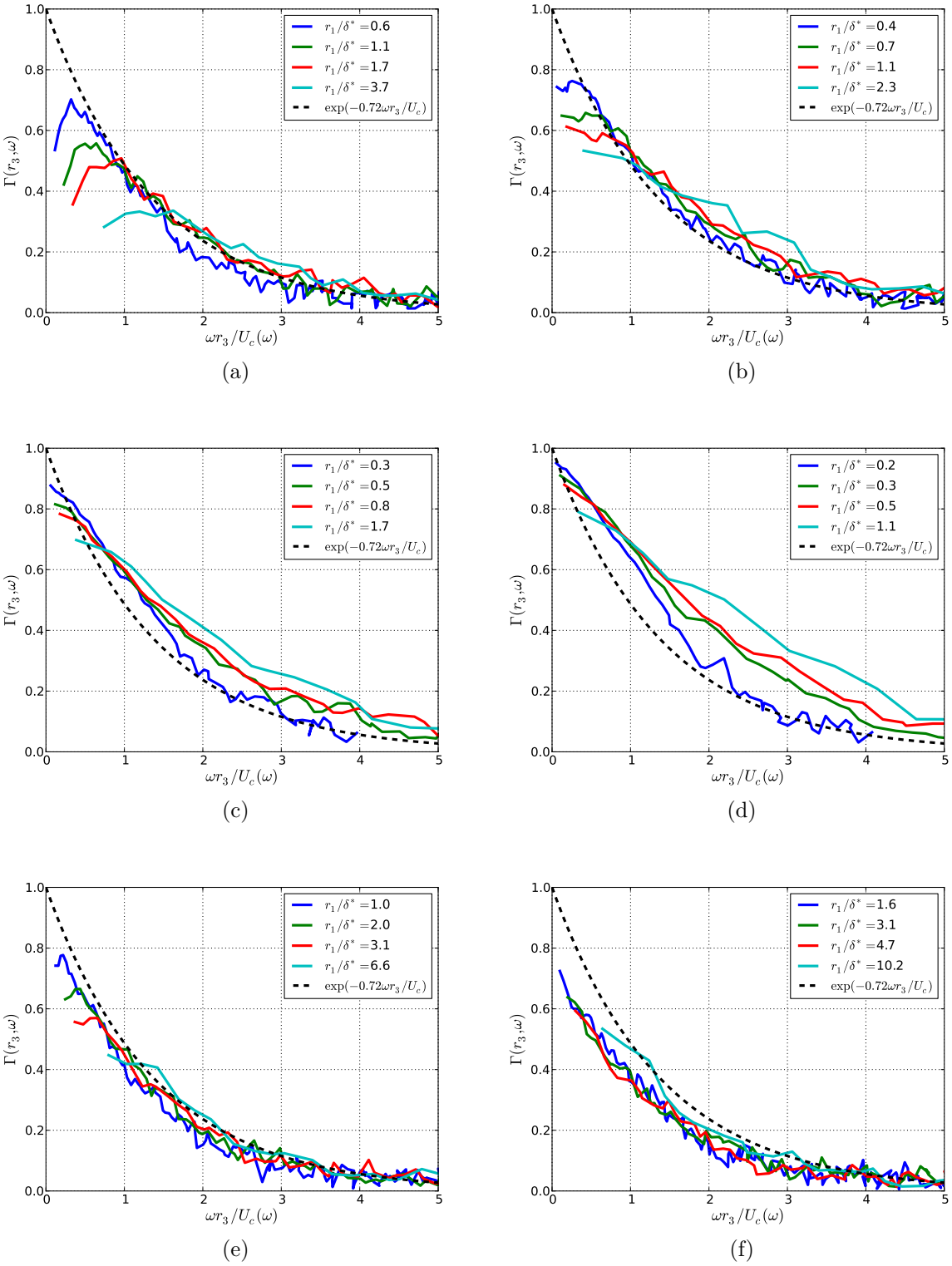

Figure 4.9: Spanwise coherence as a function of $\omega r_3/U_c(\omega)$ at the free-stream velocity of 30.2 m/s; (a) ZPG; (b) APG -6°; (c) APG -10°; (d) APG -14°; (e) FPG 12°; (f) FPG 14°.

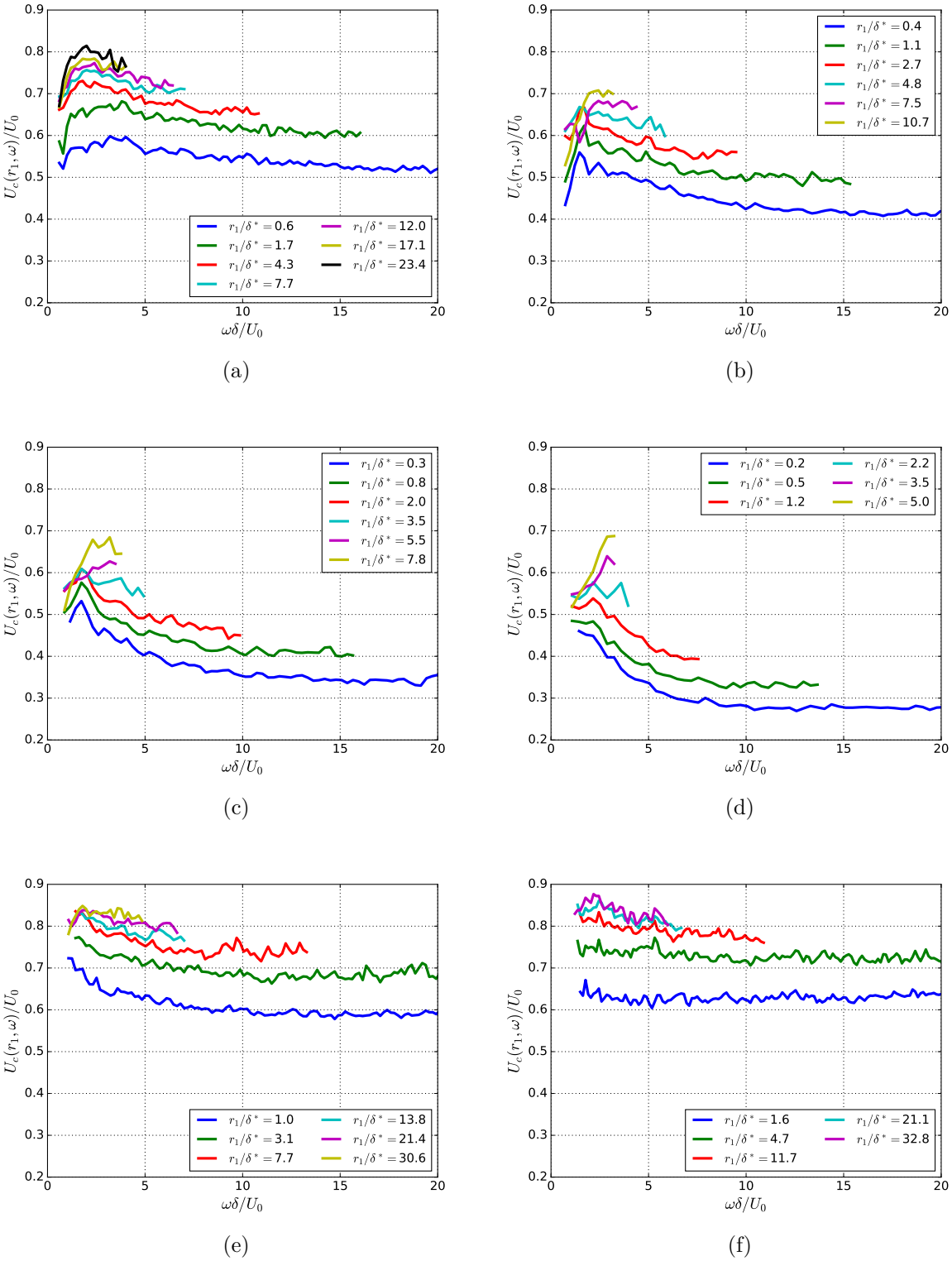

Figure 4.10: Phase velocities as a function of $\omega\delta/U_c(r_1,\omega)$; (a) ZPG; (b) APG -6°; (c) APG -10°; (d) APG -14°; (e) FPG 12°; (f) FPG 14°.

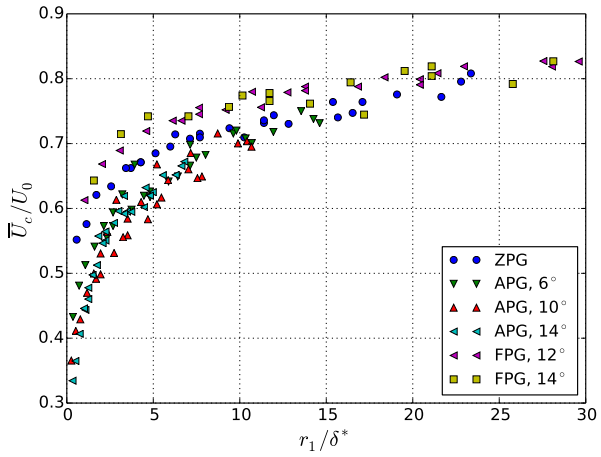

Figure 4.11: Mean convective velocity $\overline{U}_c$ at the free-stream velocity of 30.2 m/s.

trend is primarily a result of the different mean velocity profile shapes for the boundary layers. The important portion $y < 0.5\delta$ in the boundary layer for the wall pressure fluctuations owns a larger mean flow velocity u/U_0 for the FPG boundary layer than the APG boundary layer, see Fig. 4.3(a). The smallest mean flow velocity in this portion is found in the APG -14° case with the smallest convective velocities.

Another view on the convective features can be obtained from the mean convection velocity $\overline{U}_c$ computed using the time shift τ of the maximum correlation for a fixed streamwise separation r_1, $\overline{U}_c(r_1) = r_1/\tau(r_1)$. The results for ZPG, APG and FPG boundary layers at the free-stream velocity of 30.2 m/s are shown in Fig. 4.11. It shows the same trend as obtained from the phase velocity, namely a FPG boundary layer has a faster convective velocity while an APG boundary layer a slower one. The maximum mean convective velocity approaches $0.82U_0$ for the FPG boundary layer and $< 0.7U_0$ for the strong APG boundary layer of 14°. The maximum mean convective velocity implies the position of the 'longest lived' eddies in the boundary layer, if we assume the obtained velocity origins from the region of the boundary layer where the eddies convect with the same velocity. It is found that the position of the 'longest lived' eddies moves far away from the wall from a FPG boundary layer to an APG boundary, see Fig. 4.3(a).

5 Formulation of an empirical model for one-point spectra

From the analysis of the one-point spectra in section 4.2, we found a good collapse of the spectral maxima by using the outer parameters to scale the spectra for zero and adverse pressure gradients, refer to Fig. 4.7. A clear trend for the slope at medium frequencies and a nearly unchanged high-frequency roll-off slope were observed. From these observations, we are encouraged to develop an empirical spectral model for adverse pressure gradient (APG) wall pressure fluctuations based on a modification of the zero pressure gradient (ZPG) wall pressure spectrum.

The measured data presented in this work are used to discuss the effect of the APG on the spectral form. The Goody model is used as the basic form and the impact of each of its parameters on the spectral form is discussed. A modification of the Goody model is made to be able to predict the measured data for the APG cases. The detailed discussion and derivation of the modification is addressed in section 5.1.

In section 5.2, datasets from five different experiments at four different test facilities, covering a large range of Reynolds number $2.6 \cdot 10^3 < Re_\theta < 1.9 \cdot 10^4$, are selected to investigate the proposed modification in section 5.1 and the published APG wall pressure spectral models. Predictions of the APG cases from the selected datasets also including one ZPG test case are made and compared to the measured spectra. Features of each published model and the proposed modification are discussed.

Based on the comparison and discussion made in section 5.2, an improvement of the proposed modification in section 5.1 is made in section 5.3. The final formulation of the new empirical model for the APG wall pressure spectra (also capable to predict the ZPG spectra) is proposed. The prediction of the proposed new model shows good agreement with the measured spectra.

5.1 Parametric analysis and modification approach

To some extent, the APG spectra have similar trends as the ZPG spectra, refer to Fig. 4.7. The spectra increase first at low frequencies, then drop at medium frequencies and roll off at high frequencies. Goody's model can well represent these trends for ZPG spectra in the three different ranges, especially at medium and high frequencies. From this point it is appropriate to take Goody's model as the starting point. Goody's model is expressed as

$$\frac{\Phi(\omega)U_e}{\tau_w^2\delta} = \frac{a \cdot (\omega\delta/U_e)^b}{[(\omega\delta/U_e)^c + d]^e + [f \cdot (\omega\delta/U_e)]^g} \ , \tag{5.1}$$

where the value of the parameters a–g was obtained by fitting the measurement data from the literature, $a = 3$, $b = 2$, $c = 0.75$, $d = 0.5$, $e = 3.7$, $f = 1.1R_T^{-0.57}$ and $g = 7$. Goody used $U_e/\tau_w^2\delta$ and $\omega\delta/U_e$ as scaling parameters for the ZPG spectra. However, based on the previous discussion in section 4.2 it is more appropriate to use $u_\tau/Q^2\theta$ and $\omega\theta/U_0$ as the

scaling parameters for the APG spectra. It is worth to mention that the chosen scaling parameters provide a better trend in fitting the maximum locations of the spectra than the other two proper scaling parameters mentioned before based on the measured data. Thus, Goody's model is rewritten as

$$\frac{\Phi(\omega)u_\tau}{Q^2\theta} = \frac{a \cdot (\omega\theta/U_0)^b}{[(\omega\theta/U_0)^c + d]^e + [f \cdot (\omega\theta/U_0)]^g} \cdot \tag{5.2}$$

The parameters a–g in this equation control the shape of the dimensionless spectra. The amplitude of the spectra is adjusted by the value of a. The slopes in different frequency ranges are driven by the combination of b, c, e and g. The parameter f determines the extension of the mid-frequency range. The maximum location is affected by the value of d, the slope at low frequencies and the trend of the transition range between the increase and decrease at low and medium frequencies.

The first step of the modification is to represent the ZPG spectra which are supposed to have a trend of $\omega^{-0.7}$ at medium frequencies and ω^{-5} at high frequencies. This trend can be realized by means of the combination of the parameters, which follows $b - c \cdot e = -0.7$ and $b - g = -5$. Goody adopted $b = 2$ from the Chase-Howe [34] model, which implies an ω^2 increase at low frequencies. Panton & Linebarger [49] and Blake [50] calculated the spectra of the wall pressure fluctuations by solving a Poisson's equation. The result is derived by integration of the contributions throughout all decks of the boundary layer. Due to the term $k_1^2/k^2 \exp(-2ky)$ in the solution, where k_1 is the wavenumber in the streamwise direction, $k^2 = k_1^2 + k_3^2$ and y is the wall-normal distance to the wall, an ω^2 increase at low frequencies is obtained. However, in the calculation the fluctuation dynamics is assumed as frozen turbulence. The spectra for both frozen turbulence and non-frozen turbulence are calculated in section 6.1, refer to Fig. 6.6. The result shows that the ω^2 increase does not hold if non-frozen turbulence is considered. While the effect of convective decaying turbulence is only noticeable at higher frequencies for the velocity spectra, the wall pressure spectra are also affected at lower frequencies due to the extra term $k_1^2/k^2 \exp(-2ky)$. As a result, the slope of the low-frequency increase turns out to be smaller. This effect was also reported by Chase [30]. Furthermore, in the referred to solution of the Poisson's equation the mean-shear turbulence term is considered as the dominant source term, thus, the turbulence-turbulence term is discarded in the calculation. Kraichnan [3] and Meecham & Tavis [29] calculated the importance of the mean-shear term and demonstrated the dominance of the mean-shear term for the wall mean square pressure. However, the simulation results in chapter 6 show that the mean-shear term and the turbulence-turbulence term have the same order of magnitude for the contribution to wall pressure fluctuations. Same statements were also made by Kim [55] and Chang *et al.* [57, 105]. The spectrum contributed from the turbulence-turbulence term shows an almost plateau-like spectrum at low frequencies, refer to Fig. 6.7 and Fig. 6.23. Thus, the turbulence-turbulence term gains the dominance at low frequencies. Consequently, the slope in the low-frequency range can be also affected by considering the effect of the turbulence-turbulence term. A precise measurement at very low frequencies is difficult mostly due to the limitation of the experimental facilities, e.g. high background noise level at low frequencies. Until now only Farabee & Casarella [8] measured the ω^2 increase at the lowest frequency range < 10 Hz ($\omega\delta/U_0 < 0.08$) by means of a noise cancellation technique. At low frequencies their results showed an approximately $\omega^{0.3}$ increase. In the literature an increase between $\omega^{0.2-0.8}$ at low frequencies is found for the ZPG spectra.

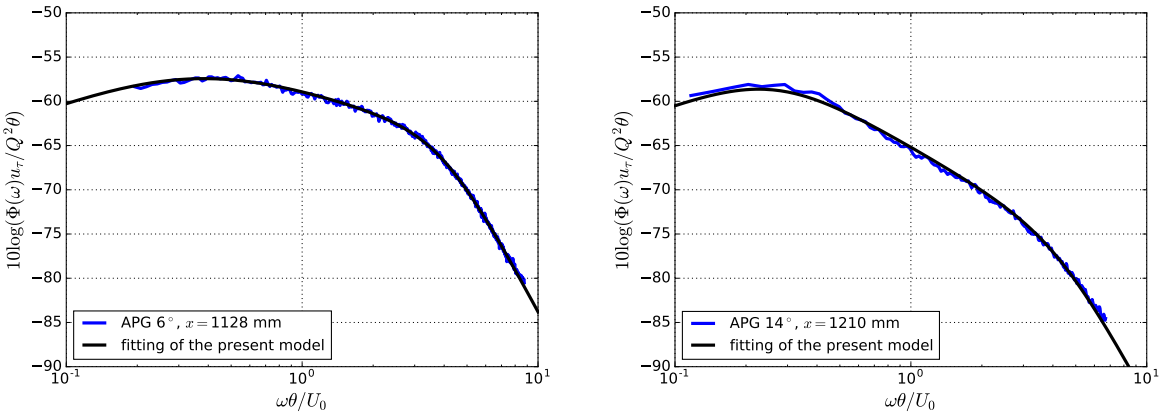

(a) (b)

Figure 5.1: Comparison between the measured data and the formulated spectra based on Eq. (5.3); (a) APG -6° at $x = 1128$ mm; (b) APG -14° at $x = 1210$ mm.

The APG spectra in the present experiment show $\omega^{0.6-1.0}$ at low frequencies. A steeper slope was found in experiments from Catlett *et al.* [43] and Suryadi & Herr [45]. The results showed a larger low-frequency increase at a greater APG and the increase can reach about $\omega^{1.4}$ as the APG boundary layer approaches separation. From those observations it can be drawn that the low-frequency slope for an APG spectrum is strongly dependent on the velocity profile of the boundary layer and probably also affected by the Reynolds number. However, for the present measured data, due to the low-frequency contamination from the free shear layer, it is not possible to figure out the dependence between the low-frequency slope and the possible important parameters. Thus, in this work a constant $b = 1.0$ is applied which is considered as an averaged value for the APG spectra. Since the value of b is fixed, we can determine $g = b + 5 = 6.0$ and $c \cdot e = b + 0.7 = 1.7$. An additional parameter h is added to govern the spectral decrease at medium frequencies, which works as a combination with c and e and prescribe the slope as $c \cdot e \cdot h - b$, e.g. a larger h leads to a steeper decrease at medium frequencies. It is noted that a steeper decrease at medium frequencies follows a more rapid transition between the increase at low frequencies and the decrease at medium frequencies. This feature requires an increasing value of c as the decrease at medium frequencies steepens, because the slope of the transition range is primarily managed by $(\omega\theta/U_0)^c$ in Eq. (5.2). Finally, to determine the values of c and e and the proper way to introduce h, the values and the combination of those parameters should be able to characterize the change of the decrease and the transition range at medium frequencies for weak and strong APGs.

Fig. 5.1 shows the perfect fit between the measured spectra under the weakest and strongest pressure gradient conditions in the present experiment and the formulated spectra using the following expression

$$\frac{\Phi(\omega)u_\tau}{Q^2\theta} = \frac{a \cdot (\omega\theta/U_0)^{1.0}}{[(\omega\theta/U_0)^{1.5 \cdot h^{1.6}} + d]^{1.13/h^{0.6}} + [f \cdot (\omega\theta/U_0)]^{6.0}}, \tag{5.3}$$

where the parameters c and e are determined as follows: $c = 1.5$ and $e = 1.13$. It is found that the change of the transition between low and medium frequencies is too

fast to be governed by a linear dependence of h, i.e. $(\omega\theta/U_0)^{1.5\,\cdot\,h}$. A formulation of $(\omega\theta/U_0)^{1.5\,\cdot\,h^{1.6}}$ can fairly well identify the change of the transition range. Furthermore, to keep a linear dependence between the change of the spectral slope at medium frequencies and the parameter h, i.e. $c \cdot e \cdot h - b \approx 1.7 \cdot h - 1$, a $h^{0.6}$ is introduced as $1.13/h^{0.6}$. Consequently, four parameters, namely a, d, h and f, remain to be determined and this is done by fitting all measured APG spectra according to Eq. (5.3). The task now is to find some dependencies between these parameters and the potential determining boundary layer parameters. The considerations are as follows: 1, the amplitude manager a depends on the parameter d. 2, the mid-frequency slope controller h is directly impacted by the boundary layer velocity profile. From the former discussion, the shape factor H is a proper choice as it directly correlates to the mean velocity profile. 3, the parameter d impacts the spectral maximum location. It is considered that it could be dependent on both the mean velocity profile and the Reynolds number. During the tests it was found that the combination of $Re_\theta H$ and $Re_\theta/(\delta/\delta^*)$ show good results. To keep the model as simple as possible by avoiding to introduce new parameters, $Re_\theta H$ is chosen. 4, the parameter f determines the extension of the mid-frequency decrease range and should depend on Re_τ. Goody used $Re_T = Re_\tau\sqrt{C_f/2}$ to prescribe the extension and good agreement to the experimental results is shown. However, for the applied time scale parameters $\omega\theta/U_0$, Re_τ shows a better agreement to the results. Fig. 5.2 shows the best-fit lines for the parameters against the selected parameters. Thus, these parameters as a function of the boundary layer parameters can be determined as follows:

$$a = (81.004d + 2.154) \cdot 10^{-7}, \tag{5.4}$$

$$d = 10^{-5.8\,\cdot\,10^{-5}Re_\theta H - 0.35}, \tag{5.5}$$

$$h = 1.169\ln(H) + 0.642, \tag{5.6}$$

$$f = 7.645Re_\tau^{-0.411}. \tag{5.7}$$

The curves of the resulting functions fit well for the determined values of the parameters, especially for h and f. This indicates that the selected boundary layer parameters can well feature the change of the wall pressure spectra under APGs.

5.2 Comparison with published models

In this section, the formulation Eq. (5.3) proposed in the previous section is compared with the other published APG pressure spectral models described in section 2.2. The major differences between the present formulation and the published models are as follows: 1, the present formulation uses a more representative normalization with $u_\tau/Q^2\theta$ for the APG spectra instead of $U_e/\tau_w^2\delta, \delta^*$ used in the other models. 2, the present formulation uses the shape factor H to operate on the mid-frequency decreasing slope. Contrarily, the other models, except the Kamruzzaman *et al.* [47] (KBLWK) model which has a constant slope at medium frequencies, use the Clauser's equilibrium parameter as the driving parameter, which based on the former discussion is not necessarily appropriate for applying in a non-equilibrium APG boundary layer. 3, the parameter b which manages the low-frequency increase is changed to be $b = 1.0$ in the present formulation. In the other models, $b = 2$ is used which is adopted from Goody's model.

Five different experiments at four different test facilities to measure wall pressure fluctuations beneath APG boundary layers are selected to investigate the spectral models.

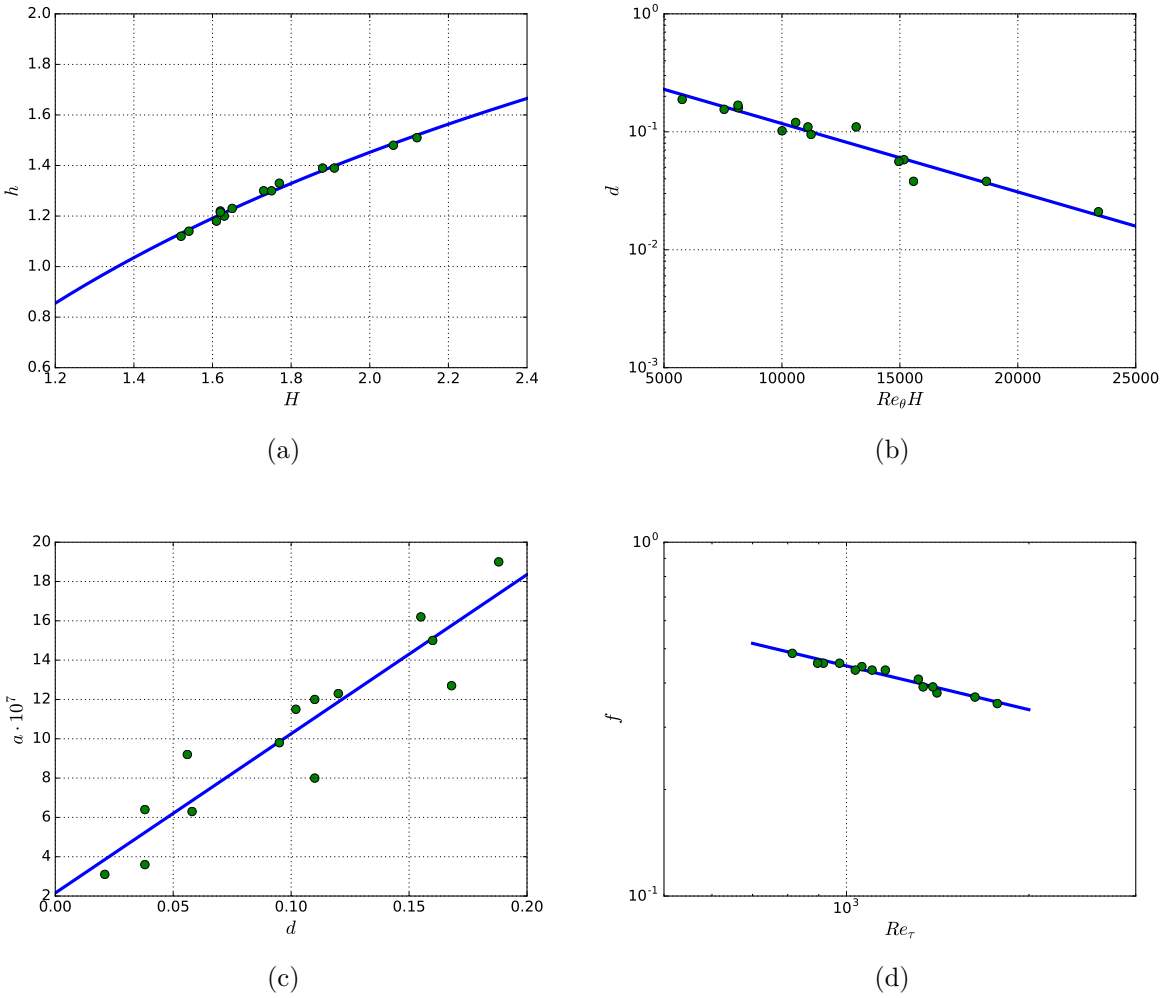

Figure 5.2: Determined values of the parameters and best-fit lines according to Eqs. (5.4-5.7).

Additionally, one beneath ZPG boundary layers is also included. APG boundary layers of the selected experiments were realized on three different conceptions: on a flat plate with airfoils on top of it (the experiment presented in this work and Schloemer [38]), on tapered trailing edges of a flat plate (Catlett *et al.* [43, 48]) and on airfoils (Suryadi & Herr [45] and Herrig *et al.* [42]). A brief summary of the experimental setups will be provided here. For detailed description of the experiments the reader is referred to the respective papers.

The experimental setup presented in this work can be found in section 3.1.

Schloemer conducted measurements in the low-turbulence subsonic wind tunnel at Stevens Institute of Technology. A flat plate was installed in the closed test section. Wall pressure spectra were measured by flush-mounted Atlantic Research type LD 107-M transducers with approximately 1.5 mm diameter. An APG was achieved by a half NACA 0015 airfoil attached on the top channel wall. Wall pressure spectra and flow properties measured by hot-wire anemometers were only provided for one single position.

Catlett *et al.* carried out measurements in the open jet section of the Anechoic Flow Facility at the Naval Surface Warfare Center, Carderock Division. Wall fluctuating pressures were measured with instrumented inserts containing flush mounted surface microphones

on tapered trailing edge sections of a flat plate with three different wedge angles (7°, 12° and 17° relating to the plate plane). Flow parameters were measured by hot-wire anemometers at several different streamwise positions. However, the flow measurements were limited to the wake region only and the mean flow velocity of the inner layer was estimated by a best fit to the theoretical boundary layer profiles.

Suryadi & Herr measured the wall pressure fluctuations with pinhole Kulite sensors on a DU96 airfoil at chord positions between $x/c = 0.77 - 0.96$ in the Aeroacoustic Wind Tunnel Braunschweig (AWB). Boundary layer parameters at the measurement positions are evaluated by XFOIL calculations. The values of pressure gradients were derived from the measured data. Data from three streamwise positions on the suction side of the airfoil at two angles of attack (AOAs) of $-0.8°$ and $3.2°$ are collected for the comparison.

Herrig *et al.* measured the wall fluctuating pressure spectra with flush-mounted 1.6 mm diameter Kulite sensors with the so called B-screen (eight 0.2 mm diameter holes around a 1.2 mm diameter circle) at the chord position $x/c \approx 0.99$ on a NACA 0012 airfoil in a closed test section in the Laminar Wind Tunnel of the University of Stuttgart. Flow properties are provided by XFOIL calculations. Data from AOAs of 0° and 4° on the suction side of the NACA 0012 airfoil were collected in this section.

Mean flow properties of turbulent boundary layers from the selected datasets are summarized in Table 5.1. In the literature, the local free-stream velocity U_0 is provided for the flat plate boundary layers (the cases of the experiment presented in this work and Schloemer) and the boundary layer edge velocity U_e is provided for the boundary layers measured on tapered trailing edges or on airfoils (the cases of Catlett *et al.*, Suryadi & Herr and Herrig *et al.*). For convenience, the boundary layer edge velocity is converted into the local free-stream velocity using the relationship $U_e = 0.99U_0$. The positions listed in the test case of the experiment presented in this work are measured as the distance downstream of the leading edge, in the test case of Catlett *et al.* are the distance upstream of the trailing edge. Boundary layer parameters from the test case of Catlett *et al.*, they are measured as acquired by digitizing the plots of measured mean flow properties [48]. However, pressure gradient values from this test case are not available and these are estimated by making a best-fit to the provided prediction of the Catlett *et al.* [43, 48] (CFAS) model.

Figs. 5.3-5.7 show comparison of the predicted spectra for APG test cases between the models, Fig. 5.8 for ZPG cases.

Spectra from the Rozenberg *et al.* [46] (RRM) model present no clearly different slopes between medium and high frequencies, except for the cases for ZPGs and very weak APGs, e.g. the experiment presented in this work, AOA=6° at $x = 1128$ mm, where the spectra roll off at high frequencies with a much faster slope than the measured ones. The reason for that is the function $A_2 = \min(3, 19/\sqrt{R_T}) + 7$ in Eq. (2.50), which could result in a faster roll-off at high frequencies for a small R_T. A poor prediction of the spectral slope at medium frequencies for the test case of Catlett *et al.* is shown in Fig. 5.4. For the test cases of the experiment presented in this work, Catlett *et al.* and Suryadi & Herr more than 5 dB discrepancy in the peak level is found and the maximum discrepancy is about 12 dB found in the test case of Suryadi & Herr. Good agreement with the test cases of Schloemer and Herrig *et al.* is obtained.

The KBLWK model formulates a constant spectral slope at low, medium and high frequencies, only the extension of the mid-frequency range and the spectral amplitude are governed by boundary layer parameters. Therefore, a slope variation at medium frequencies due to APG effects shown in test cases of the experiment presented in this

Table 5.1: Boundary layer parameters from the experimental test cases.

Position	U_0 (m/s)	δ (mm)	δ^* (mm)	θ (mm)	H	u_τ (m/s)	Re_τ	Re_θ	dp/dx (Pa/m)	β_{δ^*}
Experiment presented in this work, AOA=6°										
$x = 1128$ mm	32.3	20.0	3.88	2.56	1.52	1.03	1338	5362	1156	3.5
$x = 1210$ mm	30.8	24.4	5.61	3.49	1.61	0.89	1410	6979	643	3.8
AOA=10°										
$x = 1128$ mm	32.0	23.0	5.09	3.12	1.63	0.88	1314	6492	1225	6.8
$x = 1210$ mm	30.4	28.7	7.68	4.39	1.75	0.745	1388	8670	518	6.0
AOA=14°										
$x = 1128$ mm	31.2	26.3	7.38	3.87	1.91	0.645	1102	7831	1084	16.2
$x = 1210$ mm	29.9	35.0	12.07	5.69	2.12	0.51	1159	11046	320	12.5
ZPG										
$x = 1210$ mm	30.2	19.7	3.51	2.49	1.41	1.125	1439	4889	42	0.1
$x = 1210$ mm	39.2	18.8	3.15	2.28	1.38	1.455	1776	5806	79	0.1
Schloemer										
-	43.6	25.6	5.26	3.33	1.58	1.30	2150	9180	1237	3.3
Catlett *et al.*, open angle=7°										
$x = 50$ mm	9.0	91.2	18.36	11.11	1.65	0.27	1616	6421	27	5.6
$x = 204$ mm	18.1	73.1	14.36	9.27	1.55	0.55	2598	10775	75	3.0
$x = 406$ mm	28.3	66.5	10.05	7.1	1.42	0.92	3992	12909	165	1.6
Open angle=12°										
$x = 154$ mm	18.4	72.0	15.84	9.99	1.59	0.51	2376	11806	282	14.5
$x = 210$ mm	28.1	68.5	11.96	8.28	1.44	0.87	3851	14947	625	8.4
Open angle=17°										
$x = 106$ mm	28.4	73.1	16.34	10.1	1.62	0.71	3388	18429	900	24.3
Suryadi & Herr, AOA=-0.8°										
$x/c = 0.77$	53.3	6.1	1.22	0.78	1.56	1.95	772	2676	6209	1.7
$x/c = 0.88$	49.6	8.0	1.72	1.06	1.63	1.54	803	3370	6574	4.0
$x/c = 0.96$	45.9	10.3	2.60	1.44	1.80	1.10	731	4242	8206	14.9
AOA=3.2°										
$x/c = 0.77$	54.0	7.4	1.65	0.99	1.66	1.77	851	3447	7724	3.4
$x/c = 0.88$	49.4	10.1	2.56	1.42	1.81	1.26	821	4493	7059	9.6
$x/c = 0.96$	45.7	13.2	4.17	1.94	2.15	0.77	658	5690	5949	35.3
Herrig *et al.*, AOA=0°										
$x/c = 0.99$	33.4	13.5	2.77	1.64	1.69	0.99	863	3521	1762	4.2
AOA=4°										
$x/c = 0.99$	62.7	12.4	3.68	2.03	1.82	1.50	1209	8166	6202	8.6

work, Catlett *et al.* and Suryadi & Herr can not be predicted and the predicted slope at medium frequencies is too steep for ZPG cases. A good prediction of the peak amplitude is obtained except for the test case of Catlett *et al.*, which shows a discrepancy of 10 dB. The spectral peak location is well predicted for most test cases. Good agreement with measured spectra at positions in the vicinity of trailing edge is shown in Figs. 5.5(c,f) and Fig. 5.7.

The CFAS model underpredicts the spectral amplitude for all test cases except for the case of Catlett *et al.*. The discrepancy can be larger than 15 dB. The trend of variation of the spectral slope at medium frequencies is not well predicted, e.g. a contradictory trend is shown in Figs. 5.3(a,f) and Figs. 5.5(a,f), where the slope at medium frequencies should be steeper due to a stronger APG.

The formulation Eq. (5.3) predicts well the spectral slope at medium frequencies and the roll-off frequency at high frequencies for test cases of the experiment presented in this work, Catlett *et al.* and Suryadi & Herr, except for one case with open angle=17° of Catlett *et al.*, which may be caused by a boundary layer separation occurring upstream of the measurement position. A good prediction of the peak amplitude is obtained, except for the test case of Suryadi & Herr, which is mainly due to the imprecisely predicted spectral peak location. A slope of ω at low frequencies used in this model shows a better agreement with the measured spectra than the other models which possess an ω^2 slope.

5.3 Validation of the proposed model

The proposed model should be capable to predict the trend of the mid-frequency slope change due to APG effects, the extension of the mid-frequency range, the spectral peak amplitude and the peak location. From the previous discussion, it is shown that the formulation Eq. (5.3) predicts well the slope change at medium frequencies using the boundary layer shape factor as the driving parameter. Furthermore, good agreement of the spectral slope at low and high frequencies with the measured spectra is shown. The peak amplitude is well predicted except for one test case, which is mainly caused by an imprecise prediction of the peak location. Therefore, the proposed model will be based on the formulation Eq. (5.3) and aims to improve the prediction of the spectral peak location. Note that, the KBLWK model formulates a constant peak location in the non-dimensional frequency domain and the prediction of the peak location shows good agreement with measured spectra.

Fig. 5.9 shows the scaled spectra from the test cases listed in Table 5.1. Configurations not included in this plot are: 1, spectra measured in the vicinity of the trailing edge, i.e. measurements from Suryadi & Herr at $x/c = 0.96$ and Herrig *et al.*. For these configurations spectra may likely be impacted by the trailing edge scatter effect. Furthermore, the boundary layer parameter provided by XFOIL calculations may be imprecise in the vicinity of the trailing edge, especially for a larger AOA [106]. 2, the measurement position located not far downstream from a boundary layer separation, i.e. the measurement from Catlett *et al.* with open angle of 17°.

An noteworthy finding from Fig. 5.9 is that the scaled spectra can be divided into three groups. Group I for the cases of the experiment presented in this work and Schloemer, APG boundary layers developed at a flat plate with airfoils mounted above, 18.8 mm $\leq$ $\delta \leq$ 35.0 mm; group II for the case of Catlett *et al.*, APG boundary layers developed

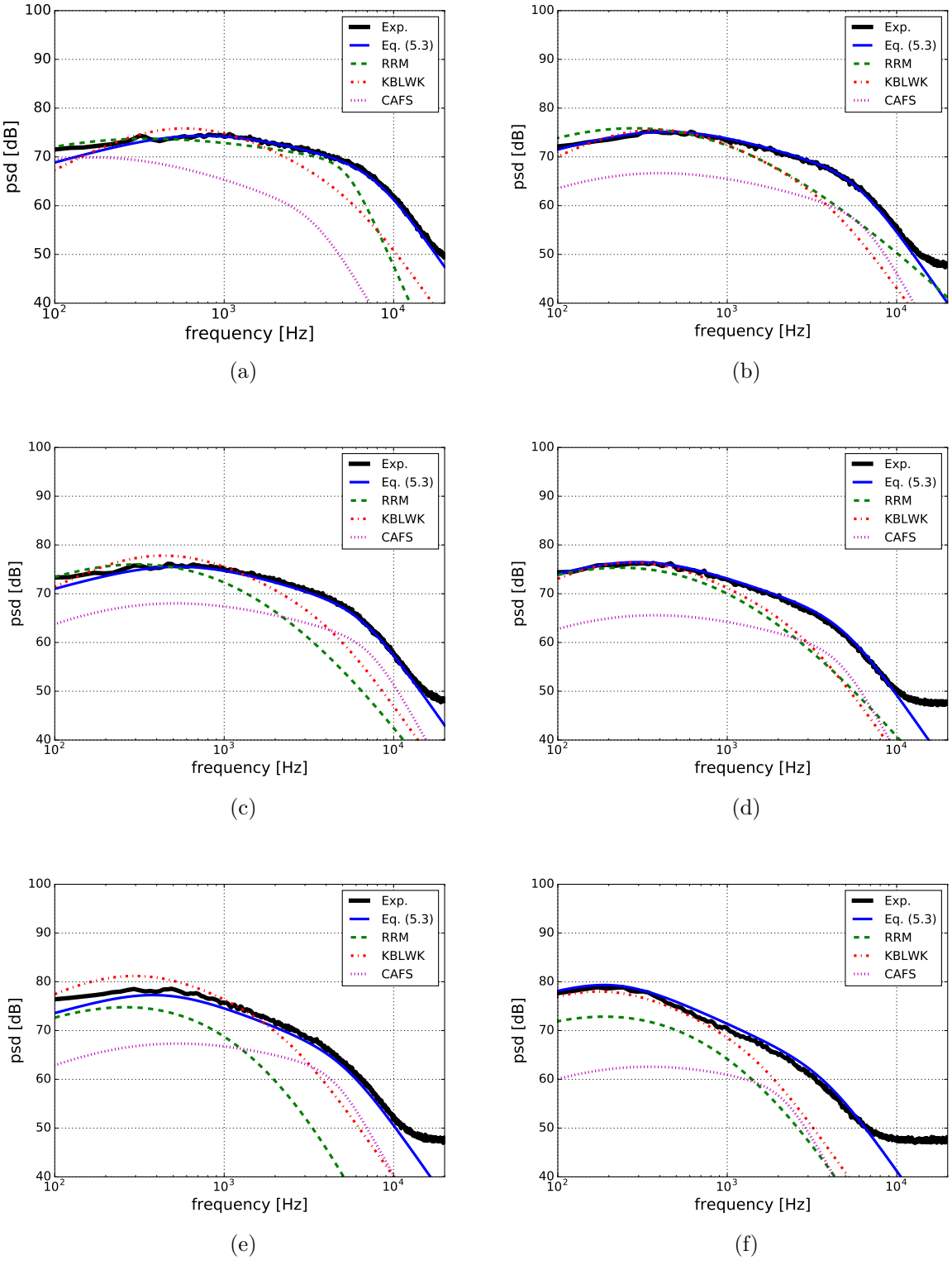

Figure 5.3: Predictions of different models for test case of the experiment presented in this work; (a) AOA=6°, $U_0 = 32.3$ m/s, distance of leading edge $x = 1128$ mm; (b) AOA=6°, $U_0 = 30.8$ m/s, distance of leading edge $x = 1210$ mm; (c) AOA=10°, $U_0 = 32.0$ m/s, distance of leading edge $x = 1128$ mm; (d) AOA=10°, $U_0 = 30.4$ m/s, distance of leading edge $x = 1210$ mm; (e) AOA=14°, $U_0 = 31.2$ m/s, distance of leading edge $x = 1128$ mm; (f) AOA=14°, $U_0 = 29.9$ m/s, distance of leading edge $x = 1210$ mm.

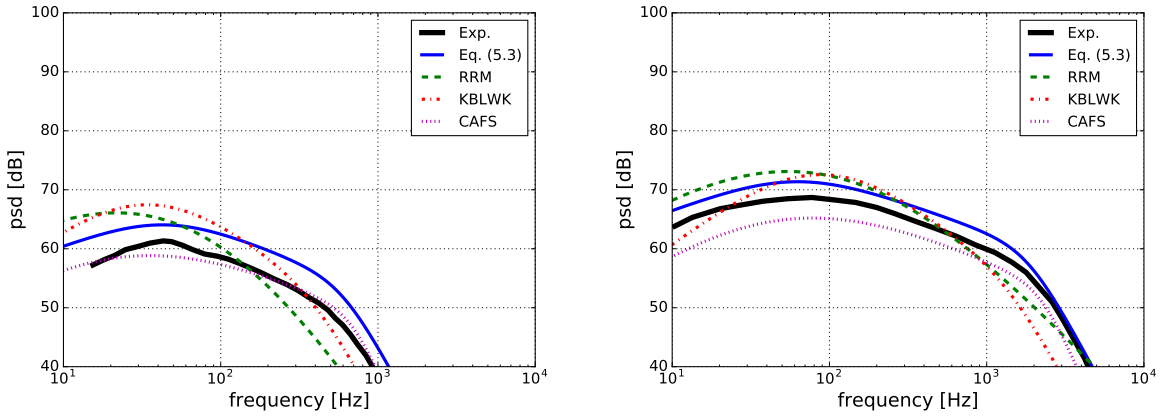

(a)

(b)

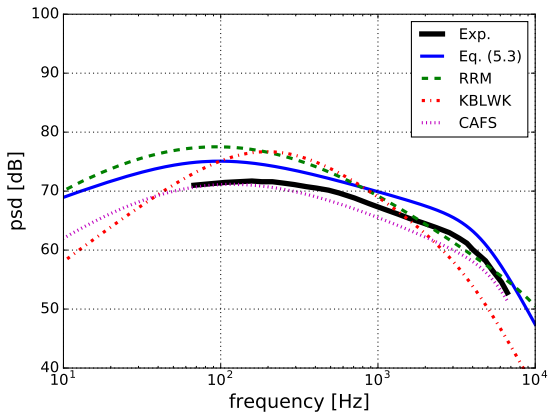

(c)

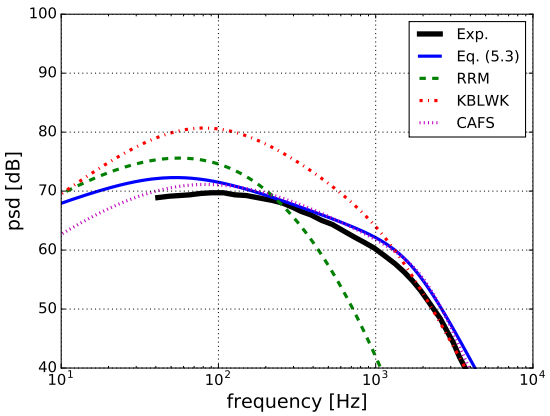

(d)

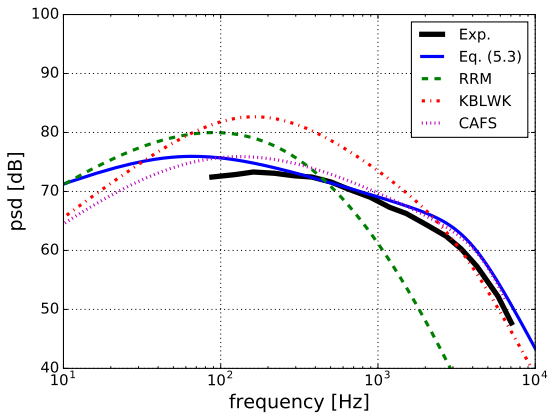

(e)

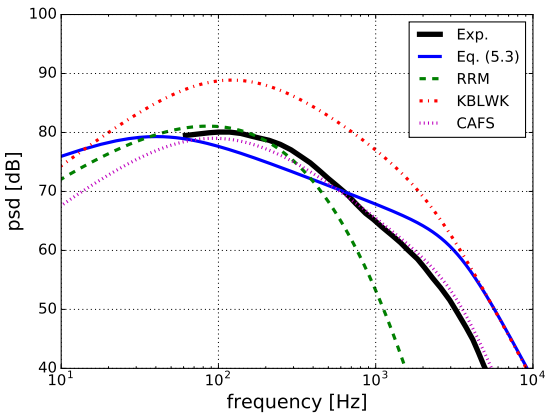

(f)

Figure 5.4: Predictions of different models for test case of Catlett *et al.*; (a) open angle=7°, $U_0 = 9.0$ m/s, distance of trailing edge $x = 50$ mm; (b) open angle=7°, $U_0 = 18.1$ m/s, distance of trailing edge $x = 204$ mm; (c) open angle=7°, $U_0 = 28.3$ m/s, distance of trailing edge $x = 406$ mm; (d) open angle=12°, $U_0 = 18.4$ m/s, distance of trailing edge $x = 154$ mm; (e) open angle=12°, $U_0 = 28.1$ m/s, distance of trailing edge $x = 210$ mm; (f) open angle=17°, $U_0 = 28.4$ m/s, distance of trailing edge $x = 106$ mm.

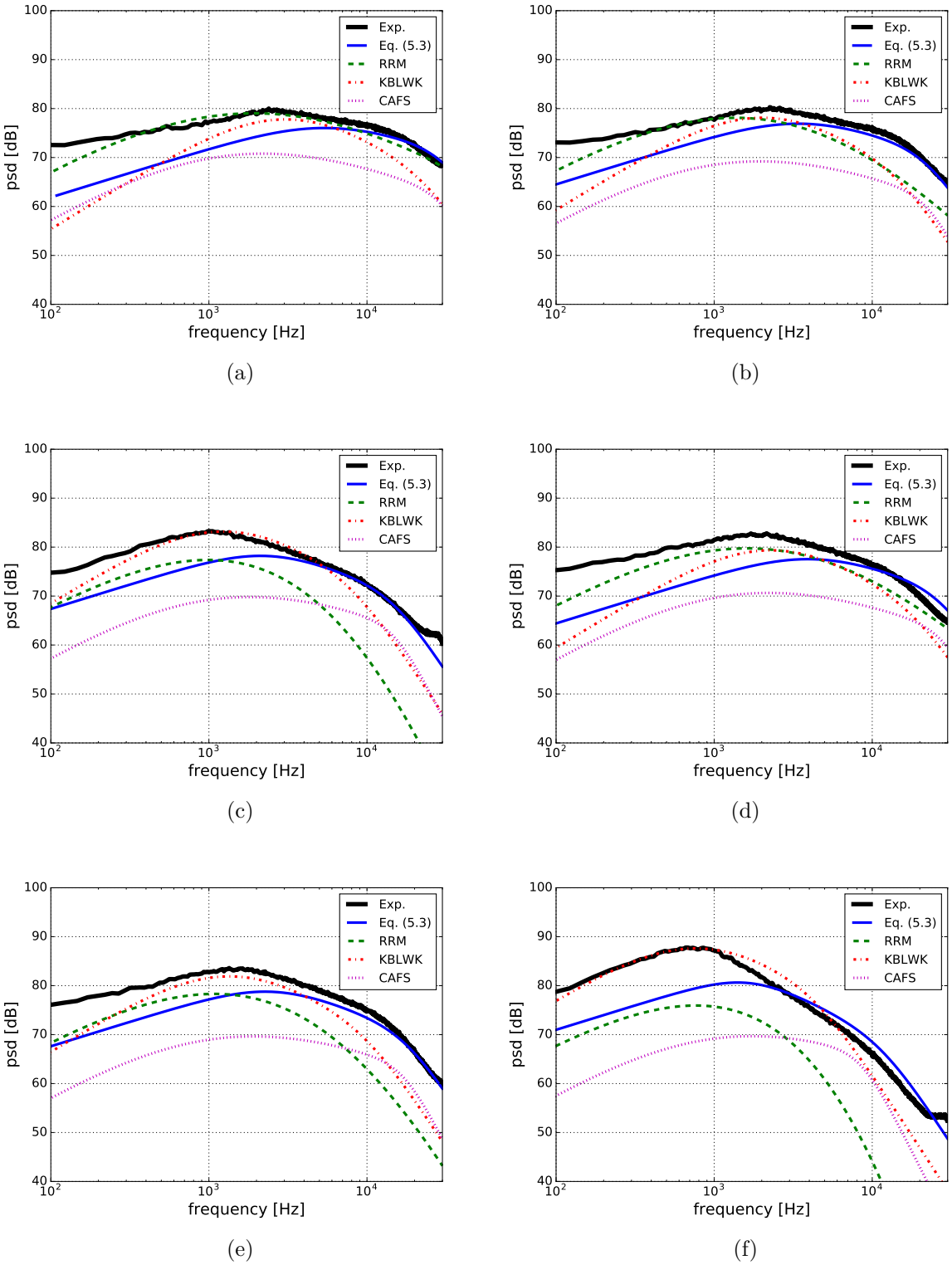

Figure 5.5: Predictions of different models for test case of Suryadi & Herr,; (a) AOA=-0.8°, $U_0 = 53.3$ m/s, chord position $x/c = 0.77$; (b) AOA=-0.8°, $U_0 = 49.6$ m/s, chord position $x/c = 0.88$; (c) AOA=-0.8°, $U_0 = 45.9$ m/s, chord position $x/c = 0.96$; (d) AOA=3.2°, $U_0 = 54.0$ m/s, chord position $x/c = 0.77$; (e) AOA=3.2°, $U_0 = 49.4$ m/s, chord position $x/c = 0.88$; (f) AOA=3.2°, $U_0 = 45.7$ m/s, chord position $x/c = 0.96$.

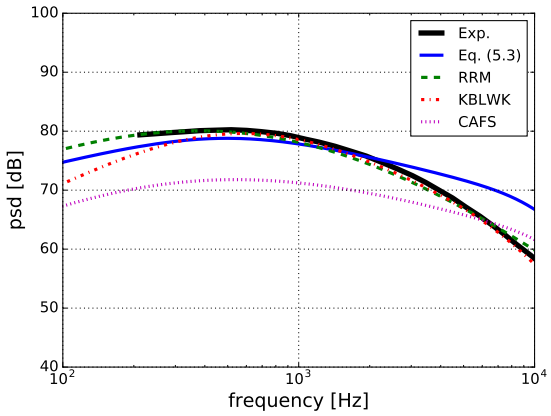

(a)

Figure 5.6: Predictions of different models for test case of Schloemer, $U_0 = 43.6$ m/s.

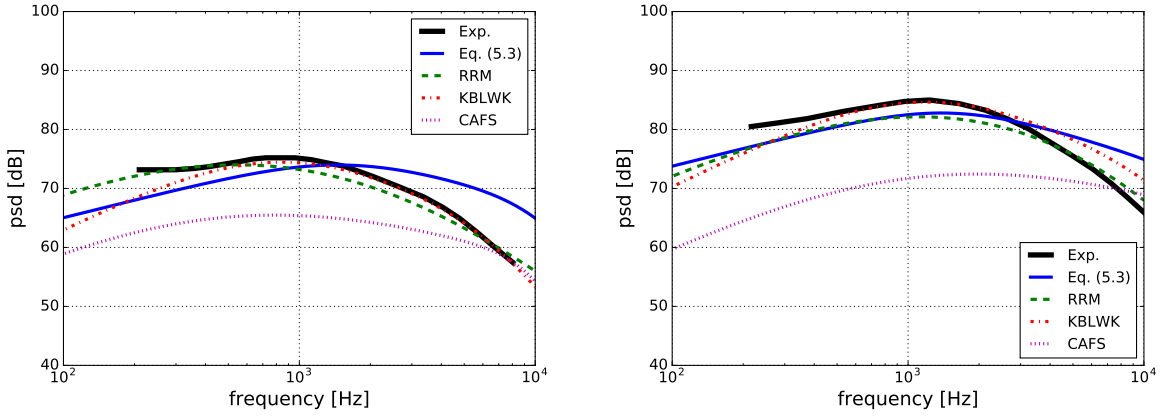

(a) (b)

Figure 5.7: Predictions of different models for test case of Herrig *et al.*; (a) AOA=0°, $U_0 = 33.4$ m/s, chord position $x/c = 0.99$; (b) AOA=4°, $U_0 = 62.7$ m/s, chord position $x/c = 0.99$.

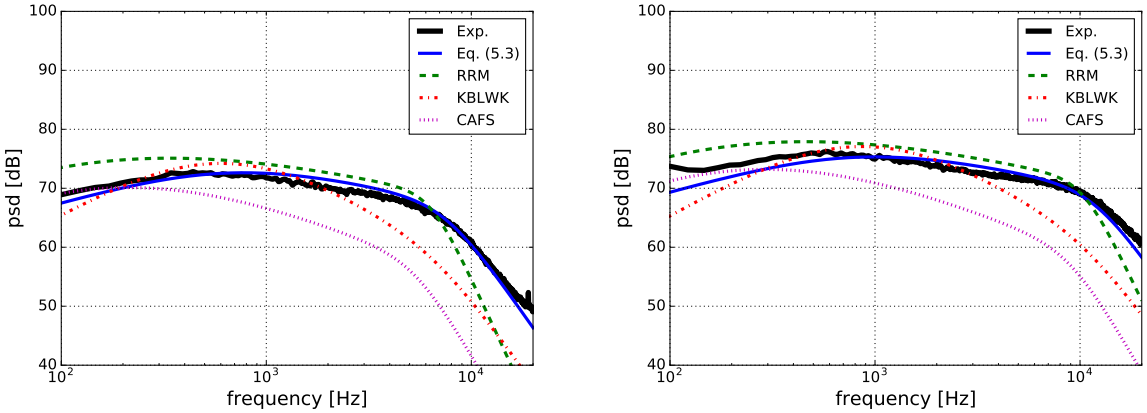

(a) (b)

Figure 5.8: Predictions of different models for test case of the experiment presented in this work for ZPG; (a) $U_0 = 30.2$ m/s, distance of leading edge $x = 1210$ mm; (b) $U_0 = 39.2$ m/s, distance of leading edge $x = 1210$ mm.

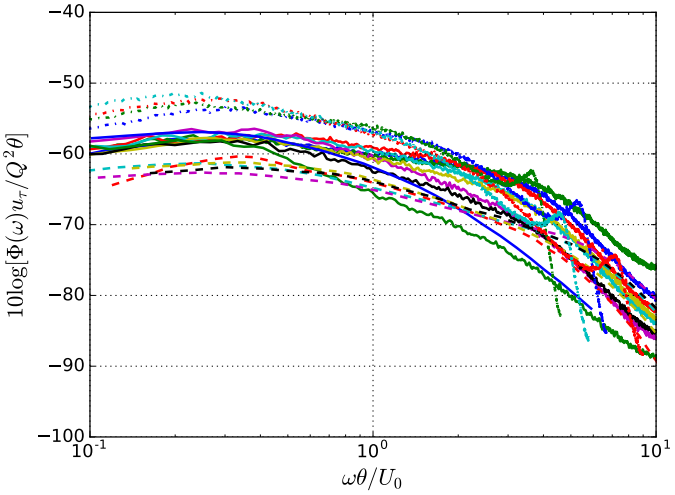

(a)

Figure 5.9: Spectra scaled by $u_\tau/Q^2\theta$ and θ/U_0 from test cases of the experiment presented in this work, Schloemer (-), Catlett *et al.* (- -) and Suryadi & Herr (-.).

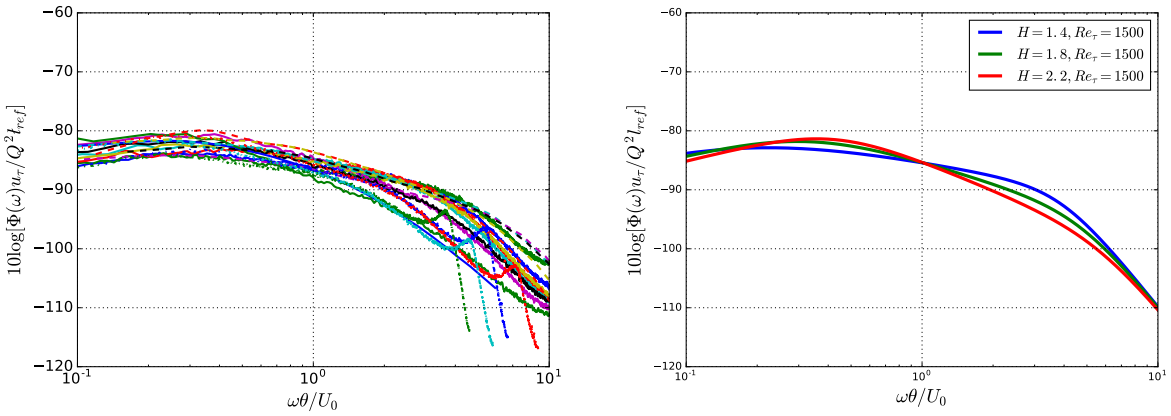

(a) (b)

Figure 5.10: (a) Spectra scaled by $u_\tau/Q^2 l_{ref}$ and θ/U_0 from test cases of the experiment presented in this work, Schloemer (-), Catlett *et al.* (- -) and Suryadi & Herr (-.); (b) spectra from Eq. (5.9) with different boundary layer shape factors.

at a tapered trailing edge section of a flat plate, 66.5 mm $\leq \delta \leq$ 91.2 mm; group III for the case of Suryadi & Herr, APG boundary layers developed on the airfoil suction side, 6.1 mm $\leq \delta \leq$ 13.2 mm. The spectral peaks of each group collapse well by itself, which may indicate a good scaling of the spectral peak is given when boundary layers experience a similar development history or the boundary layer thicknesses have the same order. Although a good peak collapse is shown in each test case by itself, the differences in peak amplitude are still about 10 dB between different test configurations.

Nevertheless, the spectral peak location is located in a small range between $\omega\theta/U_0$ of $0.2 - 0.35$. Based on the good prediction of the peak location from the KBLWK model with a constant for predicting the peak location, a constant value for the parameter d in the denominator in Eq. (5.3) is searched, with which the peak can be located in the range between $\omega\theta/U_0$ of $0.2 - 0.35$, and a value of $d = 0.07$ is found. The spectral amplitude in Eq. (5.3) is nearly independent on the choice of the value of d at higher frequencies. Therefore, the amplitude function can keep the form as it is. Thus, the model Eq. (5.3) is rewritten as

$$\frac{\Phi(\omega)u_\tau}{Q^2\theta} = \frac{(81.004d + 2.154) \cdot 10^{-7} \cdot (\omega\theta/U_0)}{\left[(\omega\theta/U_0)^{1.5h^{1.6}} + 0.07\right]^{1.13/h^{0.6}} + \left[7.645 {Re_\tau}^{-0.411} \cdot (\omega\theta/U_0)\right]^6}\,, \tag{5.8}$$

where $\log_{10}(d) = -5.8 \cdot 10^{-5} \cdot Re_\theta H - 0.35$ and $h = 1.169\ln(H) + 0.642$. Note that, a function of the boundary layer shape factor H and the momentum Reynolds number Re_θ is used in this expression to compensate the difference of peak amplitude between each test cases, i.e if the spectral peak collapses well for each test case, a constant can be placed herein instead of the function of H and Re_θ.

A good collapse of the spectral peak is found using $u_\tau/Q^2 l_{ref}$ as the pressure scaling parameter, shown in Fig. 5.10(a), where $l_{ref} = 1$ m served as a reference length instead of the common boundary layer based length scale. This may imply that, for the APG cases the spectral peak is weakly dependent on the boundary layer thickness. The u_τ

is dependent on the shape factor and the boundary layer thickness, e.g. a larger shape factor and a thicker boundary layer thickness lead to a smaller u_τ. This feature from u_τ seems to be able to reflect the APG effects on the spectral peak level. Based on the well scaled spectra from the different configurations, the function of H and Re_θ used in Eq. (5.8) for adjusting the spectral amplitude can be replaced by a constant, namely a value of $3.1 \cdot 10^{-9}$ is found to achieve good agreement with the measured spectra. A new expression of the model reads

$$\frac{\Phi(\omega)u_\tau}{Q^2 l_{ref}} = \frac{3.1 \cdot 10^{-9} \cdot (\omega\theta/U_0)}{\left[(\omega\theta/U_0)^{1.5h^{1.6}} + 0.07\right]^{1.13/h^{0.6}} + \left[7.645 {Re_\tau}^{-0.411} \cdot (\omega\theta/U_0)\right]^6} , \tag{5.9}$$

where $l_{ref} = 1$ m and $h = 1.169\ln(H) + 0.642$. Fig. 5.10(b) shows the formulated spectra from Eq. (5.9) for three different boundary layer shape factors at Reynolds number $Re_\tau = 1500$. Peak amplitude and location of the formulated spectra are in good agreement with the measured spectra, see comparison between Fig. 5.10(a) and Fig. 5.10(b).

Figs. 5.11-5.15 show predictions from the proposed model with two different expressions from Eq. (5.8) and Eq. (5.9) for the APG test cases, and Fig. 5.16 for the ZPG case. Both expressions of the proposed model show good agreement with the measured spectra. The spectral slope over the whole frequency range is well predicted.

Exceptions are the slope at medium and high frequencies for measurements from Schloemer and Herrig *et al.*. For those measurements, flush-mounted sensors with diameters of 1.5 mm and 1.6 mm were used to measure the wall pressure fluctuations, which cause an attenuation in spectral amplitude at medium and high frequencies due to the large sensor size. Although the measured spectra were corrected using the Corcos correction [16], uncertainties at higher frequencies could still be caused, which may explain the difference at higher frequencies between the prediction and those measurements. The Corcos correction assumed a uniform sensitivity for the sensors, whereas an actual sensor has a deflective sensitivity, e.g. for a condenser microphone the sensitivity has the maximum at the center and decreases near the edge. Blake [50] showed that the measured acceptance of a condenser microphone at higher wavenumber domain could be more than 5 dB smaller than the calculated theoretical acceptance with a uniform sensitivity. The difference is noticeable from $\omega U_c/r > 1$. This discrepancy at the acceptance will cause a smaller amplitude at higher frequencies even after using the Corcos correction. A new (own) result [107] for the wall pressure spectra measured by flush-mounted 2.54mm diameter Kulite sensors with the so called B-screen for ZPG boundary layers using an almost identical experimental setup as the setup presented in section 3.1 shows an under-correction using the Corcos correction from about $\omega U_c/r > 0.5$. However, a different conclusion for the Corcos correction was made from Lueptow [108], who argued that the Corcos correction over-corrects the wall spectra at higher frequencies. The reason for the different results is because different acceptances of the sensors were used. The one Lueptow applied is given by Smol'yakov and Tkachenko [109], who assumed an idealized deflection sensor and described its sensitivity distribution with the first vibration mode of the membrane with a Bessel function. The formulated acceptance has a larger value at higher wavenumber domain than the one with a uniform sensitivity. Another issue which should be also considered when using the Corcos correction is that the wall pressure convection velocity is much smaller for an APG boundary layer than for a ZPG boundary. To the author, it makes more sense to use the phase velocity determined from the closest distance (the order of the sensor size). The convection velocity $U_c(\omega)$ for an APG boundary layer at the

closest distance could be less than $0.3U_0$ at higher frequencies, refer to Fig. 4.10, which is much slower than the usually used $0.6 - 0.8U_0$. The too large convection velocity used in the Corcos correction will lead to an under-correction for the wall spectra. Furthermore, the APG increases the streamwise turbulence decay compared to the ZPG. A larger turbulence decay can further increase the attenuation due to the finite sensor size.

Besides the sensor effect, as discussed previously, the trailing edge scatter effect and a possible inaccuracy of the boundary layer parameters in the vicinity of trailing edge provided by XFOIL calculation could produce the prediction uncertainty and increase the discrepancy compared to the measured spectra. This issue affects the results for the case of Herrig *et al.* and the case of Suryadi & Herr at $x/c = 0.96$, and the discrepancy is larger at a larger AOA. A poor prediction is made for the case of Catlett *et al.* with an open angle of 17°, which is probably due to a separated boundary layer located near upstream of the measurement position. In addition, a good prediction is also obtained for the ZPG boundary layers.

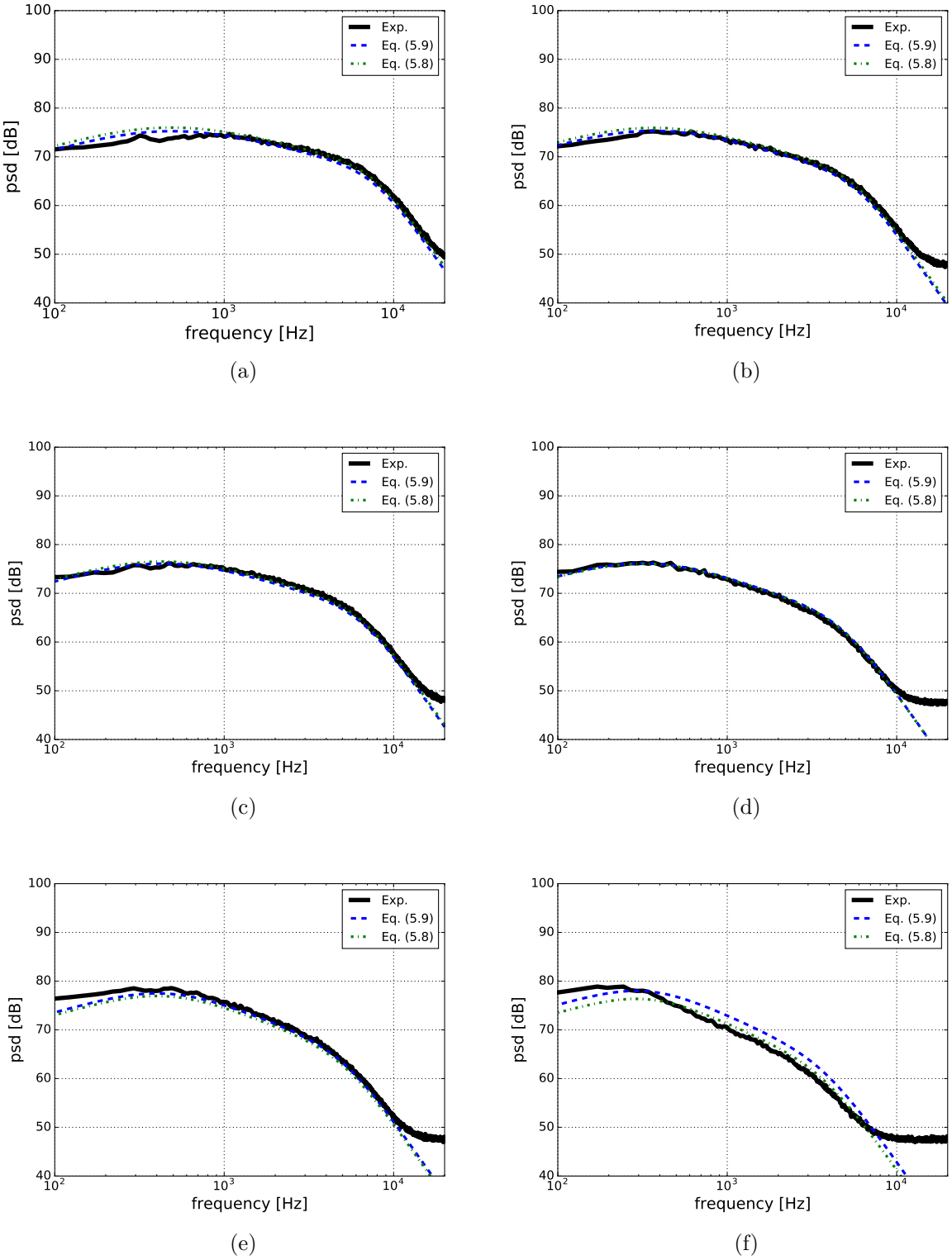

Figure 5.11: Predictions of the new model with two expressions for test case of the experiment presented in this work; (a) AOA=6°, U_0 = 32.3 m/s, distance of leading edge x = 1128 mm; (b) AOA=6°, U_0 = 30.8 m/s, distance of leading edge x = 1210 mm; (c) AOA=10°, U_0 = 32.0 m/s, distance of leading edge x = 1128 mm; (d) AOA=10°, U_0 = 30.4 m/s, distance of leading edge x = 1210 mm; (e) AOA=14°, U_0 = 31.2 m/s, distance of leading edge x = 1128 mm; (f) AOA=14°, U_0 = 29.9 m/s, distance of leading edge x = 1210 mm.

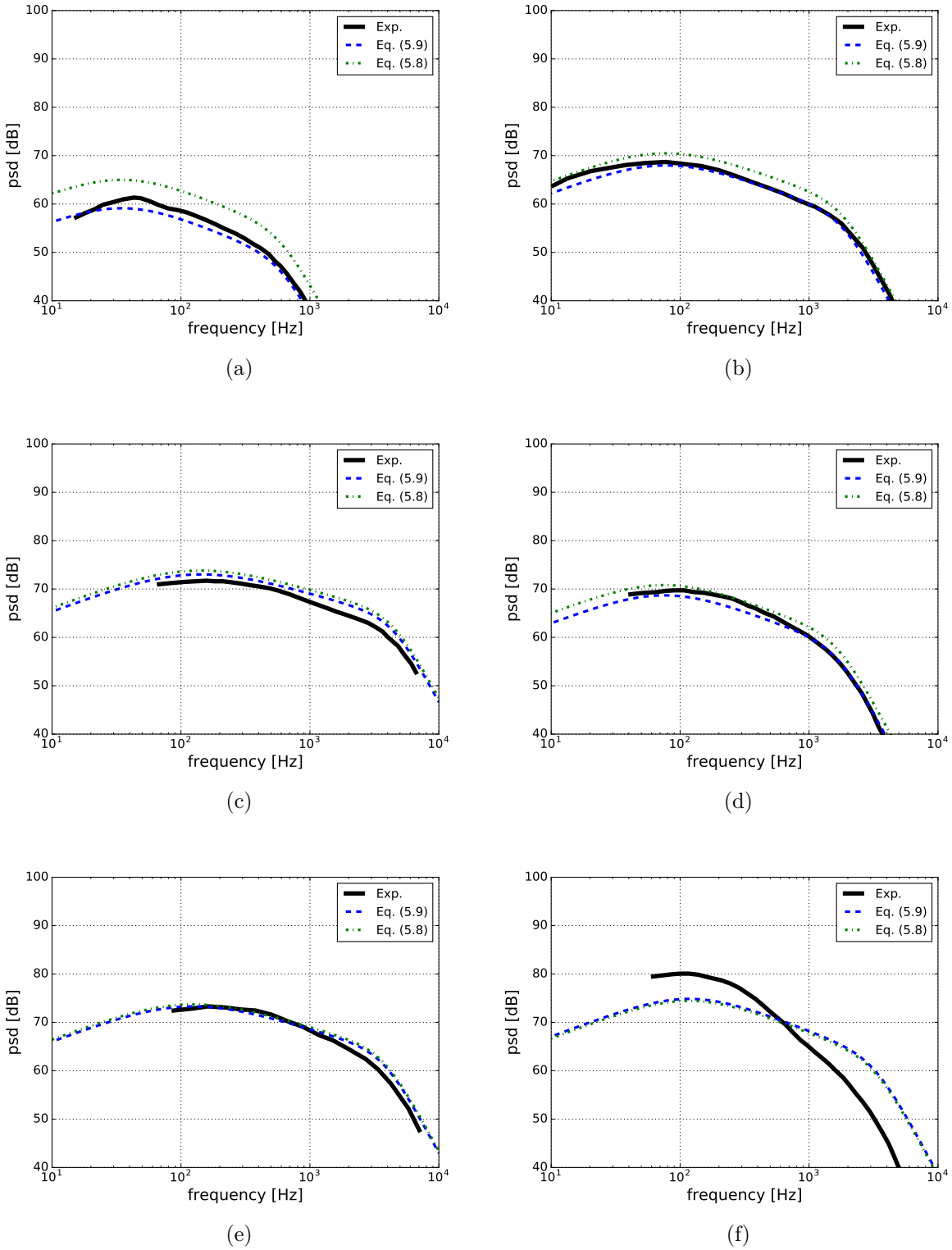

Figure 5.12: Predictions of the new model with two expressions for test case of Catlett *et al.*; (a) open angle=7°, U_0 = 9.0 m/s, distance of trailing edge x = 50 mm; (b) open angle=7°, U_0 = 18.1 m/s, distance of trailing edge x = 204 mm; (c) open angle=7°, U_0 = 28.3 m/s, distance of trailing edge x = 406 mm; (d) open angle=12°, U_0 = 18.4 m/s, distance of trailing edge x = 154 mm; (e) open angle=12°, U_0 = 28.1 m/s, distance of trailing edge x = 210 mm; (f) open angle=17°, U_0 = 28.4 m/s, distance of trailing edge x = 106 mm.

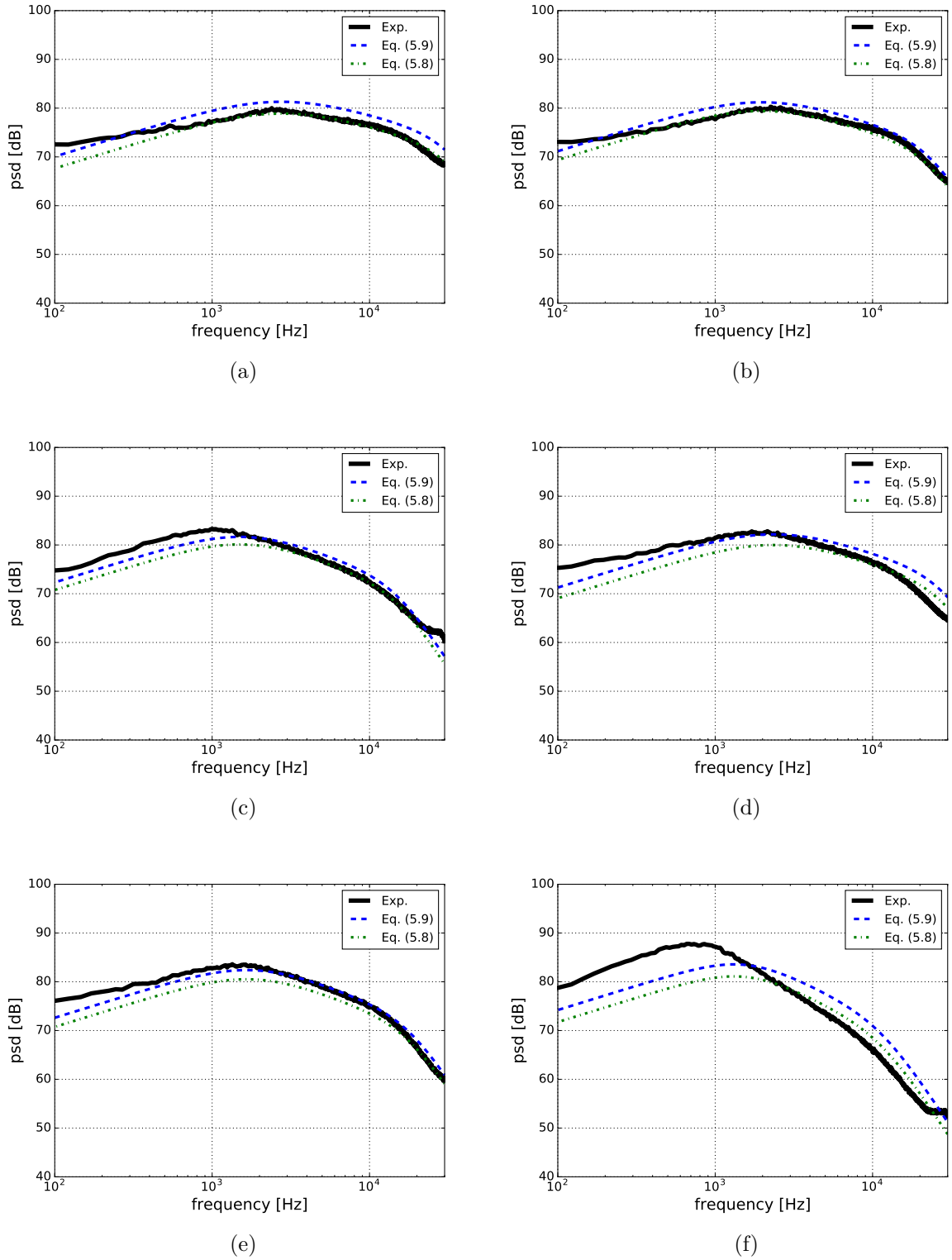

Figure 5.13: Predictions of the new model with two expressions for test case of Suryadi & Herr; (a) AOA=-0.8°, U_0 = 53.3 m/s, chord position x/c = 0.77; (b) AOA=-0.8°, U_0 = 49.6 m/s, chord position x/c = 0.88; (c) AOA=-0.8°, U_0 = 45.9 m/s, chord position x/c = 0.96; (d) AOA=3.2°, U_0 = 54.0 m/s, chord position x/c = 0.77; (e) AOA=3.2°, U_0 = 49.4 m/s, chord position x/c = 0.88; (f) AOA=3.2°, U_0 = 45.7 m/s, chord position x/c = 0.96.

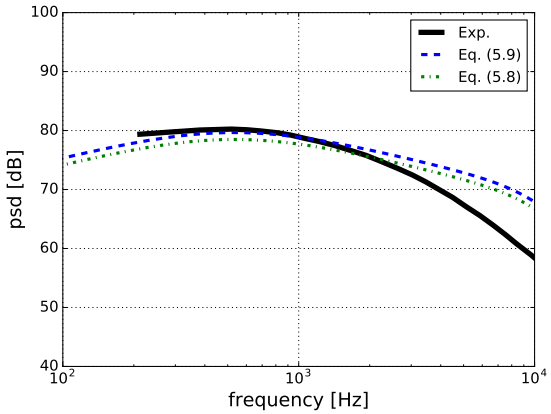

(a)

Figure 5.14: Predictions of the new model with two expressions for test case of Schloemer, $U_0 = 43.6$ m/s.

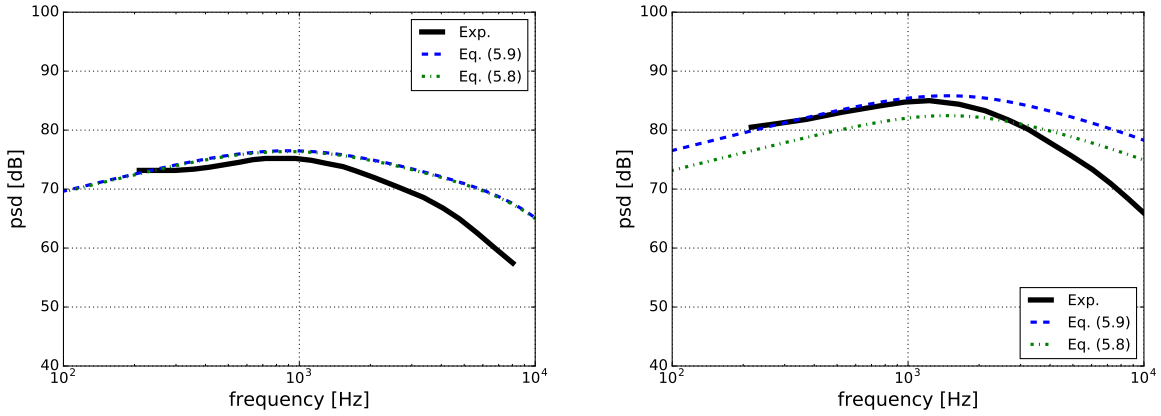

(a) (b)

Figure 5.15: Predictions of the new model with two expressions for test case of Herrig *et al.*; (a) AOA=0°, $U_0 = 33.4$ m/s, chord position $x/c = 0.99$; (b) AOA=4°, $U_0 = 62.7$ m/s, chord position $x/c = 0.99$.

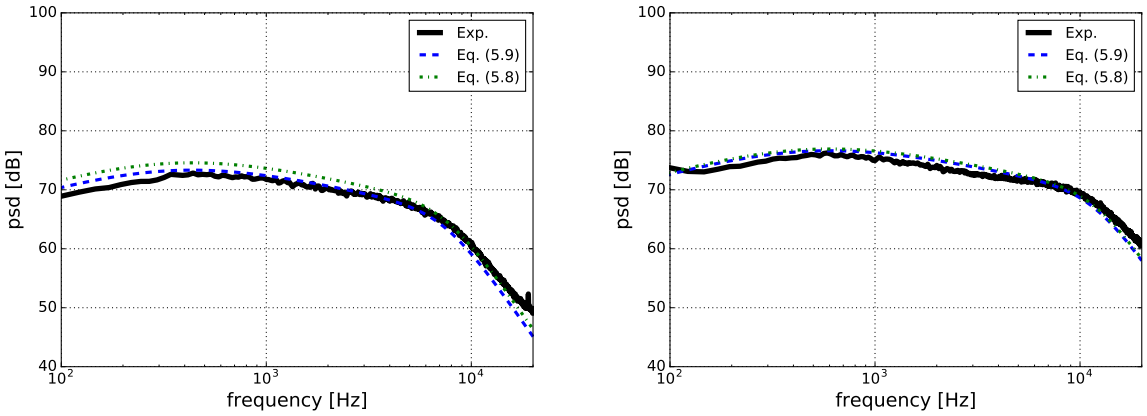

(a) (b)

Figure 5.16: Predictions of the new model with two expressions for test case of the experiment presented in this work for ZPG; (a) $U_0 = 30.2$ m/s, distance of leading edge $x = 1210$ mm; (b) $U_0 = 39.2$ m/s, distance of leading edge $x = 1210$ mm.

6 Numerical analysis

The pressure fluctuations within the turbulent boundary layer are simulated based on the method described in section 3.2. To verify and validate the numerical method, zero pressure gradient (ZPG) boundary layers for a generic test case are calculated. The features of the pressure fluctuations from the obtained numerical results are extensively analyzed and compared to the experimental and numerical results from the literature in section 6.1.

Furthermore, the wall pressure fluctuations of ZPG and adverse pressure gradient (APG) boundary layers for the experimental case presented in this work are calculated. The one-point wall pressure spectra and the two-point features including cross-spectra and convective velocities are calculated and compared to the measured results, addressed in section 6.2.

6.1 Numerical verification and validation

6.1.1 Computational setup and flow parameters

Mean flow statistics for 2-D flows over a flat plate are gained from RANS solutions. Two velocities related to Mach numbers $Ma = 0.1$ and $Ma = 0.2$ are calculated using DLR's in-house computational fluid dynamics (CFD) solver TAU [110, 111]. The Reynolds stress model with specific dissipation (ω) equation is used for the computation. A structured grid with approximately 200 k mesh points is used and the boundary layer is solved with the first cell layer $y^+ < 1$. The geometry of the computational domain is sketched in Fig. 6.20. The length of the whole plate is 2.8 m with an elliptical leading edge and a parabolic-shaped trailing edge. The leading edge and trailing edge sections have a length of 18 cm and 22 cm, respectively. The thickness of the plate is 6 cm.

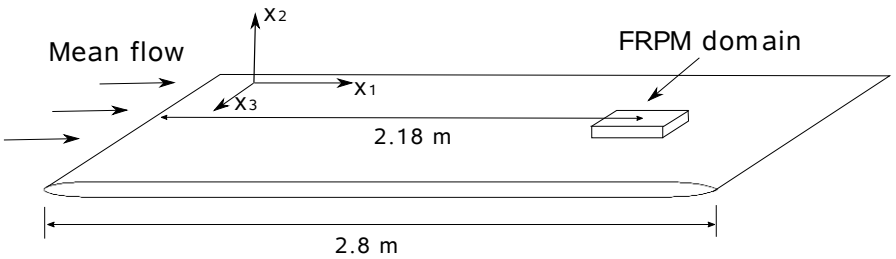

Figure 6.1: Sketch of the computational domain.

Synthetic turbulence is realized by the Fast Random Particle-Mesh Method (FRPM) for a 3-D rectangular domain with its center located 2.18 m downstream of the leading edge, see Fig. 6.20. The extension of the FRPM computational domain in streamwise, wall-normal and spanwise directions, respectively, are $L_1 = 7\delta$, $L_2 = 1.2\delta$ and $L_3 = 4\delta$,

Table 6.1: Turbulent boundary layer parameters

Ma	δ (mm)	δ^* (mm)	θ (mm)	H	Re_x	$Re_\tau = u_\tau \delta/\nu$	$Re_\theta = u\theta/\nu$	u_τ(m/s)
0.1	30.0	4.85	3.63	1.34	$4.9 \cdot 10^6$	2513	8257	1.29
0.2	27.5	4.20	3.22	1.31	$9.7 \cdot 10^6$	4357	14668	2.44

where δ denotes the boundary layer thickness at the center of the domain. Since Hockney's method demands for a grid with 2^N mesh points in each direction, a Cartesian grid with $128 \times 64 \times 128$ points is chosen for the calculations. A smaller time step is needed for the $Ma = 0.2$ case due to the Courant-Friedrichs-Lewy (CFL)-like constraint of FRPM, refer to section 2.2. Therefore, two time steps i.e. $\Delta t = 4.37 \times 10^{-5}$ and $\Delta t = 2 \times 10^{-5}$ are used, the smaller one for the $Ma = 0.2$ case and the $Ma = 0.1$ case with detailed two-point statistics analysis, while the larger one was used for other $Ma = 0.1$ cases. The calculations are run on a desktop computer with Inter Xeon E5-2630 2.4GHz CPUs. Each calculation for the pressure fluctuations is computed with 4 CPUs (8 threads) and the calculation time for 1s with the coarser time step is approximately 450 CPU hours and approximately 1000 hours for the case with the smaller time step. For the present simulations, a detailed two-point statistics analysis is conducted for the $Ma = 0.1$ case and 2 s real time; all other cases utilize 1 s simulation time samples.

The characteristics of the turbulent boundary layer at the center position of the domain ($x_1 = 2.18$ m) are listed in table 6.2. The obtained boundary layer shape factors $H = 1.34$ for $Re_\theta = 8257$ and $H = 1.31$ for $Re_\theta = 14668$ show very good agreement ($\pm$ 1%) with the prediction from Chauhan *et al.* [103]. The mean velocity profiles show good agreement with the LES result from Eitel-Amor *et al.* [112] at a comparable Reynolds number, see Fig. 6.2(a). Figs. 6.2(b)-(e) show comparison of the Reynolds stress between RANS solutions and the numerical datasets. The RANS results underpredict the Reynolds stress tensor $\overline{u_1' u_1'}$ in the sublayer and the logarithmic region compared to the LES results. The Reynolds stress tensor components $\overline{u_2' u_2'}$ and $\overline{u_3' u_3'}$ show good agreement with the LES results, except for some discrepancies in the region very close to the wall. For a 2-D boundary layer, the Reynolds stress tensors $\overline{u_1' u_3'}$ and $\overline{u_2' u_3'}$ are equal to 0 [98]. The length scale predicted by Eq. (3.13) as an averaged isotropic length scales is compared to the experimental results from Kamruzzaman *et al.* [68] in Fig. 6.2(f). The smaller value is the measured length scale for u_2' and was measured at 1% chord length downstream of the trailing edge of a NACA 0012 airfoil at 0° angle of attack (AOA). The larger one is the modified length scale obtained by using an isotropic turbulence approach to fit the measured velocity fluctuation spectra. The length scale from RANS solutions fit the modified length scale better in the outer layer and the measured one in the inner layer.

6.1.2 Turbulence velocity fluctuations realization

Turbulent velocity fluctuations realized by FRPM are used to prescribe the fluctuating source terms of the Poisson's equation (3.2) to derive unsteady wall pressure fluctuations. In a first step, isotropic fluctuations are realized by using a constant (isotropic) length scale in the spatial filter function Eq. (3.11) for each direction, i.e. $l_1 = l_2 = l_3 = l_s$. Furthermore, an isotropic scaling according to Eq. (3.25) is used. Fig. 6.3(a) shows the reconstructed turbulence kinetic energy and the reconstructed variance of the velocity

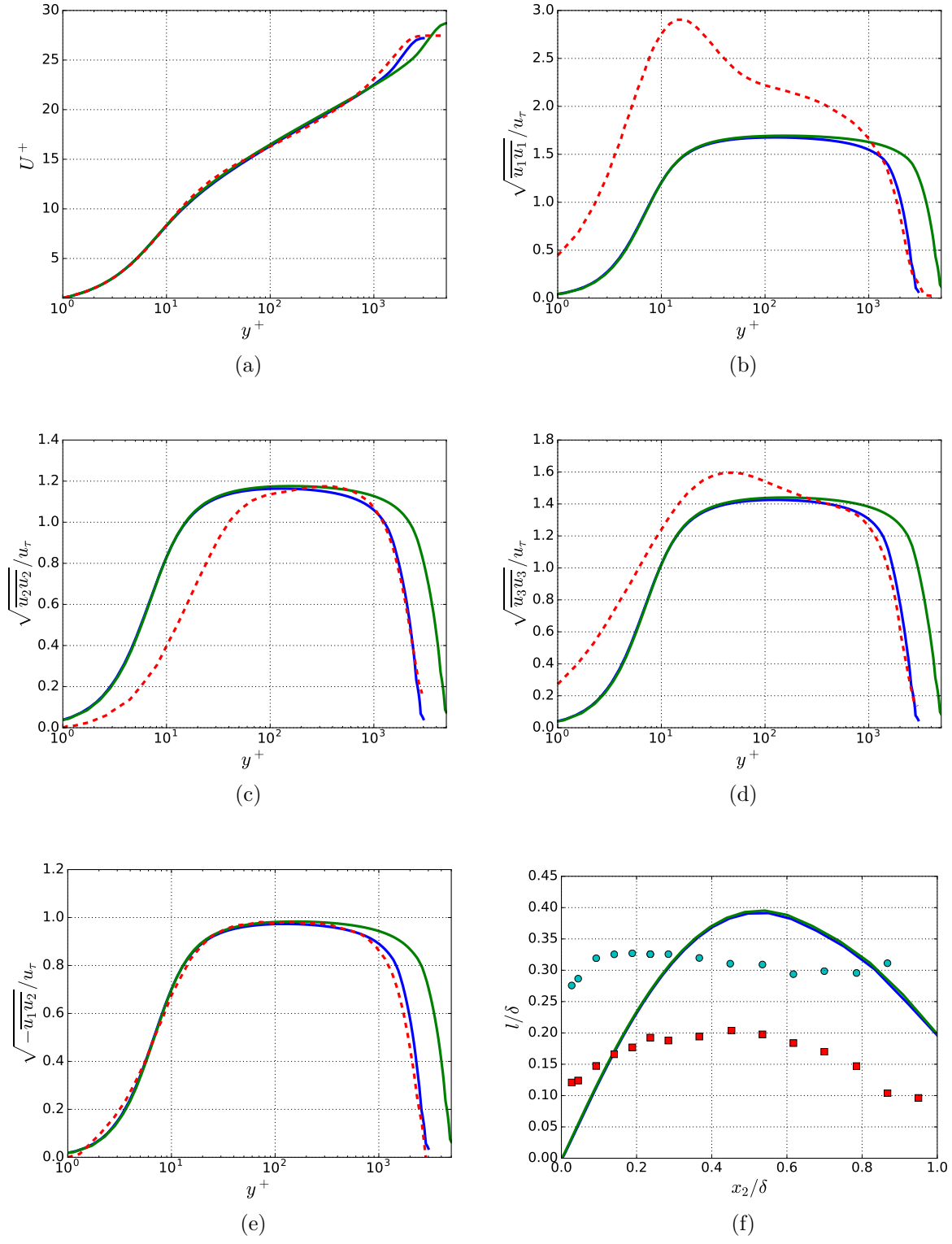

Figure 6.2: Boundary layer parameters at $x_1 = 2.18$ m along direction normal to the wall; (–), RANS solutions with $Ma = 0.1$ at $Re_\theta = 8257$ with blue lines and $Ma = 0.2$ at $Re_\theta = 14668$ with green lines; (- -), LES results from [112] at $Re_\theta = 7500$; ■, measured length scale and ●, modified length scale for an isotropic turbulence approach from [68] at $Re_\theta = 5363$, (a) mean flow profile; (b)-(e) root-mean-squared Reynolds stress tensor elements; (f) length scale from Eq. (3.13).

fluctuations for the $Ma = 0.1$ flow in comparison to the target within the boundary layer. The variance of the velocity fluctuations are nearly equally well realised for each component based on the isotropic turbulence approach. In the outer region $> 0.4\delta$ a perfect reconstruction of the kinetic energy is visible. A lack of kinetic energy level is evident in the region close to the wall, especially for $< 0.1\delta$. The reason for the loss in reconstructed energy is mainly because of a grid resolution not fine enough to resolve the small turbulence structures close to the wall. Note, for a technical application of the method, it is sufficient to resolve structures only in the regime of interest, which typically demands a truncation of the realization at a smallest resolved length scale (FRPM mesh resolution limit), typically considerably above the Kolmogorov scale. Otherwise, if all scales would be entirely reproduced, the resolution requirement of the mesh would be driven by similar constraints as those present in LES or DNS.

FRPM realizes 1-D Gaussian turbulence spectra $\Phi_{ii}(k_1)$ as analytically derived in Appendix B. A relationship between velocity spectra $\Phi_{ij}(\omega)$ and $\Phi_{ij}(k_1)$ is presented by Eq. (A.14) in Appendix A. The result depends on whether turbulence decay (finite decay time scale τ_s) is considered or if the assumption of frozen turbulence (Taylor's hypothesis) is applied by choosing $\tau_s \to \infty$. Practically, considering a uniform mean flow in the x_1-direction, the frequency spectrum of frozen turbulence is obtained by replacing wavenumber k_1 by ω/U_c, where U_c is the convection velocity in the x_1-direction. Figs. 6.3(b-d) show the realized velocity spectra compared to the analytical Gaussian velocity spectra with frozen and non-frozen turbulence. The spectra are calculated with a window length of 512 samples for the case with the larger time step and 1024 samples for the case with the smaller time step. The sampling rate is 23kHz and 50kHz for the larger and smaller time steps, respectively, which results a frequency resolution of approximately 45Hz and 49Hz. Furthermore, the spectra are averaged at 3 different positions in the spanwise direction within a distance of 2.7δ where nearly no correlations of the data between each position exist. The same condition for spectral estimation is made for the wall pressure spectra. Spectra at two different wall-normal positions, viz $x_2 = 0.08\delta$ and $x_2 = 0.61\delta$, are considered. The realized spectra show an excellent agreement with the analytical results at 0.61δ. However, at 0.08δ an attenuation of the spectral magnitude is shown at higher frequencies, e.g. above 2 kHz for spectra of u_2' and u_3'. This is because the used grid cannot resolve small turbulence structures in the near-wall region, which causes the attenuation of kinetic energy reconstruction in this region shown in Fig. 6.3(a). As a result of the introduced turbulence decay the non-frozen turbulence spectra present a less steep roll-off for higher frequencies compared with that of frozen turbulence. The reason is that the form of the moving-axis spectrum $\phi_m(\omega - U_c k_1)$ changes from $\delta(\omega - U_c k_1)$ to a broadband form, refer to the discussion in Appendix A. As a consequence of an exchange of the δ function by a mollified distribution in the convolution integral Eq. (A.14), the energy of the frozen turbulence spectrum is spread out into the neighbourhood, in this case from the lower frequencies into the higher frequencies. It is worth to note that the spectral contribution from turbulence decay depends on the form of ϕ_m.

The anisotropy of wall turbulence for the FRPM turbulence realization is obtained by realizing anisotropic Reynolds stress components and using a stretching factor γ in the integral length scale, refer to section 2.2. Fig. 6.4(a) shows that in the inner region the reconstruction of turbulence kinetic energy with the anisotropic turbulence approach is slightly better than the one with the isotropic turbulence approach. The reason for that could be the applied stretching factor, which causes a larger vortex structure in the

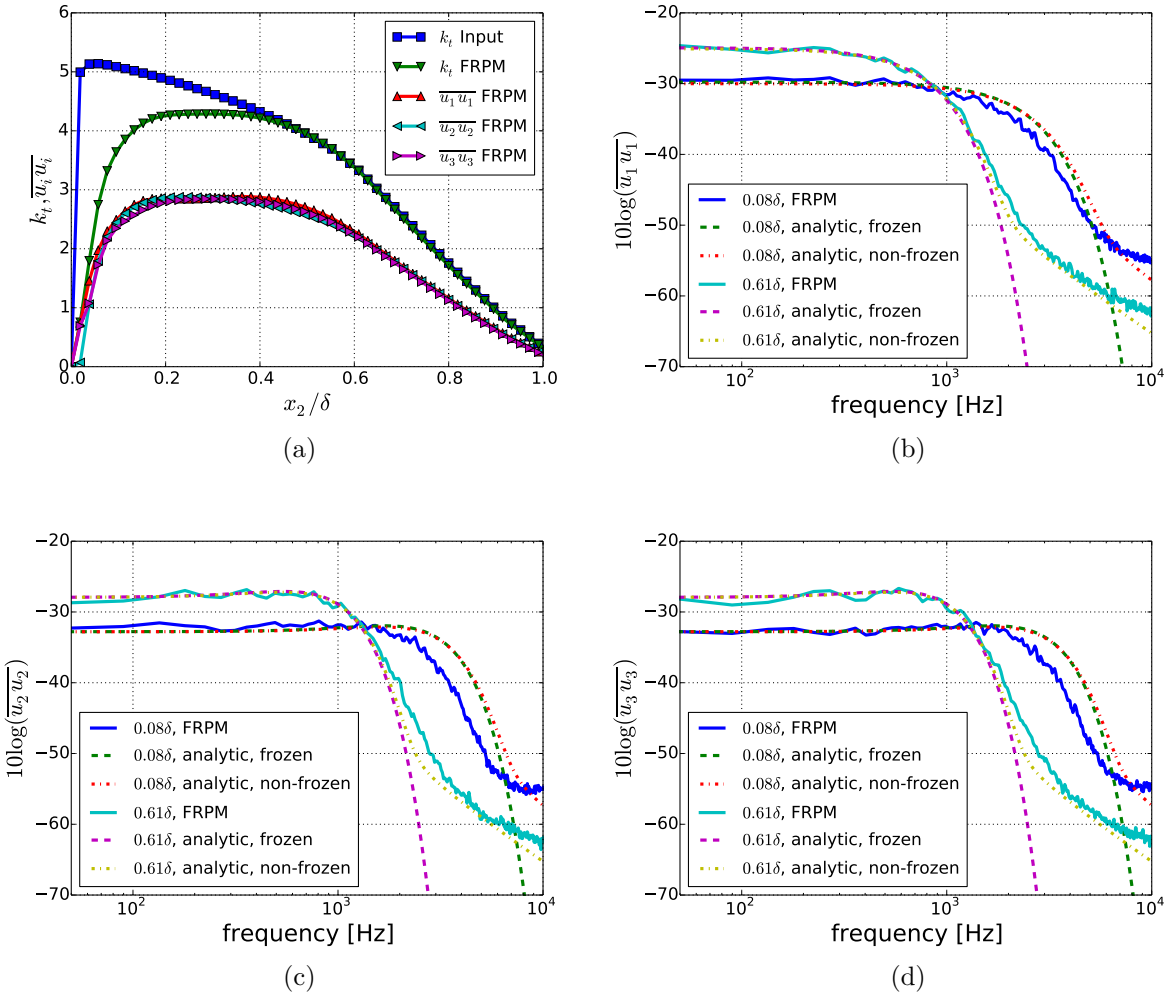

Figure 6.3: Realisation of the velocity fluctuations from FRPM within the boundary layer based on the isotropic turbulence approach; (a) turbulent kinetic energy reconstruction; (b) u_1' spectra; (c) u_2' spectra;(d) u_3' spectra; for frozen ($\tau_s \to \infty$) and non-frozen (τ_s from Eq. (3.17)) turbulence.

streamwise direction and thus benefitting from a higher points-per-wavelength value on the used FRPM grid owing to the coarsest resolution in the streamwise direction. Fig. 6.4(b) shows the realized Reynolds stress components, the ratio between them follows the ratio from the RANS solution shown in Fig. 6.2.

6.1.3 One-point spectra

The source term of the Poisson's equation (3.2) comprises two contributions, viz the mean-shear turbulence interaction term and the turbulence-turbulence interaction term. Since

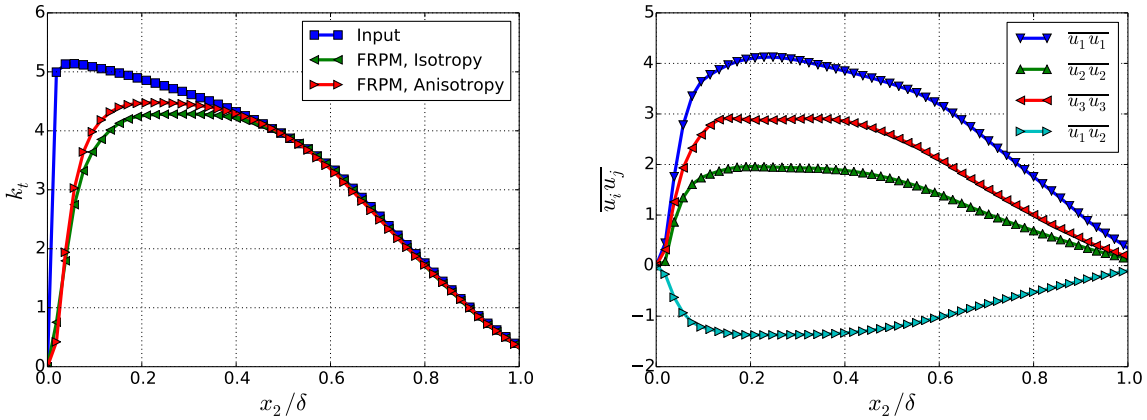

(a) (b)

Figure 6.4: Realisation of the velocity fluctuations from FRPM within the boundary layer with both the isotropic and anisotropic turbulence approach, stretching factor $\gamma = 1.5$; (a) turbulent kinetic energy reconstruction; (b) Reynolds stress tensors.

the Poisson's equation is linear, the pressure fluctuations can be separately solved,

$$p'^{(I)}_{ms}(\mathbf{x},t) = -2\rho_0 \int_{\mathbf{V_s}+\mathbf{V'_s}} \frac{\partial \overline{u}_1}{\partial x_2} \frac{\partial u'_2(\mathbf{y},t)}{\partial x_1} \cdot g(\mathbf{x}-\mathbf{y})\,\mathrm{d}^3\mathbf{y}, \tag{6.1}$$

$$p'^{(I)}_{tt}(\mathbf{x},t) = -\rho_0 \int_{\mathbf{V_s}+\mathbf{V'_s}} \frac{\partial^2}{\partial x_i \partial x_j}(u'_iu'_j - \overline{u'_iu'_j})(\mathbf{y},t) \cdot g(\mathbf{x}-\mathbf{y})\,\mathrm{d}^3\mathbf{y}, \tag{6.2}$$

where p'_{ms} denotes the pressure fluctuations for the mean-shear term and p'_{tt} for the turbulence-turbulence term. Index (I) denotes the options to realise the integral. Integration by parts allows to shift the derivatives acting on terms with fluctuating velocity to the Green's function, providing two other options:

$$p'^{(II)}_{ms}(\mathbf{x},t) = 2\rho_0 \int_{\mathbf{V_s}+\mathbf{V'_s}} \frac{\partial \overline{u}_1}{\partial x_2} u'_2(\mathbf{y},t) \cdot \frac{\partial g(\mathbf{x}-\mathbf{y})}{\partial x_1}\,\mathrm{d}^3\mathbf{y}, \tag{6.3}$$

$$p'^{(II)}_{tt}(\mathbf{x},t) = \rho_o \int_{\mathbf{V_s}+\mathbf{V'_s}} \frac{\partial}{\partial x_i}(u'_iu'_j - \overline{u'_iu'_j})(\mathbf{y},t) \cdot \frac{\partial g(\mathbf{x}-\mathbf{y})}{\partial x_j}\,\mathrm{d}^3\mathbf{y}, \tag{6.4}$$

$$p'^{(III)}_{tt}(\mathbf{x},t) = -\rho_0 \int_{\mathbf{V_s}+\mathbf{V'_s}} (u'_iu'_j - \overline{u'_iu'_j})(\mathbf{y},t) \cdot \frac{\partial^2 g(\mathbf{x}-\mathbf{y})}{\partial x_i \partial x_j}\,\mathrm{d}^3\mathbf{y}. \tag{6.5}$$

Hence, instead of numerical derivatives of the velocity fluctuations analytical derivatives of the Green's function occur. The realized Reynolds stress is taken as input values for $\overline{u'_iu'_j}$. Finally, Eqs. (6.1) and (6.3) represent two approaches for p'_{ms} and Eqs. (6.2), (6.4) and (6.5) give three for p'_{tt}.

Fig. 6.5 shows the one-point spectra for the wall pressure fluctuations at $Ma = 0.1$ calculated with isotropic turbulence. Both approaches for p'_{ms} show nearly identical results. This indicates that either the approach with $\partial u'_2/\partial x_1$ or with $\partial g/\partial x_1$ is well suited for the given computational setup. Comparable results for p'_{tt} are obtained for both approaches using $\partial g/\partial x_j$ or $\partial^2 g/\partial x_i \partial x_j$, respectively. In contrast, large discrepancies are obtained by

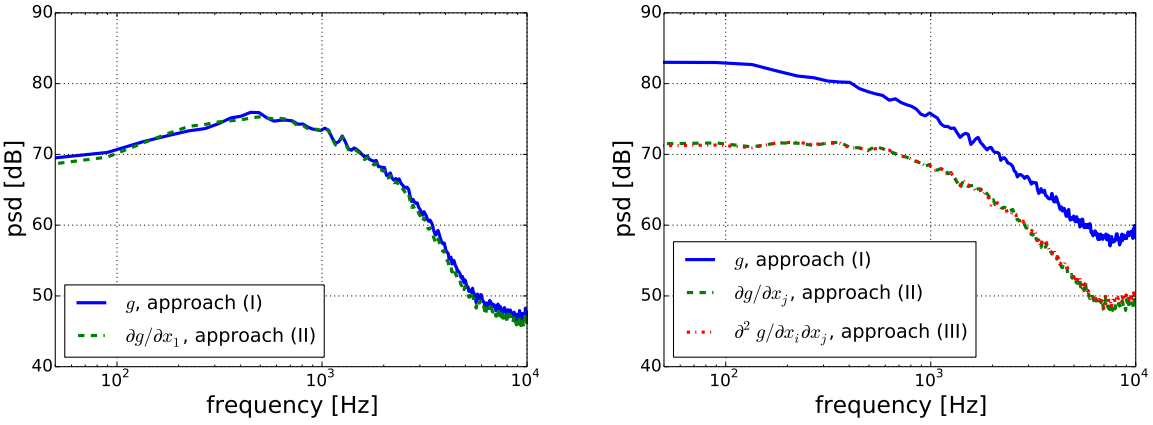

Figure 6.5: Wall pressure fluctuations for different approaches; (a) spectra for p'_{ms}; (b) spectra for p'_{tt}.

the approach with $\partial^2(u'_i u'_j - \overline{u'_i u'_j})/\partial x_i \partial x_j \cdot g$. This is because of the involved numerical errors by calculating the double derivative $\partial^2/\partial x_2 \partial x_2$ in the last couple of cell layers close to the wall.

To avoid the singularity of the Green's function a minimum threshold r_{min} is applied. The value of r_{min} is set to be equal to the mesh size in x_2-direction which is the finest resolution of the used grid. Note that, the local pressure fluctuations within the boundary layer can be altered by the choice of r_{min} for approaches involving g or $\partial^2 g/\partial x_i \partial x_j$. In contrast, the approach with $\partial g/\partial x_j$ is independent of r_{min}, insofar its value is not larger than the smallest mesh size of the used grid. From the results for p'_{ms} and p'_{tt} and the good solution for the singularity problem, it is concluded that the approach based on $\partial g/\partial x_j$ provides the best consistent numerical realization. Thus, p'_{total} is calculated with

$$p'_{total}(\mathbf{x},t) = p^{(II)}_{ms}(\mathbf{x},t) + p^{(II)}_{tt}(\mathbf{x},t)$$

$$= \rho_0 \int_{\mathbf{V_s}+\mathbf{V'_s}} \left\{ 2\frac{\partial \overline{u}_1}{\partial x_2} u'_2(\mathbf{y},t) \cdot \frac{\partial g(\mathbf{x}-\mathbf{y})}{\partial x_1} + \frac{\partial}{\partial x_i}(u'_i u'_j - \overline{u'_i u'_j})(\mathbf{y},t) \cdot \frac{\partial g(\mathbf{x}-\mathbf{y})}{\partial x_j} \right\} \mathrm{d}^3\mathbf{y}. \tag{6.6}$$

Theoretically, the wall pressure spectrum for p'_{ms} defined by $\Phi_{ppms}(\omega)$ can be analytically solved for statistically stationary turbulence using the mean-flow one-point statistics together with the two-point cross-correlation model that underlies the synthetic turbulence generation. The deviation of the analytical solution of Eq. (6.1) is given in section 2.1, it reads

$$\begin{aligned} \Phi_{ppms}(\omega) \;=\; & 4\rho_0^2 \int_0^{\delta} \int_{-\infty}^{\infty} \int_{-\infty}^{\infty} \frac{k_1^2}{k^2} \exp(-2kx_2) [\frac{\partial \overline{u}_1(x_2)}{\partial x_2}]^2 \Phi_{22}(k_1,k_3,x_2) \\ & \phi_m(\omega - k_1 U_c(x_2)) \Lambda_2(x_2)\, \mathrm{d}k_1\, \mathrm{d}k_3\, \mathrm{d}x_2, \end{aligned} \tag{6.7}$$

where k_i is wavenumber component in each direction and $k^2 = k_1^2 + k_3^2$. $\Phi_{22}(k_1,k_3,x_2)$ is the wavenumber spectrum for velocity fluctuations in the wall-normal direction, $\overline{u}_1(x_2)$ is the local flow velocity and $U_c(x_2)$ is the local flow convective velocity. For the present problem

with convection in the x_1-direction and assumed statistical stationarity in x_1, $U_c(x_2)$ can be calculated from the maximum of the cross-correlation function $R_{uu}(\Delta x_1, 0, \tau)$, the convective velocity follows from $U_c = \Delta x_1/\tau(\Delta x_1)$, where τ is the time shift for the velocity fluctuations at which R_{uu} is maximal, and Δx_1 indicates the two-point separation in the x_1-direction. The local convection velocity $U_c(x_2)$ is obtained using the simulation data. The results indicate $U_c(x_2) = \overline{u}_1(x_2)$ across the boundary layer. The same results were reported by Wooldridge & Willmarth [113] through measuring the correlation between the velocity fluctuations and the wall pressure fluctuations. In Eq. (6.7) $\Lambda_2(x_2)$ is the double-sided correlation length in the wall-normal direction, i.e. $\Lambda_2(x_2) = 2l_s(x_2)$, where l_s is the integral length scale used in FRPM. The velocity wavenumber spectrum of the vertical fluctuating velocity $\Phi_{22}(k_1, k_3, x_2)$ can be obtained by $\int \Phi_{22}(k_1, k_2, k_3, x_2)\,\mathrm{d}k_2$. The form of $\Phi_{22}(k_1, k_2, k_3)$ for FRPM is represented in Appendix B. The function $\phi_m(\omega - k_1 U_c(x_2))$ is the moving axis spectrum which in FRPM is implicitly defined through the turbulence decay term $\exp(-\tau/\tau_s)$, ref to Eq. (A.11).

Fig. 6.6 shows an excellent agreement at low and medium frequencies between the theoretical prediction for the non-frozen turbulence and the simulated spectrum. Discrepancies between the theoretical and simulated spectra are found for frequencies above 2kHz due to the attenuation of the realized velocity fluctuation spectra, see Fig. 6.3(c). Eq. (6.7) provides the wall pressure spectrum as an integral over all decks of the boundary layer. The theoretical contributions to the wall pressure fluctuations from different wall-normal positions are also presented in Fig. 6.6. This shows that positions closer to the wall are responsible for the higher frequencies. For example, the position at 0.08δ has a large contribution for frequencies 1-2 kHz. The outer region at 0.61δ shows only little relevance to the wall pressure fluctuations. Due to the term $k_1^2/k^2 \exp(-2kx_2)$ in Eq. (6.7) the contribution of the boundary layer to the wall pressure spectra especially vanishes at lower and higher frequencies. For example the maximum contributions of the boundary layer at 0.08δ and 0.61δ are located around 1.5 kHz and 300 Hz, respectively. If we compare these contributions with the theoretical velocity fluctuation spectra of u_2' in the boundary layer shown in Fig. 6.3(c), it is interesting to find that the maximum contributions occur in the plateau region of the $\overline{u_2'u_2'}$ spectrum. This indicates that the energy-containing range of the spectra dominates the contribution to the wall pressure fluctuations, and the inertial subrange, not well represented by the realized Gaussian spectrum due to the rapid roll off at higher frequencies, only plays a minor role. Unlike for velocity spectra, for which the impact of turbulence decay is primarily found at high frequencies, the turbulence decay increases the contributions to the pressure spectra at low frequencies as well. Consequently, the near-wall region becomes also relevant to wall pressure fluctuations at low frequencies. Note that, a flatter slope than the classic ω^2 rise is visible at low frequencies as a result of the turbulence decay.

Fig. 6.7 shows the calculated spectra for p'_{ms}, p'_{tt} and p'_{total} at $Ma = 0.1$ with the different isotropic and anisotropic turbulence approaches. The p'_{ms} spectra show a maximum at medium frequencies and an increase behaviour at low frequencies because of the derivative in the streamwise direction $\partial/\partial x_1$ of the mean-shear source term. In contrast, the p'_{tt} spectra own a low-pass behaviour with maximum plateau at low frequencies. This is mainly attributed to the turbulence-turbulence source terms with the double derivatives in the spanwise and wall-normal directions, i.e. $\partial^2/\partial x_2 \partial x_2$, $\partial^2/\partial x_2 \partial x_3$ and $\partial^2/\partial x_3 \partial x_3$. Due to this behaviour, the p'_{tt} spectra gain dominance at low frequencies. It is noteworthy to mention that above 2 kHz the realized velocity fluctuation spectra decay due to the

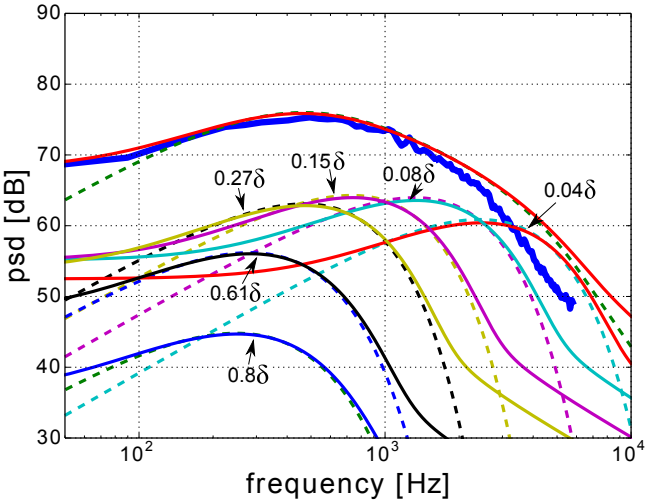

Figure 6.6: Wall pressure fluctuations for p'_{ms} and the contributions to the wall pressure fluctuations from different positions at 0.04δ, 0.08δ, 0.15δ, 0.27δ 0.61δ and 0.8δ; (–), numerical result; (–), theoretical results for non-frozen turbulence; (- -), theoretical results for frozen turbulence.

mesh size, refer to Fig. 6.3. Therefore, comparison and discussion of both spectra are restricted to the frequency range below 2 kHz. At medium frequencies from, where the maximum amplitude for the p'_{ms} spectrum is located, to 2 kHz, both p'_{ms} and p'_{tt} show similar trends.

The importance of both p'_{ms} and p'_{tt} is impacted by the anisotropy of turbulence. For the isotropic approach the maximum difference of spectral amplitude between the two terms is found at medium frequencies, where the p'_{ms} is approximately 5 dB larger than the p'_{tt}. The difference becomes smaller when the anisotropy of Reynolds stress is applied and even disappears when an anisotropic length scale is applied. Note that, the spectral amplitude for p'_{tt} is hardly impacted by the anisotropy of the turbulence. In contrast, for p'_{ms} the amplitude decreases when anisotropy of Reynolds stress and length scale anisotropy are applied. The reason for that could be that p'_{tt} is driven by the turbulence kinetic energy, however, p'_{ms} only by the u'_2 which is more sensitively altered by the anisotropy of turbulence. Another effect of the anisotropy is that the maximum of p'_{ms} spectra shifts to a lower frequency. This is probably due to the anisotropy of Reynolds stress tensor $\overline{u'_1 u'_2}$. This correlates the velocity fluctuations u'_1 which contain more energy at lower frequencies to u'_2. The result with anisotropic Reynolds stress and a length scale stretching factor $\gamma = 1.5$ is mostly consistent with the results from Kim [55] and Chang *et al.* [57], which demonstrated that both terms have the same order for the contribution to the wall pressure fluctuations. The spectral trend of both terms show also good agreement with the spectra calculated by Kim [55], which show a flat behaviour at lower frequencies for p'_{tt} and the maximum of p'_{ms} is approximately 1 dB above p'_{tt} levels. Note that, in the present calculation the velocity fluctuations for u'_1 from RANS solutions are smaller than the ones from LES, refer to Fig. 6.2(b). This will cause an attenuation of the spectral amplitude for p'_{tt}. The attenuation at low and medium frequencies is estimated to be less than 0.5 dB.

Fig. 6.8(a) shows a spectral scaling between the cases for $Ma = 0.1$ and $Ma = 0.2$.

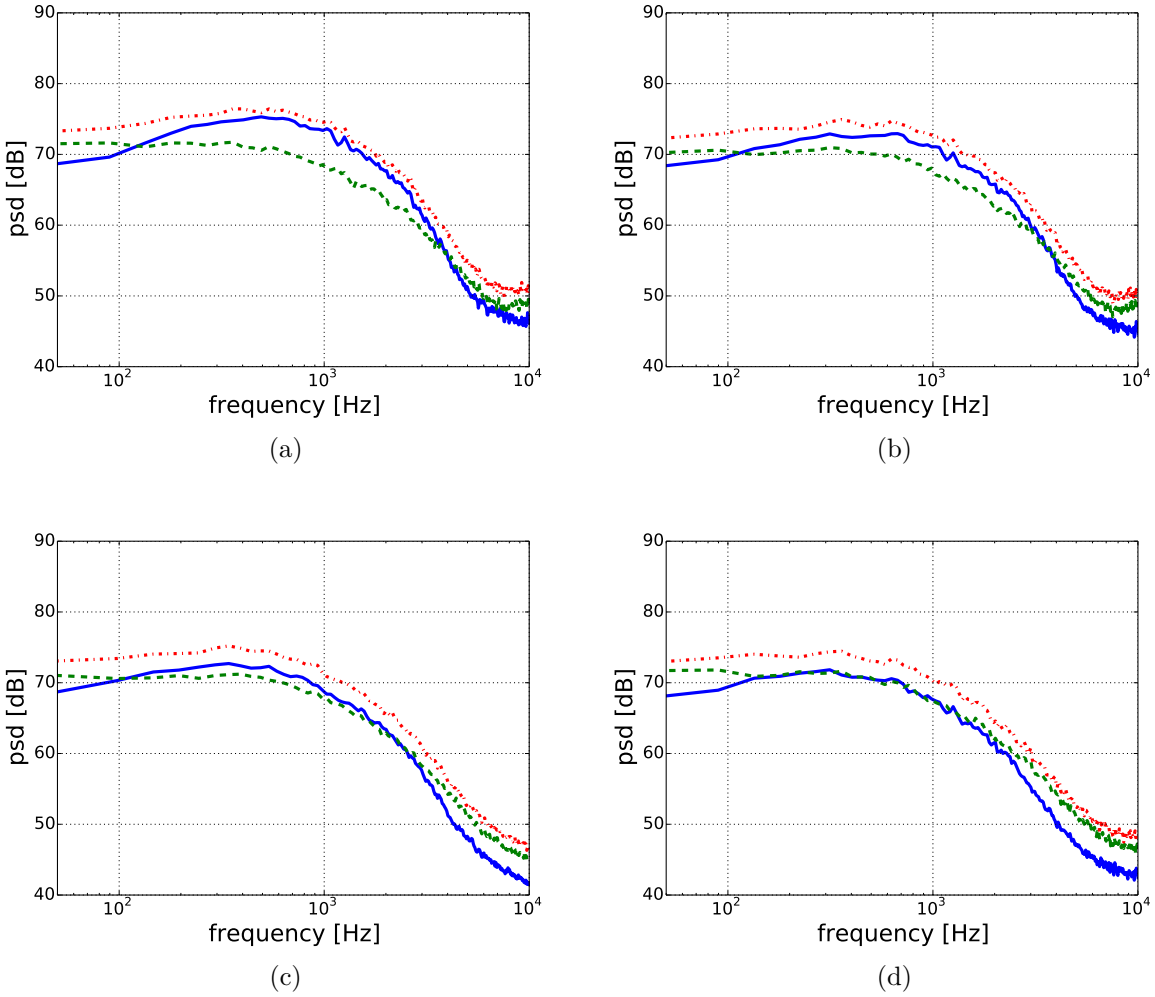

Figure 6.7: Wall pressure spectra for (–), p'_{ms}; (- -), p'_{tt}; (- · -), p'_{total}; (a) isotropic turbulence approach; (b) anisotropy of Reynolds stress tensors; (c) anisotropy of Reynolds stress tensors and length scale anisotropy with $\gamma = 1.5$; (d) anisotropy of Reynolds stress tensors and length scale anisotropy with $\gamma = 2$.

The results are gained with the anisotropic turbulence Reynolds stress and the stretching factor $\gamma = 1.5$ and also for the remaining results shown in the thesis. All the components p'_{ms}, p'_{tt} and p'_{all} collapse for the calculated velocities. A Reynolds number effect which causes an elongated extension of the spectral slope at medium frequencies as the Reynolds number increases is not found in the present result. This is mainly because the used mesh resolution cannot resolve the fine structure of the turbulence and therefore the Reynolds number effect at higher frequencies cannot be calculated. A comparison between the scaled spectrum for $Ma = 0.1$ and the wall pressure model spectra is shown in Fig. 6.8(b). At medium frequencies the calculated spectrum shows good agreement with the models. However, at higher frequencies the slope of the calculated spectrum departs from $\omega^{-0.7}$ from the Goody model [36] and ω^{-1} from the Herr model [37], which is due to the lack of the realized turbulent kinetic energy in the near-wall region. Also a different trend is found at low frequencies. The models have a ω^2 behaviour at low frequencies which is based on the mean-shear part for a frozen turbulence.

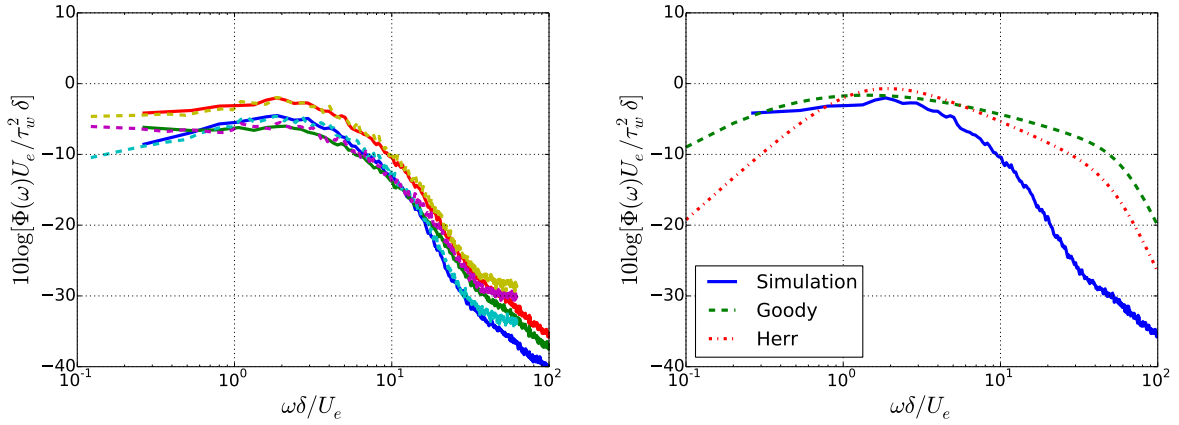

(a) (b)

Figure 6.8: Wall pressure fluctuations; (a) scaled spectra for p'_{ms}, p'_{tt} and p'_{total} for (–), $Ma = 0.1$ and (- -), $Ma = 0.2$; (b) comparison between the numerical result and the models.

6.1.4 Root mean square pressure

Figs. 6.9(a,b) show the root mean square value of pressure fluctuations for p'_{ms}, p'_{tt} and p'_{total} normalized by the wall shear stress τ_w across the boundary layer. The pressure fluctuations show very similar trends for both velocities. At the wall the magnitude for p'_{ms} and p'_{tt} are the same order and within the boundary layer the magnitude of p'_{tt} is larger than p'_{ms}. A similar trend is also found by Kim [55].

A comparison between the present results for p'_{total} and results from the literature is shown in Figs. 6.9(c). The present results show an excellent agreement with the results from Schlatter *et al.* [115] and Jimenez *et al.* [114] in the outer region $> 0.3\delta$. However, approaching the wall, the discrepancies become larger due to the lack of the realized kinetic energy shown in Fig. 6.4(a). A Reynolds number effect is visible in the results from the literature that increases the maximum value of the pressure fluctuations and shifts the maximum position closer to the wall as the Reynolds number increases. The increase of magnitude is mainly caused by the fine-scale turbulence and its produced energy at higher frequencies, e.g. an elongated extension of the $\omega^{-0.7}$ or ω^{-1} slope to higher frequencies for the wall pressure fluctuations. However, this effect is not found in the present study due to the limited mesh resolution used.

6.1.5 Broadband correlations

The normalized space-time correlation of the pressure fluctuations is defined by

$$\tilde{R}_{pp}(\mathbf{x}, \mathbf{r}, \tau) = \frac{R_{pp}(\mathbf{x}, \mathbf{r}, \tau)}{R_{pp}(\mathbf{x}, 0, 0)}, \tag{6.8}$$

where the correlation R_{pp} can be obtained from Eq. (2.53). For the calculation domain the boundary layer grows slowly, so the flow field can be treated as a homogeneous field. Hence, $\tilde{R}_{pp}(\mathbf{x}, \mathbf{r}, \tau) \simeq \tilde{R}_{pp}(\mathbf{r}, \tau)$.

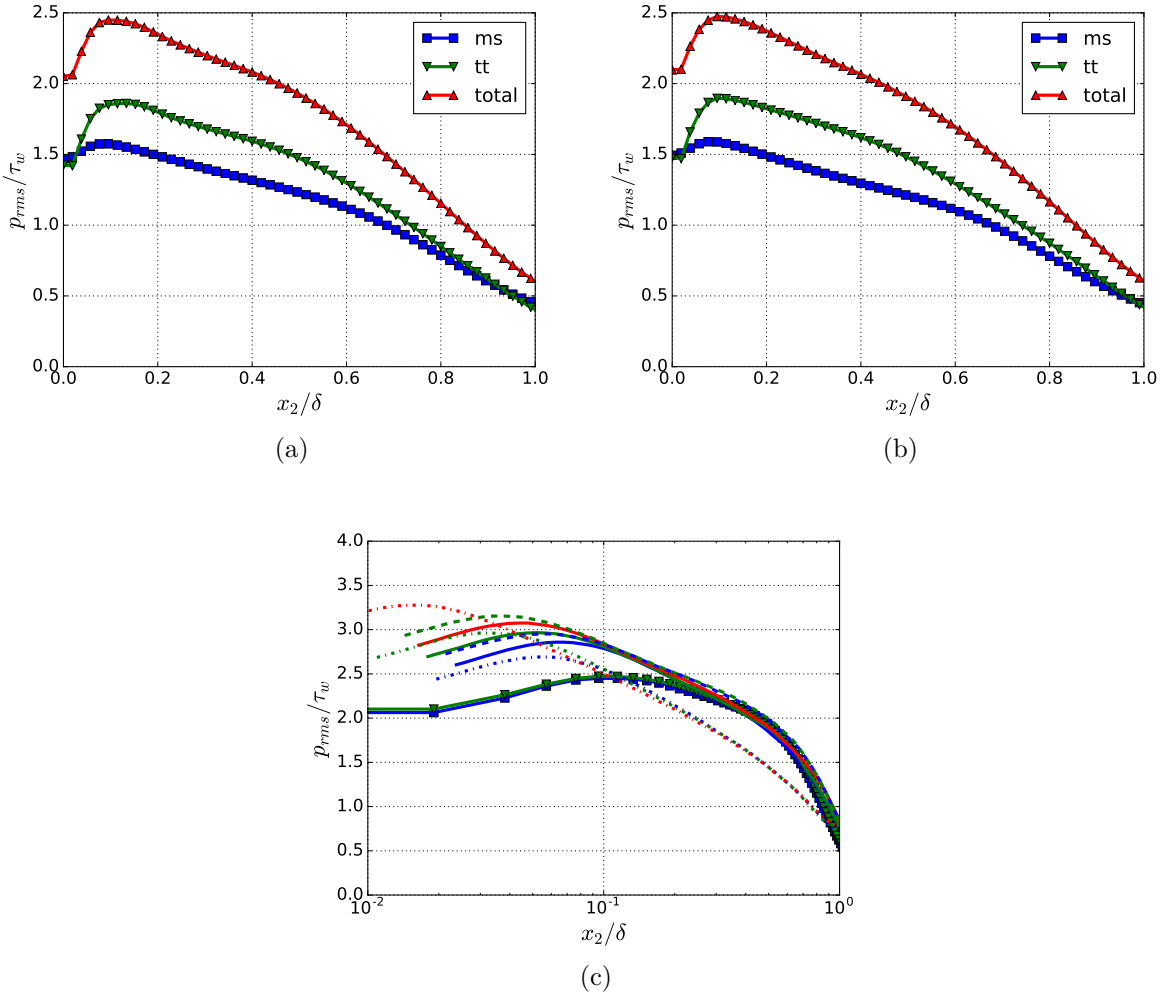

Figure 6.9: Root mean square of pressure fluctuations across the boundary layer, calculated with anisotropy of Reynolds stress tensors and length scale anisotropy with $\gamma = 1.5$; (a) trend of p'_{rms}/τ_w for p'_{ms}, p'_{tt} and p'_{total} for $Ma = 0.1$, $Re_\tau = 2513$; (b) trend of p'_{rms}/τ_w for p'_{ms}, p'_{tt} and p'_{total} for $Ma = 0.2$, $Re_\tau = 4357$; (c) comparison for p'_{total} between the present results and results from literatures over logarithmic scale; (-■-), (-▼-), present calculation, $Re_\tau = 2513$ and $Re_\tau = 4357$; (–), [114], $Re_\tau = 445-690$; (- -), [115], $Re_\tau = 500$ and $Re_\tau = 800$; (- · -), [116], $Re_\tau = 550 - 2003$.

Streamwise space-time correlation and mean convection velocity

Fig. 6.10 shows the results for streamwise space-time correlation for p'_{ms}, p'_{tt} and p'_{total} according to Eq. (6.8) with $p'(\mathbf{x}, t)$ derived from Eq. (6.6). The analysis for the two-point statistics herein and the rest of the thesis is based on the results from the $Ma = 0.1$ flow. The correlation for p'_{tt} drops off much faster than for p'_{ms}, because the turbulence decay acts stronger on the second-order turbulence-turbulence term. The correlation decay for p'_{total} is in between p'_{ms} and p'_{tt} and follows as a weighted average from the two parts. The correlation curves become broader with the increasing streamwise distance (r_1) of the sensors. This is because the smaller eddies close to the wall with lower velocities decay

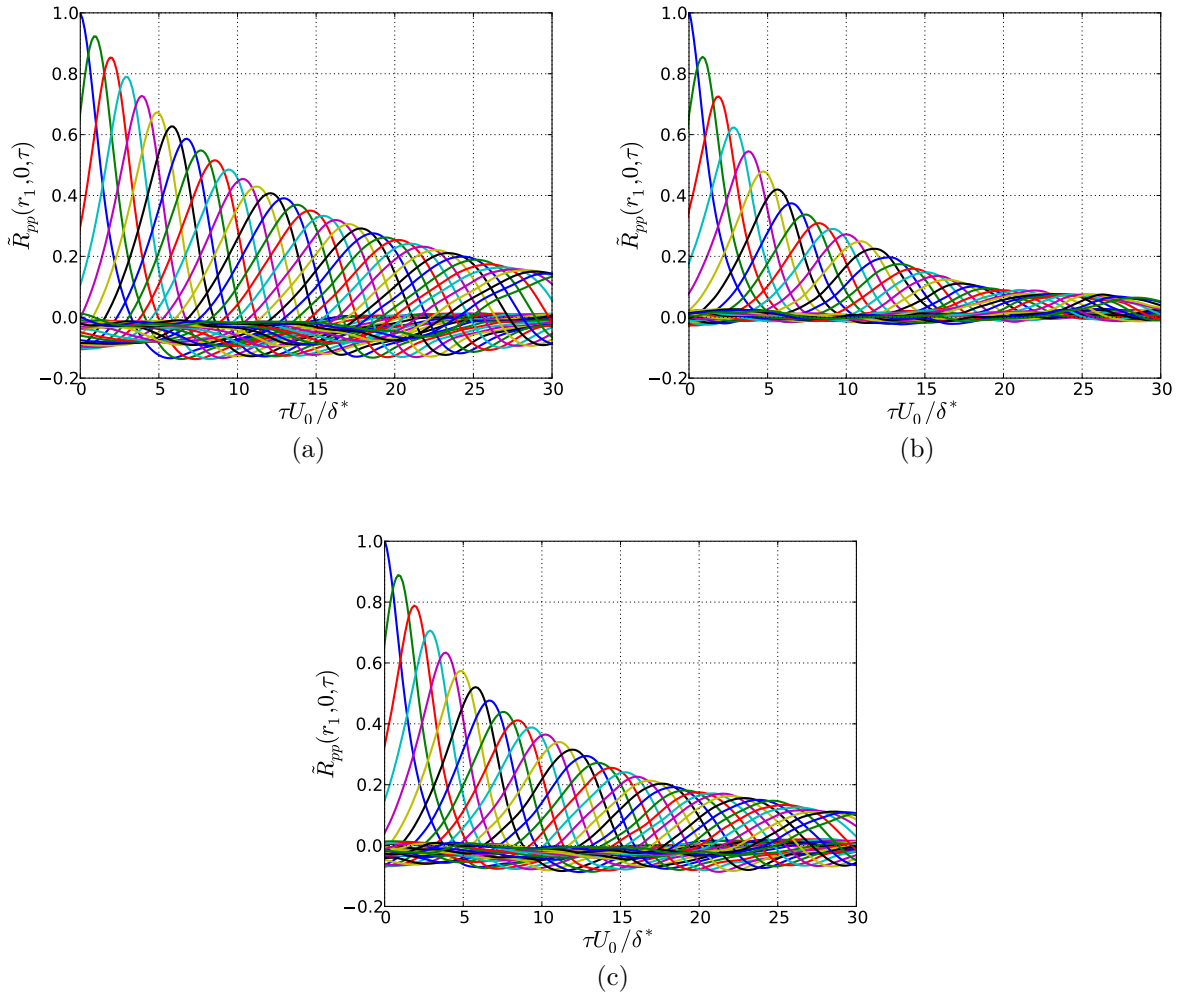

Figure 6.10: Normalized streamwise space-time correlation as a function of $\tau U_0/\delta^*$ for fixed space increments, $r_1 = 0.68\delta^* - 25\delta^*$ with increment of $0.68\delta^*$; (a) mean-shear contribution to $\tilde{R}_{pp}(r_1, 0, \tau)$; (b) turbulence-turbulence contribution to $\tilde{R}_{pp}(r_1, 0, \tau)$; (c) combined contribution to $\tilde{R}_{pp}(r_1, 0, \tau)$.

stronger than the larger eddies with higher velocities. Consequently, the correlation at larger r_1 is rather dominated by the larger eddies.

The mean convection velocity $\overline{U}_c$ can be estimated by using the time shift τ of the maximum correlation for a fixed distance r_1, $\overline{U}_c(r_1) = r_1/\tau(r)$. The results shown in Fig. 6.11(a) illustrate a growth of $\overline{U}_c$ with increasing distances. This indicates the larger eddies with higher velocities dominate progressively at larger r_1. The trend for p'_{total} fits well to the measured results from Bull [6] and Blake [7] at larger distances, however, at closer distances $r_1/\delta^* < 5$ the present results show larger velocities. The reason is the lack of energy at higher frequencies in the present calculation, since the small eddies moving with lower speed are primarily responsible for the higher frequency range. However, at the very closest distance the convective velocity goes up. The reason for that is not clear to the author. In general, the convective velocity for p'_{tt} shows a larger value than p'_{ms}, which may indicate that the source for p'_{tt} for the wall pressure fluctuations at low and medium frequencies is located a little farther away from the wall than the source for p'_{ms}.

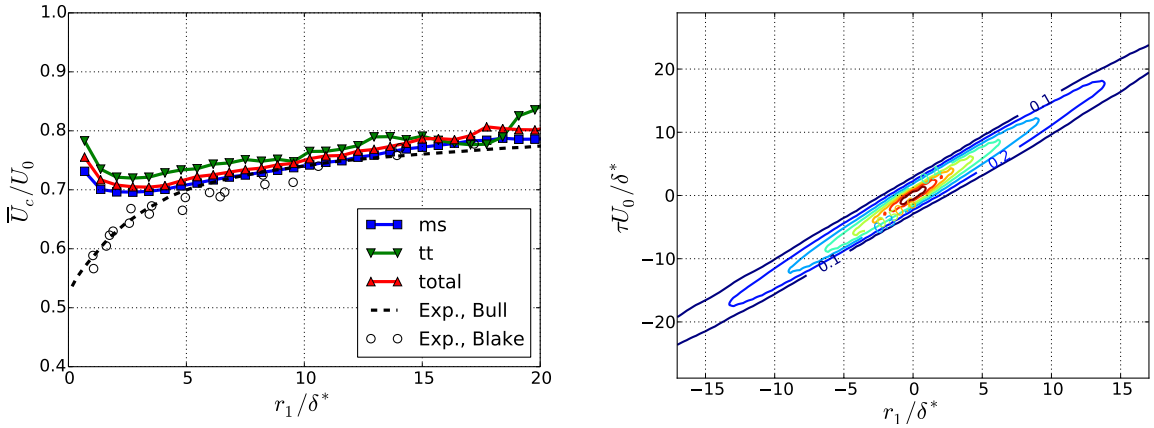

(a) (b)

Figure 6.11: (a) Mean convective velocity $\overline{U}_c(r_1)$; (b) contour plot of normalized streamwise space-time correlation.

Fig. 6.11(b) shows the contour plot of streamwise space-time correlation for p'_{total}. The iso-contour lines have an elongated shape with two distinct apexes of specific distance r_1/δ^* to the origin of the plot. Contours of different apex distances appear slightly rotated to one another in the counter clockwise sense upon stepping up contour levels, representing a growing convection velocity with increasing distance r_1/δ^*. The asymmetrical and broadened correlation at larger r_1 known from experimental results can also be seen in this contour plot.

Spatial correlation

For $\tau = 0$, we can calculate the spatial correlation $\tilde{R}_{pp}(r_1, r_3, 0)$. Results shown in Fig. 6.12 represent similar contour shapes for p'_{ms} and p'_{total}. Their contour plots illustrate an elongated shape of iso-correlated curves in the spanwise direction and a negative correlation region in the streamwise direction. In contrast, p'_{tt} exhibits isotropic correlation characteristics. The results for p'_{total} show good agreement with the data by Bull [6], Viazzo *et al.* [31] and Gloerfelt & Berland [58].

Plots of streamwise and spanwise correlation are shown in Fig. 6.13. In the spanwise direction the correlation of p'_{tt} is much shorter than p'_{ms}. An overshoot with negative value of p'_{ms} is present in the flow direction. This is caused by the streamwise derivative of the velocity fluctuations u'_2. The correlation $< p'u'_2 >$ yields a value of zero for a point underneath the vortex core at the wall and exhibits an odd-shaped distribution in streamwise direction relative to point zero. After reaching the maximum the correlation drops slowly down to zero. As a consequence of this shape, the correlation $< p\partial u'_2/\partial x_1 >$ exhibits a 'mexican hat' shape in up- and downstream directions and therefore yields negative dips for the streamwise spatial wall pressure correlation.

Fig. 6.14 shows the comparison between different turbulence approaches for the streamwise and spanwise correlations. For the anisotropic turbulence, an increase in the streamwise direction and a decrease in the spanwise direction of the correlation are found compared to the isotropic case.

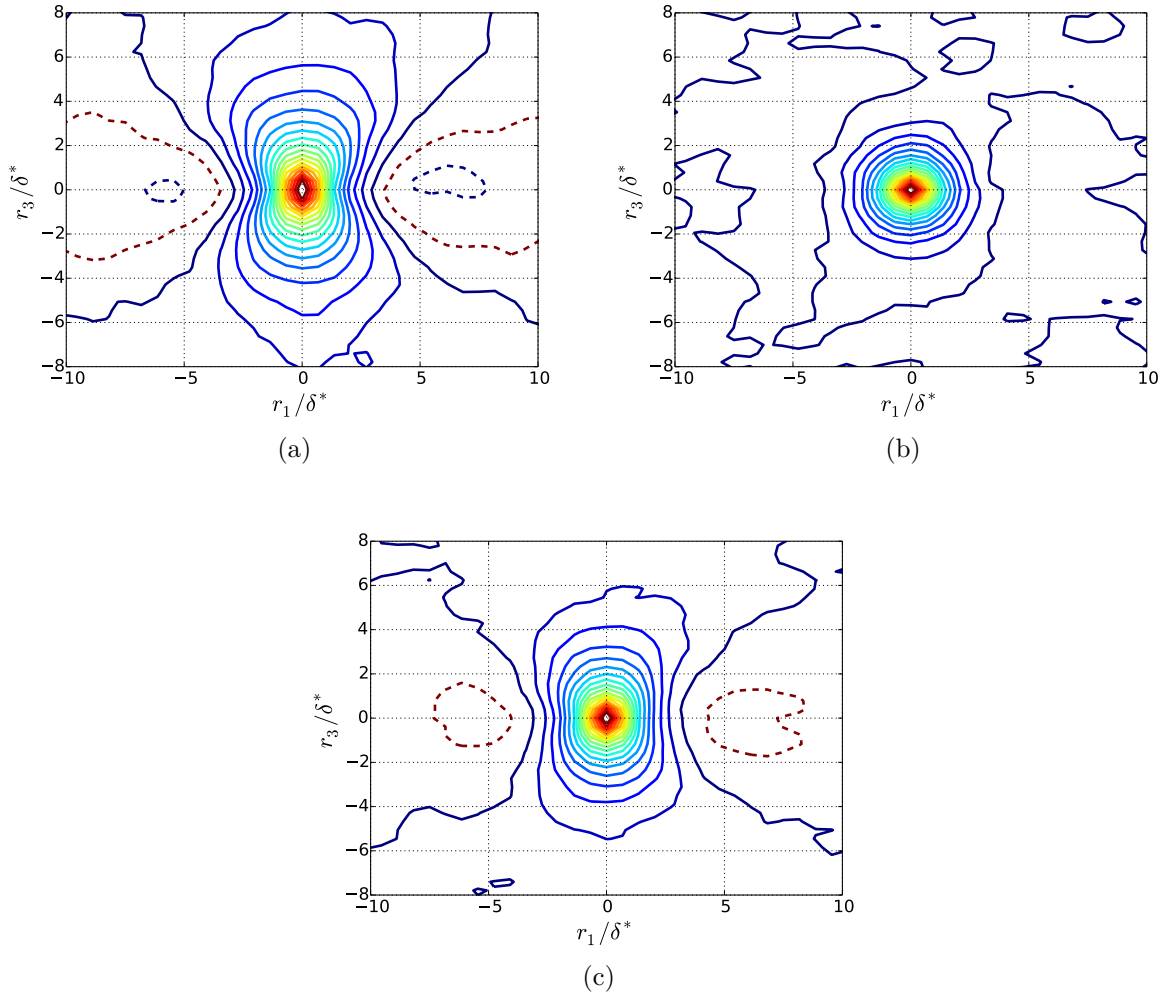

Figure 6.12: Contour plots of normalized spatial correlation; (-), iso-contours, 0 to 0.9 with increment of 0.05; (- -), iso-contours, -0.05 and -0.1; (a) mean-shear contribution to $\tilde{R}_{pp}(r_1, r_3, 0)$; (b) turbulence-turbulence contribution to $\tilde{R}_{pp}(r_1, r_3, 0)$; (c) combined contribution to $\tilde{R}_{pp}(r_1, r_3, 0)$.

6.1.6 Cross-spectra and phase velocities

Cross-spectra are calculated by taking Fourier transform of τ for the space-time correlation $R_{pp}(\mathbf{x}, \mathbf{r}, \tau)$. Based on the Fourier transform as specified in Appendix A, the cross-spectrum reads,

$$\Phi_{pp}(\mathbf{x}, \mathbf{r}, \omega) = \frac{1}{2\pi} \int_{-\infty}^{\infty} R_{pp}(\mathbf{x}, \mathbf{r}, \tau) \exp(-i\omega\tau)\, \mathrm{d}\tau. \tag{6.9}$$

If $\mathbf{r} = 0$, we obtain the one-point spectrum $\Phi_{pp}(\mathbf{x}, \omega)$ at location $\mathbf{x}$. The coherence spectrum is defined by

$$\Gamma(\mathbf{x}, \mathbf{r}, \omega) = \frac{\Phi_{pp}(\mathbf{x}, \mathbf{r}, \omega)}{\sqrt{|\Phi_{pp}(\mathbf{x}, \mathbf{0}, \omega)|}\sqrt{|\Phi_{pp}(\mathbf{x}, \mathbf{r}, \omega)|}}, \tag{6.10}$$

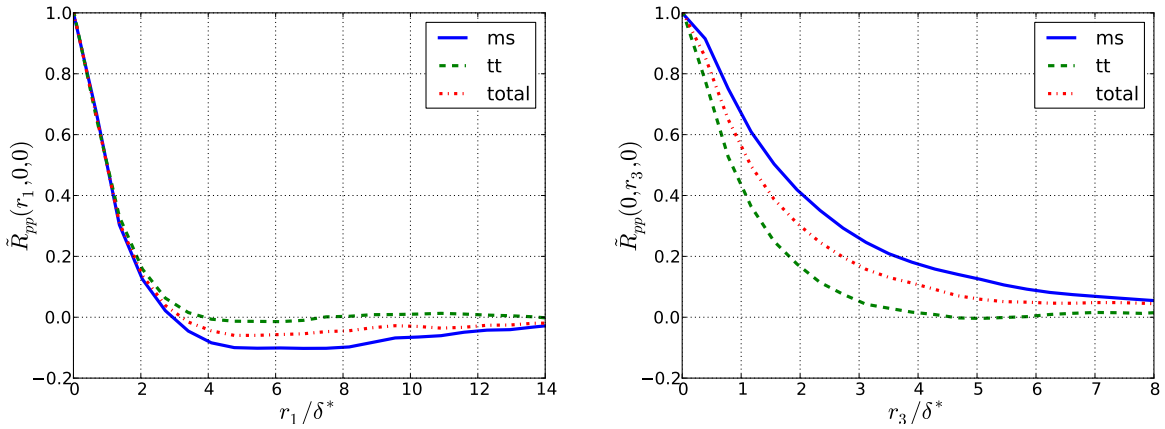

Figure 6.13: Normalized spatial correlation for p'_{ms}, p'_{tt} and p'_{total}; (a) streamwise spatial correlation $\tilde{R}_{pp}(r_1,0,0)$; (b) spanwise spatial correlation $\tilde{R}_{pp}(0,r_3,0)$.

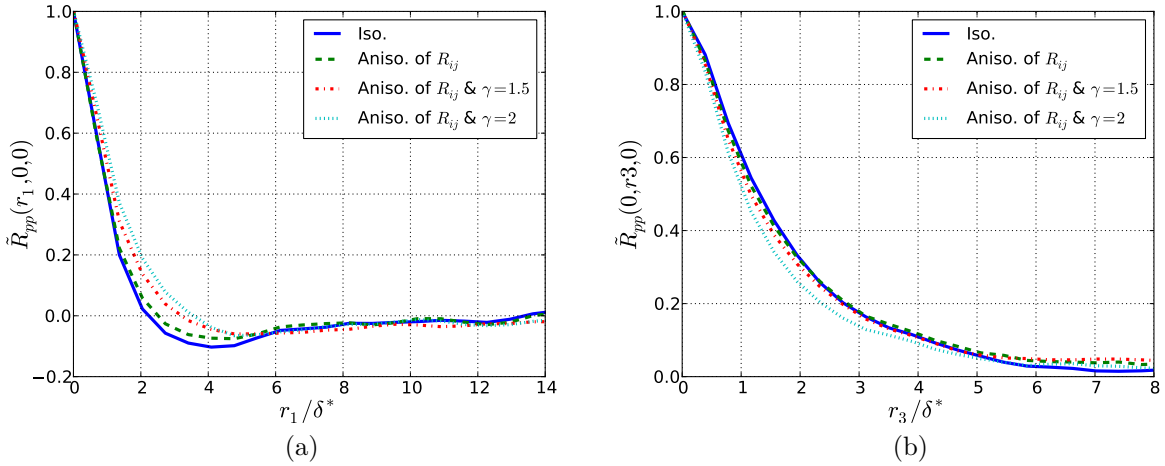

Figure 6.14: Normalized spatial correlation for p'_{total} with different turbulence approaches; (a) streamwise spatial correlation $\tilde{R}_{pp}(r_1,0,0)$; (b) spanwise spatial correlation $\tilde{R}_{pp}(0,r_3,0)$.

and the phase velocity can be calculated by

$$U_c(r_1,\omega) = \frac{r_1\omega}{\theta(r_1,\omega)}, \tag{6.11}$$

where $\theta(r_1,\omega)$ is the phase difference of $\Gamma(r_1,0,\omega)$. Phase velocities and coherence are calculated with a window length of 512 samples, resulting a frequency resolution of approximately 98Hz. The velocities increase first and after arriving at the maximum fall gradually at higher frequencies, as shown in Fig 6.15. The small U_c at low frequencies may be caused by the contributions of the small eddies close to the wall moving with slower velocities. The maximum U_c/U_0 reaches approximately 0.8 and occurs in the region where the highest energy of the wall pressure fluctuations is contained. Similar trends were measured by Farabee & Casarella [8] and Leclercq & Bohineust [9] and also in the present

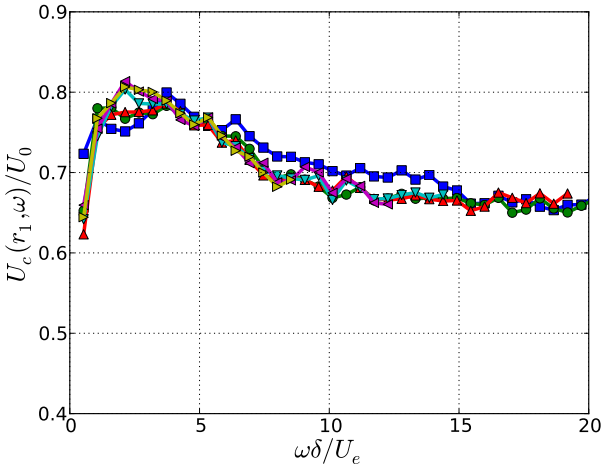

Figure 6.15: Phase velocities as a function of $\omega\delta/U_e$ for fixed space increments, $r_1 = 1.36\delta^* - 8.18\delta^*$ with increment of $1.36\delta^*$;

work, refer to Fig. 4.10. In their measurements lower phase velocities for smaller distances were reported. The reason is that the eddies closer to the wall move with a slower velocity and die out over a shorter distance. They contribute to the wall pressure fluctuations not only at high frequencies but also at low frequencies. Thus, a slower velocity over a broadband frequency range was measured at a closer distance. This effect is not or only weakly present in the calculated results due to the lack of the contribution from the slowly moving small eddies.

Fig. 6.16 and Fig. 6.17 show the streamwise, $\mathbf{r} = r_1 \cdot \mathbf{e}_1$, and the spanwise coherence, $\mathbf{r} = r_3 \cdot \mathbf{e}_3$, as a function of $\omega r_{1,3}/U_c(r_1, \omega)$. In the spanwise direction $U_c(\omega)$ determined for the closest distance is used. At larger value of $\omega r_{1,3}/U_c$ the results seem to collapse together. The coherence function can be described using exponential functions (Corcos's model [51], addressed in section 2.2),

$$|\Gamma(r_1, r_3, \omega)| = \exp(-\alpha\omega r_1/U_c)\exp(-\beta\omega r_3/U_c), \tag{6.12}$$

where α and β are empirically determined decay constants for the streamwise and spanwise directions. In Fig. 6.16 a dashed line with $\alpha = 0.125$ is plotted, whose value is obtained from Farabee & Casarella [8] and the present experimental results in this work measured at a comparable Reynolds number. The value of β is found between 0.7-0.72 from the literature [6, 50] and the present experimental results in this work. The present results for coherence show good agreement with the results from the literature.

The comparison between p'_{ms} and p'_{tt} show that the coherence decays stronger for p'_{tt} than for p'_{ms} in both streamwise and spanwise directions. This impacts the results for p'_{total} for different turbulence approaches due to the different ratio of p'_{ms} and p'_{tt}. In general, the more the p'_{tt} term contains, the stronger the coherence decays. The value of α is found between $0.9 - 1.35$ for the isotropic turbulence approach and the anisotropic turbulence with stretching factor $\gamma = 2$, and β is between $0.45 - 0.72$. The spanwise coherence is also impacted by the length scale stretching and its coherence decreases as the stretching factor γ increases.

Note that, at low values of $\omega r_{1,3}/U_c$ the curves do not follow the Corcos model approach-

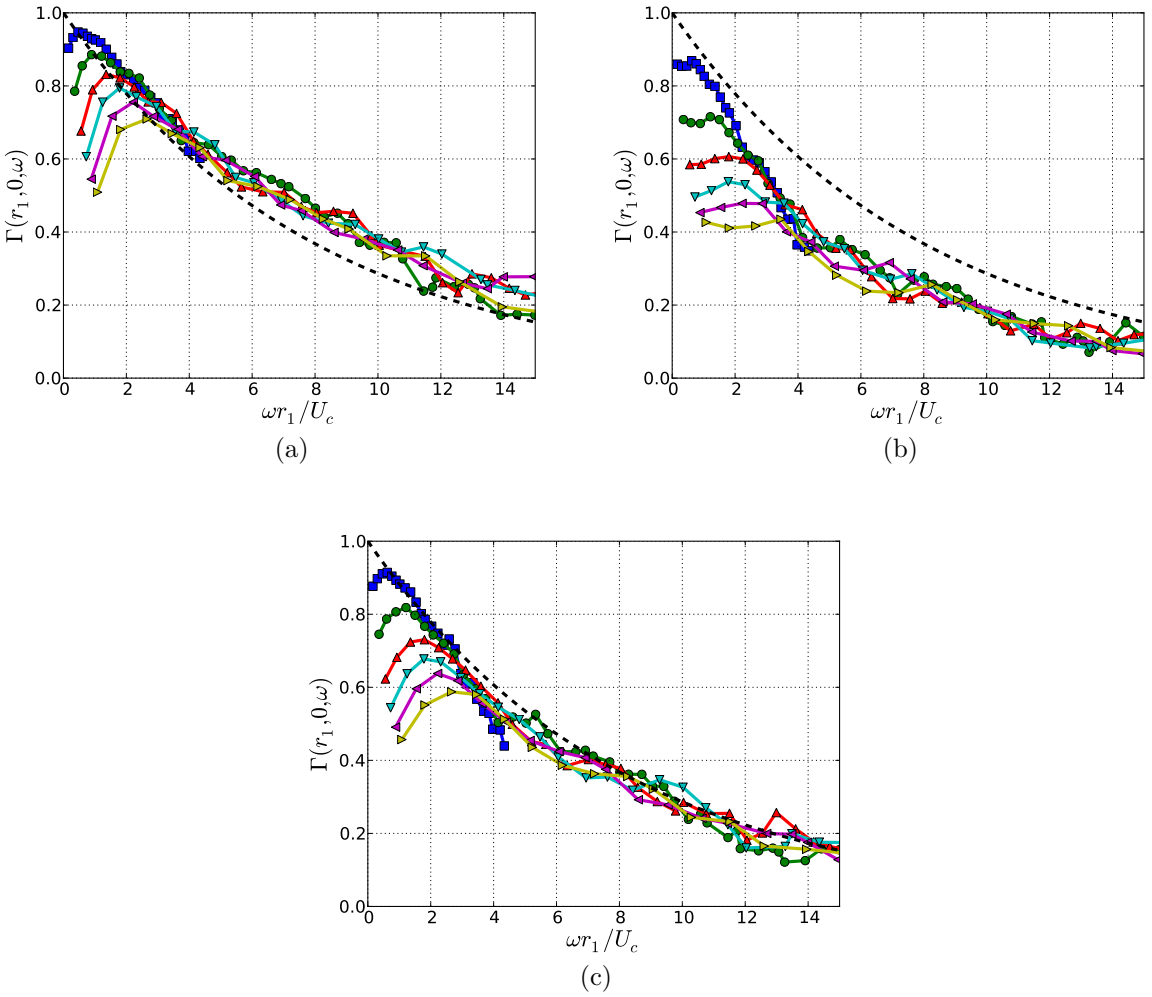

Figure 6.16: Streamwise coherence as a function of $\omega r_1/U_c$ for fixed space increments, $r_1 = 1.36\delta^* - 8.18\delta^*$ with increment of $1.36\delta^*$; (- -), $\exp(-\alpha\omega r_1/U_c)$ with $\alpha = 0.125$; (a) coherence for p'_{ms}; (b) coherence for p'_{tt}; (c) coherence for p'_{total}.

ing 1, but rather decay. Besides the explanation argued by Farabee & Casarella [8] that this is a physical requirement from the pressure fluctuation field (addressed in section 2.2). Another explanation could be that not only the outer region but also the inner region of the boundary layer contributes significantly to the wall pressure fluctuations at low frequencies, refer to Fig. 6.6. Therefore, the decay of the small eddies close to the wall can accelerate the coherence loss at low frequencies.

6.1.7 Wavenumber-frequency spectra

Wavenumber-frequency spectra are calculated by taking the spatial Fourier transform of the cross-spectra,

$$\Phi_{pp}(k_1, k_3, \omega) = \frac{1}{(2\pi)^2} \int_{-\infty}^{\infty} \int_{-\infty}^{\infty} \Phi_{pp}(r_1, r_3, \omega) \exp(ik_1 r_1) \exp(ik_3 r_3) \, \mathrm{d}r_1 \, \mathrm{d}r_3. \tag{6.13}$$

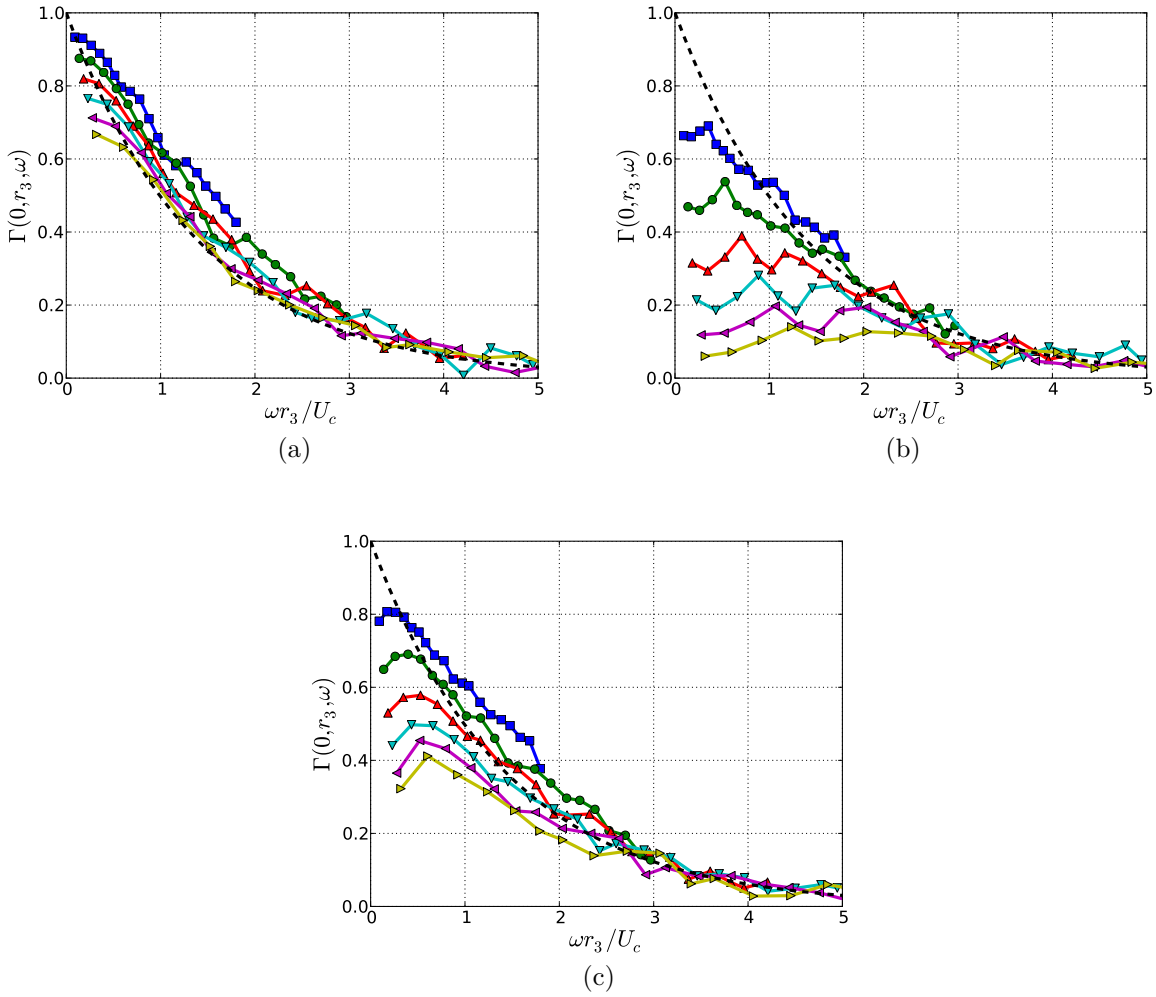

Figure 6.17: Spanwise coherence as a function of $\omega r_1/U_c$ for fixed space increments, $r_3 = 0.78\delta^* - 2.73\delta^*$ with increment of $0.39\delta^*$; (- -), $\exp(-\beta\omega r_1/U_c)$ with $\beta = 0.7$; (a) coherence for p'_{ms}; (b) coherence for p'_{tt}; (c) coherence for p'_{total}.

The resolution of the wavenumber domain is defined by $\Delta k_1 = 2\pi/L_1$ and $\Delta k_3 = 2\pi/L_3$, where L_1 and L_3 is the streamwise and spanwise array size of the calculation domain for the wavenumber-frequency spectra analysis. In the simulation a virtual microphone array is used with spatial extensions $L_1 \approx 177$ mm and $L_3 \approx 99$ mm. The corresponding values $\Delta k_1 \approx 17.7$ (m^{-1}) (coherence in both upstream and downstream directions are considered) and $\Delta k_3 \approx 63.5$ (m^{-1}) are too coarse to provide a proper resolution. Unfortunately, the convective ridge is located at a relatively low wavenumber range especially for low frequencies, e.g. at $f = 300$ Hz gives $k_1 = \omega/U_c \approx 67$ (m^{-1}). To reduce the resolution problem, the calculation domain was extended to a spatial extension $L_1 \approx 1062$ mm and $L_3 \approx 396$ mm with zero padding in the appended domain.

2-D wavenumber-frequency spectra $\Phi_{pp}(k_1, \omega)$ can be obtained by integrating over k_3,

$$\Phi_{pp}(k_1, \omega) = \int_{-\infty}^{\infty} \Phi_{pp}(k_1, k_3, \omega)\, \mathrm{d}k_3. \tag{6.14}$$

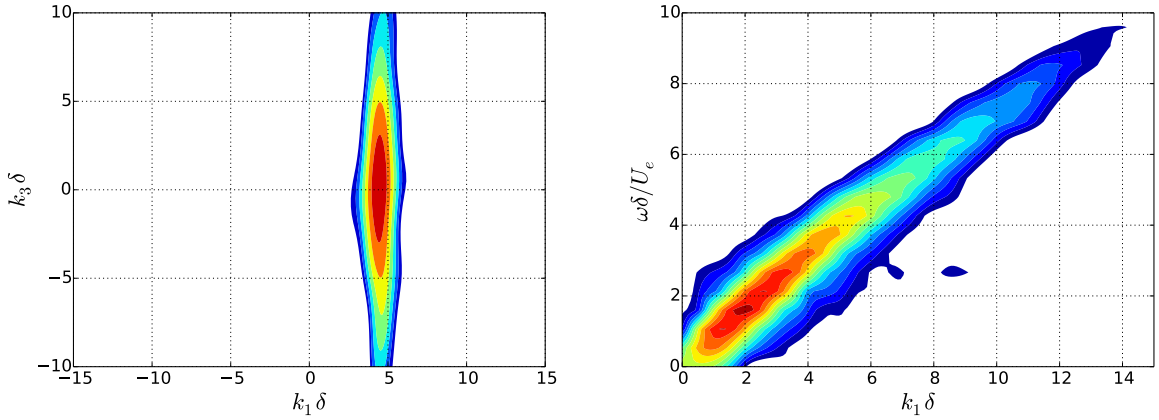

Figure 6.18: (a) Contour plots of wavenumber-frequency spectra $\Phi_{pp}(k_1, k_3, \omega)$ at 686 Hz with levels between -86 dB and -79 dB; (b) contour plots of wavenumber-frequency spectra $\Phi_{pp}(k_1, \omega)$ with levels between -72 dB and -59 dB.

Fig. 6.18(a) shows the contour plot of $\Phi_{pp}(k_1, k_3, \omega)$ for p'_{total} at $f = 686$ Hz. The convective ridge is well identified and shows good agreement with the measured data by Arguillat *et al.* [13] and Ehrenfried & Koop [14]. The maximum of the convective ridge is located at $k_1\delta \approx 4.4$, which yields the corresponding convective velocity $U_c \approx 0.83U_0$. The value shows good agreement with the result obtained by the phase velocities which provides $U_c \approx 0.8U_0$ at $f = 686$ Hz ($\omega\delta/U_e \approx 3.7$). The 2-D spectra $\Phi_{pp}(k_1, \omega)$ in Fig. 6.18(b) reveal the convective nature of the wall pressure fluctuations. The main energy centres at $k_1 \approx \omega/U_c$. The shape of the contour twists to a lower value of $\omega\delta/U_e$ at larger $k_1\delta$, which implies a slower convective velocity at higher frequencies.

1-D spectra of $\Phi_{pp}(k_1, 0, \omega)$ and $\Phi_{pp}(k_1, \omega)$ for single frequencies between 98 Hz $\leq f \leq$ 686 Hz are shown in Fig. 6.19. The spectra tend to be flat at very low wavenumbers of k_1. This feature was also simulated by Viazzo *et al.* [31] and Gloerfelt & Berland [58]. The dominant energy is located at larger $k_1\delta$ for higher frequencies, which corresponds to the convection velocities.

6.2 Application for different cases

6.2.1 Test cases and computational setups

The mean flow statistics are obtained from RANS calculations using DLR's CFD code TAU. The Reynolds stress model with g-equation is used for the computation [117]. The boundary layer is solved on a structured grid with the first cell layer $y^+ < 1$. In total, about 100K grid points are used for the ZPG case and 130K for the APG case, where a grid with 200 nodes is distributed along the airfoil's upper and lower side respectively. Fig. 6.20 shows a sketch of the computational domain. The length of the whole plate is 1370 mm with a leading edge length of 120 mm. A 12° beveled trailing edge on the underside of the plate is used to develop a ZPG boundary layer on the topside in the rear area [91]. For the APG case, a NACA 0012 airfoil with a chord length of 400 mm is placed

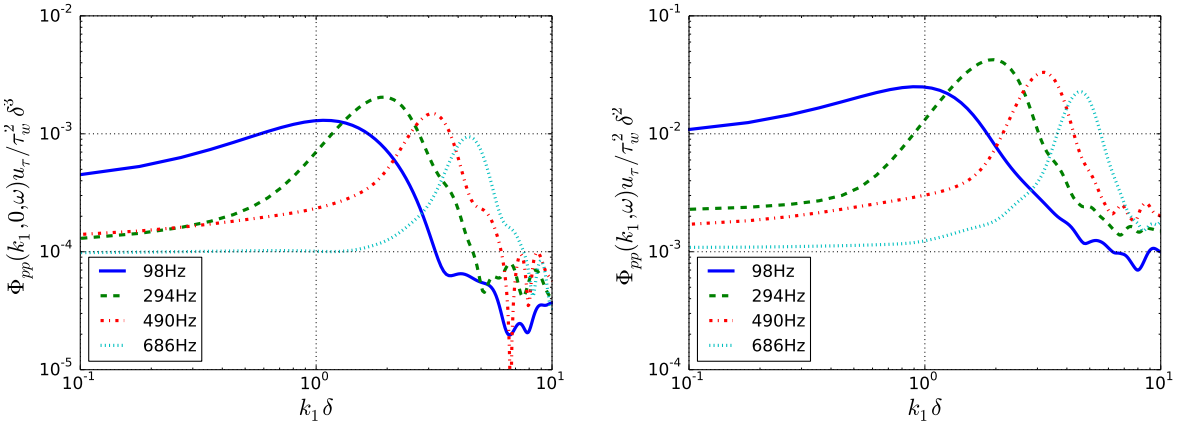

(a) (b)

Figure 6.19: Wavenumber-frequency spectra between 98 Hz and 686Hz; (a) $\Phi_{pp}(k_1, 0, \omega)$; (b) $\Phi_{pp}(k_1, \omega)$.

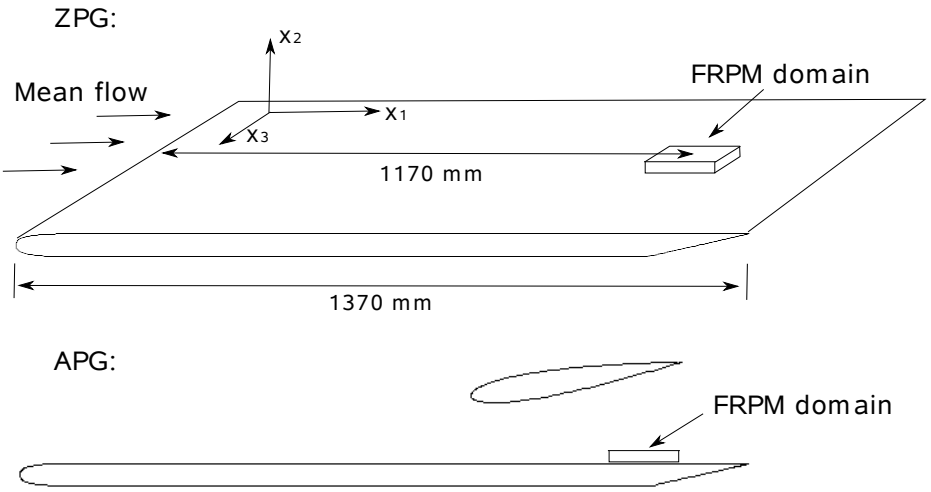

Figure 6.20: Sketch of the computational domain for the ZPG flow (top) and the side view for the APG flow (down).

above the flat plate. The rotation axis is at 41% of the chord length. The geometries for the flat plate and the NACA airfoil are identical to those from the experiment, refer to section 3.1.

The wall fluctuating pressure beneath the boundary layer is calculated in a 3-D rectangular FRPM domain with its center located at $x_1 = 1170$ mm, see Fig. 6.20. The dimensions of the FRPM domain is $L_1 = 127$ mm, $L_2 = 21$ mm and $L_3 = 63$ mm. Since the Hockney method demands a grid with 2^N mesh points in each direction, a cartesian grid with $128 \times 64 \times 64$ points is used in the calculation. The corresponding mesh size is $\Delta x_1 = \Delta x_3 = 1$ mm and $\Delta x_2 = 1/3$ mm. The calculated boundary layers have similar boundary layer thicknesses, thus, a same sized FRPM domain is used for all the calculation cases. Calculations were carried on a desktop computer equipped with Intel Xeon

Table 6.2: Comparison of the boundary layer parameters between the results from RANS calculations and the experiment.

	U_0 (m/s)	δ (mm)	δ^* (mm)	θ (mm)	H	u_τ (m/s)	$Re_\theta = U_0\theta/\nu$
ZPG for two different velocities, $x_1 = 1210$ mm							
RANS	30.1	20.0	3.34	2.42	1.38	1.16	4737
Experiment	30.2	19.7	3.51	2.49	1.41	1.13	4889
RANS	58.8	17.9	2.90	2.15	1.35	2.15	8230
Experiment	58.7	18.5	3.13	2.28	1.37	2.08	8685
APG, $x_1 = 1128$ mm							
RANS	32.9	15.6	3.32	2.09	1.59	0.83	4464
Experiment	32.0	23.0	5.09	3.12	1.63	0.88	6492
APG, $x_1 = 1210$ mm							
RANS	30.4	19.7	5.05	2.93	1.72	0.64	5772
Experiment	30.4	28.7	7.68	4.39	1.75	0.75	8670

E5-2630V3 processors. For each case, 4 CPUs (8 threads) was used and about 13000 steps can be calculated per day. The time steps were chosen based on the 'CFL'-like constraint of FRPM, i.e. $\Delta t = 3.21 \times 10^{-5}$ for the case of ZPG for 30.1 m/s, $\Delta t = 1.66 \times 10^{-5}$ for the case of ZPG for 58.8 m/s and $\Delta t = 2.92 \times 10^{-5}$ for the case of APG. In the present work, a one-second simulation was made for each case. The computation time is about 2.5 days for the case with the largest time step and less than 5 days for the case with the finest time step.

The mean velocity profiles were measured at $x_1 = 1210$ mm for ZPG and APG boundary layers and an additional point at $x_1 = 1128$ mm for the APG boundary layer. The normalized mean flow velocity profiles from RANS calculations are compared to the measured profiles, shown in Fig. 6.21. Results from RANS calculations show good agreement with the measured results. Boundary layer parameters obtained from both RANS calculations and the experiment are listed in table 6.2. Note that, the boundary layer thickness for the APG boundary layer does not match the experimental results. The calculated boundary layer thickness is much thinner than the measured one. This is mainly because the present RANS calculations do not take the open jet wind tunnel environment into account. The presence of the shear layer in the open jet wind tunnel seems to be important for the APG case calculation due to the additional NACA airfoil, although the measured static pressure in the spanwise direction ($\Delta x_3 = 180$ mm at $x_1 = 1110$ mm) showed an almost 2-D flow condition in the mid-span region, refer to C.3 in Appendix C. For the APG calculation case, modifications of the airfoil position are made in order to obtain a similar boundary layer development between $1128 < x_1 < 1210$ mm. In the calculation the rotation axis of the airfoil is located 150 mm above the flat plate while in the measurement 120 mm. The geometric AOA of the airfoil is 9° in the calculation while 10° in the measurement.

Comparisons of the turbulence kinetic energy and the Reynolds stress components between RANS calculations and measurement results at $x_1 = 1210$ mm are shown in Fig. 6.22. For the APG case the kinetic energy was only measured at $x_1 = 1210$ mm in the experiment. In general, the turbulence kinetic energy obtained from RANS calculations show good agreement to the measured data. However, a more rapid decrease trend in

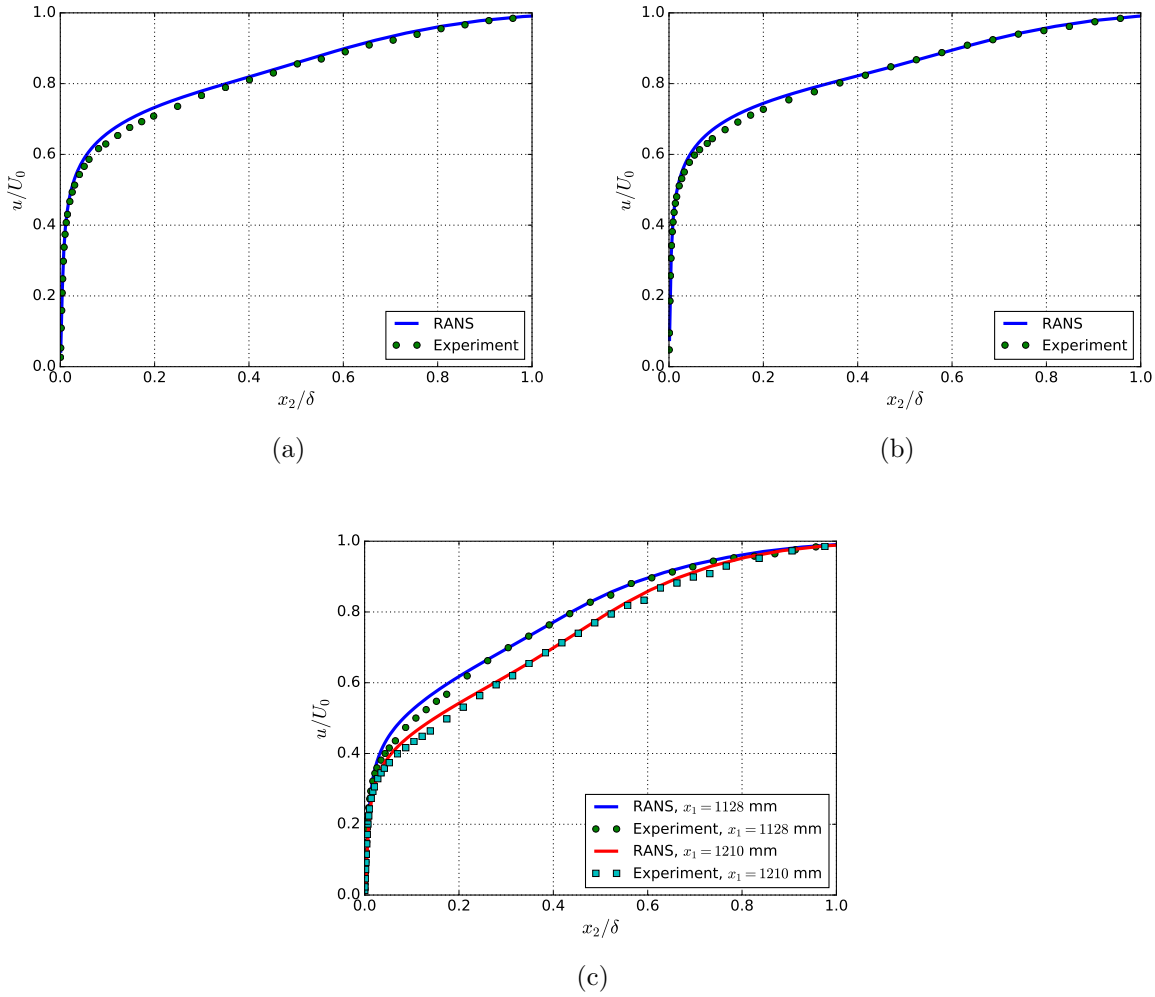

Figure 6.21: Comparison of the normalized mean velocity profiles between RANS calculations and the experimental results; (a) ZPG for 30.1 m/s at $x_1 = 1210$ mm; (b) ZPG for 58.8 m/s at $x_1 = 1210$ mm; (c) APG at $x_1 = 1128$ mm and 1210 mm.

the outer region $x_2 > 0.5\delta$ is shown. One reason may be the nearly zero turbulence intensity outside the boundary layer in the calculation domain. This forces the kinetic energy to approach zero at the boundary layer edge while in the measurement the free-stream flow has a larger turbulence intensity. The position of the maximum kinetic energy for the APG boundary layer is well predicted from the RANS calculation, however, the level is larger compared to the measurement. This may be caused by the thinner boundary layer obtained from the RANS calculation. The comparison of the Reynolds stresses shows that for the ZPG cases, r_{22} and r_{33} from the RANS calculations are over-estimated in the near wall region, whereas the r_{11} is under-estimated. A good agreement with the measured results is found for r_{12}. The components $r_{13} = 0$ and $r_{23} = 0$ within a 2-D boundary layer [98]. For the APG case all the components are over-estimated due to the reason discussed previously. It should be mentioned that the Reynolds stresses were measured using hot-wire X-probes with an jaw angle of about 6° to the flow direction. The measured r_{11} and r_{22} were corrected with the angle correction. However, the value of r_{33} cannot be

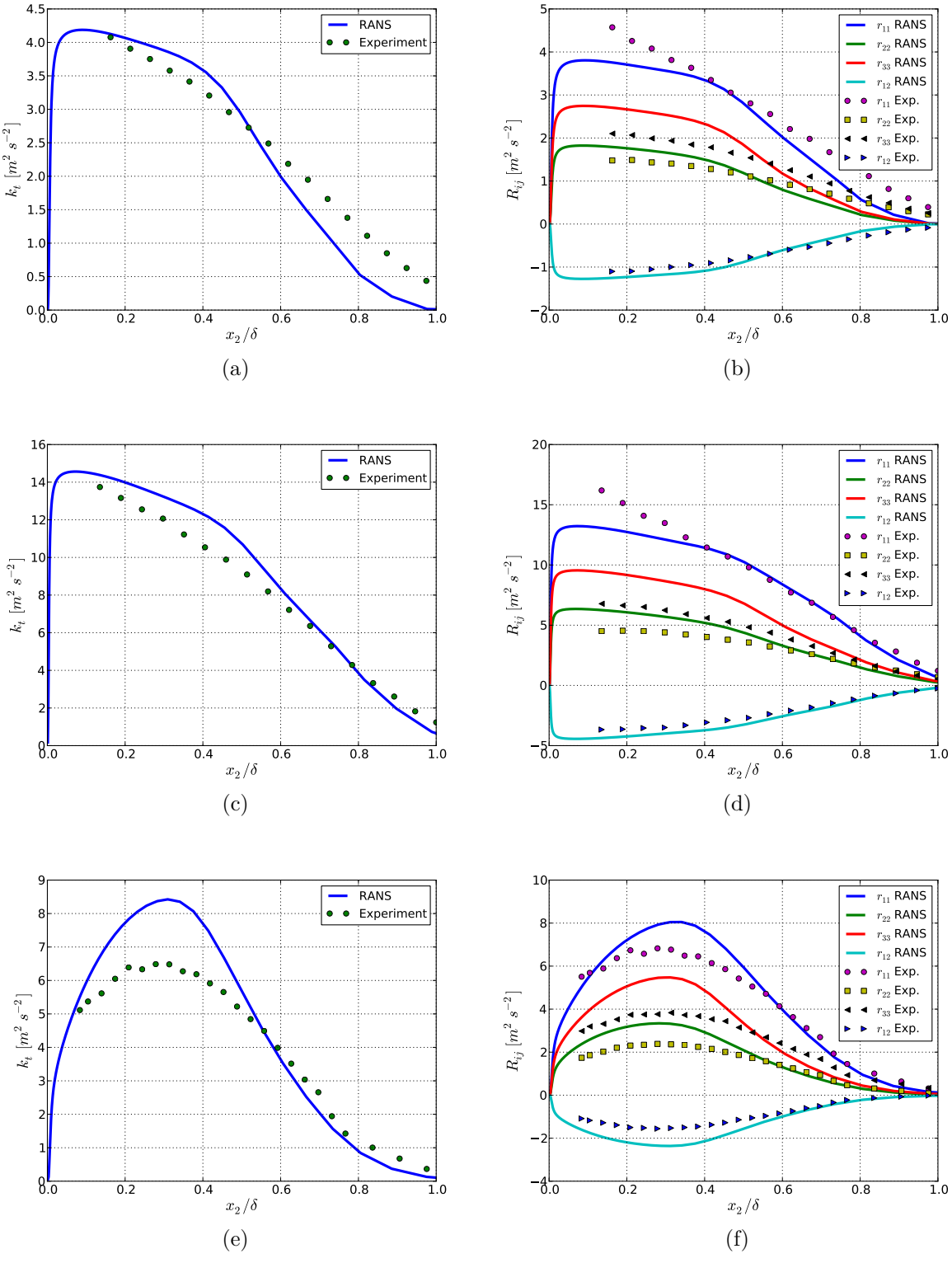

Figure 6.22: Comparison of the turbulent kinetic energy and the Reynolds stress tensors between RANS calculations and experimental results at $x_1 = 1210$ mm; (a,b) ZPG for 30.1 m/s; (c,d) ZPG for 58.8 m/s; (e,f) APG.

corrected, which can produce some measurement uncertainties.

6.2.2 One-point spectra

The wall pressure one-point spectra are calculated according to Eq. (6.6). Figure 6.23 shows the simulated one-point spectra of p'_{total}, p'_{ms} and p'_{tt} for the different cases. The one-point spectra herein are analyzed with a window length of 512 samples for all the cases. The sampling rate is about 31.2 kHz and 60.2 kHz for ZPG with $U_0 = 30.1$ m/s and $U_0 = 58.8$ m/s and 34.2 kHz for the APG case, which results in a frequency resolution of approximately 61 Hz and 118 Hz for the ZPG cases and 67 Hz for the APG case. The obtained one-point spectra have the same features as the results shown in section 6.1.3. The spectra of p'_{ms} show a maximum at medium frequencies and an increasing behavior at low frequencies. In contrast to p'_{ms}, spectra of p'_{tt} show a rather flat behavior at lower frequencies. A comparison between the isotropic and anisotropic turbulence approaches for ZPG case at $U_0 = 30.1$ m/s is given between Figs. 6.23(a,b). For an isotropic turbulence boundary layer, the results show p'_{ms} to be the dominant contribution to the wall pressure fluctuations and the level difference at the spectral peak position between p'_{ms} and p'_{tt} is about 5 dB. However, when the turbulence anisotropy (both the Reynolds stress and the turbulence length scales) is taken into account, the level difference becomes smaller and is about only 2 dB at the spectral peak position. The scaled spectra for ZPG cases with different velocities collapse well for all pressure fluctuation parts, i.e. p'_{ms}, p'_{tt} and p'_{total}. The spectral level for the APG case increases and for both p'_{ms} and p'_{tt} compared to the ZPG case with a comparable velocity, see Figs. 6.23(b,f). One major reason for the increase of the level is the increase of the velocity fluctuations level. In general, $p'_{ms} \sim u'_2$ and $p'_{tt} \sim u'_i u'_j$, i.e. p'_{tt} increases faster than p'_{ms} due to the increase of the velocity fluctuations level. However, the difference of the spectral maximum level between p'_{ms} and p'_{tt} for the APG case has not become smaller than for the ZPG case. This can be explained by the fact that the APG boundary layer has a larger mean flow gradient $\partial\overline{u}_1/\partial x_2$ in the region $0.1 < x_2/\delta < 0.3$ than the ZPG boundary layer, where the contribution plays a major role on the spectral peak, and a larger $\partial\overline{u}_1/\partial x_2$ leads to a larger level of p'_{ms}.

The simulated spectra of p'_{total} calculated with the anisotropic turbulence approach are compared to the experimental results, shown in Fig. 6.24. The spectral trends at low and medium frequencies and the maximum level of the simulated spectra are well predicted. However, the simulated spectra drop too fast at high frequencies. This is primarily due to the lack of reconstructed kinetic energy in the near wall region, which contributes mostly to high frequencies. This behaviour is also shown for the generic test case in section 6.1.3. Note that, the RANS calculation over-predicts the kinetic energy level for the APG case, which can lead to an over-prediction of the spectral level. However, the boundary layer thickness for the simulated APG boundary layer is much thinner than in the measured case, which can cause a spectral shift to higher frequencies and a possible spectral level decrease. In any case, the development of the APG spectra which shift to lower frequencies in the downstream direction is well represented.

6.2.3 Cross-spectra and convective velocities

The cross spectra are calculated according to Eq. (6.10). A window length of 256 samples for all the cases is used to evaluate the cross-spectra. The measured empirical constants

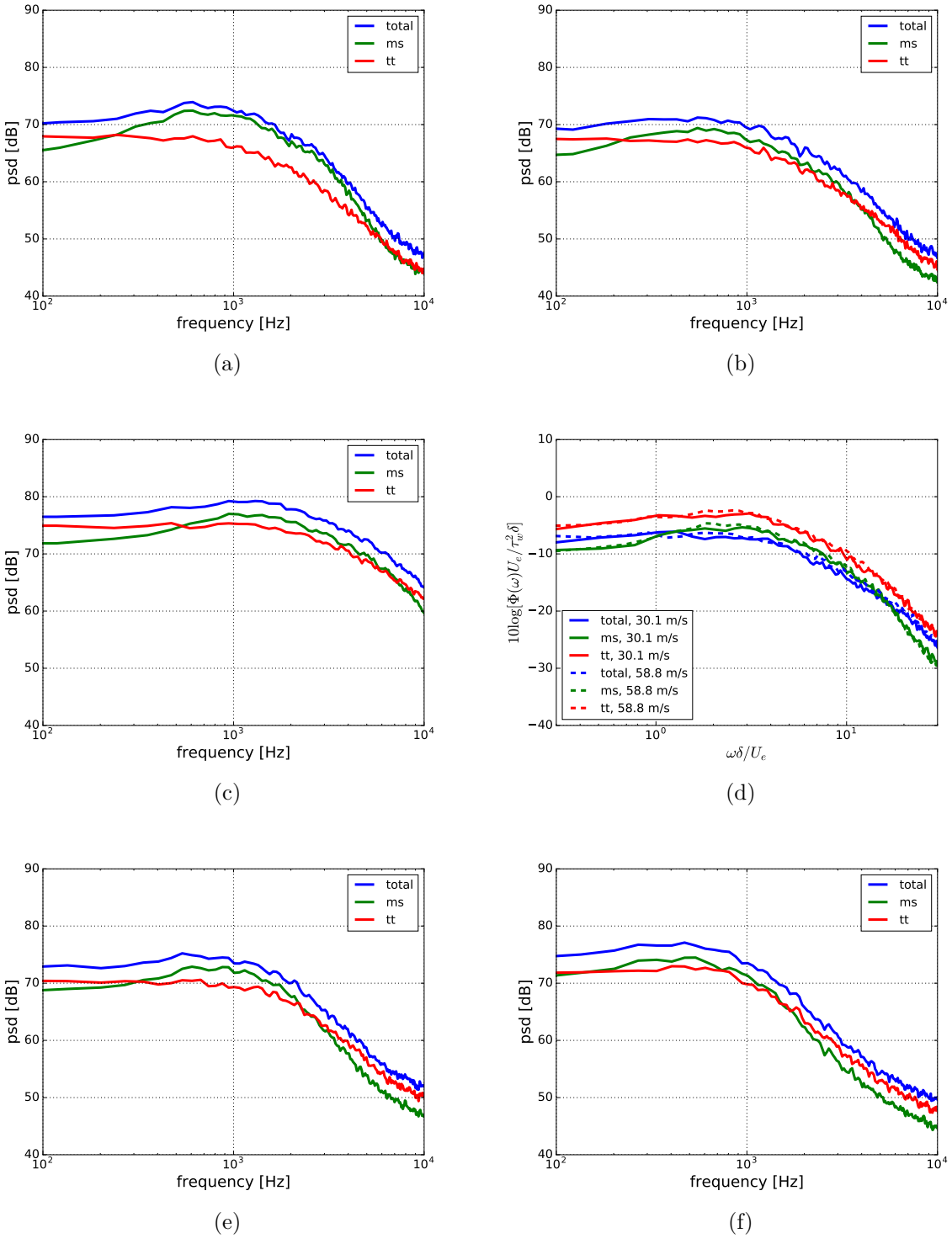

Figure 6.23: One-point spectra of p'_{ms}, p'_{tt} and p'_{total}; anisotropic turbulence approach for (b-f); (a) ZPG for 30.1 m/s calculated with the isotropic turbulence approach; (b) ZPG for 30.1 m/s; (c) ZPG for 58.8 m/s; (d) scaling for ZPG cases; (e) APG for $x_1 = 1128$ mm; (f) APG for $x_1 = 1210$ mm.

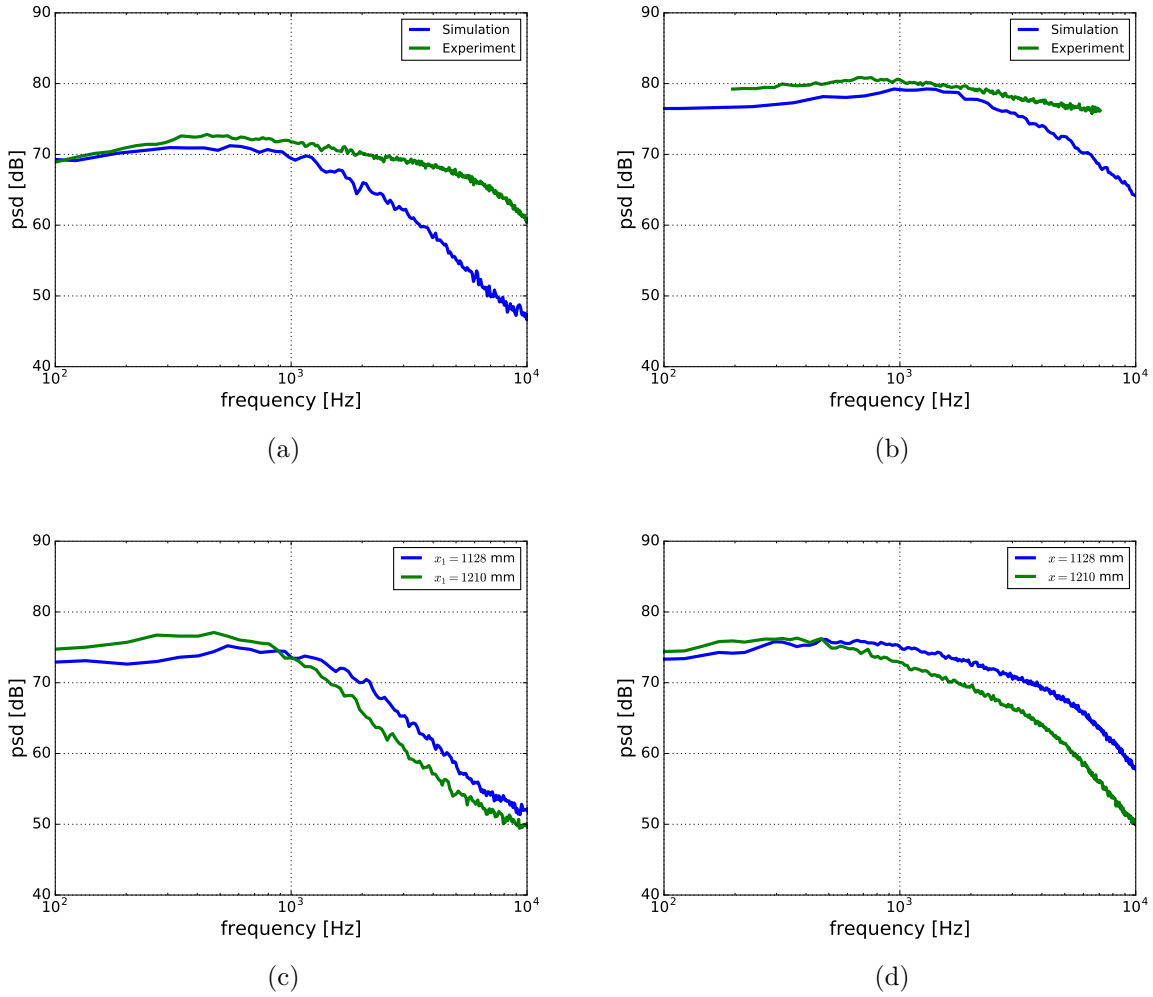

Figure 6.24: Comparison between one-point spectra calculated with the anisotropic turbulence approach and the measured spectra; (a) ZPG for 30.1 m/s; (b) ZPG for 58.5 m/s; (c) APG, simulated spectra; (d) APG, measured spectra.

obtained in section 4.3 are used to express the coherence in both streamwise and spanwise directions and to compared the numerical results. Values of $\alpha = 0.14$ and 0.125 for the ZPG boundary layers at velocities of 30.2 m/s and 58.7 m/s are obtained from the measurement. Generally, the value of α depends on the Reynolds number and a larger Reynolds number results in a smaller value. For the spanwise decay a value of $\beta = 0.72$ was measured for both velocities. For the APG boundary layer the coherence spectra cannot be well characterized with a single exponential curve. However, for convenience in view of the comparison an exponential function for both streamwise and spanwise directions is drawn from the experiment results. The obtained value of the constants follows $\alpha = 0.23$ and $\beta = 0.55$.

Fig. 6.25 shows the streamwise coherence of p'_{ms} and p'_{tt} for the anisotropic turbulence approach as a function of $\omega r_{1,3}/U_c$. The results show that the decay in the streamwise direction from the turbulence-turbulence term p'_{tt} is much stronger than for the mean-shear term p'_{ms}. The obtained exponential curves from the experiment for prescribing the coherence are also plotted for comparison.

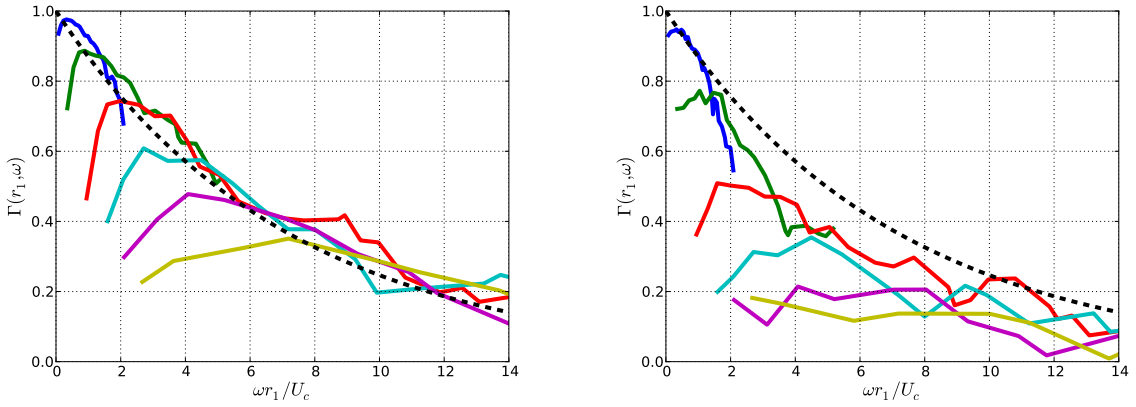

(a) (b)

Figure 6.25: Streamwise coherence calculated with the anisotropic turbulence approach, ZPG for 30.1 m/s, $0.6\delta^* < r_1 < 12.6\delta^*$; (-), simulation; (- -), experiment, $\exp(-0.14\omega r_1/U_c)$; (a) p'_{ms}; (b) p'_{tt}.

Fig. 6.26 shows the streamwise coherence of p'_{total}. A very good agreement with the experimental results is obtained for the numerical results with the anisotropic turbulence approach. The results show a much stronger coherence decay for the APG boundary layer than the ZPG boundary layers. Furthermore, a slightly slower decay for the ZPG boundary layer with the higher velocity is also presented in the simulation. The obtained coherence from the isotropic turbulence approach is larger than the one from the anisotropic turbulence approach, see Fig. 6.26(a,b). This is because for the isotropic turbulence approach p'_{ms} is the dominant part (see Fig. 6.23), which has a larger coherence.

Fig. 6.27 shows the spanwise coherence of p'_{ms} and p'_{tt} for the anisotropic turbulence approach as a function of $\omega r_{1,3}/U_c$. The phase velocity U_c does not depend on the spanwise separations. A single phase velocity $U_c(\omega)$ obtained by the closest virtual microphones $r_1 = 2$ mm is used to plot the spanwise coherence. The same as the results shown for the streamwise coherence, the coherence decay of p'_{tt} is much stronger than p'_{ms} also for the spanwise direction.

Fig. 6.28 shows the obtained spanwise coherence compared to the exponential curves which are derived from the measurement. The results for the anisotropic turbulence approach are consistent with the experimental results for all calculated cases. Again, the one with the isotropic turbulence approach shows a larger coherence than the measured curves, which is due to the larger portion of the p'_{ms} part. Because p'_{ms} has a larger coherence also in the spanwise direction shown in Fig. 6.27.

Fig. 6.29 shows the comparison of the convective phase velocity for ZPG at velocity of 30.1 m/s. The simulated velocity of p'_{total} increases at low frequencies, after reaching the maximum it decreases gradually with increasing frequencies. The maximum velocity is about $0.8U_0$ and located around $\omega\delta/U_0 = 2$. The frequency behaviour and the obtained maximum of the simulated phase velocity show good agreement with the measured results. However, the increasing velocity with a larger streamwise distance, is only poorly presented in the simulation results because of the lack of the realized kinetic energy from FRPM in the near wall region.

A comparison between numerically and experimentally obtained phase velocities for

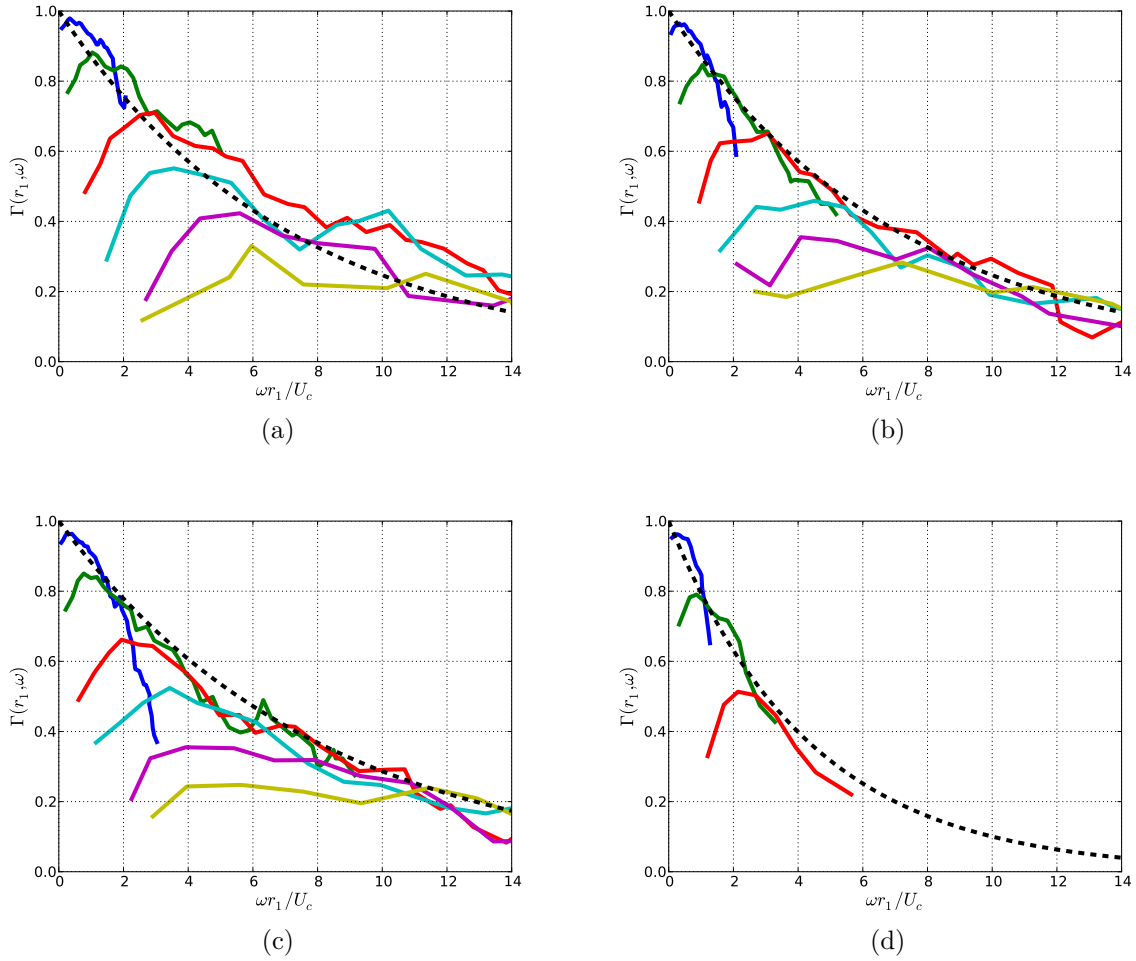

Figure 6.26: Comparison of the streamwise coherence, anisotropic turbulence approach for (b-d); (-), simulation for p'_{total}; (- -), experiment; (a) ZPG for 30.1 m/s, $0.6\delta^* < r_1 < 12.6\delta^*$, isotropic turbulence approach; (- -), $\exp(-0.14\omega r_1/U_c)$; (b) ZPG for 30.1 m/s, $0.6\delta^* < r_1 < 12.6\delta^*$; (- -), $\exp(-0.14\omega r_1/U_c)$; (c) ZPG for 58.5 m/s, $0.7\delta^* < r_1 < 14.5\delta^*$; (- -), $\exp(-0.125\omega r_1/U_c)$; (d) APG, $0.4\delta^* < r_1 < 3.0\delta^*$; (- -), $\exp(-0.23\omega r_1/U_c)$.

ZPG 30.1 m/s and APG 30.4 m/s at $\Delta r_1 = 15$ mm is shown in Fig. 6.30. The phase velocity for the APG boundary layer is much smaller than the one for the ZPG, which is well presented in the numerical results.

Fig. 6.31 shows the comparison of the mean convective velocity $\overline{U}_c$, which is obtained by using the time shift τ of the maximum time-space correlation $R_{pp}(r_1, \tau)$ for a fixed streamwise separation r_1, $\overline{U}_c(r_1) = r_1/\tau(r_1)$. Results for the maximum correlation smaller than 0.03 are not considered. Curves presenting the experimental results are drawn by best fit of the measured data. Simulated mean velocities of p'_{total} show similar trends to the measured results. The velocity increases at larger distances and is larger for the ZPG boundary layers than the APG. However, the measured velocities at closer distances are smaller than the simulated results. This is due to the lack of the realized kinetic energy from FRPM in the computation as discussed before. However, the particularly large value

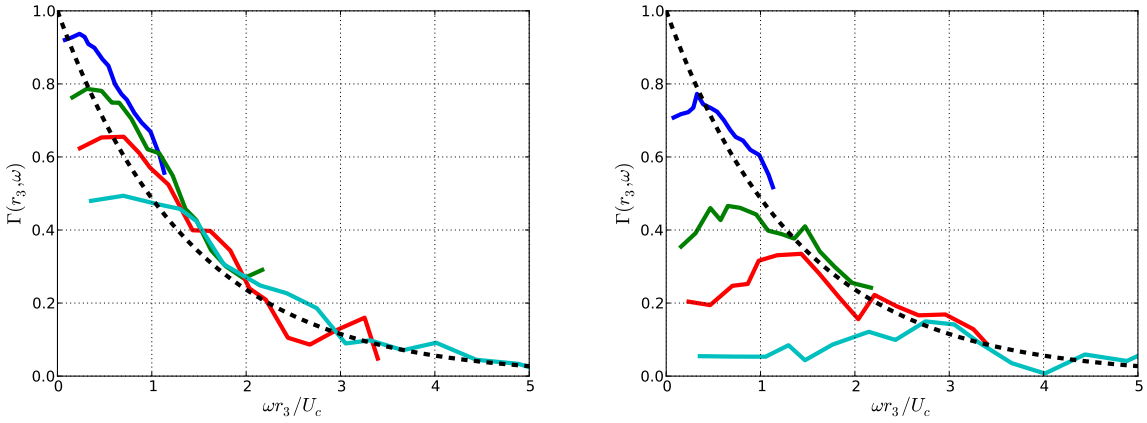

Figure 6.27: Spanwise coherence calculated with the anisotropic turbulence approach, ZPG for 30.1 m/s, $0.6\delta^* < r_3 < 2.7\delta^*$; (-), simulation; (- -), experiment, $\exp(-0.72\omega r_1/U_c)$; (a) p'_{ms}; (b) p'_{tt}.

obtained for the closest distance also visible for the phase velocity in Fig. 6.29 is not clear to the author. This behaviour is also shown for the generic test case in section 6.1.6.

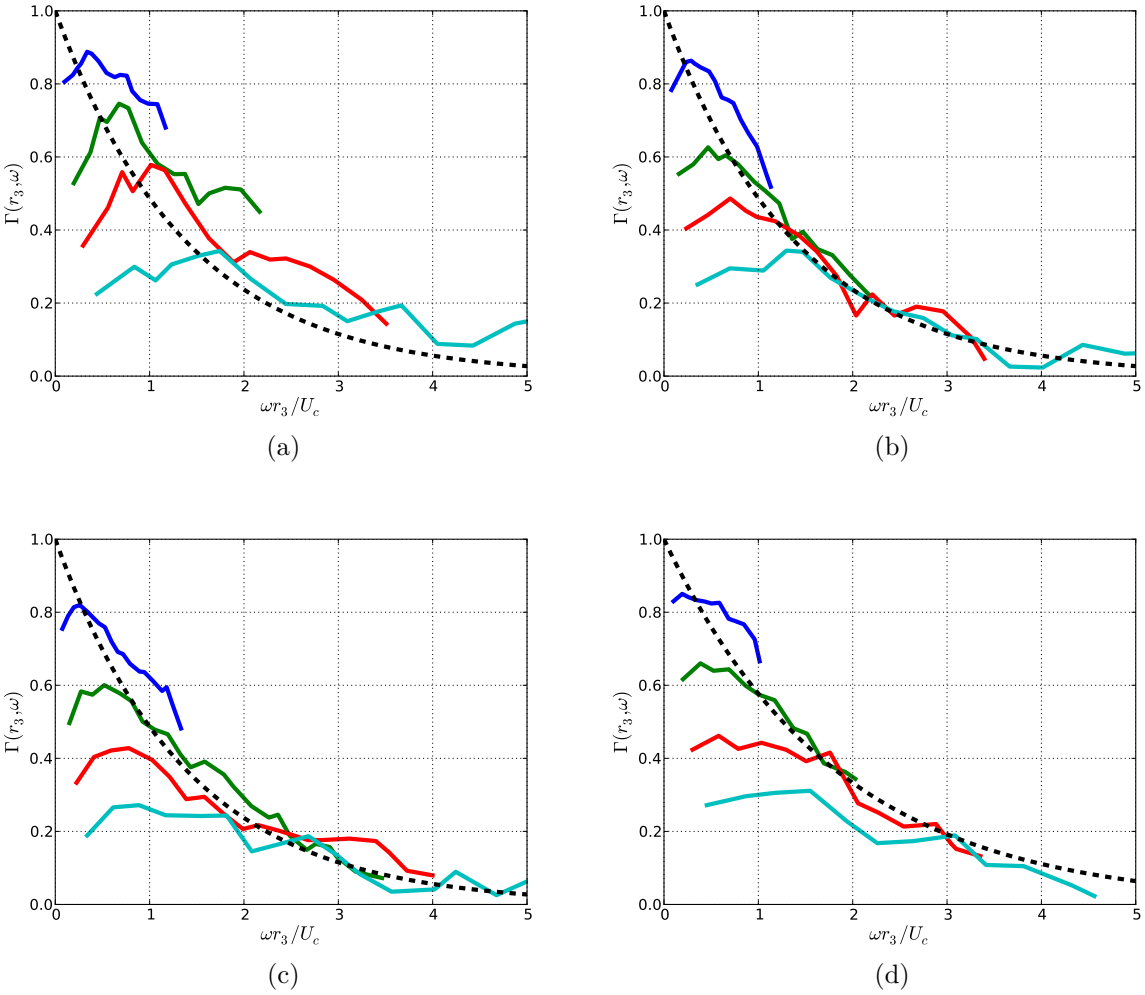

Figure 6.28: Comparison of the spanwise coherence, anisotropic turbulence approach for (b-d); (-), simulation; (- -), experiment; (a) ZPG for 30.1 m/s, $0.6\delta^* < r_3 < 2.7\delta^*$, isotropic turbulence approach; (- -), $\exp(-0.72\omega r_3/U_c)$; (b) ZPG for 30.1 m/s, $0.6\delta^* < r_3 < 2.7\delta^*$; (- -), $\exp(-0.72\omega r_3/U_c)$; (c) ZPG for 58.5 m/s, $0.7\delta^* < r_3 < 3.1\delta^*$; (- -), $\exp(-0.72\omega r_3/U_c)$; (d) APG, $0.4\delta^* < r_3 < 1.8\delta^*$; (- -), $\exp(-0.55\omega r_3/U_c)$.

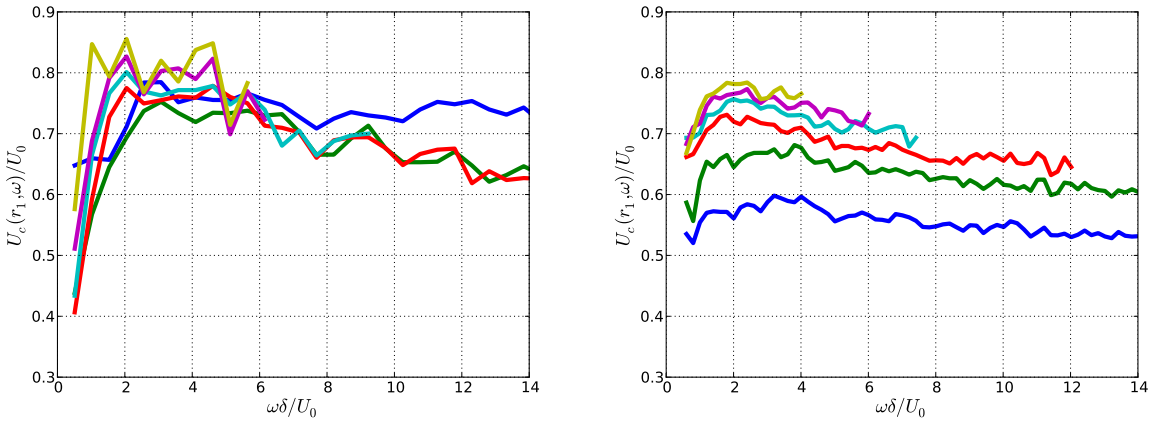

Figure 6.29: Comparison of the convective phase velocity for ZPG at velocity of 30.1 m/s; (a) simulation results calculated with the anisotropic turbulence apporach, $0.6\delta^* < r_1 < 18.0\delta^*$; (b) experimental results, $0.6\delta^* < r_1 < 17.1\delta^*$.

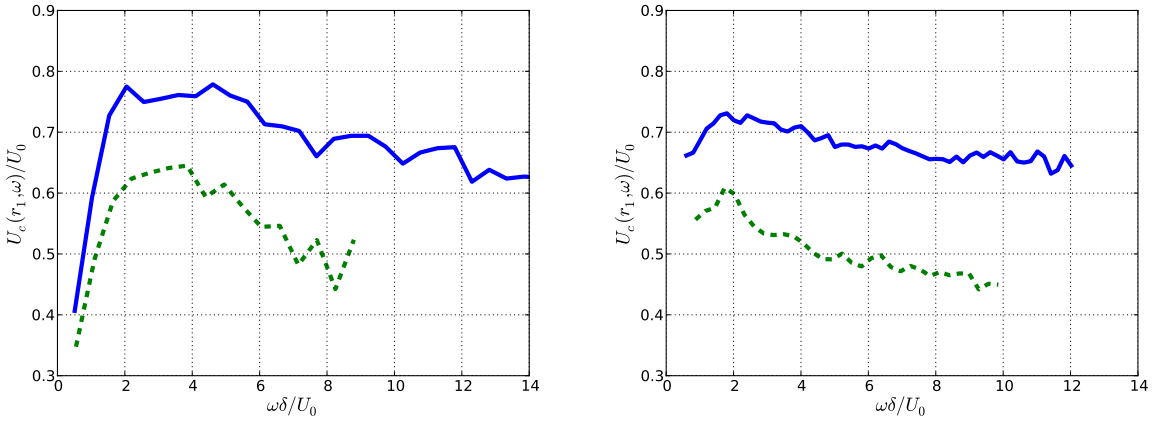

Figure 6.30: Comparison of the convective phase velocity at $\Delta r_1 = 15$ mm for ZPG for 30.1 m/s and APG for 30.4 m/s; (a) simulation results calculated with the anisotropic turbulence approach; (b) experimental results.

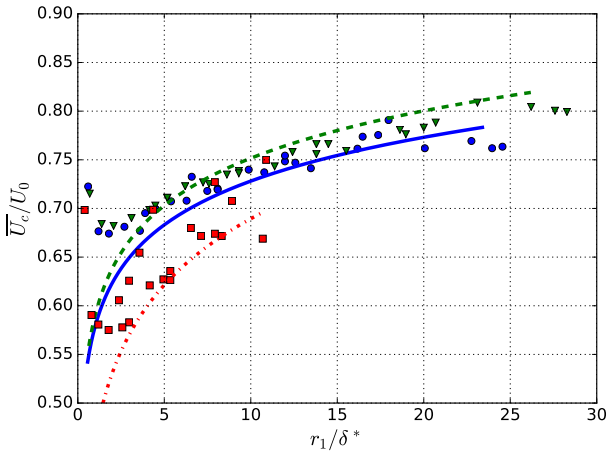

(a)

Figure 6.31: Comparison of the mean convective velocity; anisotropic turbulence approach. ZPG for 30.1 m/s: ●, simulation, (-), experiment; ZPG for 58.8 m/s: ▼, simulation, (- -), experiment; APG: ■, simulation, (-.-), experiment.

7 Conclusions and outlook

7.1 Conclusions

In this work, the feature of wall pressure fluctuations beneath zero and non-zero pressure gradient turbulent boundary layers was studied comprehensively through experimental and numerical investigations.

An experiment was conducted on a flat plate configuration in the Aeroacoustic Wind Tunnel Braunschweig (AWB) and the non-zero pressure gradient test case was realized by installing a NACA 0012 airfoil above the plate model. The mean flow property of the boundary layers was measured using a single hot-wire anemometer. The effect of the pressure gradient on the boundary layer mean velocity profile was well identified. Also the Reynolds stress for selected test cases was obtained using a crossed hot-wire anemometer. Twelve subminiature Kulite sensors were placed in the streamwise and spanwise directions in order to measure both the one-point spectra and the two-point statistics of the wall pressure fluctuations.

The level of the one-point spectra increases for an adverse pressure gradient (APG) boundary layer and the spectral maximum location shifts to a lower frequency when compared to a zero pressure gradient (ZPG) boundary layer. The slope of the mid-frequency roll off becomes steeper for an APG boundary layer, whereas it tends to flatten for a favorable pressure gradient (FPG) boundary layer. The change of the spectral slope due to the pressure gradient is stronger when the pressure gradient is larger or the streamwise distance of the boundary layer under which the pressure gradient acts is longer. It is found that the change of the spectral slope at medium frequencies can be well characterized by the boundary layer shape factor H. It is also worth to note that the APG wall pressure spectral peak collapses well by using dynamic pressure as the pressure scaling parameter, i.e. $u_\tau/Q^2\theta$, $u_\tau/Q^2\delta$ and $U_0/Q^2\delta^*$. This indicates that the outer parameter is more appropriate to scale the wall pressure spectra for the APG boundary layers than the wall shear stress τ_w. This is probably due to the increasing importance of the boundary layer outer layer for the wall pressure spectral peak.

The effects of the pressure gradient on the cross-spectra and the convection velocities of the wall pressure fluctuations are discussed. For the APG boundary layer the coherence decay rate increases in the streamwise direction and decreases in the spanwise direction, when compared to the ZPG boundary layer. The stronger the APG is, the larger the effect is. Only a slight decrease of the decay rate in the streamwise direction and a slight increase in the spanwise direction are found for a FPG boundary layer. The convective velocity decreases for an APG boundary layer and increases for a FPG boundary layer.

Based on the measured data and a selected dataset of four other test cases at three other test facilities, an new wall pressure spectral model suitable for both ZPG and APG cases was proposed. The ZPG wall pressure spectral model from Goody is taken as the basic form to develop the new model. This is because of the good collapse of the spectral peak using the dynamic pressure as the scaling parameter, a clear trend of the spectral slope change at medium frequencies due to the pressure gradient and a nearly unchanged

spectral slope at high frequencies compared to the ZPG cases. The proposed model in this work is compared to the published spectral models for the APG cases. There are three major differences between the proposed model and the other models. Firstly, instead of $U_e/\tau_w^2\delta(\delta^*)$, $u_\tau/Q^2\theta$ was used based on a good collapse of the spectral peaks for the measured spectra at ZPG and APG when scaling with this parameter, whereas over 15 dB difference among the spectra was found when scaled using $U_e/\tau_w^2\delta$. As discussed before, the dynamic pressure Q could be more appropriate to scale the APG spectra than the usually used τ_w. Secondly, the boundary layer shape factor was used to evaluate the spectral slope at medium frequencies instead of Clauser's equilibrium parameter. Overall, the wall pressure fluctuations are mostly affected by the boundary layer mean velocity profile and the Reynolds stresses. The Reynolds stresses are again tightly related to the mean velocity profile. Therefore, the boundary layer mean velocity profile could be an essential criterion to determine the shape of the wall pressure spectra. The connection between the mean velocity profile and the wall pressure spectral shape was demonstrated. On the one hand, the spectrum is almost only affected by the local boundary layer; on the other hand, the local boundary layer parameters are predominantly determined by its upstream history. The measured data illustrated that the shape factor indicates correct trends of the boundary layer profile development for different configurations and streamwise positions whereas the Clauser's parameter can fail at different streamwise positions where the pressure gradients change rapidly. An excellent match of the spectral slope at medium frequencies between the predictions and the measured data was shown using the shape factor as the control parameter. Thirdly, instead of an ω^2 increase at low frequencies, a slope of ω was used in the model which was derived as an averaged value from the measured data and results from the literature for the APG cases. Arguments for replacement of the classic ω^2 are: 1, the slope of ω^2 is obtained by assuming a frozen flow and only counting the mean-shear source term. However, when dealing with a non-frozen flow the slope becomes flatter because the energy from higher frequencies spreads into lower frequencies [30]. 2, wall pressure fluctuation spectra of the turbulence-turbulence source term show a plateau at lower frequencies and take over the importance of the mean-shear term in the spectra for a ZPG boundary layer [30, 22, 55, 57, 105]. These features are also demonstrated in this work, which can cause a flatter slope at low frequencies as well. However, an exact knowledge of the importance of the turbulence-turbulence term for a non-ZPG boundary layer is still lacking.

Two expressions of the new model are proposed based on two different approaches to predict the spectral amplitude. The first one (Eq. (5.8)) uses a function of the momentum Reynolds number and the boundary layer shape factor to adjust the spectral amplitude. The second one (Eq. (5.9)) takes advantage of a new pressure scaling parameter, which allows the spectral peak to collapse within approximately 4 dB for different experimental configurations from the selected dataset. Therefore, a constant value for controlling the spectral amplitude can be applied.

Results of the present model with both formulations are compared to measured spectra from the selected dataset. Very good agreement is obtained, except for some specific configurations. These are: 1, spectra measured in the vicinity of a trailing edge. The reason for that could be the trailing edge scattering effect and possible imprecise estimations of input boundary layer parameters in the trailing edge area, where not available from the measurements. These are provided by means of XFOIL calculations in the current study. 2, spectra measured at positions not far away downstream from a boundary-layer separation.

Uncertainty of ± 2 dB compared to the selected dataset excluding the mentioned specific cases is shown using the expression Eq. (5.9), the uncertainty is larger for the expression Eq. (5.8), which is about ± 4 dB. Good agreement for ZPG boundary layers from the present model is also obtained.

For the numerical investigation, an efficient numerical procedure based on solving a Poisson's equation and a model for synthetic turbulence was developed. The Poisson's equation was solved in the wavenumber domain according to Hockney's method. The source terms on the right-hand side of the Poisson's equation were realized by synthetic turbulence which is generated by the Fast Random Particle-Mesh Method (FRPM). The kinetic energy was well reconstructed except for the near-wall region, especially for $< 0.1\delta$. This is acceptable for the purpose which is orientated to practical applications, because the region close to the wall impacts mostly the high frequencies but not the main features for the wall pressure fluctuations. Moreover, the high frequencies are generally irrelevant to the vibration due to the poor transmission efficiency for the structural response. Both the mean-shear turbulence term and the turbulence-turbulence term were considered. The results demonstrated that the wall pressure fluctuations contributed from both terms are of the same order of magnitude if anisotropic turbulence is considered. For isotropic turbulence the mean-shear term is the dominant term. In contrast to the spectra with a peak at medium frequencies for the mean-shear term, the spectra for the turbulence-turbulence term show a maximum plateau at lower frequencies. The calculated one-point spectrum for the mean-shear term is verified by comparing to the theoretical prediction using the turbulence statistics provided by FRPM. Compared to the spectral models from the literature a stronger decay at high frequencies was found which is mainly because of the limited grid resolution which was not fine enough to resolve the small turbulence structures close to the wall. The two-point correlation properties were consistent with the database from other investigators. It was found that the small eddies in the inner region could affect the one-point spectra and the two-point correlation properties at low frequencies due to the temporal turbulence decay. The convection velocities were well estimated. The wavenumber-frequency spectra were also calculated. The convective ridge can be clearly determined. Furthermore, a calculation using the developed numerical procedure for the experiment presented in this work was also performed. The calculated wall pressure features show good agreement with the experimental results.

7.2 Outlook

Based on the experimental and numerical work conducted in this thesis, a deeper insight into the wall pressure fluctuations was obtained. From the obtained experience and knowledge, some possible improvements for the current work and suggestions for the further investigations are provided below.

From the experimental results, disturbances at low frequencies on the wall pressure spectra have been found and these are more pronounced at higher velocities. This is because the disturbances caused by the free shear layer of the wind tunnel increases more significantly with an increasing free-stream velocity than the wall pressure fluctuations beneath a turbulent boundary layer. The impact of the shear layer on the wall pressure spectra is strengthened when the NACA 0012 airfoil is installed. The local acceleration or slowdown of the free stream due to the present airfoil will decrease or increase the pressure

in the region underneath the airfoil, which can shrink the shear layer inwards or spread it outwards. This effect can strengthen the impact of the shear layer on the measured wall pressure spectra. Also the suspicious mid-frequency hump measured by the FPG wall pressure spectra might be due to this effect. To suppress the impact of the shear layer, side walls as extensions on the wind tunnel nozzle exit can be considered. The side wall might be mounted on the plate model and for the non-ZPG test cases it might be extended until the leading edge of the airfoil.

Another improvement for the experiment can be made for the hot-wire measurement. As mentioned in this thesis, the measurement uncertainty of the spanwise velocity fluctuations due to a jaw angle of the hot-wire probe to the plate cannot be corrected. Therefore, a small traverse system might be designed and applied, which can be directly mounted on the plate model. With this configuration of the traverse system, it allows to measure the Reynolds stress with the crossed hot-wire parallel or with a much smaller angle to the plate and will reduce the measurement uncertainty.

The proposed spectral model in this thesis has a good prediction accuracy for both ZPG and APG cases and shows a significant improvement compared to the other published models. In spite of this, the author has made some considerations or suggestions for further investigations which may improve the spectral model or provide a more deeper insight into the wall pressure spectra.

Firstly, the determination of the spectral peak location is difficult. There is no function applied to adjust the peak location in the proposed model. From the experimental results in this work it is shown that this location can be dependent on the boundary layer shape factor and the boundary layer thickness based Reynolds number. However, the applied function can not predict the spectral peak location accurately for the other experimental results. It would be of great value to find out if the spectral peak location can be predicted based on the boundary layer parameters.

Secondly, a slope of ω^1 for the low-frequency range was applied in the proposed model. This is determined by taking an averaged value of the measured spectra for the APG cases from the literature. Due to the disturbances from the shear layer on the measured spectra at low frequencies in this work or generally for many other test cases, it is not possible to investigate the dependence of the spectral slope at low frequencies on the boundary layer parameters. However, from the measured ZPG spectra it seems that a relationship between the spectral extension at medium frequencies and the spectral slope at low frequencies exists. The boundary layer shape factor is a conceivable parameter which may also impact the spectral slope.

Thirdly, the spectral model is proposed for ZPG and APG boundary layers. Actually, for FPG turbulent boundary layers, the change of the spectral slope at medium frequencies can also be identified by the boundary layer shape factor. The slope at high frequencies seems to be unchanged compared to the ZPG and APG wall pressure spectra. Furthermore, if the FPG wall pressure spectral peaks collapse with the ZPG and APG spectra, the scaling with the dynamic pressure is also suitable for the FPG boundary layers (it is the case if the measured FPG spectra without the hump at medium frequencies which may be caused by the measurement setup. A flattened FPG spectrum was reported by other researchers). This indicates that the present model would also have the potential to be applied for the FPG turbulent boundary layers. Certainly, a different relationship between the spectral slope at medium frequencies and the boundary layer shape factor is needed.

Fourthly, as mentioned in this work, the Reynolds stress and the boundary layer mean

velocity profile could be the key impact factor for the wall pressure spectra. On the other hand, the Reynolds stress is tightly related to the boundary layer profile. Therefore, the boundary layer shape factor is taken as an important parameter in the present model to determine the spectral level and form. However, the open question is what is the role of the previous development history and the local development of the boundary layer on the wall pressure spectra. Whether a similar boundary layer profile implies a similar Reynolds stress? If a large difference in Reynolds stress could exist under similar boundary layer profiles, the respective impact on the wall pressure spectra cannot be reflected based on the present model or any other published models.

Lastly, the author questioned the Corcos correction which can give an under-correction for the wall pressure spectra at frequencies approximately $\omega U_c/r > 0.5$. This first knowledge was obtained from a not yet published experimental result. Further systematic investigations on the spectral attenuation measured by a 'large' sensor are strongly recommended for an extensive assessment and evaluation of the Corcos correction.

A numerical approach to calculate the wall pressure fluctuations was developed in this work. The approach was verified and validated by comparing to the analytical, numerical and experimental results from the literature and the present experimental results in this thesis. Based on the knowledge obtained during the investigation, following discussions and suggestions are given below, which may provide a deeper assessment of this approach compared to the reality and expand the possibilities for its practical applications.

The synthetic turbulence applied in this method is realized using a Gaussian filter. Compared to the more realistic spectrum such as von Kármán spectra and Liepmann spectra, the Gaussian spectrum cannot well represent the spectrum in the inertial subrange. The spectrum rolls off much faster in this range than the von Kármán spectrum, the Liepmann spectrum and the measured spectrum. This difference plays only a minor role on the wall pressure fluctuations, because the energy-containing range of the spectrum dominates the contribution to the wall pressure fluctuations. However, the difference between the modeled spectra in the energy-containing range may have an impact on the wall pressure fluctuations. Also, the impact of the difference by an isotropic or an anisotropic turbulence approach is of interest.

The turbulence length scale is a key parameter to give an accurate prediction of the wall pressure fluctuations. However, some differences in the length scale provided by the RANS calculation are shown when compared to the length scale acquired by experimental results and semi-empirical assumptions. We need a better understanding of the RANS provided length scale and the impact on the wall pressure fluctuations caused by the differences in the applied length scales. Furthermore, anisotropy of the length scale in different directions is applied in this work and the effect of the turbulence anisotropy on the wall pressure fluctuations is demonstrated. However, anisotropy between the different fluctuating velocity components could not directly be simulated with the used RANS turbulence model and this also impacts the wall pressure fluctuations. An application of this anisotropy and an assessment of its impact may be one direction for the further studies.

The numerical approach applied in this work, solving a Poisson's equation, can calculate the pressure fluctuations within an incompressible turbulent boundary layer. For a compressible flow, the pressure fluctuations are not governed by the Poisson's equation, but the acoustic wave equation. However, results from experiments carried out in the Transonic-Wind-Tunnel Göttingen [14] and on the Advanced Research Technology Aircraft of the

German Aerospace Center [118] showed that, the acoustic contribution to the wall pressure fluctuations is negligible compared to the hydrodynamic contribution. Therefore, we are encouraged to compute the pressure fluctuations via the Poisson's equation even for the high-subsonic and transonic flow. The first calculation [119] on the wall pressure one-point spectra for the high-speed flow shows very good agreement with the experimental results. However, an impact of the flow convection on the wall pressure cross-spectra and the spectra in the wavenumber domain is probably to be expected. Therefore, further investigations for an extensive assessment of the application possibility of this method for the compressible flow case is required.

Furthermore, for a broader practical application, calculations on a complex geometry, e.g. on a curved surface, are desired. A classical example is the calculation on the aircraft fuselage. Currently, we bend the curved surface of the fuselage back to a flat surface. So far, the calculation on the 'flat' surface shows satisfactory results. However, when dealing with a large curvature, e.g. the cockpit region, this treatment may fail. A new method based on solving the Poisson's equation using a differential method is an ongoing task.

A Temporal turbulence decay

The space-time correlation R_{ij} of the velocity fluctuations for turbulent flow can be generally formulated as the product of three distinct functions, for convenience the indices ij are dropped in the following discussion.

$$R(\mathbf{r},\tau) = R_1(r_1 - U_c\tau)R_n(\mathbf{r_n})R_m(\tau). \tag{A.1}$$

Here, $\mathbf{r_n}$ represents the surface two-point distance vector with components r_2 and r_3, which is independent of τ. $R_m(\tau)$ is the temporal turbulence decay factor. In our case for decaying turbulence $R_m(\tau) = \exp(-|\tau|/\tau_s)$. For frozen turbulence $\tau_s \to \infty$, hence $R_m(\tau) \equiv 1$.

The wavenumber spectrum can be derived by taking the Fourier transform of the space-time correlation using the following definition of the Fourier transforms in space and time,

$$\begin{cases} f(r) = \int_{-\infty}^{\infty} f(k)\exp(-ikr)\,\mathrm{d}k, \quad f(k) = \dfrac{1}{2\pi}\int_{-\infty}^{\infty} f(r)\exp(ikr)\,\mathrm{d}r. \\ f(\omega) = \dfrac{1}{2\pi}\int_{-\infty}^{\infty} f(t)\exp(-i\omega t)\,\mathrm{d}t, \quad f(t) = \int_{-\infty}^{\infty} f(\omega)\exp(i\omega t)\,\mathrm{d}\omega. \end{cases} \tag{A.2}$$

The wavenumber spectrum reads,

$$\Phi(\mathbf{k},\omega) = \frac{1}{(2\pi)^4}\int_{-\infty}^{\infty}\int_{-\infty}^{\infty}\int_{-\infty}^{\infty}\int_{-\infty}^{\infty} R(\mathbf{r},\tau)\exp(-i\omega\tau + ik_1r_1 + ik_2r_2 + ik_3r_3)\,\mathrm{d}r_1\,\mathrm{d}r_2\,\mathrm{d}r_3\,\mathrm{d}\tau. \tag{A.3}$$

Since r_2 and r_3 are τ independent,

$$\begin{aligned} \Phi(\mathbf{k},\omega) &= \frac{1}{(2\pi)^4}\int_{-\infty}^{\infty}\int_{-\infty}^{\infty} R_n(\mathbf{r_n})\exp(ik_2r_2 + ik_3r_3)\,\mathrm{d}r_2\,\mathrm{d}r_3 \\ &\quad \int_{-\infty}^{\infty}\int_{-\infty}^{\infty} R_1(r_1 - U_c\tau)R_m(\tau)\exp(-i\omega\tau + ik_1r_1)\,\mathrm{d}r_1\,\mathrm{d}\tau. \end{aligned} \tag{A.4}$$

Let $\xi := r_1 - U_c\tau$ and the wavenumber spectrum of r_2 and r_3 be written as $\phi_n(\mathbf{k_n})$,

$$\Phi(\mathbf{k},\omega) = \phi_n(\mathbf{k_n})\frac{1}{(2\pi)^2}\int_{-\infty}^{\infty}\int_{-\infty}^{\infty} R_1(\xi)\exp(ik_1\xi)\,\mathrm{d}\xi R_m(\tau)\exp(-i\omega\tau + ik_1U_c\tau)\,\mathrm{d}\tau, \tag{A.5}$$

where

$$\phi_n(\mathbf{k_n}) = \frac{1}{(2\pi)^2}\int_{-\infty}^{\infty}\int_{-\infty}^{\infty} R_n(\mathbf{r_n})\exp(ik_2r_2 + ik_3r_3)\,\mathrm{d}r_2\,\mathrm{d}r_3. \tag{A.6}$$

In that follows, we can also express the resulting wavenumber spectrum as the product of three contributions,

$$\Phi(\mathbf{k},\omega) = \phi_1(k_1)\phi_n(\mathbf{k_n})\phi_m(\omega - U_ck_1), \tag{A.7}$$

where

$$\phi_1(k_1) = \frac{1}{2\pi}\int_{-\infty}^{\infty} R_1(\xi)\exp(ik_1\xi)\,\mathrm{d}\xi, \tag{A.8}$$

$$\phi_m(\omega - U_c k_1) = \frac{1}{2\pi}\int_{-\infty}^{\infty} R_m(\tau)\exp(-i(\omega - U_c k_1)\tau)\,\mathrm{d}\tau. \tag{A.9}$$

The function $\phi_m(\omega - U_c k_1)$ is the so-called moving-axis spectrum. For frozen turbulent flow ($\tau_s \to \infty$) the temporal turbulence decay factor is $R_m = 1$, and since the Fourier transform of the unity function is Dirac delta function [120], the moving axis spectrum follows

$$\phi_m(\omega - U_c k_1) = \delta(\omega - U_c k_1). \tag{A.10}$$

For non-frozen turbulent flow $R_m = \exp(-|\tau|/\tau_s)$. Hence,

$$\begin{aligned}\phi_m(\omega - U_c k_1) &= \frac{1}{2\pi}\int_{-\infty}^{\infty} \exp\left(-\frac{|\tau|}{\tau_s}\right)\exp(-i(\omega - U_c k_1)\tau)\,\mathrm{d}\tau \\ &= \frac{\tau_s}{\pi(1 + (\omega - U_c k_1)^2\tau_s^2)}\,.\end{aligned} \tag{A.11}$$

Taking the integration of $\Phi(\mathbf{k},\omega)$ over $\mathbf{k}$ we can obtain the spectrum in frequency domain,

$$\begin{aligned}\Phi(\omega) &= \int_{-\infty}^{\infty}\int_{-\infty}^{\infty}\int_{-\infty}^{\infty} \Phi(\mathbf{k},\omega)\,\mathrm{d}k_1\,\mathrm{d}k_2\,\mathrm{d}k_3 \\ &= \int_{-\infty}^{\infty}\int_{-\infty}^{\infty}\int_{-\infty}^{\infty} \phi_1(k_1)\phi_n(\mathbf{k_n})\phi_m(\omega - U_c k_1)\,\mathrm{d}k_1\,\mathrm{d}k_2\,\mathrm{d}k_3 \\ &= \int_{-\infty}^{\infty} \Phi(k_1)\phi_m(\omega - k_1 U_c)\,\mathrm{d}k_1,\end{aligned} \tag{A.12}$$

where

$$\Phi(k_1) = \phi_1(k_1)\int_{-\infty}^{\infty}\int_{-\infty}^{\infty} \phi_n(\mathbf{k_n})\mathrm{d}k_2\,\mathrm{d}k_3. \tag{A.13}$$

Reintroducing indices ij and assuming similar turbulent decay for each Reynolds stress component, i.e. $R_m(\tau) = R_{m(ij)}(\tau)$. This follows $\phi_m(\omega - k_1 U_c) = \phi_{m(ij)}(\omega - k_1 U_c)$, hence Eq. (A.12) becomes,

$$\Phi_{ij}(\omega) = \int_{-\infty}^{\infty} \Phi_{ij}(k_1)\phi_m(\omega - k_1 U_c)\,\mathrm{d}k_1. \tag{A.14}$$

B Wavenumber spectra of velocity fluctuations

The streamwise $f(r)$ and spanwise $g(r)$ correlation functions of isotropic turbulence as realised with FRPM read

$$f(r) = \exp\left(-\frac{\pi r^2}{4l_s^2}\right), \tag{B.1}$$

$$g(r) = \left(1-\frac{\pi r^2}{4l_s^2}\right)\exp\left(-\frac{\pi r^2}{4l_s^2}\right). \tag{B.2}$$

1-D wavenumber spectra can be achieved by taking the Fourier transform of the spatial correlations $f(r)$ and $g(r)$,

$$\Phi_{ii}(k_j) = \begin{cases} \dfrac{\overline{u_i^2}}{2\pi}\displaystyle\int_{-\infty}^{\infty} f(r)\exp(-ik_jr)\,\mathrm{d}r, & i=j. \\ \dfrac{\overline{u_i^2}}{2\pi}\displaystyle\int_{-\infty}^{\infty} g(r)\exp(-ik_jr)\,\mathrm{d}r, & i\neq j. \end{cases} \tag{B.3}$$

refer to [96]. Velocity fluctuation spectra $\Phi_{ij}(\omega)$ are related to $\Phi_{ij}(k_1)$ as introduced by Eq. (A.14). Hence to obtain the variance of the velocity fluctuations $\overline{u_iu_i}$, $\Phi_{ii}(k_1)$ is of great interest. Specifically, from Eq. (B.3) we obtain,

$$\Phi_{11}(k_1) = \frac{\overline{u_1^2}l_s}{\pi}\exp\left(\frac{-k_1^2l_s^2}{\pi}\right), \tag{B.4}$$

$$\Phi_{22}(k_1) = \Phi_{33}(k_1) = \frac{\overline{u_{2,3}^2}l_s}{2\pi^2}\exp\left(\frac{-k_1^2l_s^2}{\pi}\right)(2k_1^2l_s^2+\pi). \tag{B.5}$$

3-D wavenumber spectra for isotropic turbulence can be determined by

$$\Phi_{ij}(k_1,k_2,k_3) = \frac{E(k)}{4\pi k^2}(\delta_{ij}-(k_ik_j)/k^2), \tag{B.6}$$

where $k^2=k_1^2+k_2^2+k_3^2$. $E(k)$ is the scalar energy spectra and FRPM generated $E(k)$ can be written as

$$E(k) = \frac{8k_tl_s^5k^4}{3\pi^3}\exp\left(\frac{-k^2l_s^2}{\pi}\right). \tag{B.7}$$

Hence the expressions of 3-D wavenumber spectra $\Phi_{ii}(k_1,k_2,k_3)$ can be derived. Integrating over k_2 and k_3 we can obtain the 1-D wavenumber spectra $\Phi_{ii}(k_1)$,

$$\Phi_{ii}(k_1) = \int_{-\infty}^{\infty}\int_{-\infty}^{\infty}\Phi_{ii}(k_1,k_2,k_3)\,\mathrm{d}k_2\mathrm{d}k_3. \tag{B.8}$$

The results are consistent with the form achieved directly from the spatial correlation, Eqs. (B.4) and (B.5).

C Figures

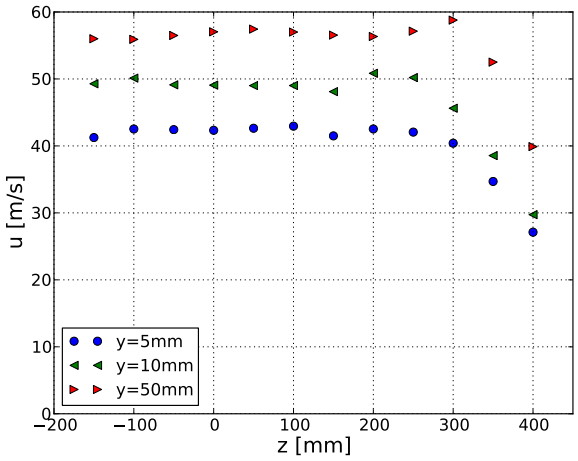

Figure C.1: Mean flow velocities measured at $x = 1210$ mm, in three wall-normal positions and different spanwise positions in between -150 mm$< z <$400 mm.

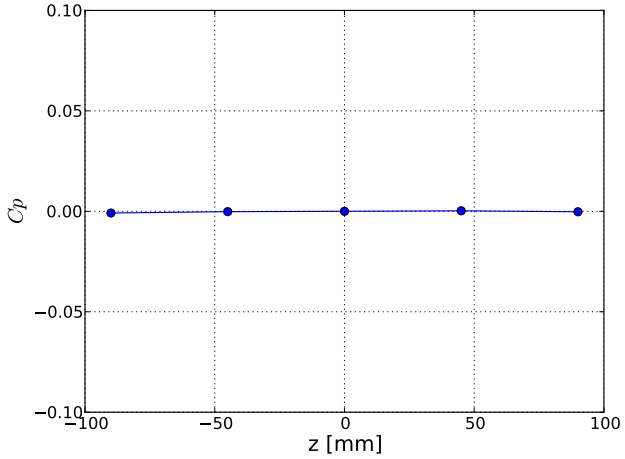

Figure C.2: Cp distributions in the spanwise direction measured at $x = 1110$ mm for ZPG.

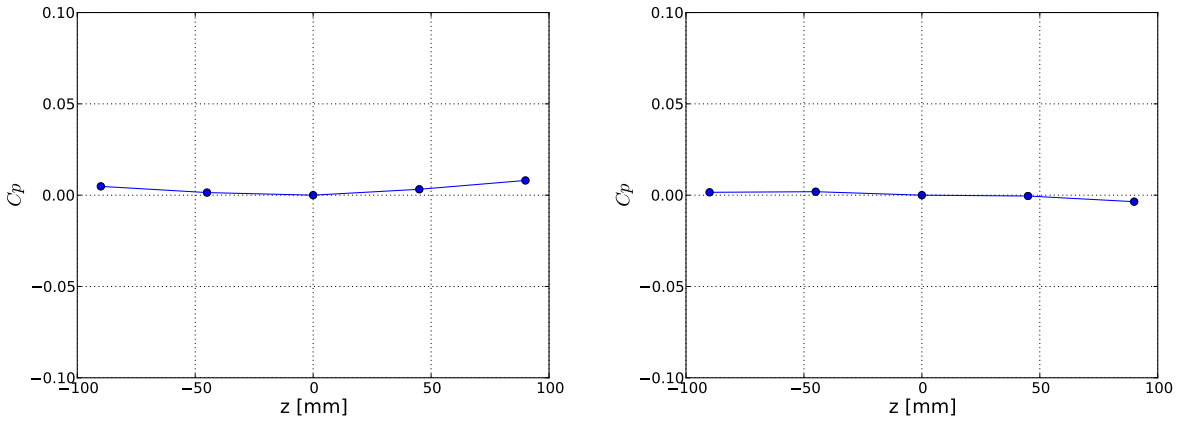

(a) (b)

Figure C.3: Cp distributions in the spanwise direction measured at $x = 1110$ mm for APG and FPG; (a) APG -14°; (b) FPG 14°.

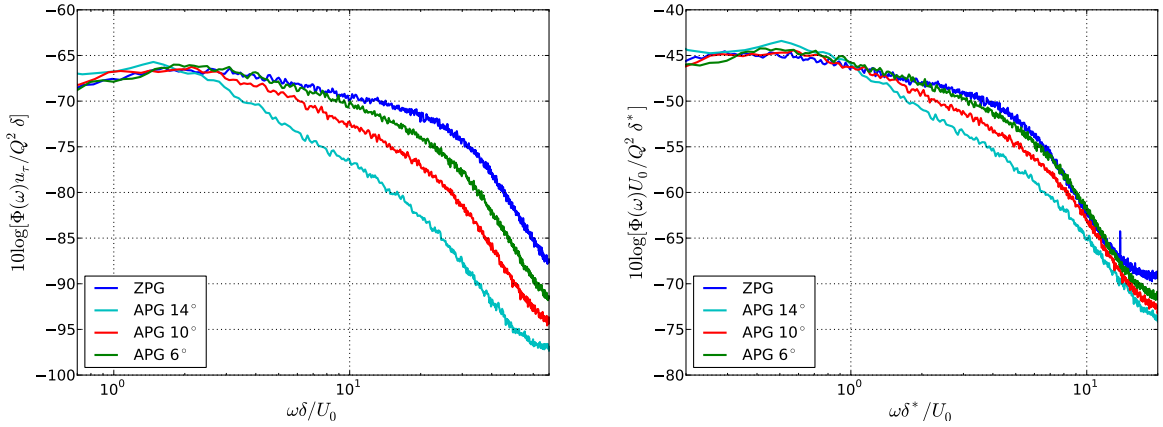

(a) (b)

Figure C.4: Scaled spectra for ZPG and APG at $x = 1210$ mm for the free-stream velocity of 30.2 m/s; (a) scaled by $u_\tau/Q^2\delta$ and $\omega\delta/U_0$; (b) scaled by $U_0/Q^2\delta^*$ and $\omega\delta^*/U_0$.

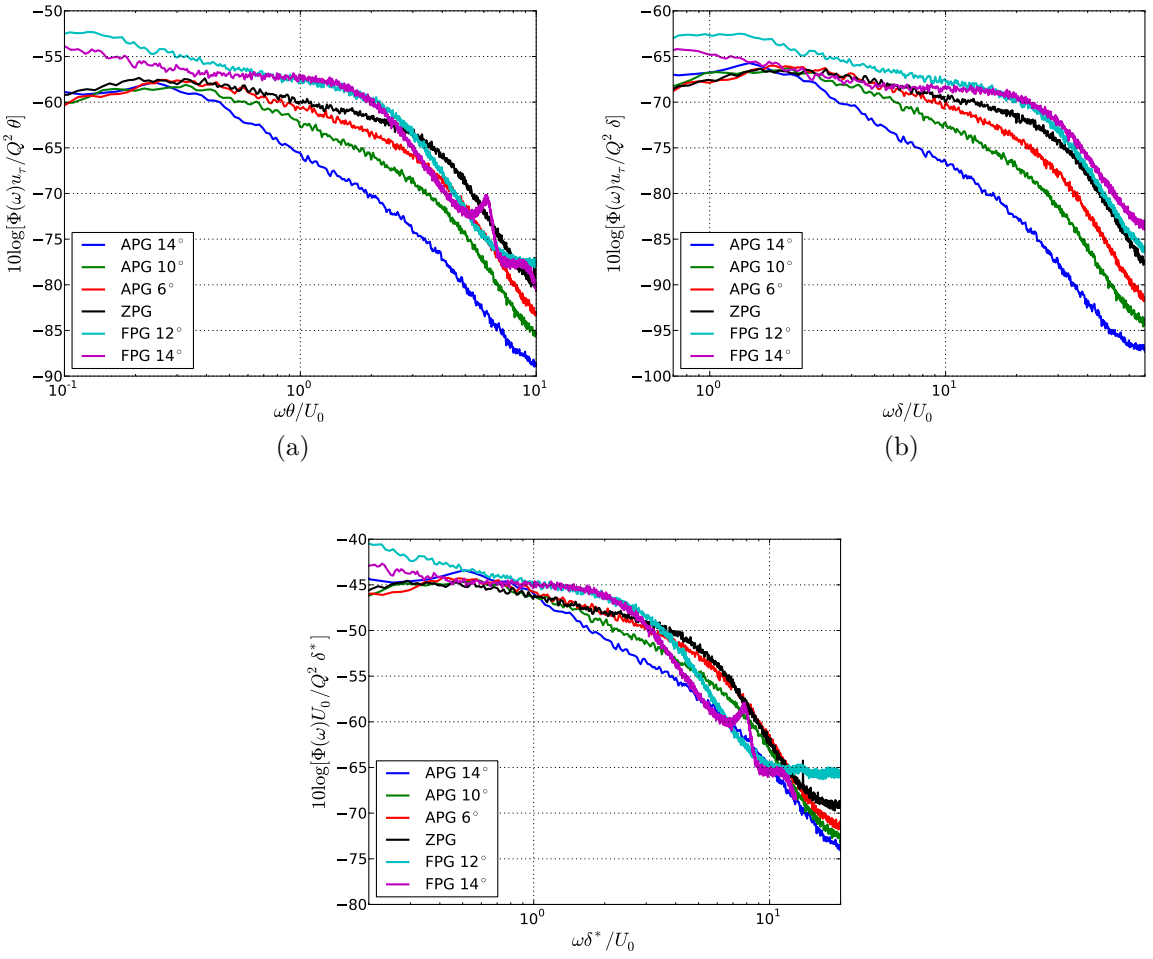

Figure C.5: Scaled spectra for ZPG, APG and FPG at $x = 1210$ mm for the free-stream velocity of 30.2 m/s; (a) scaled by $u_\tau/Q^2\theta$ and $\omega\theta/U_0$; (b) scaled by $u_\tau/Q^2\delta$ and $\omega\delta/U_0$; (c) scaled by $U_0/Q^2\delta^*$ and $\omega\delta^*/U_0$.

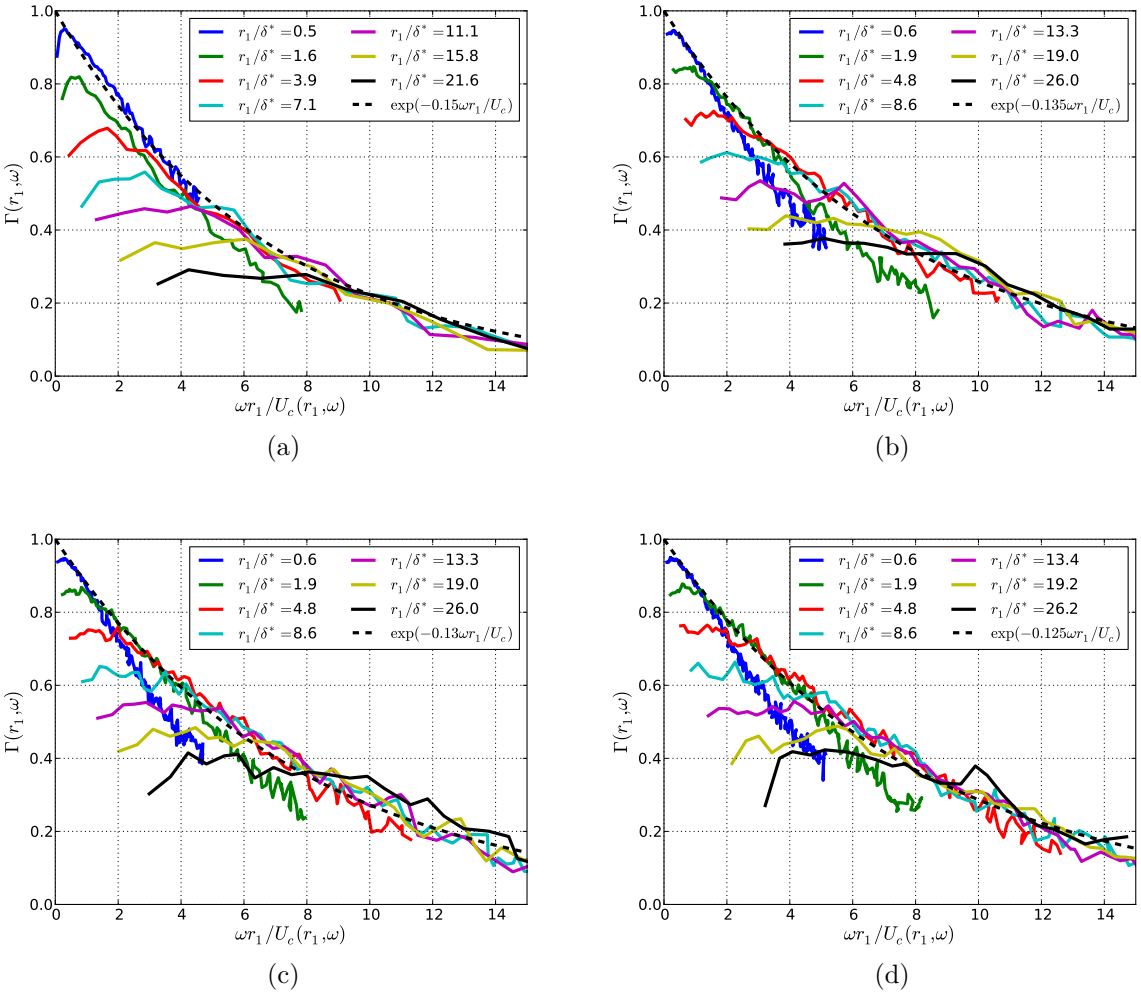

Figure C.6: Streamwise coherence as a function of $\omega r_1/U_c(r_1,\omega)$ for ZPG; (a) $U_0 = 20.3$ m/s; (b) $U_0 = 39.2$ m/s; (c) $U_0 = 49.1$ m/s; (d) $U_0 = 58.7$ m/s.

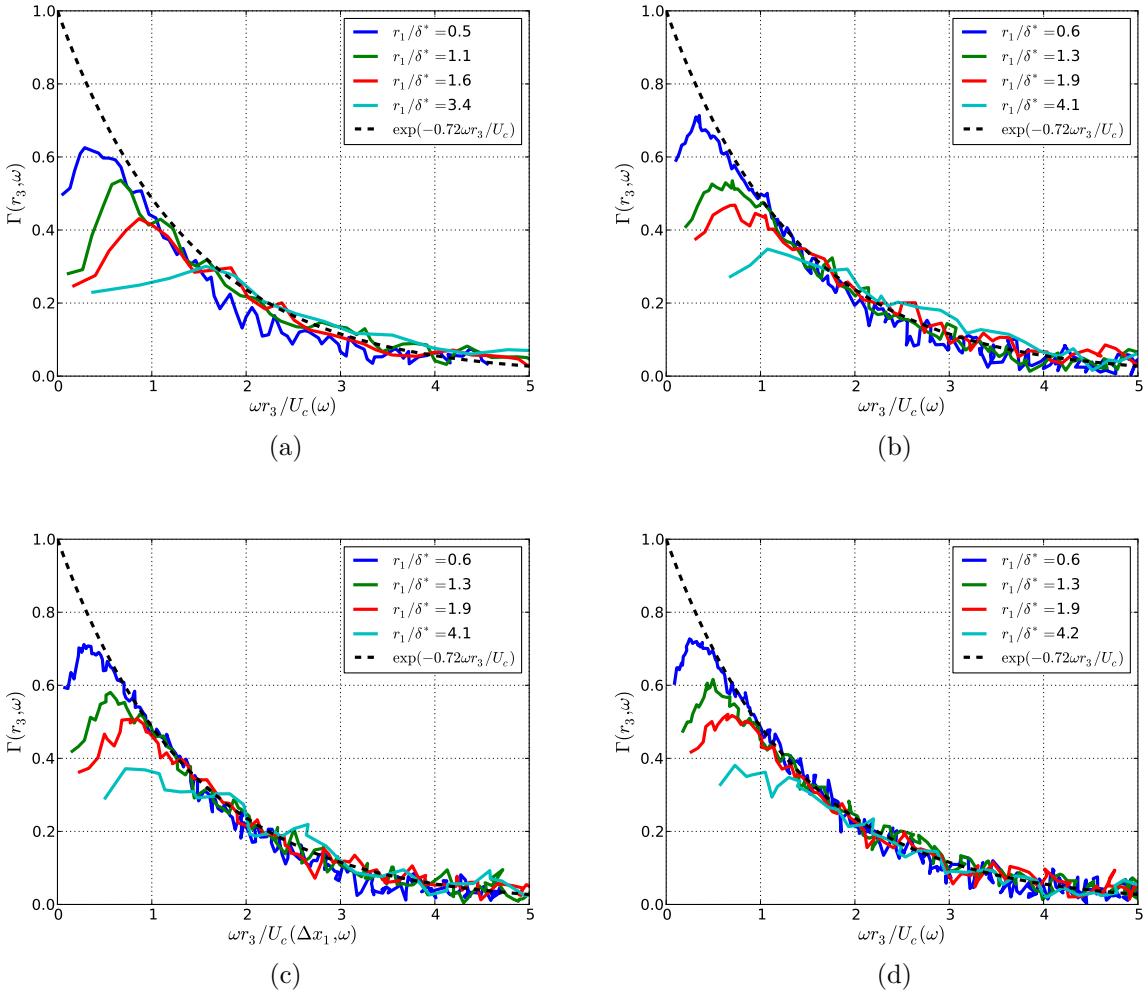

Figure C.7: Spanwise coherence as a function of $\omega r_3/U_c(\omega)$ for ZPG; (a) $U_0 = 20.3$ m/s; (b) $U_0 = 39.2$ m/s; (c) $U_0 = 49.1$ m/s; (d) $U_0 = 58.7$ m/s.

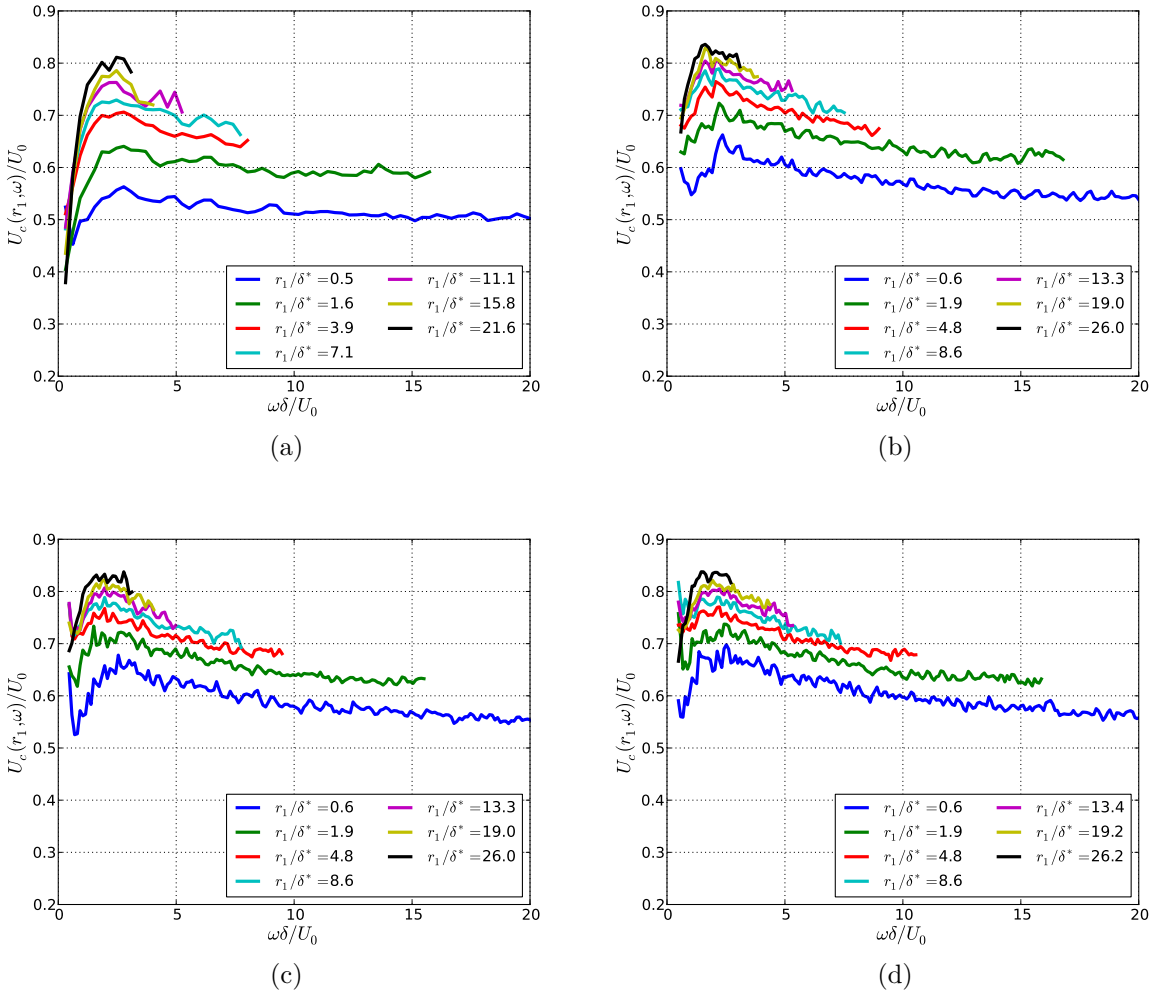

Figure C.8: Phase velocities as a function of $\omega\delta/U_c(r_1,\omega)$ for ZPG; (a) $U_0 = 20.3$ m/s; (b) $U_0 = 39.2$ m/s; (c) $U_0 = 49.1$ m/s; (d) $U_0 = 58.7$ m/s.

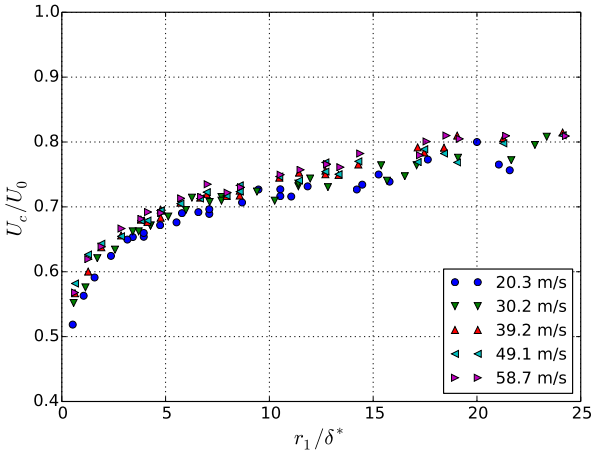

Figure C.9: Mean convection velocity $\overline{U}_c$ for ZPG at different freestream velocities.

References

[1] N. Hu, H. Buchholz, M. Herr, C. Spehr, and S. Haxter, "Contributions of different aeroacoustic sources to aircraft cabin noise," *AIAA Paper 2013-2030*, 2013.

[2] N. Hu, H. Buchholz, M. Herr, C. Spehr, and S. Haxter, "Cabin noise source ranking based on A320 flight test data. In: Aeroacoustics research in Europe: The CEAS-ASC report on 2012 highlights," *J. Sound Vib.*, vol. 332, pp. 6630–6632, 2013.

[3] R. H. Kraichnan, "Pressure fluctuations in turbulent flow over a flat plate," *J. Acoust. Soc. Am.*, vol. 28(3), pp. 378–390, 1956.

[4] W. W. Willmarth, "Wall pressure fluctuations in a turbulent boundary layer," *J. Acoust. Soc. Am.*, vol. 28, pp. 1048–1053, 1956.

[5] W. W. Willmarth and C. E. Wooldridge, "Measurements of the fluctuating pressure at the wall beneath a thick turbulent boundary layer," *J. Fluid Mech.*, vol. 14, pp. 187–210, 1962.

[6] M. K. Bull, "Wall pressure fluctuations associated with subsonic turbulent boundary layer flow," *J. Fluid Mech.*, vol. 28, pp. 719–754, 1967.

[7] W. K. Blake, "Turbulent boundary layer wall pressure fluctuations on smooth or rough walls," *J. Fluid Mech.*, vol. 44(4), pp. 637–660, 1970.

[8] T. M. Farabee and M. J. Casarella, "Spectral features of wall pressure fluctuations beneath turbulent boundary layers," *Phys. Fluids*, vol. A3(10), pp. 2410–2420, 1991.

[9] D. J. J. Leclercq and X. Bohineust, "Modeling the wave-vector frequency spectrum of turbulent boundary layer wall pressure," *J. Sound Vib.*, vol. 257(3), pp. 477–501, 2002.

[10] W. K. Blake and D. M. Chase, "Wavenumber frequency spectra of turbulent-boundary-layer pressure measured by microphone arrays," *J. Acoust. Soc. Am.*, vol. 49, pp. 862–877, 1970.

[11] T. M. Farabee and F. E. Geib, "Measurements of boundary layer pressure fluctuations at low wavenumbers on smooth and rough walls," *Symposium on flow noise modelling, measurement and control*, vol. NCA-Vol. 11/FED-Vol. 130, pp. 55–68, 1991.

[12] B. M. Abraham and W. L. Keith, "Direct measurements of turbulent boundary layer wall pressure wavenumber-frequency spectra," *J. Fluids Eng.*, vol. 120, pp. 29–39, 1998.

[13] B. Arguillat, D. Ricot, G. Robert, and C. Bailly, "Measurements of wavenumber-frequency spectrum of wall pressure fluctuations under turbulent flows," *AIAA Paper 2005-2855*, 2005.

[14] K. Ehrenfried and L. Koop, "Experimental study of pressure fluctuations beneath a compressible turbulent boundary layer," *AIAA Paper 2008-2800*, 2008.

[15] C. Gabriel, S. Müller, F. Ullrich, and R. Lerch, "A new kind of sensor array for measuring spatial coherence of surface pressure on a car's side window.," *J. Sound Vib.*, vol. 333(3), pp. 901–915, 2014.

[16] G. M. Corcos, "Resolution of pressure in turbulence," *J. Acoust. Soc. Am.*, vol. 35, pp. 192–199, 1964.

[17] R. B. Gilchrist and W. A. Strawderman, "Experimental hydrophone-size connection factor for boundary layer pressure fluctuations," *J. Acoust. Soc. Am.*, vol. 38, pp. 298–302, 1965.

[18] P. H. White, "Effect of transducer size, shape, and surface sensitivity on the measurement of boundary layer pressure," *J. Acoust. Soc. Am.*, vol. 41, pp. 1358–1363, 1967.

[19] D. M. Chase, "Turbulent boundary layer pressure fluctuations and wave number filtering by non-uniform spatial averaging," *J. Acoust. Soc. Am.*, vol. 46, pp. 1350–1365, 1969.

[20] M. K. Bull and A. S. W. Thomas, "High frequency wall-pressure fluctuations in turbulent boundary layers," *Phys. Fluids*, vol. 19, pp. 597–599, 1976.

[21] H. R. Mull and J. S. Algranti, "Preliminary flight survey of aerodynamic noise on an airplane wing," tech. rep., NACA RM E55K07, 1956.

[22] T. H. Hodgson, *Pressure fluctuations in shear flow turbulence*. PhD thesis, University of London, 1962.

[23] W. V. Bhat, "Flight test measurement of exterior turbulent boundary layer pressure fluctuations on boeing model 737 airplane," *J. Sound Vib.*, vol. 14(4), pp. 439–457, 1971.

[24] S. A. Rizzi, R. G. Rackl, and E. V. Andrianov, "Flight test measurements from the Tu-144ll structure/cabin noise experiment," tech. rep., NASA/TM-2000-209858, 2000.

[25] D. Palumbo, "Determining correlation and coherence lengths in turbulent boundary layer flight data," *J. Sound Vib.*, vol. 331, pp. 3721–3737, 2012.

[26] C. Spehr, H. Hennings, H. Buchholz, M. Bouhaj, S. Haxter, and A. Hebler, "In-flight sound measurements: A first overview," *AIAA Paper 2012-2208*, 2012.

[27] S. Haxter and C. Spehr, "Two-dimensional evaluation of turbulent boundary layer pressure fluctuations at cruise flight conditions," *AIAA Paper 2012-2139*, 2012.

[28] G. M. Lilley, "Pressure fluctuations in an incompressible turbulent boundary layer," tech. rep., The College of Aeronautics Cranfield, 1960.

[29] W. C. Meecham and M. T. Tavis, "Theoretical pressure correlation functions in turbulent boundary layer," *Phys. Fluids*, vol. 23, pp. 1119–1131, 1980.

[30] D. M. Chase, "Modeling the wave-vector frequency spectrum of turbulent boundary layer wall pressure," *J. Sound Vib.*, vol. 70, pp. 29–68, 1980.

[31] S. Viazzo, A. Dejoan, and R.Schiestel, "Spectral features of the wall-pressure fluctuations in turbulent wall flows with and without perturbations using LES," *J. Heat and Fluid Flow*, vol. 22, pp. 39–52, 2001.

[32] J. Robertson, "Prediction of in-flight fluctuating pressure environments including protuberance induced flow," tech. rep., CR-119947, NASA, Wyle Laboratories, Huntsville Facility, 1971.

[33] B. Efimtsov, "Similarity criteria for the spectra of wall pressure fluctuations in a turbulent boundary layer," *Sov. Phys. Acoust*, vol. 30, pp. 33–35, 1984.

[34] M. Howe, *Acoustics of fluid-structure interactions*. Cambridge University Press, 1998.

[35] A. Smol'yakov, "Calculation of the spectra of pseudospund wall-pressure fluctuations in turbulent boundary layers," *Acoustical Physics*, vol. 3, pp. 342–347, 2000.

[36] M. C. Goody, "Empirical spectral model of surface pressure fluctuations," *AIAA Journal*, vol. 42(9), pp. 1788–1794, 2004.

[37] M. Herr, *Trailing-Edge Noise - Reduction Concepts and Scaling Laws*. PhD thesis, Institute of Aerodynamics and Flow Technology, German Aerospace Center, 2013.

[38] H. H. Schloemer, "Effects of pressure gradients on turbulent-boundary-layer wall-pressure fluctuations," *J. Acoust. Soc. Am.*, vol. 42(1), pp. 93–113, 1967.

[39] T. E. Burton, "Wall pressure fluctuations at smooth and rough surfaces under turbulent boundary layers with favorable and adverse pressure gradients," tech. rep., Acoustics and vibration Lab. Massachusetts Inst. of Technology, 1973.

[40] W. K. Blake, "A statistical description of pressure and velocity fields at trailing edges of a flat strut," tech. rep., David W. Taylor Naval Ship Research and Development Center, 1975.

[41] R. Simpson, M. Ghodbane, and B. McGrath, "Surface pressure fluctuations in a separation turbulent boundary layer," *J. Fluid Mech.*, vol. 177(1), pp. 167–186, 1987.

[42] A. Herrig, *Validation and application of a hot-wire based method for trailing edge noise measurements on airfoils*. PhD thesis, University of Stuttgart, 2012.

[43] M. R. Catlett, J. B. Forest, J. M. Anderson, and D. O. Stewart, "Empirical spectral model of surface pressure fluctuations beneath adverse pressure gradients," *AIAA Paper 2014-2910*, 2014.

[44] E. Salze, C. Bailly, O. Marsden, E. Jondeau, and D. Juvé, "An experimental characterisation of wall pressure wavevector-frequency spectra in the presence of pressure gradients," *AIAA Paper 2014-2909*, 2014.

[45] A. Suryadi and M. Herr, "Wall pressure spectra on a du96-w-180 profile from low to pre-stall angles of attack," *AIAA Paper 2015-2688*, 2015.

[46] Y. Rozenberg, G. Robert, and S. Moreau, "Wall-pressure spectral model including the adverse pressure gradient effects," *AIAA Journal*, vol. 50(10), pp. 2168–2179, 2012.

[47] M. Kamruzzaman, D. Bekiropoulos, T. Lutz, and W. Würz, "A semi-empirical surface pressure spectrum model for airfoil trailing-edge noise prediction," *International journal of aeroacoustics*, vol. 14, 2015.

[48] M. R. Catlett, J. M. Anderson, J. B. Forest, and D. O. Stewart, "Empirical modeling of pressure spectra in adverse pressure gradient turbulent boundary layers," *AIAA Journal*, vol. 54(2), 2016.

[49] R. L. Panton and J. H. Linebarger, "Wall pressure spectra for equilibrium boundary layers," *J. Fluid Mech.*, vol. 65, pp. 261–287, 1974.

[50] W. K. Blake, *Mechanics of flow-induced sound and vibration.* Academic Press, Inc., 1986.

[51] G. M. Corcos, "The structure of the turbulent pressure field in boundary layer flows," *J. Fluid Mech.*, vol. 18, pp. 353–378, 1964.

[52] J. E. F. Williams, "Boundary layer pressures and the Corcos model: a development to incorporate low-wavenumber constraints," *J. Fluid Mech*, vol. 125, pp. 9–25, 1982.

[53] D. M. Chase, "The character of the turbulent wall pressure spectrum at subconvective wavenumbers and a suggested comprehensive model," *J. Sound Vib.*, vol. 112, pp. 125–147, 1987.

[54] P. R. Spalart, "Direct simulation of a turbulent boundary layer up to Re_θ =1410," *J. Fluid Mech.*, vol. 187, pp. 61–98, 1988.

[55] J. Kim, "On the structure of pressure fluctuations in simulated turbulent channel flow," *J. Fluid Mech.*, vol. 205, pp. 421–451, 1989.

[56] H. Choi and P. Moin, "On the space-time characteristics of wall-pressure fluctuations," *Phys. Fluids*, vol. A2(8), pp. 1450–1460, 1990.

[57] P. Chang, U. Piomelli, and W. K. Blake, "Relationship between wall pressure and velocity-field sources," *Phys. Fluids*, vol. 11, pp. 3434–3448, 1999.

[58] X. Gloerfelt and J. Berland, "Turbulent boundary-layer noise: direct radiation at mach number 0.5," *J. Fluid Mech.*, vol. 723, pp. 318–351, 2013.

[59] M. Siefert, R. Ewert, H. Olaf, and U. Oliver, "A synthetic wall pressure model for the efficient simulation of boundary layer induced cabin noise," *AIAA Paper 2010-3760*, 2010.

[60] M. Alaoui, X. Gloerfelt, O. Collery, and M. Etchessahar, "Effect of pressure gradients on turbulent boundary layer vortical structures and wall pressure fluctuations," *AIAA Paper 2015-3116*, 2015.

[61] W. W. Willmarth, "Pressure fluctuations beneath turbulent boundary layers," *Annu. Rev. Fluid Mech.*, vol. 7, pp. 13–38, 1975.

[62] M. K. Bull, "Wall-pressure fluctuations beneath turbulent boundary layers: some reflections on forty years of research," *J. Sound Vib.*, vol. 190(3), pp. 299–315, 1996.

[63] L. J. Peltier and S. A. Hambric, "Estimating turbulent-boundary-layer wall-pressure spectra from CFD RANS solutions," *J. Fluids and Structures*, vol. 23, pp. 920–937, 2007.

[64] A. V. Johansson, J. Y. Her, and J. H. Haritonidis, "On the generation of high-amplitude wall-pressure peaks in turbulent boundary layers and spots," *J. Fluid Mech.*, vol. 175, pp. 119–142, 1987.

[65] R. Parchen, "Progress report DRAW, a prediction scheme for trailing edge noise based on detailed boundary layer characteristics," tech. rep., TNO Institute of Applied Physics, TU Delft, 1998.

[66] H. L. Grant, "The large eddies ofturbulent motion," *J. Fluid Mech.*, vol. 4, pp. 149–190, 1958.

[67] A. J. Favre, "Review on space-time correlations in turbulent fluids," *J. Appl. Mech.*, vol. 32, pp. 241–257, 1965.

[68] M. Kamruzzaman, T. Lutz, A. Herrig, and E. Krämer, "Semi-empirical modeling of turbulent anisotropy for airfoil self-noise predictions," *AIAA Journal*, vol. 50(1), pp. 46–60, 2012.

[69] C. Rautmann, J. Dierke, R. Ewert, N. Hu, and J. Delfs, "Generic airfoil trailing-edge noise prediction using stochastic sound sources from synthetic turbulence," *AIAA Paper 2014-3298*, 2014.

[70] M. Herr, R. Ewert, C. Rautmann, M. Kamruzzaman, D. Bekiropoulos, A. Iob, R. Arina, P. Batten, S. Chakravarthy, and F. Bertagnolio, "Broadband trailing-edge noise predictions - overview of BANC-III results," *AIAA Paper 2015-2847*, 2014.

[71] J. A. Sillero, J. Jiménez, and R. D. Moser, "Two-point statistics for turbulent boundary layers and channels at Reynolds numbers up to $\delta^+ \approx 2000$," *Phys. Fluids*, vol. 26, pp. 1–30, 2014.

[72] G. I. Taylor, "Diffusion by continuous movements," *Proc. London Math. Soc.*, vol. 20, pp. 196–212, 1922.

[73] S. P. Gravante, A. M. Naguib, C. E. Wark, and H. M. Nagib, "Characterization of the pressure fluctuations under a fully developed turbulent boundary layer," *AIAA Journal*, vol. 36(10), pp. 1808–1816, 1998.

[74] M. C. Goody and R. L. Simpson, "Surface pressure fluctuations beneath two- and three-dimensional turbulent boundary layers," *AIAA Journal*, vol. 38(10), pp. 1822–1831, 2000.

[75] R. W. Hockney and J. W. Eastwood, *Computer simulation using particles*. Taylor & Francis, Inc., 1988.

[76] B. Efimtsov, "Characteristics of the field of turbulent wall pressure fluctuations at large reynolds numbers," *Sov. Phys. Acoust*, vol. 28, pp. 289–292, 1982.

[77] F. H. Clauser, "Turbulent boundary layers in adverse pressure gradients," *Journal of the Aeronautical Sciences*, vol. 21(2), pp. 91–108, 1954.

[78] A. Wolf, M. Kamruzzaman, W. Würz, T. Lutz, and E. Krämer, "Wall pressure fluctuation (WPF) and trailing-edge noise measurements on a NACA64-418 airfoil," tech. rep., Institute of Aerodynamics and Gas Dynamics, University of Stuttgart, 2009.

[79] Y. Rozenberg, *Modélisation analytique du bruit aérodynamique à large bande des machines tournantes: utilisation de calculs moyennés de mécanique des fluides*. PhD thesis, L' École Centrale de Lyon, 2007.

[80] F. Bertagnolio, "Boundary layer measurements of the NACA0015 and implications for noise modeling," tech. rep., RISOE DTU, National Laboratory for Sustainable Energy, 2011.

[81] A. Garcia-Sagrado and T. Hynes, "Stochastic estimation of flow near the trailing edge of a NACA0012 airfoil," *Experiments in Fluids*, vol. 51, pp. 1057–1071, 2011.

[82] T. F. Brooks and T. H. Hodgson, "Trailing edge noise prediction from measured surface pressure," *J. Sound Vib.*, vol. 78(1), pp. 69–117, 1981.

[83] G. L. Mellor and D. M. Gibson, "Equilibrium turbulent boundary layers," *J. Fluid Mech.*, vol. 24(2), pp. 225–253, 1966.

[84] D. Cole, "The law of the wake in the turbulent boundary layer," *J. Fluid Mech.*, vol. 1(2), pp. 191–226, 1956.

[85] F. M. White, *Viscous fluid flow*. McGraw-Hill Inc., 2nd ed., 1991.

[86] M. Pott-Pollenske and J. Delfs, "Enhanced capabilities of aeroacoustics wind tunnel Braunschweig," *AIAA Paper 2008-2910*, 2008.

[87] R. Ewert, J. Dierke, J. Siebert, A. Neifeld, C. Appel, M. Siefert, and O. Kornow, "CAA broadband noise prediction for aeroacoustic design," *J. Sound Vib.*, vol. 330, pp. 4139–4160, 2011.

[88] H. Schlichting, *Boundary-layer theory*. McGraw-Hill Inc., 1968.

[89] H. Buchholz and A. Buschbaum, "Geschwindigkeitsverteilungen im Freistahl des akustischen Windkanals in Braunschweig (AWB) mit der $0.8 \times 1.2 m^2$ Rechteckdüse," tech. rep., Internal DLR Report, 1996.

[90] R. Narasimha and S. N. Prasad, "Leading edge shape for flat plate boundary layer studies," *Experiments in Fluids*, vol. 17(5), pp. 358–360, 1994.

[91] M. M. Mosallem, "Numerical and experimental investigation of beveled trailing edge flow fields," *Journal of Hydrodynamics*, vol. 20(3), pp. 273–279, 2008.

[92] R. Ewert, "Canonical stochastic realization of turbulent sound sources via forced linear Advection-Diffusion-Dissipation equation," *AIAA Paper 2016-2965*, 2016.

[93] D. C. Wilcox, *Turbulence modeling for CFD*. DCW Industries, Inc., La Cañada, California, 3rd ed., 2006.

[94] C. Bailly and D. Juvé, "A stochastic approach to compute subsonic noise using linearized Euler's equations," *AIAA Paper 1999-1872*, 1999.

[95] C. K. W. Tam and L. Auriault, "Jet mixing noise from fine-scale turbulence," *AIAA Journal*, vol. 37(2), pp. 145–153, 1999.

[96] G. K. Batchelor, *The Theory of Homogeneous Turbulence*. Cambridge Science Classics, Press Syndicate of the University of Cambridge, 1982.

[97] R. Ewert, "Broadband slat noise prediction based on CAA and stochastic sound sources from a fast random particle-mesh (RPM) method," *Computers & Fluids*, vol. 37, pp. 369–387, 2008.

[98] S. Pope, *Turbulent flows*. Cambridge University Press, 2000.

[99] M. Siefert and R. Ewert, "Sweeping sound generation in jets realized with a random particle-mesh method," *AIAA Paper 2009-3369*, 2009.

[100] D. B. Spalding, "A single formula for the law of the wall," *J. Appl. Mech.*, vol. 28, pp. 455–457, 1961.

[101] D. E. Coles and E. A. Hirst, "Computation of turbulent boundary layers," *AFOSRIFP Stanford Conference*, vol. 2, 1968.

[102] J. Nikuradse, "Turbulente reibungsschichten an der platte," *ZWB, R.Oldenbourg, München and Berlin*, 1942.

[103] K. A. Chauhan, P. A. Monkewitz, and H. M. Nagib, "Criteria for assessing experiments in zero pressure gradient boundary layers," *Flud Dyn. Res.*, vol. 41, p. 021404, 2009.

[104] H. J. Herring and J. F. Norbury, "Some experiments on equilibrium turbulent boundary layers in favorable pressure gradients," *J. Fluid Mech.*, vol. 27(3), pp. 541–549, 1967.

[105] P. A. Chang, "Wavenumber-frequency characteristics of partial wall pressures from large eddy simulations of a turbulent channel flow," tech. rep., Naval Surface Warfare Center, 2001.

[106] A. Suryadi, S. Martens, and M. Herr, "Trailing-edge noise reduction technologies for applications in wind energy," *AIAA Paper 2017-3534*, 2017.

[107] N. Hu and L. Erbig, "Effect of flush-mounted sensors and upstream flow development on measured wall pressure spectra," *AIAA Paper 2018-3276*, 2018.

[108] R. M. Lueptow, "Transducer resolutionn and the turbulent wall pressure spectrum," *J. Acoust. Soc. Am.*, vol. 97 (1), 1995.

[109] A. V. Smol'yakov and V. M. Tkachenko, *The measurement of turbulent fluctuations: an introduction to hot-wire anemometry and related transducers.* Springer-Verlag, Berlin Heidelberg New York, 1983.

[110] D. Schwamborn, T. Gerhold, and R. Kessler, "DLR-TAU code - an overview," *1st ONERA/DLR Aerospace Symposium, Paris*, 1999.

[111] D. Schwamborn, T. Gerhold, and R. Heinrich, "The DLR TAU-Code: recent applications in research and industry," *ECCOMAS CFD 2006: Proceedings of the European Conference on Computational Fluid Dynamics*, 2006.

[112] G. Eitel-Amor, R. Örlü, and P. Schlatter, "Simulation and validation of a spatially evolving turbulent boundary layer up to Re_θ =8300," *Int. J. Heat Fluid Flow*, vol. 47, pp. 57–69, 2014.

[113] C. E. Wooldridge and W. W. Willmarth, "Measurements of the correlation between the fluctuating velocities and the fluctuating wall pressure in a thick turbulent boundary layer," tech. rep., The university of Michigan, Department of Aeronautical and Astronautical Engineering, 1962.

[114] J. Jiménez, S. Hoyas, M. P. Simens, and Y. Mizuno, "Turbulent boundary layers and channels at moderate Reynolds numbers," *J. Fluid Mech.*, vol. 657, pp. 335–360, 2010.

[115] P. Schlatter, R.Örlü, Q. Li, J. Fransson, A. Johansson, P. H. Alfredsson, and D. S. Henningson, "Turbulent boundary layers up to Re_θ through simulation and experiments," *Phys. Fluids*, vol. 21, p. 05702, 2009.

[116] S. Hoyas and J. Jiménez, "Scaling of the velocity fluctuations in turbulent channels up to Re_τ =2003," *Phys. Fluids*, vol. 18, p. 011702, 2006.

[117] V. Togiti and B. Eisfeld, "Assessment of g-equation formulation for a second-moment Reynolds stress turbulence model," *AIAA Paper 2015-2925*, 2015.

[118] S. Haxter and C. Spehr, "In-flight determination of acoustic and hydrodynamic pressure fluctuations," *DAGA Paper*, 2013.

[119] N. Hu, "Simulation of wall pressure fluctuations for high subsonic and transonic turbulent boundary layers," *DAGA Paper*, 2017.

[120] D. G. Crighton, A. P. Dowling, J. E. F. Williams, M. Heckl, and F. G. Leppington, *Modern Methods in Analytical Acoustics.* Lecture Notes, Springer-Verlag, 1992.

[121] N. Hu and M. Herr, "Characteristics of wall pressure fluctuations for a flat plate turbulent boundary layer with pressure gradients," *AIAA Paper 2016-2749*, 2016.

[122] N. Hu, C. Appel, M. Herr, N. Reiche, and R. Ewert, "Numerical study of wall pressure fluctuations for zero and non-zero pressure gradient turbulent boundary layers," *AIAA 2016-2911*, 2016.

[123] N. Hu, N. Reiche, and R. Ewert, "Numerical investigation for wall pressure fluctuations using synthetic turbulence. In: Aeroacoustics research in Europe: The CEAS-ASC report on 2015 highlights," *J. Sound Vib.*, vol. 381, pp. 109–110, 2016.

[124] N. Hu, "Empirical spectral model of wall pressure fluctuations including adverse pressure gradient effects," *AIAA Paper 2017-3203*, 2017.

[125] N. Hu, N. Reiche, and R. Ewert, "Numerical investigation of wall pressure fluctuations for zero and adverse pressure gradient turbulent boundary layers using synthetic anisotropic turbulence," *AIAA Paper 2017-3200*, 2017.

[126] N. Hu, N. Reiche, and R. Ewert, "Simulation of turbulent boundary layer wall pressure fluctuations via Poisson equation and synthetic turbulence," *J. Fluid Mech.*, vol. 826, pp. 421–454, 2017.

[127] N. Hu, "Empirical model of wall pressure one-point spectra beneath zero and adverse pressure gradient boundary layers. In: Aeroacoustics research in Europe: The CEAS-ASC report on 2016 highlights," *J. Sound Vib.*, vol. 427, pp. 194–195, 2018.

[128] N. Hu, "Empirical model of wall pressure spectra in adverse pressure gradients," *AIAA Journal (Accepted)*, 2018.